ABSTRACT

MOHAMED, WALID MOHAMED FAROUK. Influence of Fast Neutron Irradiation on Mechanical Properties and Microstructure of Nanocrystalline Copper. (Under the direction of Dr. K. L. Murty and Dr. Jacob Eapen).

The development of advanced nuclear energy systems, both fission and fusion, has accelerated the search for a new class of materials with superior radiation resistance. Degradation of materials properties is attributed to the accumulation of early irradiation induced point defects such as vacancies and interstitials followed by the formation of more complex extended defects such as dislocations, twins and voids that lead to macroscopic changes such as hardening and embrittlement. Therefore, the ability to remove the incipient point defects is a key material characteristic which can enhance the radiation tolerant behavior of nuclear fuel, clad and structural materials.

Recently it is hypothesized that grain boundaries and interfaces can act as sinks for radiation–induced point defects. This suggests that materials with a large volume of internal interfaces can exhibit enhanced radiation resistance. Polycrystalline materials with grain sizes that are of the order of 100 nm, often classified as nanocrystalline (*nc*) materials, exhibit superior strength as well as appealing thermo–mechanical properties. As nanocrystalline materials also have a large volume of interfaces compared to conventional materials with micrometer sized grains, they are candidate materials for enhanced radiation tolerance.

In this dissertation, the effect of neutron irradiation is investigated on nanocrystalline copper (*nc*-copper) samples with a mean grain size of 34 nm along with conventional copper samples with a mean grain size of 38 μm. Alongside, molecular dynamics (MD) simulations

are performed on controlled grain boundary interfaces and irradiation conditions for understanding the atomistic mechanisms of possible radiation tolerant behavior. In the experimental investigation, *nc* and conventional copper samples are irradiated in the NC State PULSTAR reactor and the Advanced Test Reactor (ATR) at Idaho National Laboratory (INL) at difference neutron fluences which correspond to 0.0034, 1 and 2 displacements per atom (*dpa*). Radiation hardening and embrittlement are observed in conventional copper at all neutron exposures. On the other hand, at low exposures (0.0034 *dpa*), *nc*-copper undergoes athermal grain growth manifested by a notable increase in the average grain size, accompanied by a reduction in the strength. As the grain size saturates at higher exposures (2 *dpa*), radiation hardening and embrittlement become the predominant response.

Microstructural investigations using electron microscopy reveal regions of high dislocations density as well as twins in the irradiated samples. Although the response of *nc*-copper is found to be controlled by the aforesaid dual mechanism, the mechanical behavior of irradiated nc-copper is found to obey the Hall-Petch relationship. Analysis of the yield stress data shows that friction hardening is the main mechanism for yielding in irradiated *nc*-copper whereas the contribution of source hardening to yielding is relatively small due to the observed increase in the grain size. Annealing experiments followed by hardness measurements reveal that the grain growth observed in *nc*-copper is not thermally induced; however, investigation of the dominant mechanism underlying the observed grain growth has not been experimentally quantified. Furthermore, the uncontrollable grain growth in the irradiated *nc*-copper samples has precluded further investigations which could have assessed the role of interfaces in enhancing radiation resistance in *nc*-materials.

Molecular Dynamics (MD) simulations have the power to investigate mechanisms at the atomistic level with controlled conditions and geometries which are often not accessible with experiments, albeit for small sample sizes and short durations of time. Using MD simulations, the role of thermally stable interfaces is investigated by monitoring the fast irradiation dynamics in copper with twist bicrystal configurations. Results show that statistically averaged atomic displacements are controlled by a hyperfast, correlated dynamic mechanism which allows interfaces to attract highly mobile atoms regardless of the direction of the impact. The interfaces are also found to hamper the motion of atoms following a radiation impact and thus they represent a sink for the point defects which are generated in the system. Comparing the behavior of a twist Σ5 interface with that of a Σ41 twist interface, it is observed that the ability of an interface to attract atoms increases as the degree of disorder of the interface structure increases. The attraction of displaced atoms toward interfaces is attributed to the evolution of a stress gradient at the interface which represents the driving force for atom migration following impact. It is thus concluded that presence of interfaces can promote radiation resistance of materials through hyperfast correlated dynamics followed by relatively slower diffusion mechanisms that are reported in the literature.

Influence of Fast Neutron Irradiation on Mechanical Properties and Microstructure of Nanocrystalline Copper

by
Walid Mohamed Farouk Mohamed

A dissertation submitted to the Graduate Faculty of
North Carolina State University
in partial fulfillment of the
requirements for the degree of
Doctor of Philosophy

Nuclear Engineering

Raleigh, North Carolina

2012

APPROVED BY:

Dr. K. L. Murty Committee Chair	Dr. Jacob Eapen Committee Co-Chair
Dr. A. I. Hawari Advisory Committee member	Dr. R. O. Scattergood Advisory Committee member

DEDICATION

To my dear parents

To my lovely kids, NourEldeen and Moamin

To my beloved wife, Heba

BIOGRAPHY

Walid Mohamed was born in Damanhour city, Egypt in 1979. Until the age of 18, Walid was living with his parents and two brothers after which, he moved to Alexandria to enroll in the department of nuclear engineering at the Alexandria University. In his undergraduate study, Walid excelled in academics and received the top of the batch award for the academic years – 1999, 2000, 2001, and 2002. Walid secured 1st rank in the graduating Bachelor of Science (B. Sc.) class of 2002 from Alexandria University in the nuclear engineering program.

After graduation Walid enrolled in the military service during which he pursued a Master of Science (MS) degree in nuclear engineering. He graduated in early 2005. Following exceptionally strong academic performance, both in the undergraduate and graduate studies, Walid was offered a faculty position at the Alexandria University which required him to start pursuing a doctoral degree in nuclear engineering.

By Fall 2005, Walid joined the nuclear engineering department at NC State University and began to pursue a doctoral degree in the field of nuclear materials. Since his research was on the state–of–the–art applications of nanoscience and technology, Walid obtained a MS degree in materials science and engineering from NC State University. His research for the doctoral degree focused on studying radiation effects on nanocrystalline metals and alloys which are candidate radiation tolerant materials for advanced nuclear energy systems. Walid utilized both experimental and simulation approaches in his research under the supervision of Dr. K. L. Murty and Dr. Jacob Eapen.

ACKNOWLEDGMENTS

I am so grateful to God (ALLAH) for providing me with the power and patience to have this work accomplished.

I would like to express my heartfelt gratitude to Dr. K. L. Murty for the invaluable support and guidance he provided me during my PhD work. He was very understanding and encouraging during the time I spent under his supervision. I would also like to thank Dr. Murty for giving me the opportunity to develop and improve my teaching skills.

I am also grateful to Dr. Jacob Eapen for advising me on the computational and simulation work. Dr. Eapen dedicated a lot of his time for discussing research progress, code development and data analysis. Let me also mention that the idea of investigating fast dynamics via MD simulations belongs to him.

I would like to thank Dr. Ayman Hawari, as a committee member and the Director of the Nuclear Reactor Program, for the support and advice in conducting the irradiation experiments at the PULSTAR reactor. I would also like to thank Dr. Ronald Scattergood for his valuable time serving as a committee member of my dissertation.

I would like to express my appreciation for those who supported me over my PhD work at the NC State University with special thanks to Ms. Hermine Kabbendjan, as well as to my present and former colleagues in the Nuclear Materials Group, especially, Dr. Srikant Gollapudi. I would also like to thank Dr. Todd Allen, Dr. Mitchell Meyer, Dr. Douglas Porter, Dr. Brandon Miller, and Ms. Mary Catherine Thelen at INL for their support during my experimental work at INL.

I would like to greatly acknowledge the NSUF-ATR support through the U. S. Department of Energy (DOE), Office of Nuclear Energy under DOE Idaho Operations Office Contract DE-AC07-051D14517.

Finally, I am so grateful to my wife for her daily support, kindness and encouragement since the first day of our marriage.

TABLE OF CONTENTS

List of Tables ……..……..ix

List of Figures ……..……..xi

Chapter 1. Introduction and Overview 1

Chapter 2. Background and Literature Survey 7

2.1 Nanocrystalline Materials 7

2.1.1 Classification and synthesis 8

2.1.2 Structure 9

2.2 Mechanical Properties of Nanocrystalline Materials 10

2.3 Thermal Stability of Nanocrystalline Materials 12

2.4 Radiation Impact on Nanocrystalline Materials 14

2.4.1 Enhanced radiation resistance of *nc* materials 15

2.4.2 Structure instability of irradiated nanocrystalline materials 21

Chapter 3. Experimental Procedures and Irradiation 26

3.1 Microstructure Characterization of As-Received Materials 26

3.1.1 Optical microscopy of as-received materials 29

3.1.2 Grain size analysis via X-ray diffraction (XRD) 31

3.1.3 Atomic force microscopy (AFM) of *nc*-copper 34

3.1.4 Pre-Irradiation transmission electron microscopy (TEM) 36

3.2 Mechanical Properties of As-Received Materials 40

3.2.1 Micro-hardness measurements of as-received materials 41

3.2.2 Tensile testing of as-received materials 44

3.3 Irradiation Experiments 53

3.3.1 Simplified model for damage calculations 53
3.3.2 The Kinchin and Pease (K-P) model to calculate ν(T) 55
3.3.3 Irradiation experiments at ATR 59
3.3.4 Irradiation experiment at PULSTAR 66
3.3.5 Damage calculations via MCNP 71
3.4 Chapter Summary 72
Chapter 4. Post Irradiation Examination and Discussion 73
4.1 PIE of Micrograined Copper 73
4.1.1 Microhardness of irradiated MG-copper 74
4.1.2 Mechanical properties of irradiated MG-copper 76
4.1.3 Microstructure of irradiated MG-copper 82
4.2 PIE of Nanocrystalline Copper 92
4.2.1 Microhardness of irradiated nc-copper 92
4.2.2 Mechanical properties of irradiated *nc*-copper 94
4.2.3 Microstructure of irradiated *nc*-copper 97
4.3 Grain Growth of nc-Copper 112
4.3.1 Thermal stability of as-received nc-copper 112
4.3.2 Investigation of grain growth via differential scanning calorimetry 115
4.3.3 Grain growth of irradiated *nc*-copper 117
4.4 Overall Radiation Response of Polycrystalline Copper 122
4.5 Chapter Summary 130
Chapter 5. Radiation Tolerance Behavior at Interfaces: A Molecular Dynamics Investigation 131
5.1 Literature Survey 132

5.1.1 Nanostructured materials 132
5.1.2 Cascade simulations on single crystals 135
5.1.3 Cascade simulations on nanostructured systems 136
5.2 Molecular Dynamics Simulations: Methodology 141
5.2.1 Embedded Atom Method (EAM) potential for copper 142
5.2.2 Single crystal copper 148
5.2.3 Construction of copper bicrystals 150
5.3 Radiation Cascade Simulations: Analysis, Results, and Discussions 155
5.3.1 Local density and structure with RDF and CNA 156
5.3.2 Dynamical propensity using iso-configurational ensemble 159
5.3.3 Directional atomic displacement 165
5.3.4 Influence of knock position and knock energy 169
5.3.5 Effect of interface structure 172
5.4 Stress Differential Mechanism for Atom Migration 173
5.4.1 Stress field mapping 174
5.4.2 Temporal variation of interface stress 176
5.5 Chapter Summary 181
Chapter 6. Conclusions and Outlook 183
References 188
Appendices 198
Appendix A 199
Damage Calculations via MCNP 199
(A.1) Methodology 199

(A.2) Simulation and calculations 200
Appendix B 204
Property Evaluation with molecular Dynamics Simulations 204
(B.1) Reduced units 204
(B.2) Potential and force calculations 204
(B.3) Temperature and pressure 206
(B.4) Radial distribution function (RDF) 206
(B.5) Evaluation of viscosity 207
(B.6) Space-time correlation functions 207

LIST OF TABLES

Table 2-1: Synthesis methods of nanocrystalline materials. 8
Table 2-2: Example studies showing enhanced radiation resistance of *nc*/ ultrafine materials 17
Table 3-1: The different microstructural characterization techniques utilized in the present study 27
Table 3-2: Etchants used for optical microscopy of copper 29
Table 3-3: The average grain size of nc-copper obtained from different techniques 40
Table 3-4: Mechanical properties of as received materials from tensile testing 47
Table 3-5: Atomic abundance of naturally occurring copper isotopes 60
Table 3-6: Cross section data for damage calculations 60
Table 4-1: Microhardness measurements of irradiated MG-copper 75
Table 4-2: Mechanical properties of MG-copper at all tested damage levels. 77
Table 4-3: Microhardness measurements of irradiated nc-copper 93
Table 4-4: Mechanical properties of nc-copper at all tested damage levels. 95

LIST OF FIGURES

Figure 1-1: Flow chart showing the main procedures involved in the present study. 5
Figure 2-1: The "loading - unloading" self-healing mechanism observed in nanostructured materials. Interstitials are attracted "loaded" to the grain boundary after which, it is unloaded back to annihilate the vacancies in the bulk [60]. 21
Figure 2-2: Grain growth observed in metals upon 600 keV Xe ions irradiation [64]. 23
Figure 2-3: The variation of defect density with grain size observed in (a) ZrO_2 and, (b) Pd irradiated by 4 MeV Kr ions [55]. 25
Figure 3-1: SEM-EDS identifying the main x-ray peaks of copper. 28
Figure 3-2: SEM-EDS identifying the main x-ray peaks of nc-copper. 28
Figure 3-3: Optical micrograph of MG-copper with average grain size ~ 38+12 μm. 30
Figure 3-4: Grain size distribution (GSD) of as received MG-copper. 30
Figure 3-5: XRD peaks of MG- copper with the major reflections peaks identified. 32
Figure 3-6: XRD peaks of nc- copper with the major reflections peaks identified. 33
Figure 3-7: AFM of as-received nc-copper. 34
Figure 3-8: Grain size distribution of nc-copper corresponding to AFM analysis showing average grain size of 47.87+15.58 nm. 35
Figure 3-9: Bright Field (BF) TEM image of micrograined copper. 37
Figure 3-10: BF TEM image of micrograined copper showing twin structure. 37
Figure 3-11: BF TEM image of nc-copper. 38
Figure 3-12: Corresponding diffraction pattern of nc-copper shown in Figure 3-11. 38
Figure 3-13: GSD of nc-copper based on TEM analysis showing average grain size of 28.32+10.93 nm. 39
Figure 3-14: Microhardness measurements over 8 mm X 6 mm disk of MG-copper with average hardness = 0.596+0.02 GPa. 42
Figure 3-15: Microhardness measurements of nc-copper over a 8 mm X 6 mm disk with average hardness = 2.5+0.05 GPa. 43
Figure 3-16: Variation of hardness with $D^{-1/2}$ for *nc*-copper. 44

Figure 3-17: Individual components of miniature tensile tester: step motor, smart step to regulate the step motor, signal conditioner to smooth displacement and load signals for data acquisition, grips holding samples while load is applied. 46
Figure 3-18: Miniature tensile tester in vertical positioning. 46
Figure 3-19: Schematic design of sub-size tensile sample. 47
Figure 3-20: Engineering stress-strain curves of as received materials with the corresponding TEM micrographs (before deformation) shown for each structure. 48
Figure 3-21: SEM of MG-copper under tension condition showing dull fracture surface indicating ductile nature of fracture. 50
Figure 3-22: Surface topography of fractured MG-copper showing the cup side of the fracture surface occurring in ductile fracture. 50
Figure 3-23: SEM of nc-copper under tension condition showing shear bands as a sign of brittle fracture. 51
Figure 3-24: Surface topography of fractured nc-copper showing approximately 45^{o} shear band at which maximum shear stress is achieved in brittle fracture. 51
Figure 3-25: Formation of dimples under tensile loading of as received MG-copper (top) and equivalent SEM surface topography seen in copper under the same loading condition [79]. 52
Figure 3-26: General procedure for dpa calculations. 54
Figure 3-27: Variation of $\nu(T)$ according to K-P model [81]. 56
Figure 3-28: ATR core cross section showing the irradiation position E-7 [82]. 59
Figure 3-29: Sample/holder design of the irradiation experiment at ATR. 63
Figure 3-30: Test train design of the irradiation experiment at ATR. 64
Figure 3-31: Test assembly for the irradiation experiemtnt at ATR East Flux Trap Position. 65
Figure 3-32: PULSTAR core cross section showing the irradiation position at radiation exposure port W (REPW). 66
Figure 3-33: Variation of induced activity with time where t_o is the irradiation time, and (t_2-t_1) is the counting time. 68
Figure 3-34: The irradiation capsule loaded in a Cd wrapped aluminum column for the PULSTAR reactor irradiation experiment. 70

Figure 4-1: Microhardness measurements of MG-copper post 0.0034 dpa irradiation showing average hardness of 0.747+0.017 GPa. 74
Figure 4-2: Variation of hardness of MG-copper with damage level. 75
Figure 4-3: Stress-strain curves of irradiated MG-copper. 76
Figure 4-4: Variation of yield and ultimate tensile stresses with damage level. The difference between yield and ultimate tensile stress decreases as dpa increases and it approaches minim at 2 *dpa*. 78
Figure 4-5: Variation of uniform and total elongation with dpa. Both e_u and e_t as well as the strain hardening exponent "*n*" decreases as dpa increases. 79
Figure 4-6: Back projection of stress-strain curve to determine the source hardening term [43]. 81
Figure 4-7: Optical microscopy of MG-copper irradiated at 0.0034 dpa with average grain size of ~ 39+7 μm. 83
Figure 4-8: Optical microscopy of MG-copper irradiated at 1 dpa with average grain size of ~ 37+11 μm. 83
Figure 4-9: Optical microscopy of MG-copper irradiated at 2 dpa with average grain size of ~ 49+14 μm. 84
Figure 4-10: BF TEM micrograph of MG-copper irradiated at 0.0034 *dpa* with dislocations network/loops in grain interior. 85
Figure 4-11: Dislocations observed in MG-copper at 1 *dpa*. 86
Figure 4-12: Dislocation structure at grain boundaries observed in MG-copper at 1 *dpa*. 86
Figure 4-13: BF TEM micrograph of MG-copper at 2 *dpa* showing formation of twins. 87
Figure 4-14: BF TEM showing high density of twins in MG-copper at 2 *dpa*. 88
Figure 4-15: BF TEM of MG-copper at 2 *dpa* showing formation of high dislocation density. 88
Figure 4-16: Fracture surface of MG-copper irradiated to 0.0034 *dpa*. 89
Figure 4-17: Fracture surface of MG-copper irradiated to 1 *dpa* showing deviation from ductile fracture observed at low damage level. 90

Figure 4-18: Fracture surface topography of MG-copper irradiated to 2 *dpa* showing fracture occurs across shear band at approximately 30^{o} 91
Figure 4-19: Microhardness measurements of nc-copper showing average hardness of 1.91+0.11 (GPa) at 0.0034 *dpa*. 92
Figure 4-20: Variation of hardness of nc-copper with *dpa*. 93
Figure 4-21: Typical stress-strain curves of irradiated *nc*-copper. 94
Figure 4-22: Variation of yield and ultimate tensile stress with dpa. Both stresses are continuously decreasing up to 1 *dpa* after which, a relatively minor increase is observed with minimal difference between yield and ultimate stress. 96
Figure 4-23: Variation of uniform and total elongation with *dpa*. 97
Figure 4-24: XRD of irradiated *nc*-copper 98
Figure 4-25: AFM of nc-copper at 0.0034 *dpa* with corresponding average grain size ~ 65+10 nm. 100
Figure 4-26: BF TEM of nc-copper post 0.0034 *dpa* irradiation showing formation of twins and dislocations. 101
Figure 4-27: BF TEM of nc-copper at 0.0034 *dpa* showing grains in the submicron regime accommodating twins and dislocation loops. 101
Figure 4-28: BF TEM of nc-copper showing nanograins still present at 0.0034 *dpa*. The diffraction rings are not as complete as it is in the as received material because some micrograins are contributing to the diffraction contrast. 102
Figure 4-29: Grain size distribution of nc-copper at 0.0034 *dpa* showing average grain size of 86.5 nm whereas the initial average grain size of the as received material ~ 34.4 nm which indicates grain growth at this damage level. 103
Figure 4-30: BF TEM of nc-copper at 1 *dpa* showing twins formed at grain boundaries. 104
Figure 4-31: High density of dislocations formed in nc-copper at 1 *dpa* with diffraction pattern revealing formation of twin structure. 104
Figure 4-32: BF TEM of nc-copper at 2 *dpa* showing high density of dislocations at twins boundaries. 105
Figure 4-33: BF TEM showing high density of twins formed in nc-copper at 2 *dpa* 105

Figure 4-34: SEM of nc-copper at 1 dpa used for grain size measurements. Arrows are pointing at grains in the submicron regime. 106
Figure 4-35: DF TEM of nc-copper at 1 *dpa* showing wide range of grain size. 107
Figure 4-36: SEM of nc-copper at 2 dpa. Arrows pointing at typical grains considered for grain size measurements. 107
Figure 4-37: Grain size distribution of nc-copper (a) at 1 dpa showing average grain size ~ 0.8+0.6 μm and (b) at 2 dpa showing average grain size ~ 0.75+0.5 μm. 108
Figure 4-38: Variation of nc-copper grain size with *dpa*. 109
Figure 4-39: SEM of deformed nc-copper at 0.0034 *dpa*. Fracture occurs through shear bands at approximately 50^{o}. 110
Figure 4-40: Semi-ductile fracture surface of nc-copper at 1 *dpa*. 110
Figure 4-41: SEM of fracture surface of deformed nc-copper at 2 *dpa*. 111
Figure 4-42: Variation of grain size with annealing temperature. Inset shows slow increase in grain size up to 450 K followed by a rapid increase starting at 500 K. 113
Figure 4-43: Arrhenius plot analyzing thermally activated grain growth of as-received *nc*-copper. 114
Figure 4-44: DSC scan of 3 mm disk of as received nc-copper heated at 10 K/ min. 116
Figure 4-45: Simulated temperature distribution of samples irradiated at 1 *dpa* (top) and 2 *dpa* (bottom). 118
Figure 4-46: Variation of hardness with annealing time at 55^{o}C. Dash lines indicate hardness of irradiated *nc*-copper at 0.0034 *dpa* level. 119
Figure 4-47: Variation of hardness with annealing time at 100^{o}C. Dash lines indicate hardness of irradiated nc-copper at 1 and 2 *dpa* level. 120
Figure 4-48: Variation of hardness with grain size of nc-copper. 124
Figure 4-49: Hall-Petch plot of polycrystalline copper. 125
Figure 4-50: Radiation hardening in irradiated polycrystalline copper. 125
Figure 4-51: Variation of yield stress with grain size at the different damage levels. 126
Figure 4-52: Variation of friction hardening of polycrystalline copper with damage level (*dpa*). 128

Figure 4-53: Variation of source hardening of MG- and nc-copper with damage level (*dpa*). 129
Figure 5-1: Defect evolution in *nc*-SiC [123]. 138
Figure 5-2: Variation of number of defects with average grain size following 10 keV displacement cascade [123]. 138
Figure 5-3: (*a*) No Frenkel-pairs remains in a Cu-Nb nanolayer after 2 ps whereas (*b*) 3 Frenkel-pairs are observed in a Cu single crystal and (*c*) 7 Frenkel-pairs are observed in a Nb single crystal at the same time [125]..... 139
Figure 5-4: Variation of vacancy formation energy with separation distance from the interface explaining the annihilation of Frenkel-pairs at the interface [125]..... 140
Figure 5-5: Degree of amophization caused by (*a*) 1.8 MeV Si ion and (*b*) 3.6 MeV I ion. 141
Figure 5-6: Variation of embedding energy as a function of the background charge density. 143
Figure 5-7: Variation of weighting function with separation distance. 144
Figure 5-8: Variation of the effective pair potential with the separation distance *r*. 145
Figure 5-9: RDF of liquid copper at different temperatures with solid squares representing reference data [135]. 146
Figure 5-10: Variation of copper viscosity with temperature as calculated from the present study compared to reference experimental data (see [136]). 146
Figure 5-11: Temperature dependence of the coefficient of thermal expansion of copper from this work compared to published MD data (see [143]) and experimental reference data (see [137, 138])..... 147
Figure 5-12: Temperature dependence of copper diffusivity from this work showing good agreement with reference data (see [135]). 147
Figure 5-13: Density correlator (self) in liquid state with current MD simulations (solid) showing excellent agreement with recent quasielastic neutron scattering data (open) [139]. 148
Figure 5-14: RDF of the single crystal Cu. Peak positions are in good agreement with values reported by Alper *et al.* [143]. 149

Figure 5-15: Perfect single crystal Cu with atoms having a CNA index = 0 (FCC) shown in green. 149
Figure 5-16: Formation of a twist Σ5 copper bicrystal. Dotted square represents the top single crystal after 36.9° rotation along [1 0 0] which is coincident with the *x*-axis of the simulation box). 150
Figure 5-17: Energy and rotation angles for twist boundaries in copper [145]. 151
Figure 5-18: Construction of Σ5 copper twist bicrystal using OVITO. 152
Figure 5-19: CNA analysis of Σ5 copper bicrystal showing an undefined CNA index for the interfacial atoms, and a CNA index of 0 for the FCC atoms (shown in green). 153
Figure 5-20: RDF of equilibrated copper perfect single crystal and Σ5 bicrystal. 154
Figure 5-21: A 2-D illustration of the cubic simulation box with sub-volume or inner box (shown in grey) for analysis of atomic displacements. Outer boundaries of the system are shown in yellow. 155
Figure 5-22: A 3-D representation of the cubic simulation box showing the inner box/ region with an arrow indicating the position and direction of impact. 156
Figure 5-23: RDF of (a) Cu single crystal and (b) Cu Σ5 bicrystal for 7 keV knock energy. 157
Figure 5-24: Variation of the number of atoms with non-FCC CNA index for 7 keV knock energy. 158
Figure 5-25: Illustration of the concept of iso-configurational (IC) ensemble average. The trajectory of each atom, which has the same initial position in all copies of the IC ensemble, is followed individually, and the trajectories (as well as the properties that are based on the trajectories) are averaged over different initial momenta. 160
Figure 5-26: Relative dynamical propensity in single crystal Cu for 7 keV knock energy at 0.01, 0.05, 0.1, 0.2, 0.4, and 0.8 ps (left-to-right, top-to-bottom). Red and blue atoms denote the most mobile and most immobile atoms, respectively. 162
Figure 5-27: Relative dynamical propensity in Σ5 Cu bicrystal for 7 keV knock energy at 0.01, 0.05, 0.1, 0.2, 0.4, and 0.8 ps (left-to-right, top-to-bottom). Red and blue atoms denote the most mobile and most immobile atoms respectively. 162

Figure 5-28: The PDF of dynamical propensity for single crystal copper with 7 keV knock energy..... 164
Figure 5-29: The PDF of dynamical propensity for Σ5 bicrystal copper with 7 keV knock energy..... 164
Figure 5-30: PDF of displacement components (*a*) X, (*b*) Y, and (*c*) Z at different times for 7 keV knock energy in single crystal copper. 166
Figure 5-31: PDF of displacement components (*a*) X, (*b*) Y, and (*c*) Z at different times for7 keV knock energy in Σ5 bicrystal copper. 167
Figure 5-32: Probability density functions (PDFs) of the X-component of the atomic displacements in a single crystal and a Σ5 bicrystal copper for7 keV knock energy. Peak shifts in Σ5 bicrystal indicates atomic displacements in the negative X-direction, opposite to the knock direction and towards the interface. This observation shows that the interface acts as an attractive sink even at hyperfast timescales. 168
Figure 5-33: PDF of the X-components of the atomic displacements in Σ5 bicrystal copper for different knock positions with7 keV knock energy. 170
Figure 5-34: PDF(X) for impact energy of (*a*) 3 keV and (*b*) 10 keV imparted at the center of the simulation box of Σ5 bicrystal copper in the X-direction. 171
Figure 5-35: PDF(X) of Σ41 and Σ5 twist bicrystal copper for 7 keV impact energy. 172
Figure 5-36: Average (normal) stress field in the XY-plane in Σ5 bicrystal (left) and single crystal (right) at 0.05 ps for 7 keV impact energy in the X-direction. 174
Figure 5-37: Normal stress fields in the XY-plane in Σ5 bicrystal (left) and single crystal (right) at different times for 7 keV impact energy. 175
Figure 5-38: 2-D illustration of the regions for stress evaluation. 176
Figure 5-39: Temporal variation of normal stress in Σ5 bicrystal system for 7 keV knock energy..... 177
Figure 5-40: Temporal variation of normal stress in a single crystal system for 7 keV knock energy..... 178

Figure 5-41: Comparison of the stress differential in a Σ5 bicrystal and a single crystal systems. 179
Figure 5-42: The "loading-unloading" self-healing mechanism observed in nanostructured materials. Interstitials are attracted or "loaded" to the grain boundary after which, they are emitted or "unloaded" back to the grain interior which annihilate the relatively immobile vacancies [60] 181

Chapter 1. Introduction and Overview

With the spiraling rise in energy demands across the world, and the imminent depletion of traditional energy reserves, the need for alternative energies, especially from renewable resources, has become evermore relevant and pressing. Currently, nuclear energy presents a compelling environmentally friendly avenue that can be trusted to meet these growing energy demands. The International Atomic Energy Agency (IAEA) data shows that more than 500 nuclear power blocks and research and other reactors, most of which are of the light water reactor type, are in operation all over the world at the present time [1]. However, there is a growing interest in developing a new generation of advanced nuclear energy systems, both fission and fusion, designed to operate at higher temperatures regimes and extremely greater radiation exposure levels. Indeed, these systems are also required to last for longer life time (up to 60 years) with minimum in-service maintenance, and needles to mention the requirement to support the efforts exerted toward nuclear nonproliferation.

In such a harsh radiation environment, elementary material damage introduced in the form of radiation-induced defects results in embrittlement and dimensional instability of both structural and fuel components. Therefore, the ability to remove radiation-induced point defects is crucial to improving the mechanical properties of irradiated materials [2]. Accordingly, the need for structural, cladding and fuel materials that are highly resistant to intense irradiation fluxes has become an essential challenge. In the past [3] it was experimentally observed that point defects and their clusters, which are formed during

irradiation, can migrate and annihilate at the interfaces of materials. This raises the exciting possibility of designing materials with large volume of interfaces to ameliorate the effects of radiation induced damage.

Engineered nanolayered composite materials that have large volume of interfaces are possible candidates for radiation tolerant materials. By properly tailoring the length scale and interface properties, nanolayered metallic composites can show high thermal and dimensional stability in response to intense radiation exposure. Interestingly, Cu-Nb nanolayered composites possess very good thermal stability at temperatures as high as 800^{o}C [4]. Investigations have shown that the enhanced radiation damage tolerance in nanocomposites is a consequence of short diffusion distance to the nearest sinks [5]. Because the diffusion distances to the interfacial sinks in these composites are short (of the order of nanometers), the point defects which are produced during irradiation are annihilated at the interfaces before they can form into relatively stable aggregates and large scale defect structures [6]. An important concern is the stability of the geometry of the nanostructured material under the extreme irradiation conditions. Enhancing the stability of the interfaces of nanolayered metallic composites is currently being explored via atomistic simulation techniques [7]. However, nanolayered metallic composites, which are currently synthesized only in the form of thin films, have very limited utility in reactors and nuclear waste matrices as structural materials.

Bulk nanocrystalline (*nc*) polycrystals, with ultra-fine grain sizes (diameter < 100 nm) and high volume fraction of interfaces, are promising radiation tolerant materials for structural applications. Nanocrystalline materials offer very desirable properties such as high

strength and superior wear resistance and have been the subject of intensive theoretical and experimental studies [8]. Advances in the processing of nanograin structured metals have resulted in very high strength materials due to reduced grain sizes (Hall-Petch relationship). However, various artifacts and impurities have also resulted in reduced ductility. Recent advances in cryo- and room-temperature milling using in-situ consolidation have resulted in ultra nanograin metals with both high strength and reasonable ductility [9-11].

Effect of radiation exposure on nanograin structural metals is of immense interest both from scientific and technological points of view. While in conventional metals, radiation produces various defects (point, line, surface and volume), it is not evident how these defects, especially dislocations (line defects) and stacking faults (surface defects), can be accommodated in the relatively minute grains of nanometer size. The response of nanograin structured metals to neutron irradiation can be expected to be different from that in micrograined metals. This response could manifest as significantly altered microstructure and mechanical properties. Currently, there are limited studies on the irradiation properties of nanocrystalline materials. A few investigations have reported changes in microstructure [12] [12] but the role of interfaces especially as facilitator of radiation tolerance has not been quantified through accurate measurements.

Bulk nanocrystalline materials have already shown promising signs as candidate materials for nuclear reactor applications. Stainless steel, which plays a major role in the field of nuclear industry [1], was shown to have enhanced radiation resistance in terms of radiation embrittlement and defects formation when it is processed in the form of ultrafine grained (0.1 to 1 μm) SUS616L stainless steel [13].

Qualifying and approving materials for intense radiation applications requires conducting a numerous number of irradiation experiments. Difficulties associated with irradiation experiments such as the limited number of equipped irradiation facilities all over the world, restrictions applied to handling irradiated materials, especially when it is highly radioactive, arose the need to utilize different techniques of modeling and simulation for two major purposes: firstly, to understand the experimental findings, and secondly, to investigate problems which are mostly impossible to approach experimentally. Over the last few decades, Molecular Dynamics (MD) simulation was harnessed as a powerful technique to study problems and phenomena that are highly related to radiation effects on materials such as defect formation and migration, structural transformation, and different elastic/plastic mechanical properties. There is no technique capable of handling the problem of studying matter at the atomistic level by simply solving the classical two- or many-body problem and in this regard, MD techniques were proven to be indispensable in both basic and applied scientific research [14].

The present study is composed of two major streams. The first stream includes experimental investigation of neutron radiation effects on the mechanical properties and developed microstructure of nanocrystalline *(nc)* copper irradiated at different damages levels. This includes the application of different microstructural investigation techniques such as X-ray diffractions (XRD), Atomic Force microscopy (AFM), and Transmission Electron Microscopy (TEM) to observe and understand the developed microstructure of irradiated nc-materials. Micrograined (MG) copper samples were concurrently irradiated along with the nc-samples to compare the response of nc-materials to neutron radiation to its

conventional counterparts in terms of mechanical properties and deformation mechanisms. Compared to other studies, the present study has the advantage of relating the developed microstructure to the mechanical properties of the irradiated material through the capability of establishing the stress-strain curves at the different damage levels which contains invaluable information when coupled to the observed microstructure.

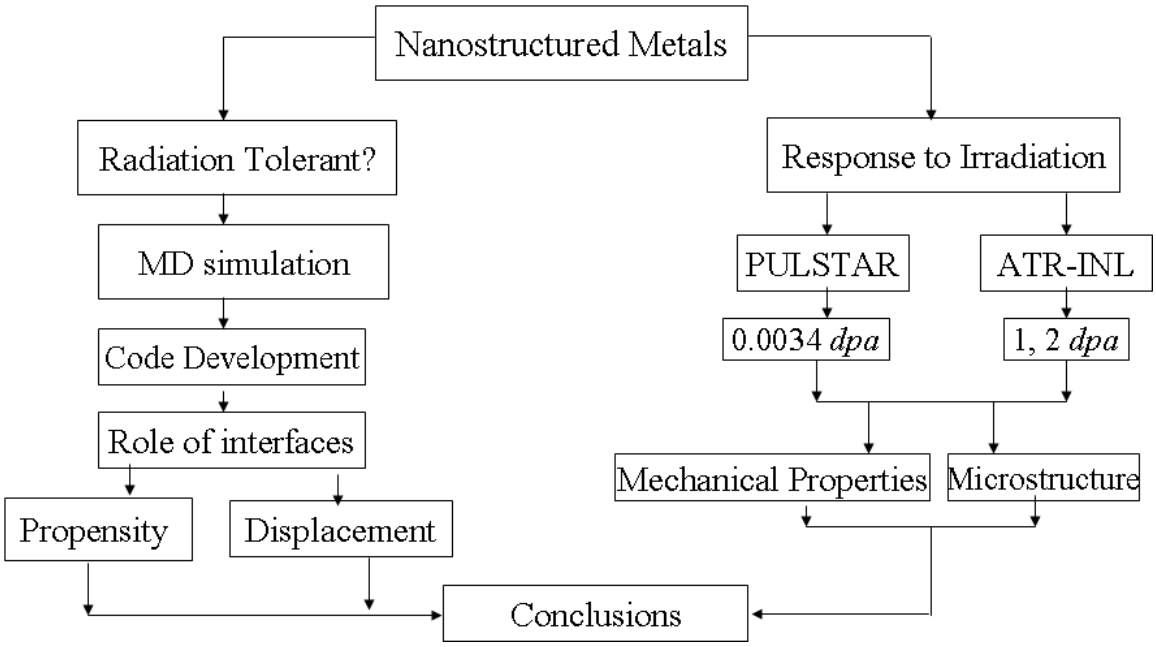

Figure 1-1: Flow chart showing the main procedures involved in the present study.

The second stream includes MD investigation of the hypothesis of radiation tolerance of nc-materials. This includes studying the rule of interfaces, which is the main feature of nanostructured systems, on the short time transport behavior of displaced atoms post knock event by observing the fast dynamics at the atomistic level following initiation of damage

cascade in the vicinity of interfaces considering two types of structures: single crystal copper, Σ5 and Σ41 bicrystal copper.

Copper, the material of interest in the present study, is historically known as one of the most appealing metals for engineering applications due to its light weight, excellent electrical conductivity and high ductility. In the field of nuclear systems, copper has a key role to play in the International Thermonuclear Experimental Reactor (ITER) which aims to demonstrate the feasibility of nuclear fusion as a reliable source of energy. In fusion based systems, superior magnetic fields are required to accelerate the hydrogen atoms and these fields can only produced with superconducting wires. Currently, superconducting materials considered for that purpose are often niobium-based in the form of thin filament inside a copper matrix. Copper does not only act as a host for the superconducting material but indeed, it carries the electric current when the superconducting material fails to do [15]. It is inevitable that first wall materials, including copper, and materials facing plasma in fusion-based power systems will experience high temperatures, and extreme levels of radiations damage in addition to high thermo-mechanical stresses [16]. Furthermore, copper is considered as one ideal material for the construction canisters for the disposal of spent nuclear fuel because of its reasonable corrosion resistance and reliable fabricability [17].

These facts represented a major motivation to studying the response of copper to intense radiation environment while the other major motivation to initiate the present study arose from the dearth of knowledge on the mechanisms of radiation tolerance and irradiation material properties of nanocrystalline materials.

Chapter 2. Background and Literature Survey

2.1 Nanocrystalline Materials

Over the past few decades, experimental observations proved the fact that most of the materials properties have a strong grain size dependency when it goes down to the nanometer scale compared to its conventional micro-grained counterparts [18]. That fact was the key to trigger a growing interest in studying materials properties at the nanoscale [19]. Nanocrystalline (*nc*), nanostructured or nanograined materials are all terms being used interchangeably in the literature to describe that class of materials with grain size < 100 nm. Nanocrystalline materials are characterized with having a large volume of interfaces which consequently leads to a larger fraction of atoms to lay in grain boundaries causing such a significant difference in properties from its conventional counterparts [20].

Recently, efforts are being directed to develop nanocrystalline materials with novel, controlled, and improved physical, chemical, mechanical, biological, and magnetic properties. These efforts are split between the different research areas related to nanocrystalline materials such as synthesis, characterization and evaluation [8, 20]. In the subsequent sections, a brief summary will be given on different aspects of nanocrystalline materials specifically regarding classification, synthesis, structure, different properties with emphasis on mechanical properties, and thermal stability. The rest of this chapter will mainly focus on the current research status on studying the radiation effects on nanocrystalline materials which is the main object of the present study.

2.1.1 Classification and synthesis

Nanocrystalline materials are mostly classified based on the number of spatial dimensions along which it is confined down to the nanoscale. According to this criterion, there are three classes of *nc* materials: (a) 1-D *nc* materials such as ultrathin films on a surface and multilayered materials, (b) 2-D *nc* materials such as nanowires, nanorods, and nanotubes, and (c) 3-D *nc* materials such as nanoparticles and nanopores. Bulk nanocrystalline materials which belong to the 3-D class are basically equiaxed such that it is confined in the three spatial dimensions [21]. They are commonly synthesized through two opposite approaches: (i) bottom-up approach by consolidating small clusters or particles and, (ii) top-down approach by breaking bulk conventional materials into smaller dimensions [20, 22, 23]. Different common synthesis methods are summarized in Table 2-1.

Table 2-1: Synthesis methods of nanocrystalline materials.

Starting phase	Technique	Dimensionality of product
Vapor	Inert gas condensation [18]	3D
	Physical vapor deposition	1D
	Plasma processing	3D
	Chemical reactions	3D, 2D
Liquid	Rapid solidification	3D
	Electrodeposition	1D, 3D
	Chemical reactions	3D
Solid	Mechanical alloying / milling [24]	3D
	Spark erosion	3D
	Sliding wear	3D

Each of these synthesis methods has its advantages and disadvantages compared to the other methods. Choosing a specific synthesis method depends mainly on the ability of that method to control the property or feature of interest.

2.1.2 Structure

The nanoscale length of nanocrystalline materials directly affects the energy band structure and consequently, it has an influence on the associated atomic structure [25]. This effect can be understood by considering the portion of atoms which are in the grain boundaries in nanocrystalline materials. Atoms located at the boundaries have less number of nearest-neighbor atoms compared to bulk atoms which give rise to difference in bonding energy which is the origin of surface tension phenomenon. Accordingly, the structure of nc materials can be divided into crystalline component, which represents the numerous and small crystallites with different orientations, and interfacial component which represents the intercrystalline regions characterized by its variation from region to region [20].

So far, the grain size represents the most crucial microstructure parameter that affects *nc* materials properties. Accurate determination of grain size is then a mandatory task for any attempt to understand structure-properties relationships in *nc* materials. Different techniques are commonly utilized to determine grain size of *nc* materials including Transmission Electron Microscopy (TEM), X-ray diffraction (XRD) and Atomic Force Microscope (AFM). Although XRD seems to be the easiest among those techniques, TEM and AFM have the advantage of their capability to provide information on the grain size distribution which is not accessible via XRD. In the present study, all those techniques were utilized more or less in the different stages of the research.

Generally speaking, the grain structure of *nc* materials seems to be similar to that of micrograined (MG) materials except that, it is not common to observe the different structural defects such as dislocations, twins, and stacking faults in nc materials. The major structural difference reported comparing nc materials to the conventional one was related to the internal strain observed in nc materials which is expected because of the high tension at the grain boundaries [26].

2.2 Mechanical Properties of Nanocrystalline Materials

Most properties of materials are heavily affected by the microstructure and more specifically the grain size and hence, it is always the case to determine materials' properties as a function of varying grain size. For example, the melting point of nanocrystalline silver was observed to increase with the grain size [27]. Mechanical properties of materials are dependent on the microstructure and the grain size and for this reason; the influence of the nanoscale length on mechanical properties was the object of tens of scientific publications [23]. Most of the mechanical properties, such as toughness, depend on the ease of formation or the presence of the different types of defects. Due to the nanoscale length structure, it becomes difficult to accommodate structural defects in *nc* materials and accordingly, mechanical properties of *nc* materials are expected to be different compared to its conventional counterparts [28].

It is common to derive the mechanical properties of bulk *nc* materials from uniaxial tensile or compression tests as well as micro or nano-indentation [29]. Generally speaking, *nc* materials show significantly higher strength, both yield and ultimate, and less ductility and

toughness when compared to its conventional counterparts [30, 31]. Furthermore, the effect of grain size on the strength of *nc* materials was observed to follow the well known Hall-Petch mechanism [32, 33] down to a specific grain size at which this mechanism begins to break down invariably and with further refinement, weakening of the material may be observed.

The Hall-Petch behavior observed in micrograined (MG) materials was attributed to the pile up of dislocations at grain boundaries which enhance the resistance to plastic flow when the grains are refined. In *nc* materials, this scenario is not clear since dislocation sources within grains at the nanoscale are not expected to operate. Indeed, dislocations were not observed in deformed *nc* samples and it is believed that dislocations are initiated and terminated at the grain boundaries which makes the Hall-Petch behavior in nc materials to be under debate to- date [28].

The low ductility and toughness of *nc* materials was attributed to the absence of an effective hardening mechanism which causes early onset of plastic instability leading to localized deformation [30]. The plastic instability in deformed nc- materials was observed as shear bands in some examples but in most cases, it was manifested as early necking followed by fracture [34]. Another interesting observation on the mechanical properties of *nc* materials was concerned with the effect of the strain rate (loading rate) on the tensile strength. It was observed that the tensile strength of *nc* materials increases with the loading rate while the dependency of the ductility on loading rate was attributed to a combination of processing route and testing technique. While conventional metals tend to have a drop of fracture strain with increasing strain rate, *nc* materials have shown an opposite trend in many reported

studies [35]. Surprisingly, other researchers have reported decrease in the ductility of *nc* nickel with increasing strain rate and the tensile strength was observed to be independent of the strain rate [36].

It is obvious that there are a lot of debates and contradictions between the different observations reported on the mechanical properties of *nc* materials which, from the researcher point of view, originates from the variation and inconsistency of the processing routes and testing methods. This observation enforced the need of having an intensive pre-irradiation characterization in the present study so that observations on the irradiated materials can be safely compared to that of unirradiated or "cold" materials without worrying about the effects of secondary factors such as testing setup and sample geometry on the reported results.

2.3 Thermal Stability of Nanocrystalline Materials

It is the nature of any physical system to attempt achieving a stable state by minimizing the total energy of the system. Polycrystalline materials tend to reduce its interfacial energy by expanding its grains which is referred to as grain growth. Nanocrystalline materials with large volume of grain boundaries and higher interfacial energy will have stronger drive force to grain growth. Since the grain size strongly affect the mechanical behavior of nc materials, it is important to understand and predict the grain growth phenomenon in nc materials and if possible, how to control it [37]. The knowledge and understanding of thermal stability and grain growth of nc materials will impact the progress in this research area both technologically, since grain growth can occur in nc

materials during consolidation of powder, and scientifically, to compare grain growth behavior of nc materials to the micrograined (MG) materials [20].

Grain growth of either conventional or *nc* materials was frequently investigated by considering isothermal grain growth kinetics described by the equation:

$$D^n - D_0^n = Kt = K_0 \exp\left(\frac{-Q}{RT}\right)t \qquad \text{Equation 2-1}$$

where D is the grain size at time t, D_0 is the initial grain size, K is a constant, K_0 is a pre-exponential constant, n is the grain growth exponent or $(1/n)$ is the time exponent, R is the gas constant and Q is the activation energy for grain growth. It is clear that both Q and n are the most important parameters describing the kinetics and mechanism of grain growth and hence, accurate determination of these two parameters would assist understanding and predicting the phenomenon of grain growth. The value of n is ideally expected to be 2 which assume a parabolic trend for grain growth; however, values ranging from 2 up to 10 were reported for nc materials [38]. Indeed, these values were also observed in conventional materials and the ideal value of 2 was only observed in conventional materials of high purity annealed at elevated homologous[♣] temperatures [39]. The high values of n observed in *nc* materials and some other cases of conventional materials were ascribed to pinning of grain boundaries and solute segregation to grain boundaries.

Determination of the activation energy, Q, for grain growth of *nc* materials and comparing it to its conventional counterpart is a common task in all studies targeting thermal stability of *nc* materials. The value of Q would provide guidance to understanding the

[♣] (T/T_m) where T_m is the melting temperature.

mechanism controlling grain growth. The activation energy for grain growth was often compared to both that for lattice diffusion, Q_l, and that for grain boundary diffusion, Q_{gb}. Data reported for Q of *nc* materials show that it has a better matching with Q_{gb} which is consistent with most data reported for micrograined materials [40]. However, Li and Ebrahimi [41] reported an interesting study regarding thermal stability of *nc* nickel in which, it suggested on the grain growth in *nc* materials to be controlled by GB diffusion at low temperature and by lattice diffusion at relatively higher temperatures.

2.4 Radiation Impact on Nanocrystalline Materials

The degradation of materials properties serving in harsh radiation environments was the topic of intense research efforts associated with the nuclear industry initiated in mid of the twenty century or even earlier. It is well established that neutron and ion irradiation causes conventional materials to possess higher strength accompanied with reduction in ductility which is referred as radiation hardening and embrittlement [42]. A large number of experiments and theoretical investigations were conducted to demonstrate the various aspects of this topic and discussing the effect of different parameters such as radiation dose, temperature, composition and structure on materials' response to radiation [43]. Radiation hardening observed in irradiated conventional materials was explained in the literature based on two mechanism: (i) 'Zone Theory of Radiation Hardening' which suggests that the vacancy clusters/ loops ,which result from the collapse of vacancy-rich zones, act as barriers to dislocations gliding in the slip plane and thus represent the main source of hardening [44, 45], (ii) formation of 'defect clouds' which declares that dislocations can not act as a

dislocation source until it is unlocked from the defect clouds formed along the dislocation line [46] and moreover, the yield strength in this case is determined by the stress needed to unlock these dislocations [47, 48].

On the contrary, it is not well established yet how *nc* materials respond to radiation and what factors control the impact of radiation on the microstructure and the various properties of this class of materials. Literature survey shows that studies concerned with investigating radiation impacts on *nc* materials have relatively a wide spectrum of results and observations and moreover, contradiction in observations can be found in the same study in some cases. The fact that nc materials are human-made class of materials added more complexity to the efforts toward characterizing its response to radiation when compared to conventional materials since additional factors such as the effect of processing route, initial grain size and thermal stability are expected to play a major role in this aspect [49].

2.4.1 Enhanced radiation resistance of *nc* materials

Ideally speaking, having materials with grain size < 100 nm would provide short diffusion paths for radiation-induced point defects toward grain boundaries and consequently, further accumulation of those point defects is greatly reduced and line, surface and volume defects have much less chances to be formed assuming that the structure of nc material retains its integrity under irradiation [50]. In nuclear reactor, formation of helium bubbles leading to swelling in structural materials is inevitable and thus, the ability to reduce the density of helium bubbles should enhance radiation resistance of materials. Nanocrystalline Fe films with average grain size ranging from 49 to 96 was irradiated by 100

keV helium ions to a fluence of 6×10^{20} ions/m^2 and density of helium bubbles as well as hardness were compared to that of bulk Fe with an average grain size of 700 nm irradiated at the same conditions [51]. Interestingly, lower density of helium bubbles was observed in *nc*-Fe films compared to the bulk Fe although the average bubble diameter was about the same in both systems. Indeed, radiation hardening in *nc*-Fe films was found to be less than that of bulk Fe which is a combined consequence of helium bubble induced hardening and irradiation induced compressive stress in nc-Fe films. Enhanced radiation resistance in terms of reduced helium bubble density was also reported for Cu/V nanolayers irradiated by helium ions [52, 53]. The density of helium bubbles and radiation hardening were found to decrease remarkably as the thickness of individual layer decreases from 200 to 5 nm moreover, radiation hardening was not observed in layer with thickness less than 2.5 nm. These observations suggest that interfaces can promote radiation resistance by effectively absorbing irradiation induced point defects.

Matsuoka *et al.* [13] investigated the influence of neutron irradiation on ultrafine grained SUS316L stainless steel with average grain size less than 300 nm compared to its coarse grained counterpart. Increase in hardness was observed in both ultrafine and coarse grained SUS316L however, that increase was much less in the ultrafine grained material. Moreover, no irradiation induced point defects were observed near grain boundaries in the ultrafine grained stainless steel.

Table 2-2 summarizes studies showing improved radiation resistance of different nanostructured systems along with the processing route(s), initial grain size, irradiation

conditions (radiation type, energy, and temperature) and corresponding results showing enhanced radiation resistance in brief.

Table 2-2: Example studies showing enhanced radiation resistance of *nc*/ ultrafine materials

Material	Irradiation	Results
Ni, SPD (115 nm) [12]	590 Mev proton, 0.56 *dpa*, RT	Significant hardening observed in SPD Ni with grain refinement and formation of low density of SFT
Ni-W alloy (6nm), ED [13]	1.14×10^{24} n/m^2 , 290^{o}C	Hardness was unchanged and TEM showing no radiation-induced defects
$Ti_{49.4}Ni_{50.6}$ (23-31 nm), SPD [51]	1.5 MeV Ar^+, RT	*nc* $Ti_{49.4}Ni_{50.6}$ retains long-range order at the same damage dose whereas conventional counterpart amorphized.
$MgGa_2O_4$ (4-12 nm), mechanical alloying [54]	300 keV Kr^{++}, 100 K	Conventional $MgGa_2O_4$ amorphized at 5×10^{19} Kr/m^2 while nc $MgGa_2O_4$ did not show amophization up to 4×10^{20} Kr/m^2
Pd / ZrO_2 (10-300 nm), inert gas condensation [55]	4 MeV Kr, 1×10^{15}- 2×10^{16} kr/cm^2	Drastic reduction of defect cluster in grain < 50 nm and / no defects detected in Pd (<30 nm) and ZrO_2 (<15 nm)

It is obvious that the majority of irradiation experiments conducted on *nc* materials utilize ions and/ or neutron accelerators as source of radiation due to the difficulties associated with conducting in-core irradiation experiments and the limited number of facilities available all over the world. Among those on reactor experiments, Yamashita *et al.* [56] investigated the effect of neutron irradiation ($E_n > 0.1$ MeV) on $Y_2Ti_2O_2$ nanoparticles in ferretic steel F95 at different dose levels up to 15 *dpa* and stability of nanoparticles size was observed.

The effect of neutron irradiation on the mechanical properties of advanced nanostructured ferritic alloys (14YWT) with high density of enriched Y, Ti and O nanoclusters developed at Oak Ridge National Laboratory was investigated recently by McClintock *et al.* [57] in comparison to conventional ODS ferritic alloys (14WT♣). Tensile samples of both alloys were irradiated at different temperatures (300, 580, and 670^{o}C) to a damage level of 1.5 *dpa*. Interestingly, the 14YWT alloy with high density of nanoclusters was found to possess higher strength (about two times) compared to the 14WT alloy pre- and post irradiation. The yield strength of the 14YWT alloy was decreased from 1450 MPa at room temperature to about 700 MPa at 600^{o}C. The 14YWT showed relatively minor radiation hardening (5-200) MPa whereas significant radiation hardening (about 250 MPa) was observed in the 14WT alloy at 300^{o}C. The overall enhancement in mechanical properties of 14YWT was attributed to the role of the nanoclusters that act as trapping centers for the early irradiation-induced point defects particularly at low temperature while at high

♣ 14WT has no Y_2O_3 addition during ball milling which is required for nanocluster formation and accordingly, the effect of nanoclusters can be investigated

temperatures, the role of the nanoclusters is less significant as the induced point defects are thermally annihilated either by migration to grain boundaries or via recombination process.

By carefully compiling results from those studies listed above and other studies with similar results [58, 59], the enhancement of radiation resistance characteristics of nanostructures systems or systems with high density of nanoclusters can be explained based on the following remarks:

I. Structures with grain size in the range of tens of nm possess large volume of interfaces and triple junction which facilitate the migration and annihilation of irradiation induced point defects.
II. Vacancy diffusion based phenomena will be less significant as the density of thermal equilibrium vacancies is much less in nanograins due the small number of atoms present in the matrix.
III. The operation of Frank-Read loops is unlikely due to the size limitation and thus dislocation density in nanograins is insignificant.
IV. As mentioned earlier, interfaces represent a short diffusion path resulting in intense diffusion flux of atoms into grain boundaries.

Although this explanation seems to be theoretically apparent, it is not very clear how to explain the ability of nanostructured materials to resist radiation at the atomic level. Furthermore, radiation damage can not be considered as an equilibrium process especially when the dependency of time and damage level is considered. As a result, a growing interest was initiated to explore the response of nanostructured materials to radiation at the

molecular/ atomic level. Recalling that the very early form of radiation damages is the interstitial- vacancy Frenkel pair, the ability of material to enforce recombination of interstitial and vacancy will determine its self-healing capability. In conventional materials, swelling occurs because of the fast migration of interstitials towards grain boundaries leaving behind vacancies and over the time, those point defects accumulate and result in obstacles to dislocation motion leading to radiation hardening and embrittlement [60].

Based on a molecular dynamics study, a self healing mechanism explaining the ability of nanostructured systems to resist radiation degradation was proposed by Bai *et al.* [61]. The interaction between defects and boundaries was investigated near a Σ11 symmetric tilt grain boundary of copper at 300 K from picosecond to microsecond time scales. It was observed that upon irradiation, interstitials were attracted or "loaded" to the boundaries similar to what occurs in conventional materials, however, those interstitial were found to be unloaded back toward the bulk of the grain resulting in vacancy annihilation with a much lower energy barrier compared to the activation energy of vacancy diffusion. Furthermore, this "loading-unloading" mechanism seems to be very efficient in annihilating immobile vacancies in the vicinity of grain boundary.

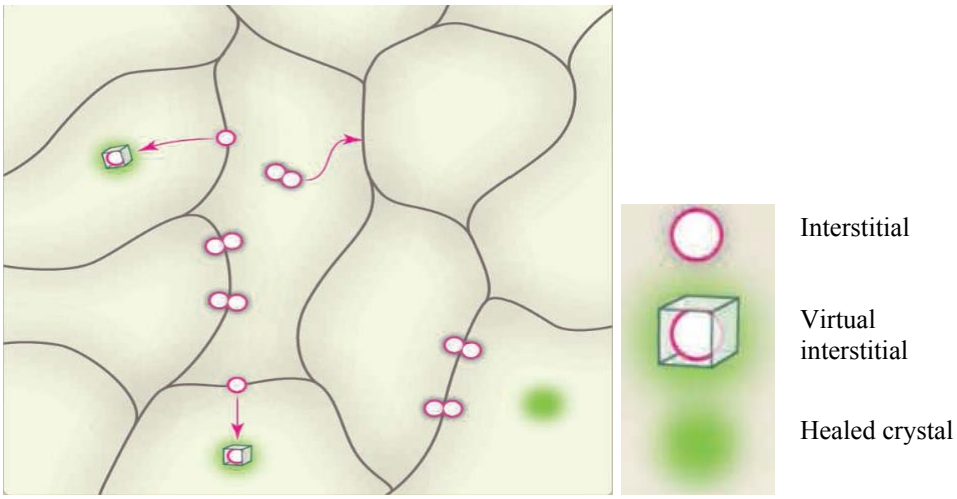

Figure 2-1: The "loading - unloading" self-healing mechanism observed in nanostructured materials. Interstitials are attracted "loaded" to the grain boundary after which, it is unloaded back to annihilate the vacancies in the bulk [60].

2.4.2 Structure instability of irradiated nanocrystalline materials

Although the studies referenced above assure great promise of nanostructured materials for radiation applications, other studies brought that promise back to the grey area. When nanocrystalline Cu-0.5Al_2O_3 processed via SPD irradiated by 590 MeV protons to 0.91 *dpa*, the grain size increased from 178 to 493 nm [12]. Moreover, Stacking faults and dislocations were observed in the irradiated samples. The researcher excluded the possibility of annealing grain growth as the irradiation temperature was around 100^{o}C whereas thermally activated grain growth in nc Cu-0.5Al_2O_3 was experimentally determined to be higher than 350^{o}C [12].

Karpe *et al.* [62] investigated the developed microstructure of thin films (70-120 nm) of nanocrystalline Fe and Fe(Zr) in response to Ar^{+} and Xe^{+} ion irradiation. At all damage

levels either in terms of fluence or dpa, a remarkable increase in grain size was observed. The authors proposed an empirical expression to describe the observed grain growth in the form of:

$$d^n - d_0^n = K\Phi \qquad \text{Equation 2-2}$$

where Φ is the dose, K and n are empirical constants and n was determined to be 2.1±0.2 and d_o, the initial grain size, was so small to be neglected. A very similar observation of ion irradiation induced grain growth was reported when Zr-Fe thin films were irradiated by 500 keV Kr ions (80-100 *dpa*) in which the average grain size was found to be monotonically increasing with the fluence up to a saturation level which seems to be temperature dependent [63].

Borgesen *et al.* [64] reported the occurrence of irradiation-induced grain growth in metals (Ni, Co, Cr, V and Ti) upon irradiation of 600 keV Xe ions at liquid nitrogen temperature which eliminate the possibility of annealing grain growth. In that study, although the different elements were processed via the same route and initial conditions, the grain growth rate was seen to vary from material to material.

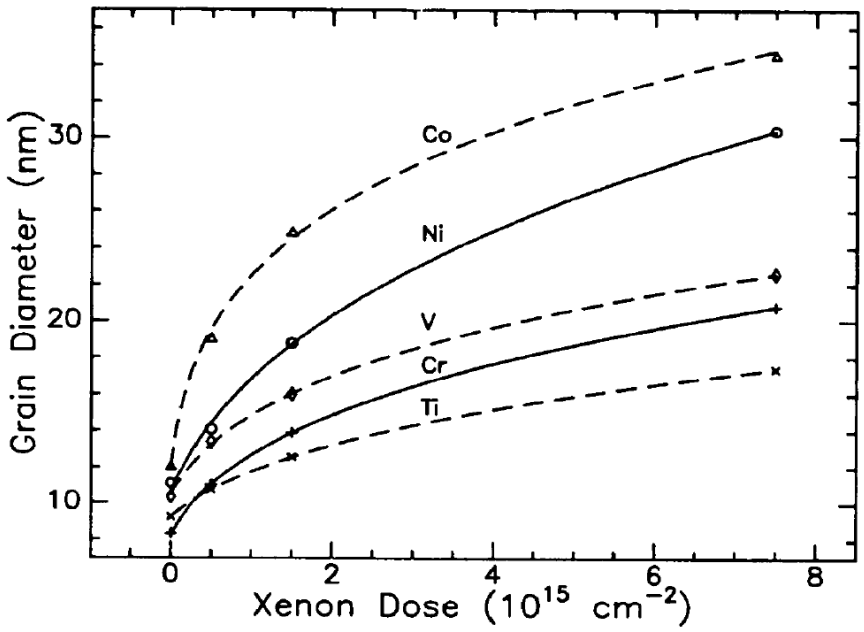

Figure 2-2: Grain growth observed in metals upon 600 keV Xe ions irradiation [64].

With many other observations of ion irradiation induced grain growth, it was mandatory to establish a model describing this phenomenon as the first step for any further attempts to eliminate it. When ion-matter interaction is considered, the resultant collision cascade was used to be well described based on the ballistic models [65, 66]. However, many of the experimental findings and observations similar to those reported by Borgesen [64] and others can not be explained within the frame work of the ballistic models [67].

Focusing on metallic systems, the deviation from the ballistic model was explained by proposing two different mechanisms governing materials response to radiation according to the temperature regime of investigation. At temperatures high enough for radiation induced point defects to become mobile, radiation enhanced diffusion mechanisms become

dominant whereas at low temperatures, the so called "Thermal-Spike" mechanisms are believed to explain those phenomenon which seems to be temperature insensitive [68, 69].

The effect of the size of the nanocrystallite on the system response to irradiation was investigated by M. Rose *et al.* [55] who observed the density of defects formed in nanocrystalline ZrO_2 and Pd with various initial grain sizes. Defect density observed in ZrO_2 seems to increase with the grain size until it saturates at a grain size of about 150 nm whereas for nc-Pd, the defect density continues to increase with no saturation regime observed (Figure 2-3). The most interesting observation was the minimum grain size at which defects were early detected which was observed in ZrO_2 to be about 15 nm while defects were not detected in nc Pd with grain size < 30 nm which implies that the initial size of the nanocrystallite is a key factor controlling the response of this class of materials to irradiation.

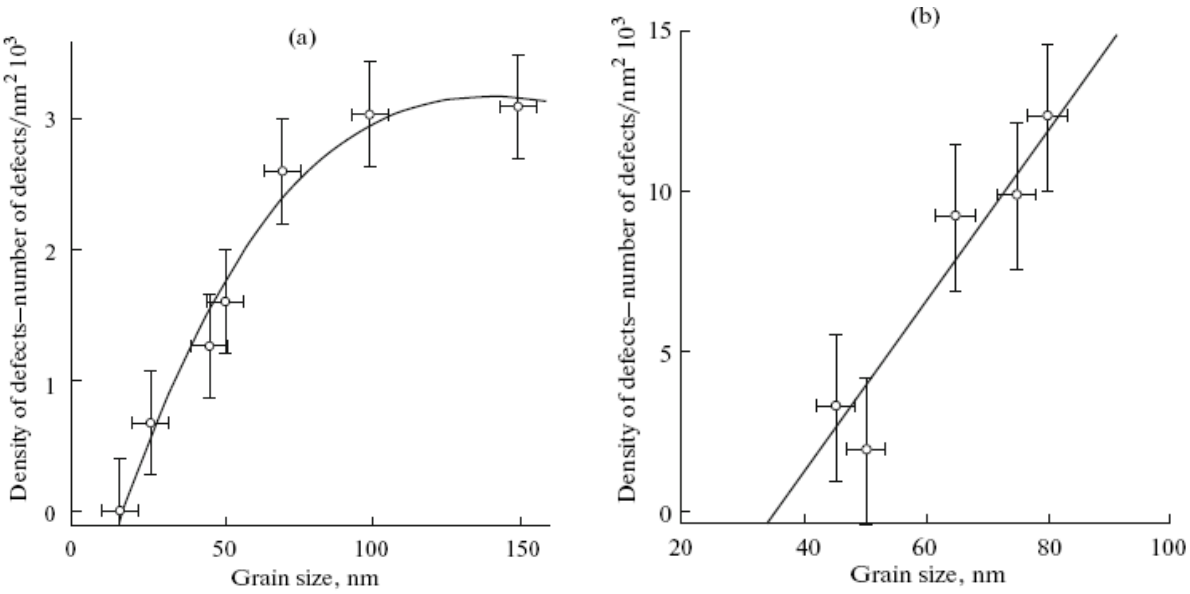

Figure 2-3: The variation of defect density with grain size observed in (a) ZrO_2 and, (b) Pd irradiated by 4 MeV Kr ions [55].

According to the summary of experimental observations and findings describing the response of nanocrystalline materials to irradiation, it is clear that a firm conclusion about the ability of nanostructured materials to serve in intense radiation resistant can not be confirmed leaving the radiation resistance characteristics of nanocrystalline materials as an open topic for further research and investigation. Indeed, such a conclusion necessitates more experimental as well as computational work concerned with neutron irradiation rather than ion irradiation which represents the core of the experimental data available to-date.

Chapter 3. Experimental Procedures and Irradiation

In this chapter, the different experimental procedures attempted in this study will be highlighted along with the details of the irradiation experiments conducted both at the PULSTAR reactor at NC State University [70] and the Advanced Test Reactor (ATR) at Idaho national Laboratory (INL) [71]. Pre-irradiation characterization of micrograined (MG) copper and nanocrystalline (*nc*) copper including microstructure and mechanical properties will be reported as an introductory to the experimental results to be presented in the next chapters.

3.1 Microstructure Characterization of As-Received Materials

In the present study, different techniques were utilized to characterize microstructures of the samples pre- and post irradiation. The choice between one technique over the other was based upon the specific phenomenon or observation under consideration and in many cases; different techniques were utilized to analyze the same microstructural feature as of the case of determining the grain size distribution. The following table lists the different techniques applied for the purpose of microstructural investigation/characterization and the purpose(s) the technique was applied for. It can be seen that, for some tasks and characterization requirements, it was necessary to apply more than one technique either for accuracy purposes or for better understanding of the experimental findings.

Table 3-1: The different microstructural characterization techniques utilized in the present study

Technique	Purposes
X-ray Diffraction (XRD)	• Grain size measurements (<200 nm) • Phase transformation detection
Scanning Electron Microscopy (SEM)	• Chemical composition analysis • Grain size measurements • Topography of fracture surfaces
Transmission Electron Microscopy (TEM)	• Gran Size Measurements • Defects detection/ characterization
Atomic Force Microscopy (AFM)	• Grain size measurements (up to hundreds of nm)
Optical Microscopy	• Grain size measurements (micro-grains)
Differential Scanning Calorimeter (DSC)	• Phase transformation detection • Grain growth detection

Electrodeposited (ED) nanocrystalline copper investigated in the present study was procured from the 3M Corporation whereas micrograined copper was available at the Nuclear Materials laboratory at NC State University both in sheet form. The chemical composition of MG- and *nc*- copper was determined via SEM- Energy Dispersion Spectroscopy (EDS). The main copper x-ray peaks ($K_{\alpha 1}$ at 8.046 keV, $K_{\beta 1}$ at 8.904 keV, $L_{\alpha 1}$ at 0.932 keV) were

identified and composition was found to be 99.999% in both materials (Figure 3-1and Figure 3-2).

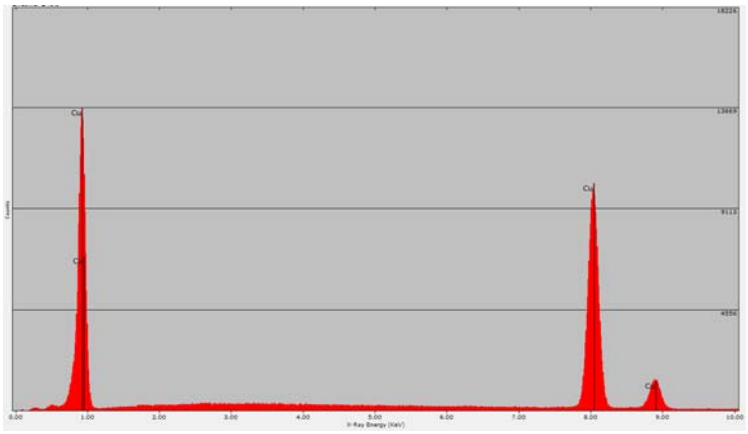

Figure 3-1: SEM-EDS identifying the main x-ray peaks of copper.

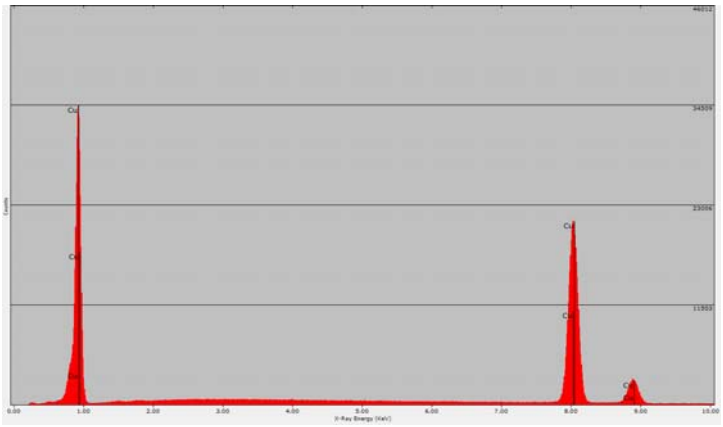

Figure 3-2: SEM-EDS identifying the main x-ray peaks of nc-copper.

In this study, microstructural investigation mainly focuses on two aspects:

I. Average grain size and grain size distribution

II. Irradiation induced defects at the different damage levels.

3.1.1 Optical microscopy of as-received materials

The average grain size and the grain size distribution of MG-copper were determined via optical microscopy. For this purpose, copper samples were ground down to 1200/24000 grit size papers to obtain reasonably scratch-free surfaces with high reflectivity. To remove finer scratches, samples were then polished using diamond suspension (3 μm and 1 μm) and then samples are ready for etching. Different etchants were attempted whereas the following two etchants gave the best results:

Table 3-2: Etchants used for optical microscopy of copper

	Composition	Comments
1	$FeCl_3$ (5 gm), HCl (10 ml), H_2O (100 ml)	This is a chemical-mechanical polish etchant. During the last stage of polishing (using the cloth mat), few drops of the etchant are added while polishing, then rinse with water.
2	NH_4OH (25 ml), H_2O (25 ml), H_2O_2 (25-50 ml)	Must be fresh, peroxide to be added last, swab sample 5-45 second.

Figure 3-3 shows microstructure of copper based on which, the grain size distribution (GSD) was estimated using ~ 100 grain counts as shown in Figure 3-4 and the average grain size of copper was estimated to be 38.24$\pm$12 μm.

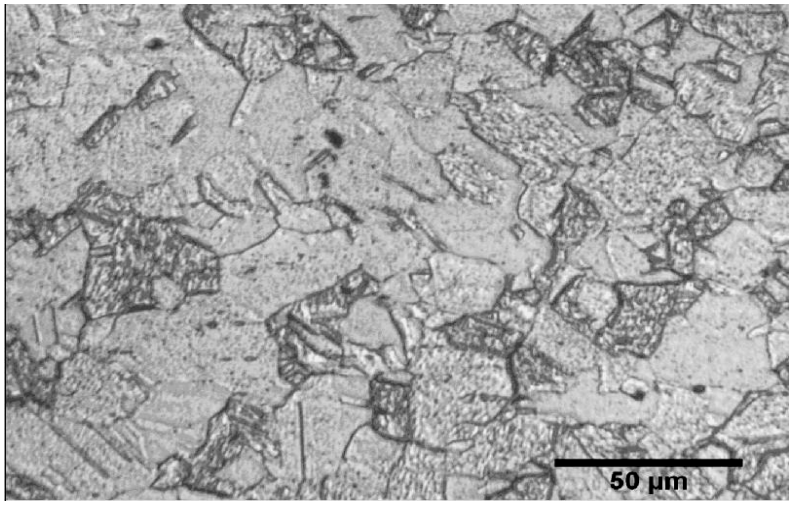

Figure 3-3: Optical micrograph of MG-copper with average grain size ~ 38±12 µm.

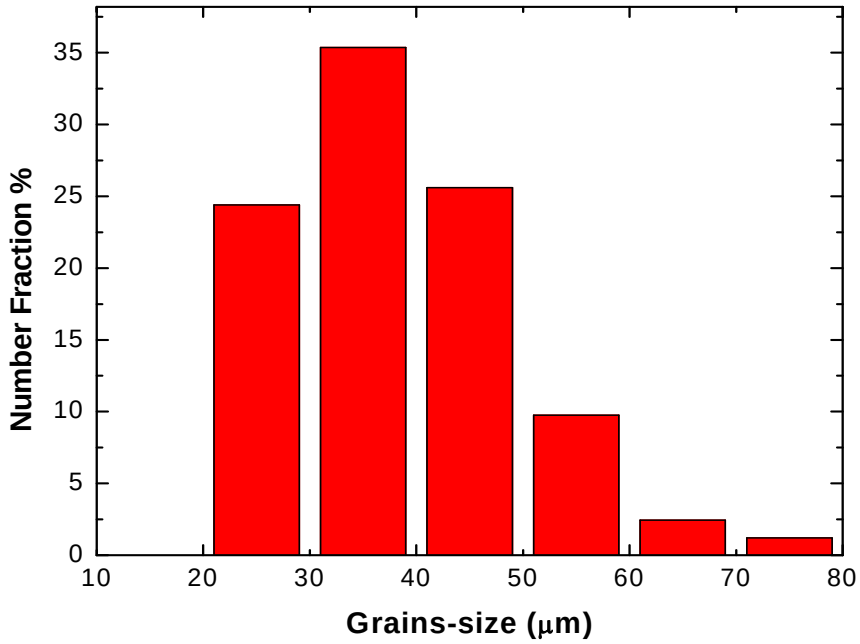

Figure 3-4: Grain size distribution (GSD) of as received MG-copper.

3.1.2 Grain size analysis via X-ray diffraction (XRD)

Because of the resolution limits of optical microscopy, the grain size of nc-copper can not be determined via this technique and alternatively, other techniques were utilized to estimate the average grain size of nc-copper and the grain size distribution as well. X-ray diffraction (XRD) is commonly used to estimate the crystallite size of nc-materials by analyzing the diffraction peaks profile broadening which is inversely proportional to the crystallite size (i.e. the smaller the crystallite size, the broader the peak profile is). The grain size (or crystallite size) can be determined from XRD data/peaks profiles via different methods/models among which, the following two methods were applied in the present study:

I. Scherrer equation: In this method, peaks profiles are analyzed individually and the crystallite size (i.e. grain size) is determined based on the diffraction angle (2θ) and the measured integral breadth of the peak profile (for simplicity, the Full Width at Half maximum "FWHM" of the diffraction peak). The equation has the form [72]:

$$L = \frac{K\lambda}{B\,Cos(\theta)} \qquad \text{Equation 3-1}$$

where K is called the Scherrer constant (~ 0.89 - 1), λ is the wave length of the x-ray anode source (~ 1.5418 A^o for copper anode source), β is the integral breadth of the peak profile expressed in radians, θ is the Bragg angle and L is the crystallite size. Although applying the Scherrer equation seems to be straight forward, it is important to recall that this method estimates the average crystallite size from a single peak profile and furthermore, it does not count for the internal strain component of the peak broadening; however, the Scherrer

equation is considered an easy and reliable method for a quick estimation of crystallite/ grain size.

II. The Williamson-Hall plot: In this method, peaks profiles at different Bragg angles are utilized simultaneously to estimate the average crystallite size and furthermore, the method determines the internal strain which contributes to peaks broadening which makes results from this method more accurate than those obtained from the Scherrer equation. The working equation of this method is given as [73]:

$$B\,Cos(\theta) = \frac{K\lambda}{L} + 2(\varepsilon)\,Sin(\theta) \qquad \text{Equation 3-2}$$

where ε refers to the lattice strain and all other parameters have the same meaning mentioned earlier. The XRD patterns of both MG-copper and *nc*-copper are shown in Figure 3-5 and Figure 3-6 respectively.

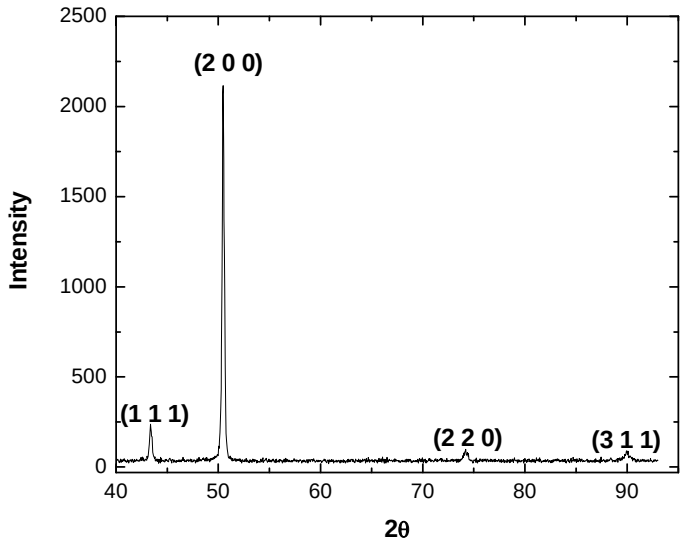

Figure 3-5: XRD peaks of MG- copper with the major reflections peaks identified.

Obviously, the diffraction peaks of MG- copper shown in Figure 3-5 are too narrow to perform peak profile analyses and XRD fails to estimate grain size in this case (according to the Williamson-Hall plot, it will return an infinite grain size - generally speaking, both the Scherrer equation and the Williamson-Hall method are limited to estimate crystallite/grain size up to 200 nm or even less). On the other hand, the broadening of the XRD peaks of *nc*-copper shown in Figure 3-6 indicates that the grain size is much smaller compared to that of the MG-copper. By averaging the grain size values obtained from Scherrer equation and Williamson-Hall plot, the average grain size of nc-copper was estimated to be ~ 28.7 nm.

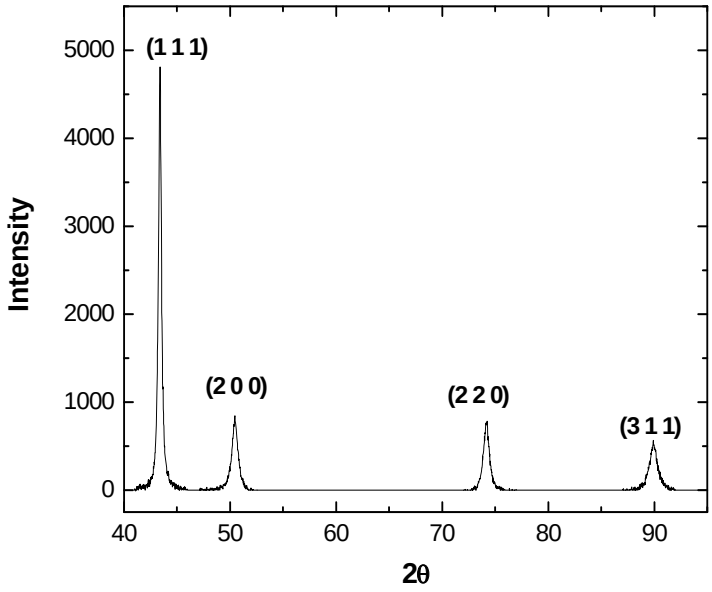

Figure 3-6: XRD peaks of nc- copper with the major reflections peaks identified.

The difference in peak intensities between micrograined and nc-copper are attributed to the differences in grain texture. The XRD of MG-copper indicates that the majority of grains are

oriented toward the [2 0 0] crystallographic direction which shows the highest intensity whereas, the majority of grains in nc-copper are oriented toward the [1 1 1] crystallographic direction. However, a reasonable fraction of grains are oriented toward the other crystallographic directions in nc-copper which is completely absent in MG- copper. Although the average grain size of nc-copper is now estimated, the grain size distribution of the material can not be established via XRD analysis and other techniques are to be attempted for that purpose.

3.1.3 Atomic force microscopy (AFM) of *nc*-copper

Atomic Force Microscopy (sometimes referred to as Scanning Force Microscopy) is a high resolution type of scanning probe microscopy. The technique has the ability of resolving fine details on the order of fractions of nanometers and accordingly, it is very suitable to scan features at the nanoscale such as nanoparticles, nanoclusters and nanograins.

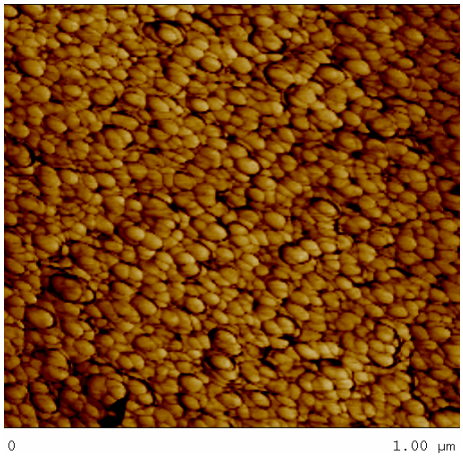

Figure 3-7: AFM of as-received nc-copper.

Moreover, the technique does not require any specific sample preparation rather than having a scratch-free surface which make it reliable technique to utilize. As shown in Figure 3-7, over a scanning area of 1 μm x 1 μm, tens, or even hundreds, of nanograins can be counted based on which the average grain size of as-received *nc*-copper was estimated to be 47.87±15.58 nm and the corresponding grain size distribution is shown in Figure 3-8 below.

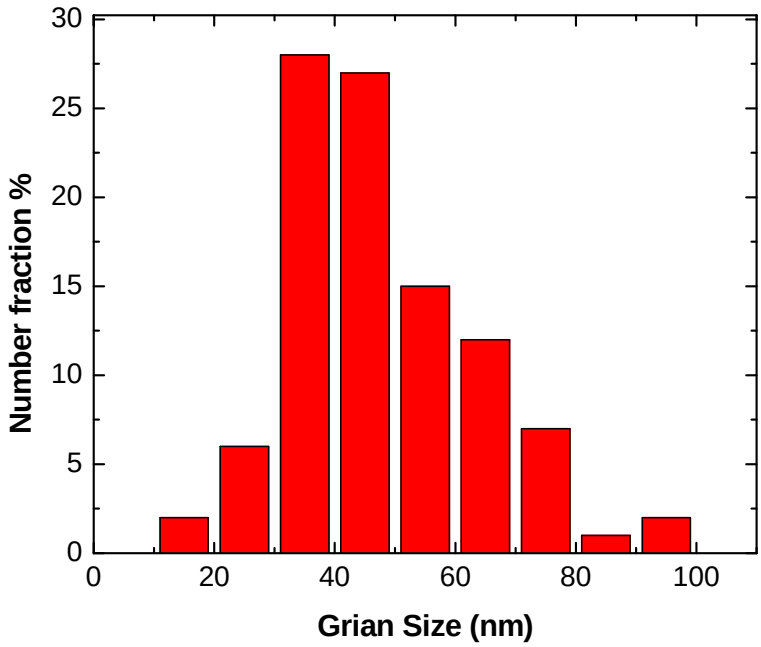

Figure 3-8: Grain size distribution of nc-copper corresponding to AFM analysis showing average grain size of 47.87±15.58 nm.

Although the average grain size from AFM is based on hundreds of grain, the fact that AFM scans different depth levels would imply inaccuracy in determining the actual diameter of

grain which might explain the difference between grain size values obtained from XRD and AFM.

3.1.4 Pre-Irradiation transmission electron microscopy (TEM)

Once material identification (chemical composition and phases) is completed, it is required then to examine the existence of any type of defects before irradiation. For that purpose, transmission electron microscopy (TEM) has the power to resolve defects and other features at the micro-scale and even at atomic level when high resolution TEM (HRTEM) is available. Sample preparation for TEM represents a critical stage and having a good transparent foil for TEM investigation is the first step to obtain a representative and reliable image of materials microstructure. In the present study, TEM foils were prepared either via electrochemical polishing (jet-polishing) or focus ion beam (FIB) techniques. For jet-polishing, the composition of the electrochemical solution used for copper is 10% Nitric Acid + 90% Methanol and dry ice is used to maintain the solution at -18^{o}C during the electrochemical polishing process. The risk that foils prepared via electrochemical polishing might not be transparent for TEM investigation enforced the attempt of preparing foils via focused ion beam (FIB) in which the thickness of the foil can be observed while the sample preparation process is in progress. FIB foils were prepared at the Analytical Instrumentation Facilities (AIF) center at NC State University using FEI Quanta 3D FEG which is a dual beam equipment with a traditional Field Emission column and a FIB column. TEM images of MG-copper showed relatively defect free grains (see Figure 3-9) and only traces of twin structures were observed in some foils as shown in Figure 3-10.

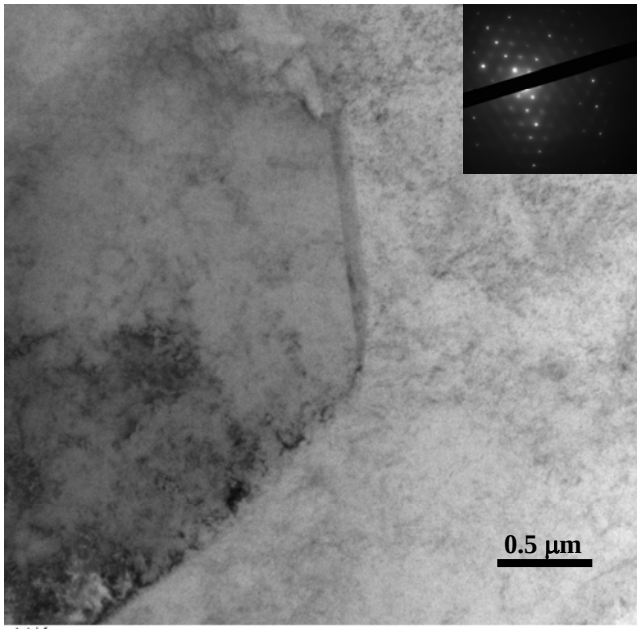

Figure 3-9: Bright Field (BF) TEM image of micrograined copper.

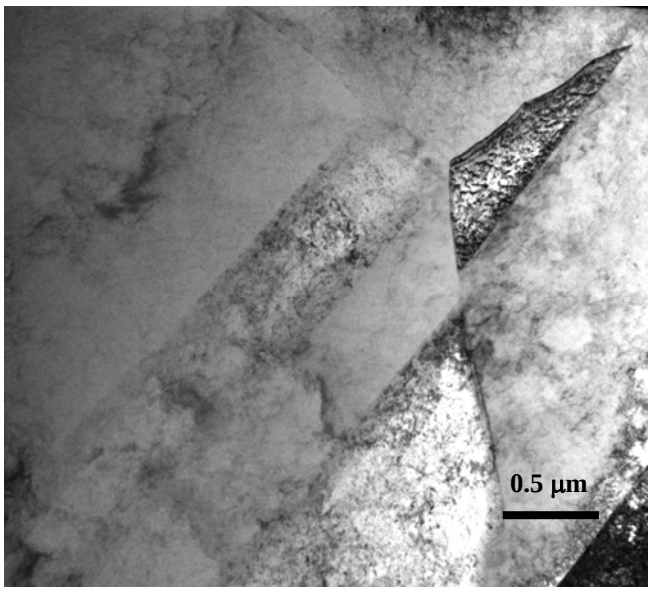

Figure 3-10: BF TEM image of micrograined copper showing twin structure.

Following the same sample preparation techniques, TEM foils of *nc*-copper were prepared and the microstructure investigation revealed the uniformity of nc-grains in all foils.

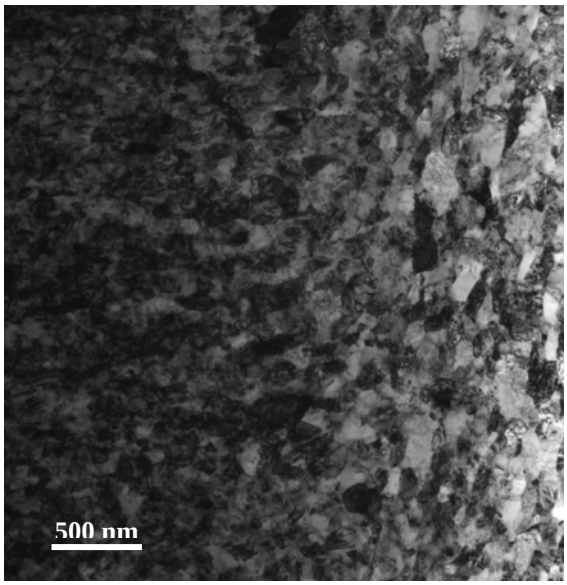

Figure 3-11: BF TEM image of nc-copper.

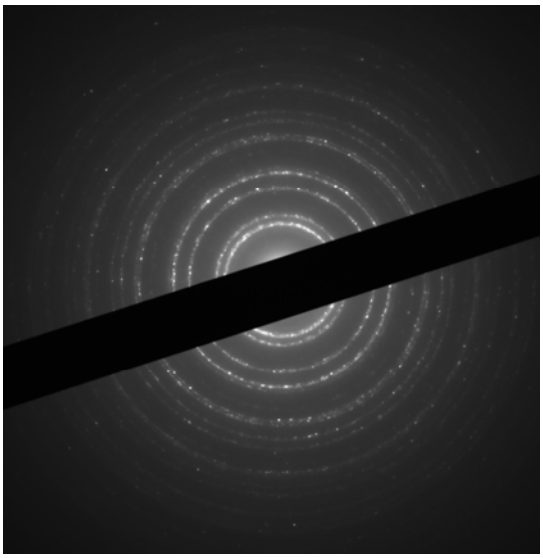

Figure 3-12: Corresponding diffraction pattern of nc-copper shown in Figure 3-11.

While the diffraction pattern of MG-copper shows diffraction spots corresponding to the different crystallographic planes, the diffraction pattern of nc-copper shown in Figure 3-12 is completely different. The near to complete diffraction rings of nc-copper originates from the diffraction on the different crystallographic planes in all grains and due to the large number of nanograins which are randomly oriented, the diffraction from each specific crystallographic plane forms a circle (a large number of diffraction spots linked together) rather than the individual diffraction spots which were observed in MG-copper. The complete diffraction rings observed in nc-copper indicates that the majority of the grains present is at the nano-scale in the sample. According to TEM investigation of different foils of nc-copper, the average grain size was estimated to be 28.32±10.93 nm and the corresponding grain size distribution was established.

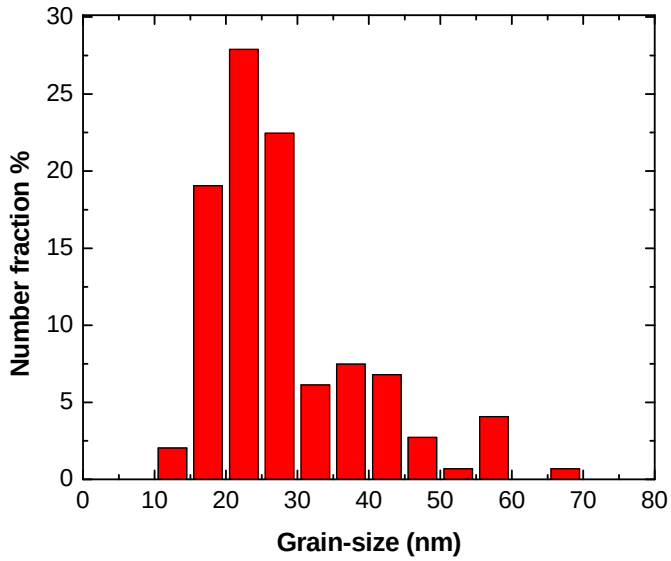

Figure 3-13: GSD of nc-copper based on TEM analysis showing average grain size of 28.32±10.93 nm.

The average values of the grain size of nc-copper obtained from the different microstructure investigation techniques reported above are listed in Table 3-3 which shows a good agreement between the results from the different techniques especially XRD and TEM.

Table 3-3: The average grain size of nc-copper obtained from different techniques

Technique	Average grain size of nc-copper
XRD (Sherrer equation)	~ 17.34 nm
XRD (Williamson-Hall- plot)	~ 44 nm
AFM	~ 47.87±15.58 nm
TEM	~ 28.32±10.93 nm

Accordingly, the average grain size of as received nc-copper was estimated by averaging the values obtained from the different techniques and it was found to be ~ 34.4 nm

3.2 Mechanical Properties of As-Received Materials

According to the literature survey covered in Chapter 2, it is clear that characterization of nc-materials response to irradiation was mainly described based on microstructure investigation which includes grain size measurements and defects analysis whereas assessment of the mechanical properties post irradiation was mostly limited to hardness measurements, and very limited number of studies involved deep characterization of irradiated nc-materials response to tensile/compression loading although the information obtained from such tests is essential to assess the ability of nc-materials to serve as structural

materials in radiation environments. The lack of mechanical testing attempts of irradiated nc-materials is mainly due to the difficulties associated with handling irradiated samples which even become more complicated in the case of neutron irradiation (which is the case under investigation) compared to ion irradiation.

In the present study, mechanical properties of micrograined and *nc*-copper are characterized by (conducting micro-indentation to estimate the overall hardness of materials and, tensile tests through which stress-strain curves are obtained and the different elastic/plastic mechanical properties of the materials are then estimated. Once the assessment of mechanical properties is available, it is then possible to discuss the relation between the developed microstructures and the response of materials to applied stress which is important to evaluate materials performance in order to qualify it for certain applications.

3.2.1 Micro-hardness measurements of as-received materials

Microhardness measurements are widely used to estimate materials strength in terms of the ability of a material to resist indentation. In the case of small size of samples, only small loads can be applied (~ hundreds of g_f) which represents the major difference between macro-hardness and micro-hardness testing setup. Materials hardness is estimated based on the applied load and the dimension of the indentation and dimensions caused by the penetration of an indenter through sample surface. According to the shape of the indenter, different microhardness testing are defined such as the Vickers test in which a square-based diamond pyramid indenter is used and the Knoop test in which a rhombohedral-shaped diamond indenter is used. The Knoop test is commonly used with thin layers where sample

thickness/volume is not enough to accommodate the plastic deformation zone to be formed underneath the indenter when the Vickers test is applied. Samples involved in the present study were thick enough to apply the Vickers hardness and all hardness measurements and values reported are based on a Vickers hardness setup using BEUHLER OmniMet® Microhardness Testing System.

To ensure homogeneity of microstructure of materials under investigation, hardness measurements were conducted over 8 mm X 6 mm disks and a grid of indentations was made based on which the average hardness was estimated.

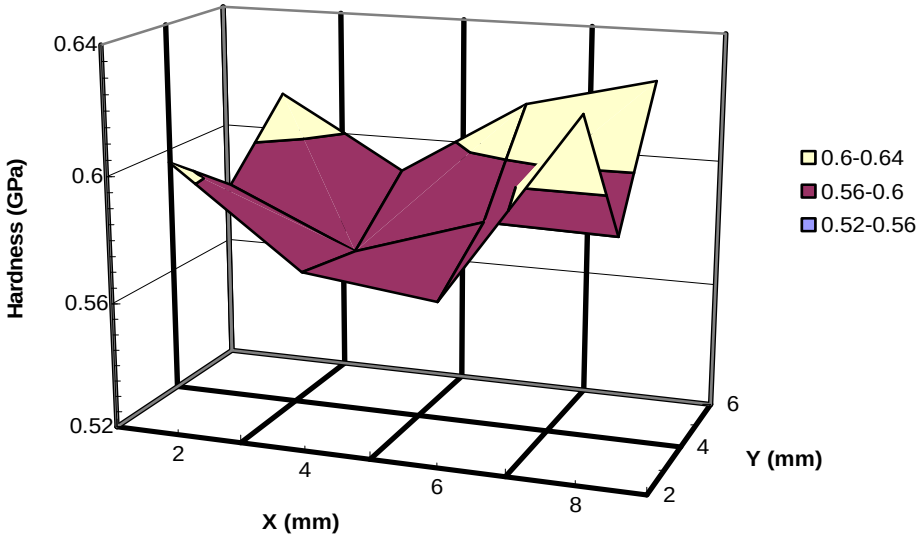

Figure 3-14: Microhardness measurements over 8 mm X 6 mm disk of MG-copper with average hardness = 0.596±0.02 GPa.

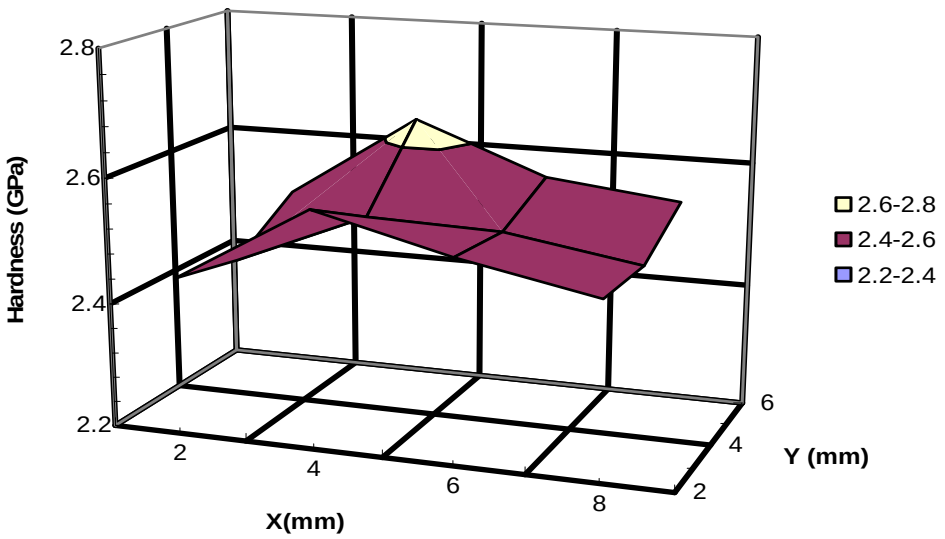

Figure 3-15: Microhardness measurements of nc-copper over a 8 mm X 6 mm disk with average hardness = 2.5±0.05 GPa.

From Figure 3-14, the microhardness of micrograined copper varies between 0.52 GPa and 0.64 GPa which reflect the uniformity of hardness and accordingly homogeneity of microstructure over the tested disk area and the overall hardness is estimated to be 0.596±0.02 GPa. Similarly, the microhardness measurements over a disk of the same size of nc-copper show a variation of hardness between 2.2 GPa and 2.8 GPa which again indicates a homogeneous structure and additionally, it implies that nanograins are uniformly formed the whole system with average hardness estimated to be 2.50±0.05 GPa which is approximately five times greater than that of micrograined copper. This difference in hardness between MG-copper and nc-copper is reasonable based on the Hall-Petch

relationship relating materials hardness to its grain size. The Hall-Petch relation of nc-copper compared to reference data is shown in Figure 3-16.

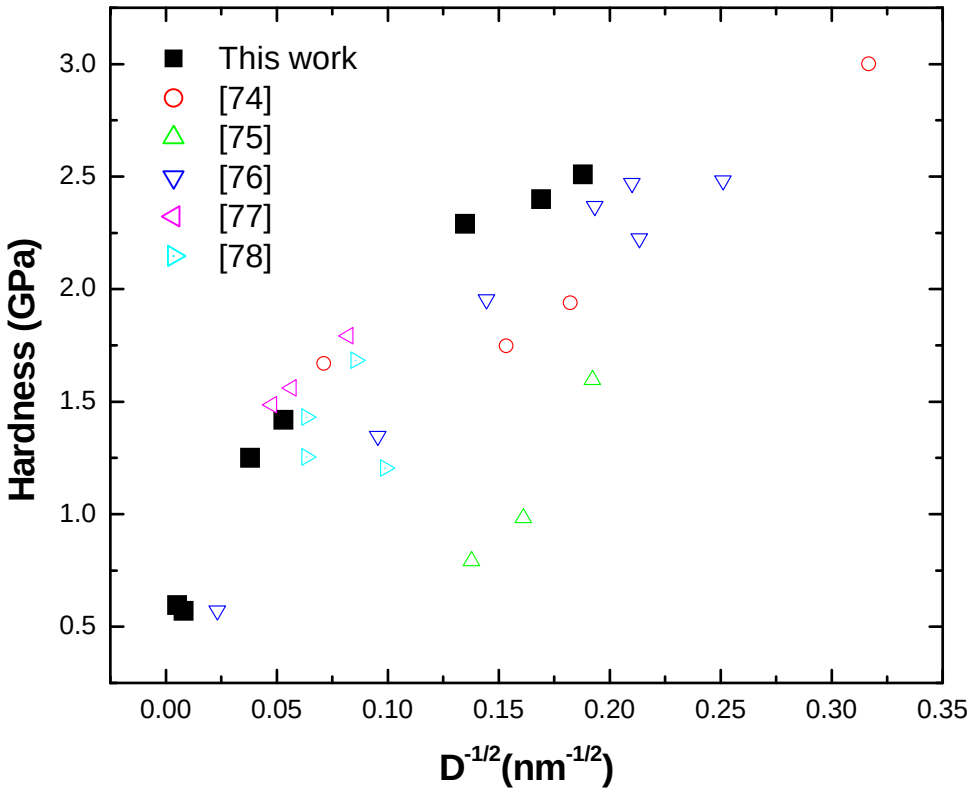

Figure 3-16: Variation of hardness with $D^{-1/2}$ for *nc*-copper.

3.2.2 Tensile testing of as-received materials

While microindentation measurements easily reveal the hardness of materials which in turn can be related to grain size, this technique is incapable of providing any information regarding other essential mechanical characteristics such as ductility and toughness.

Although microhardness was found to be related to the yield strength of materials, microindentation can not provide precise description of the yield point phenomenon observed in some materials such as ferritic steel or irradiated FCC at certain damage levels. Ductility, toughness, and yield point phenomenon are commonly assessed by subjecting materials to tensile loading and by properly analyzing the recorded displacement and load data. Stress-strain curves can be established from which most of the mechanical properties can be evaluated.

Tensile testing of micrograined materials can be conducted using any of the commonly used universal tensile frames and standard tensile samples can be machined according to the American Society for Testing and Materials (ASTM). On the other hand, the fact that, nc-materials are not being processed yet on large scale and can only be obtained in the form of sheets of few centimeters, would require machining of sub-size tensile samples with relatively much shorter gauge lengths and smaller cross sections. With such sub-size tensile samples, standard universal testing frames and grips can not be used as it is practically hard to accurately detect and record displacement and load signals from such small samples and for that reason, a miniature tensile tester was built for the tensile testing of nc-copper sample (see Figure 3-17 and Figure 3-18).

Step motor

Smart step

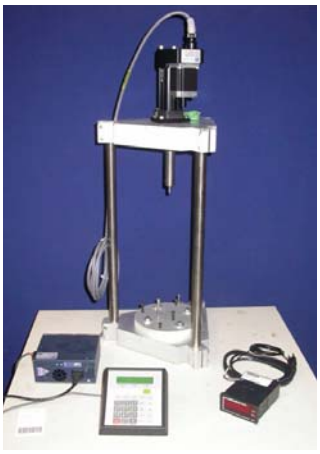

Main Frame

Signal conditioner

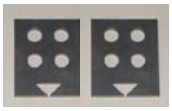

Grips

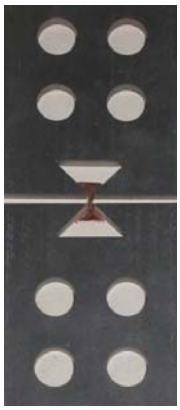

Figure 3-17: Individual components of miniature tensile tester: step motor, smart step to regulate the step motor, signal conditioner to smooth displacement and load signals for data acquisition, grips holding samples while load is applied.

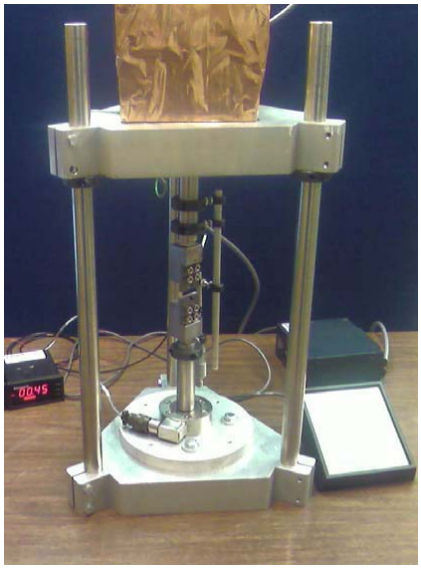

Figure 3-18: Miniature tensile tester in vertical positioning.

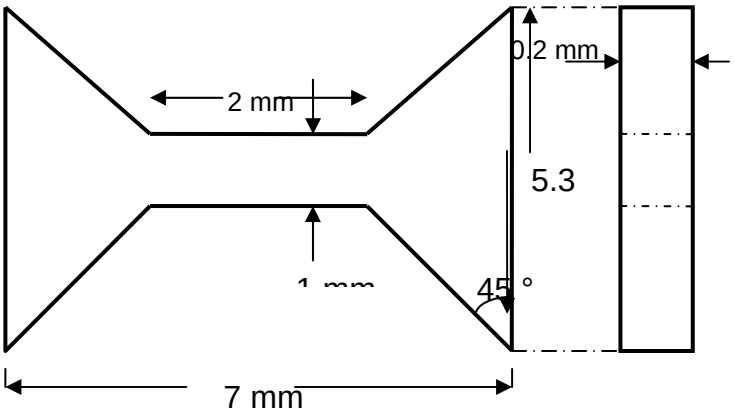

Figure 3-19: Schematic design of sub-size tensile sample.

In order to take away any effect related to sample geometry/dimensions, sub-size tensile samples with the dimensions shown in Figure 3-19 were machined from both micrograined and nc-copper. Tensile testing of as received micrograined and nc-copper was conducted at room temperature and at a constant strain rate of 10^{-5} s^{-1}. Engineering stress-strain curves of micrograined and nc-copper are shown in Figure 3-20 along with TEM micrographs prior to testing of both structures. Table 3-4 summarizes the mechanical properties obtained for the as-received materials.

Table 3-4: Mechanical properties of as received materials from tensile testing

	S_y (MPa)	UTS (MPa)	e_u	e_t	n
MG- copper	80± 6	174± 21	0.43± 0.07	0.66± 0.02	0.35 ± 0.05
nc-copper	557± 5	731± 21	0.052± 0.004	0.079±001	0.05 ± 0.004

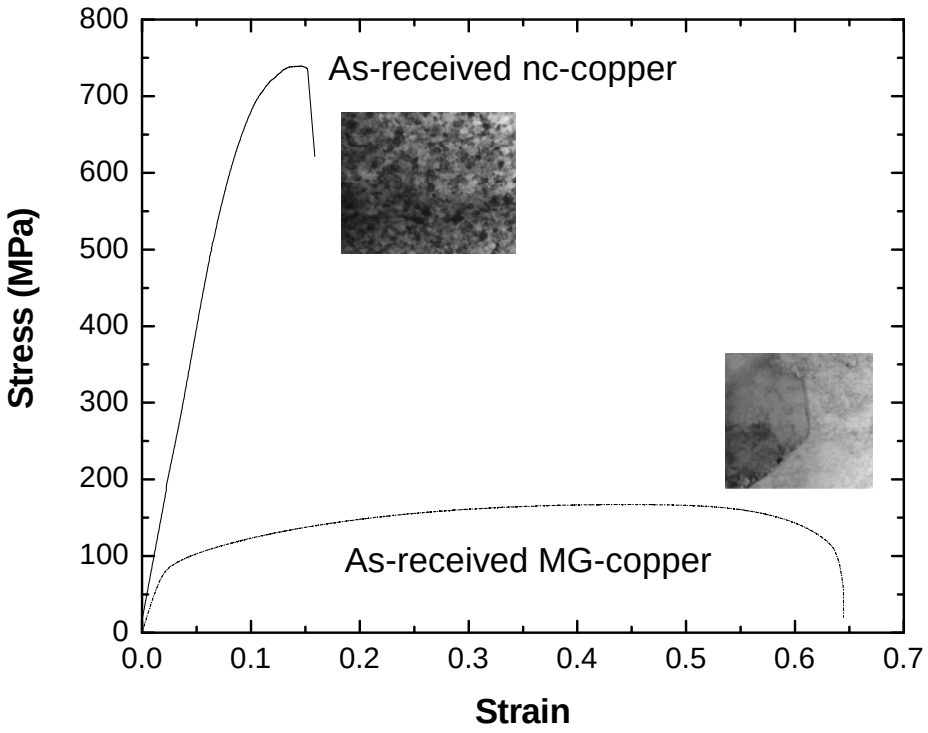

Figure 3-20: Engineering stress-strain curves of as received materials with the corresponding TEM micrographs (before deformation) shown for each structure.

The response to tensile loading clearly reveals the huge difference in mechanical behavior between MG-copper and nc-copper which can be simply seen in the higher strength of nc-copper on one side and extreme ductility of MG-copper on the other side. Both properties, strength and ductility, are strongly coupled in most cases and their relation to grain size of materials is described by what is called the grain boundary strengthening mechanism (Hall-Petch plot). It is well known that materials ductility originates from the existence of the various types of imperfections, dislocations in particular, at the micro-level and is proportional to the mobility of those imperfections. Materials strength can be enhanced when

pinning points created by some method impede propagation of dislocations. Grain boundaries are considered to be acting as pinning points for two reasons:

I. adjacent grains, separated by grain boundaries, have different orientations which means that more energy is required by a dislocation to change direction and to jump from one grain to another

II. due to the high degree of disorder characterizing grain boundaries, it becomes very difficult for a dislocation to move in a continued slip plane

For either of the two reasons, a dislocation trip is very likely to end at a grain boundary which is seen in this case as a sink for dislocations. From this view, the variation of materials strength and ductility with grain size is well understood and the difference in mechanical behavior/response between MG-copper and nc-copper is very reasonable based on the large difference in grain size reported for the two structures.

While stress-strain curves quantitatively describe materials ductility and strength, it is also possible to extract information regarding the nature of materials response to applied loads by investigating the topography of the fracture surfaces and for this purpose, SEM was utilized to characterize the fractured sub-size samples of MG- and nc-copper. The fracture surface of MG-copper showed typical characteristics of ductile fracture where the cup-cone was identified along with poor reflectivity of the surface. The fracture surface of nc-copper seems to be quite similar to that observed in brittle polycrystalline materials except that the fracture surface shows multiple shear bands rather than a single band which causes the surface of nc-copper to be less shiny compared to that of brittle polycrystalline materials.

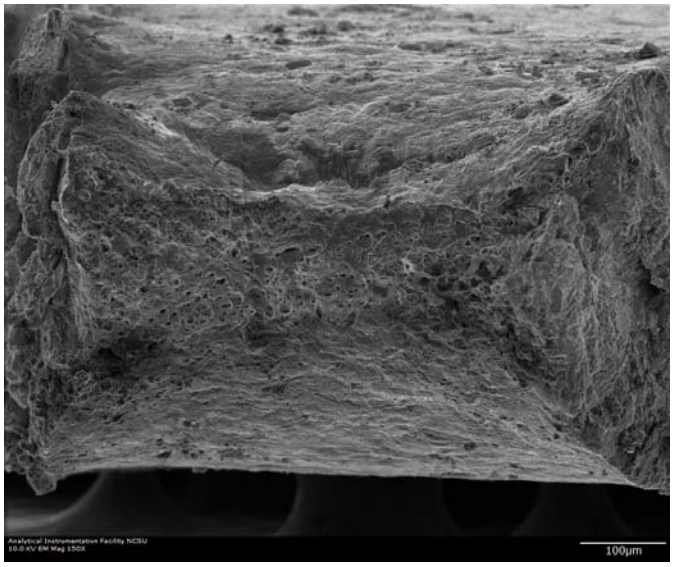

Figure 3-21: SEM of MG-copper under tension condition showing dull fracture surface indicating ductile nature of fracture.

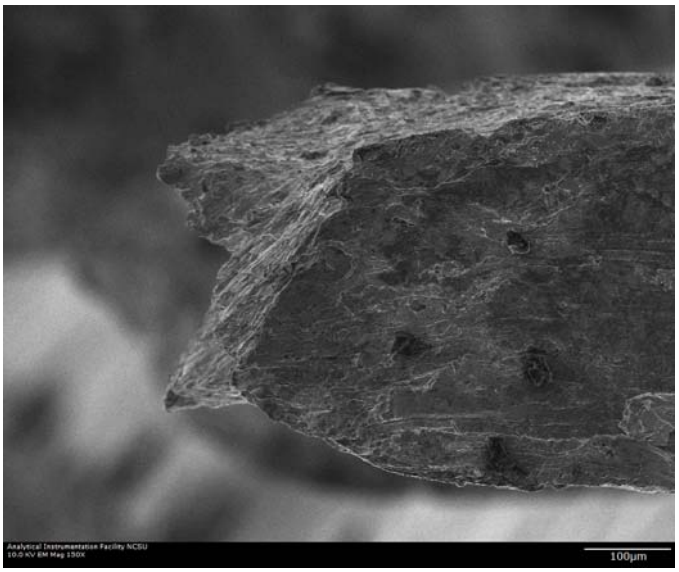

Figure 3-22: Surface topography of fractured MG-copper showing the cup side of the fracture surface occurring in ductile fracture.

Figure 3-23: SEM of nc-copper under tension condition showing shear bands as a sign of brittle fracture.

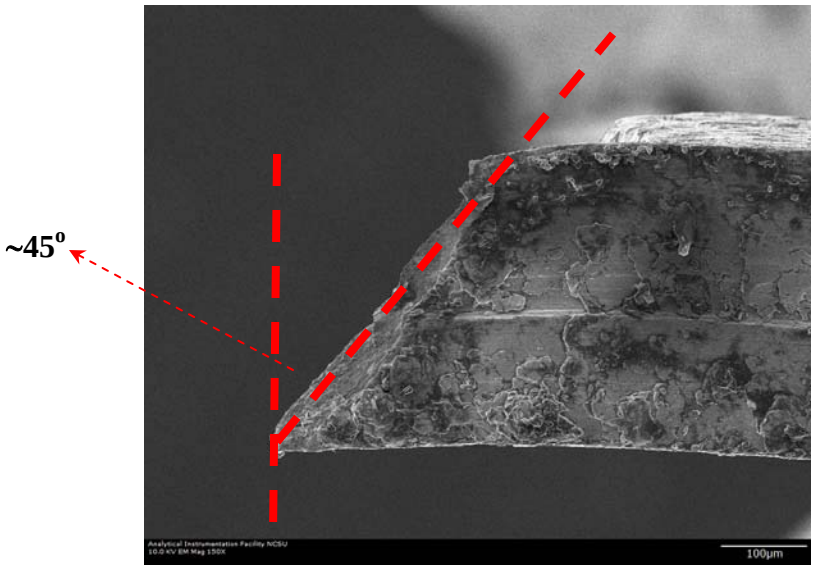

Figure 3-24: Surface topography of fractured nc-copper showing approximately 45° shear band at which maximum shear stress is achieved in brittle fracture.

In order to assure the judgments based on fracture topography, high magnification of fracture surface of as received MG-copper shown in Figure 3-25 was compared to surface topography of copper sample under condition of tension loading shown in reference [79] and a good agreement between the two micrographs is noted.

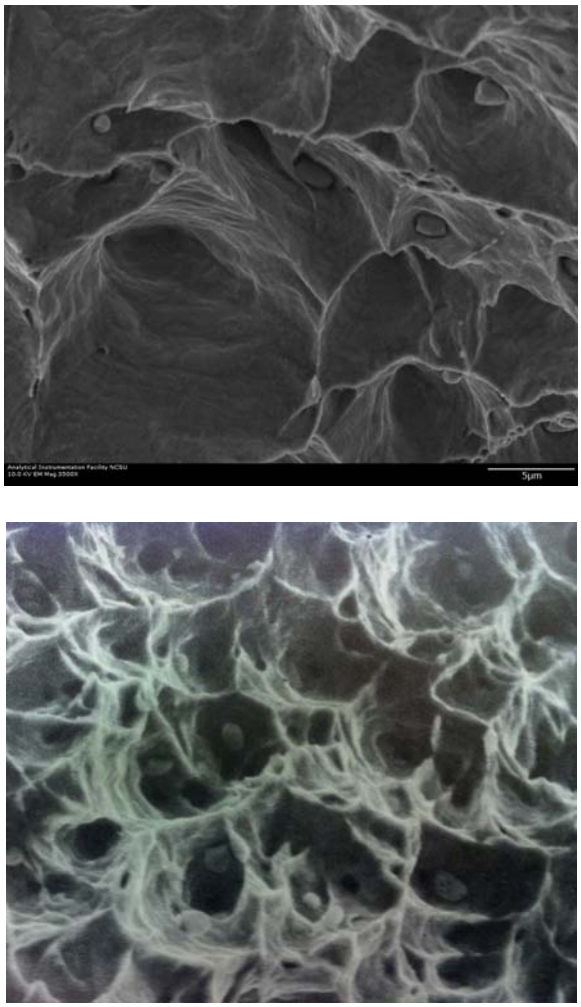

Figure 3-25: Formation of dimples under tensile loading of as received MG-copper (top) and equivalent SEM surface topography seen in copper under the same loading condition [79].

3.3 Irradiation Experiments

In this section, the setup of the irradiation experiments both at the PULSTAR reactor and the Advanced Test Reactor (ATR) will be highlighted. Since irradiation was conducted at two different facilities, it was necessary to express the damage in terms of *dpa* rather than neutron fluence so that data and results collected from both experiments can be discussed jointly. The model which was used to estimate the dpa along with all working equations will be reported as well.

3.3.1 Simplified model for damage calculations

The major design parameters in irradiation experiments can be divided into parameters related to the irradiation facility such as the neutron spectrum, and parameters related to the irradiated materials such as isotopic abundances, density and displacement energy, while cross section data are dependent on both the neutron spectrum and the material under investigation. In order to achieve a specific damage level, the irradiation time is then the only parameter left. As mentioned earlier, irradiation experiments conducted at PULSTAR reactor were aimed to investigate response of nc-copper to neutron irradiation at relatively low damage level whereas higher damage levels experiments were conducted at the ATR where higher levels of neutron flux can be achieved. The flow chart (Figure 3-26) shows the general procedure followed to estimate the irradiation time needed to achieve a specific damage level in terms of *dpa* that is the average number of displacements per atom when a material is exposed to neutron flux.

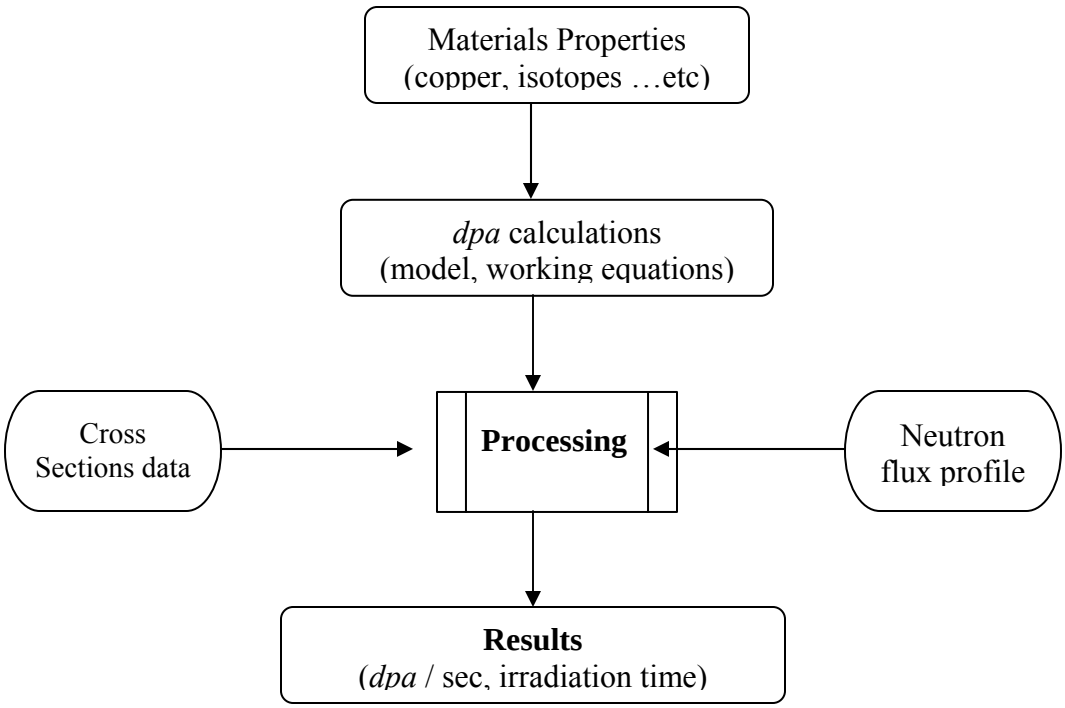

Figure 3-26: General procedure for dpa calculations.

Working equations for damage calculations

Let $\phi(E_n)$ be the flux (per cm^2 per sec) of neutrons with Energy E_n. The rate of atomic displacement, R_d, is proportional to the number of target atoms per cm^3 (N) and the displacement cross-section, $\sigma_d(E_n)$, for neutrons with energy E_n,

$$R_d = N \times \sigma_d(E_n) \times \phi(E_n) \qquad \text{Equation 3-3}$$

By definition, the number of displacements per atom is given by:

$$dpa = \frac{R_d\, t}{N} = t \int_{E_d/\gamma}^{\infty} \sigma_d(E_n)\phi(E_n)dE_n \approx t\int_0^{\infty} \sigma_d(E_n)\phi(E_n)dE_n \qquad \text{Equation 3-4}$$

The displacement cross-section is given by the sum of the number of atomic displacement, ν(T), produced by Primary Knock-on Atoms (PKAs) with energies T from E_d (the threshold displacement energy) to the maximum transferable energy T_{max} where:

$$T_{\max} = \gamma E_n \qquad \text{Equation 3-5}$$

where for neutron atom interaction: $\gamma = \frac{4A}{(1+A)^2}$ Equation 3-6

The interaction probability is given by the differential energy transfer cross-section $\sigma_n(E_n,T)dT$ for producing a PKA with energy between (T) and (T+ dT) due to interaction with a neutron of energy E_n:

$$\sigma_d(E_n) = \int_{E_d}^{\gamma E_n} \sigma_n(E_n,T)\upsilon(T)dT \qquad \text{Equation 3-7}$$

Now, it is required to find an expression for ν(T) in Equation 3-7

3.3.2 The Kinchin and Pease (K-P) model to calculate ν(T)

The K-P model [80] is a very conservative model in determining the number of atoms being displaced by a single PKA. The model is based on the following assumptions:

1. Collisions between atoms is analyzed as a two-body elastic collision
2. The energy transfer cross section is represented by the hard sphere model
3. Atoms are assumed to be randomly arranged
4. Atomic displacement occurs only when PKA energy is higher than E_d
5. E_d is neglected in energy balance equations

6. Energy loss by electron stopping occurs only if PKA energy is above a cut-off energy E_c

Considering the first collision between a PKA and a stationary atom and based on the six assumptions listed above, an explicit expression of $\upsilon(T)$ in different energy regimes was derived which is shown graphically in Figure 3-27 :

$$\upsilon(T) = \begin{cases} 0 & T < E_d \\ 1 & E_d < T < 2E_d \\ \dfrac{T}{2E_d} & 2E_d < T < 2E_c \\ \dfrac{T}{2E_c} & T \geq E_c \end{cases} \qquad \text{Equation 3-8}$$

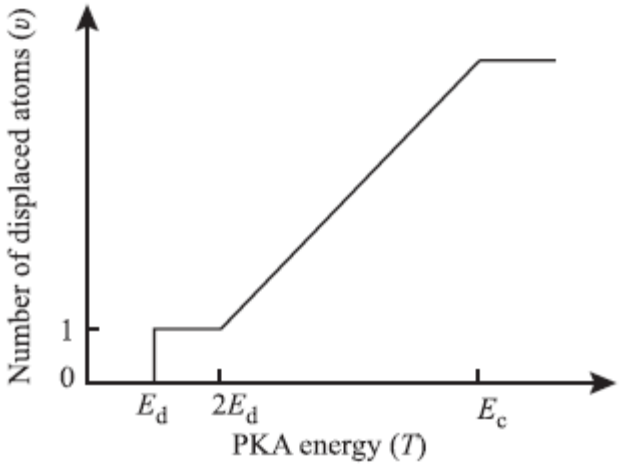

Figure 3-27: Variation of ν(T) according to K-P model [81].

That cross section term in Equation 3-7 can be applied to all possible regimes of scattering interactions which might contribute to the displacement process. The contribution of inelastic scattering to the displacement cross section can be ignored for neutron energies below 1 to few MeV and accordingly, it is possible to assume that the main contribution to the displacement event is due to elastic scattering with cross section expressed as:

$$\sigma_s\left(E_n,T\right)=\frac{4\pi}{\gamma E_n}\sigma_s\left(E_n,\theta\right) \qquad \text{Equation 3-9}$$

where θ is the scattering angle. By assuming the isotropic elastic scattering, the expression in Equation 3-9 can be simplified to:

$$\sigma_s\left(E_n,T\right)=\frac{4\pi}{\gamma E_n}\frac{\sigma_s\left(E_n\right)}{4\pi} \qquad \text{Equation 3-10}$$

Thus, substituting by Equation 3-10 in Equation 3-7, the displacement cross section is now given by:

$$\sigma_{Ds}(E_n)=\frac{\sigma_s(E_n)}{\gamma E_n}\int_{E_d}^{\gamma E_n}\upsilon(T)dT \qquad \text{Equation 3-11}$$

Inserting Equation 3-8, with the expression for ν(T) based on K-P model given in Equation 3-11, in Equation 3-4, the rate of atomic displacement, R_d, can be calculated as:

$$R_d=N\int_0^{\infty}\int_{E_d}^{\gamma E_n}\frac{\sigma_s(E_n)}{\gamma E_n}\frac{T}{2E_d}dT\phi(E_n)dE_n \qquad \text{Equation 3-12}$$

and considering the elastic scattering cross section to be constant over a wide range of energy, the rate of atomic displacements is then given by:

$$R_d = \left(\frac{N\sigma_n^{el}}{2\gamma E_n E_d}\right)\int_0^{\infty}\int_{E_d}^{\gamma E_n} T dT \phi(E_n) dE_n$$
$$= \left(\frac{N\sigma_n^{el}\gamma}{4E_d}\right)\int_0^{\infty} E_n \phi(E_n) dE_n \qquad \text{Equation 3-13}$$

The energy dependent neutron flux is then replaced by the total neutron flux,Φ , with an average energy $\bar{E}_n$ given as:

$$\Phi = \int_0^{\infty} \phi(E_n) dE_n$$
$$\bar{E}_n = \frac{\int_0^{\infty} E_n \phi(E_n) dE_n}{\int_0^{\infty} \phi(E_n) dE_n} \qquad \text{Equation 3-14}$$

The integral in Equation 3-13 is replaced by $\Phi\,\bar{E}_n$, and the expression for the rate of atomic displacement is then given as:

$$R_d = \frac{N\sigma_n^{el}}{4E_d}\bar{E}_n\,\Phi \qquad \text{Equation 3-15}$$

and the final expression for the dpa becomes:

$$dpa = \frac{R_d t}{N} = \sigma_n^{el}\frac{\gamma\,\bar{E}_n}{4E_d}\Phi t \qquad \text{Equation 3-16}$$

According to Equation 3-16, the elastic cross section, E_d, and γ are all material dependent where the average neutron energy and the accumulated flux are characteristics of the

irradiation facility and hence, the irradiation time (t) is the only design parameter left to be determined in order to achieve a specific dpa level.

3.3.3 Irradiation experiments at ATR

The Advanced Test Reactor (ATR) represents a unique irradiation facility because of the availability of various irradiation positions with variable neutron flux levels which make the design of an experiment to be more flexible. Furthermore, access to the hot cell facilities accelerates the post irradiation examination which greatly narrows the time frame. The main object was to investigate the response of nc-copper to relatively higher damage levels (1, and 2 *dpa*) and according to availability of irradiation positions and for other technical limits, samples of MG- and *nc*-copper were irradiated at the East Flux Trap (EFT) at position E-7 (see Figure 3-28).

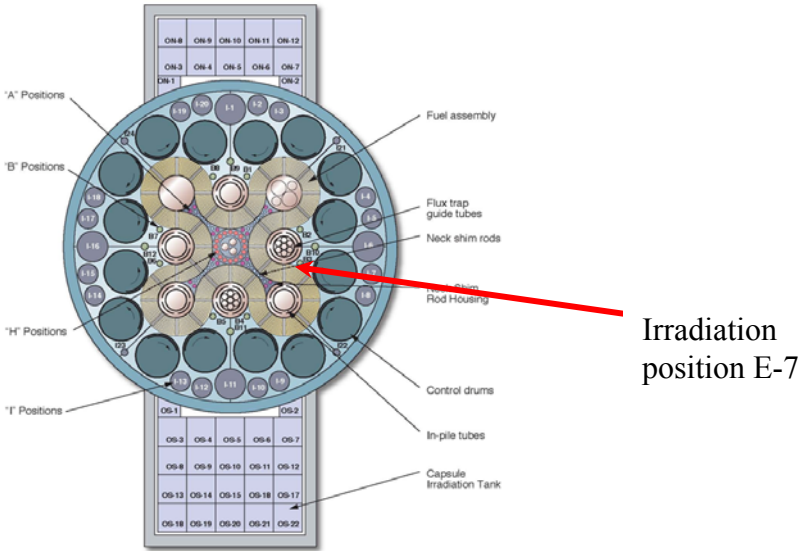

Figure 3-28: ATR core cross section showing the irradiation position E-7 [82].

In order to estimate the rate of atomic displacements at that position, unperturbed four-energy- group neutron flux given in [82] are considered along with the following isotopic data for copper.

Table 3-5: Atomic abundance of naturally occurring copper isotopes

Isotope	Abundance (a/0)
Cu-63	69.17
Cu-65	30.83

The cross-section data for the two naturally occurring copper isotopes was generated through the Evaluated Nuclear Data File (ENDF) (National Nuclear Data Center) for the five-energy-group. Cross-sections data was generated at the average energy of each neutron-energy group.

Table 3-6: Cross section data for damage calculations

	ϕ1 (0.05276MeV)	ϕ2 (1.5)MeV	ϕ3 (0.55)MeV	ϕ4 (2.76E-3)MeV
Cu-63	2.264113 b	2.242574 b	4.8264 b	6.8689 b
Cu-65	3.26408 b	2.50953 b	4.2767 b	12.4296

Equation 3-16 for *dpa* will be applied in the following format to count for the different neutron-energy groups:

$$dpa/t = \frac{\gamma}{4E_d}\sum_{i}^{m}\sigma_n^{el}(i)\,\bar{E}_n(i)\Phi(i) \qquad \text{Equation 3-17}$$

where *m* refers to the number of energy-groups neutron flux. For copper, γ~0.0606 and E_d is taken to be 30 eV [81]. Substituting with all numerical values in Equation 3.17 yields:

$$dpa/\sec = 7.552\times10^{-7} \qquad \text{Equation 3-18}$$

and accordingly, the irradiation time to achieve 1 *dpa* is approximately 16 days and in terms of ATR cycles (1 cycle = 2 weeks) 1 and 2 *dpa* are achieved approximately within 1 and 2 ATR cycles respectively.

For the different purposes of Post Irradiation Examination (PIE), three major sample geometries were irradiated:

- TEM specimens which are 3 mm diameter disks,
- Miniature tensile test samples as previously shown in Figure 3-19
- Small square plates for hardness measurements.

The test train array holding the samples during irradiation was constructed from aluminum to avoid any flux perturbation and samples were loaded in capsules which are stacked vertically in the test train. Within each capsule is a 'test train' assembly consisting of aluminum blocks (see Figure 3-29) that hold the samples. Each test train (see Figure 3-30) contains eighteen, 0.230" diameter, 0.4" long sample holder assemblies designed to hold two tensile samples

each; three holders are required for each of six material types. Eight other sample holder assemblies (0.150" long) hold all of the TEM sample blanks. Then the sample holder assemblies were strung together using aluminum rods (thick wire). The irradiation test capsule assembly and test train assemblies are shown in Figure 3-29, Figure 3-30, and Figure 3-31.

The irradiation test assembly consists of the experiment basket, sleeve and capsule assemblies, which contain the test trains (aluminum blocks and samples). The experiment basket of the test assembly is an aluminum tube designed to interface the capsule assembly with the ATR. Each capsule assembly was about 16-in. tall and holds a test train of 14-in. long.

A basic design objective for each capsule was to operate at 200°C or below. The internal heating for each capsule was planned to be calculated using the MCNP coupled with ORIGEN2 (MCWO) analysis methodology. Prelimary thermal-hydraulic analyses using typical heating rates for these types of materials indicated sample temperature range from 65°C to 85°C.

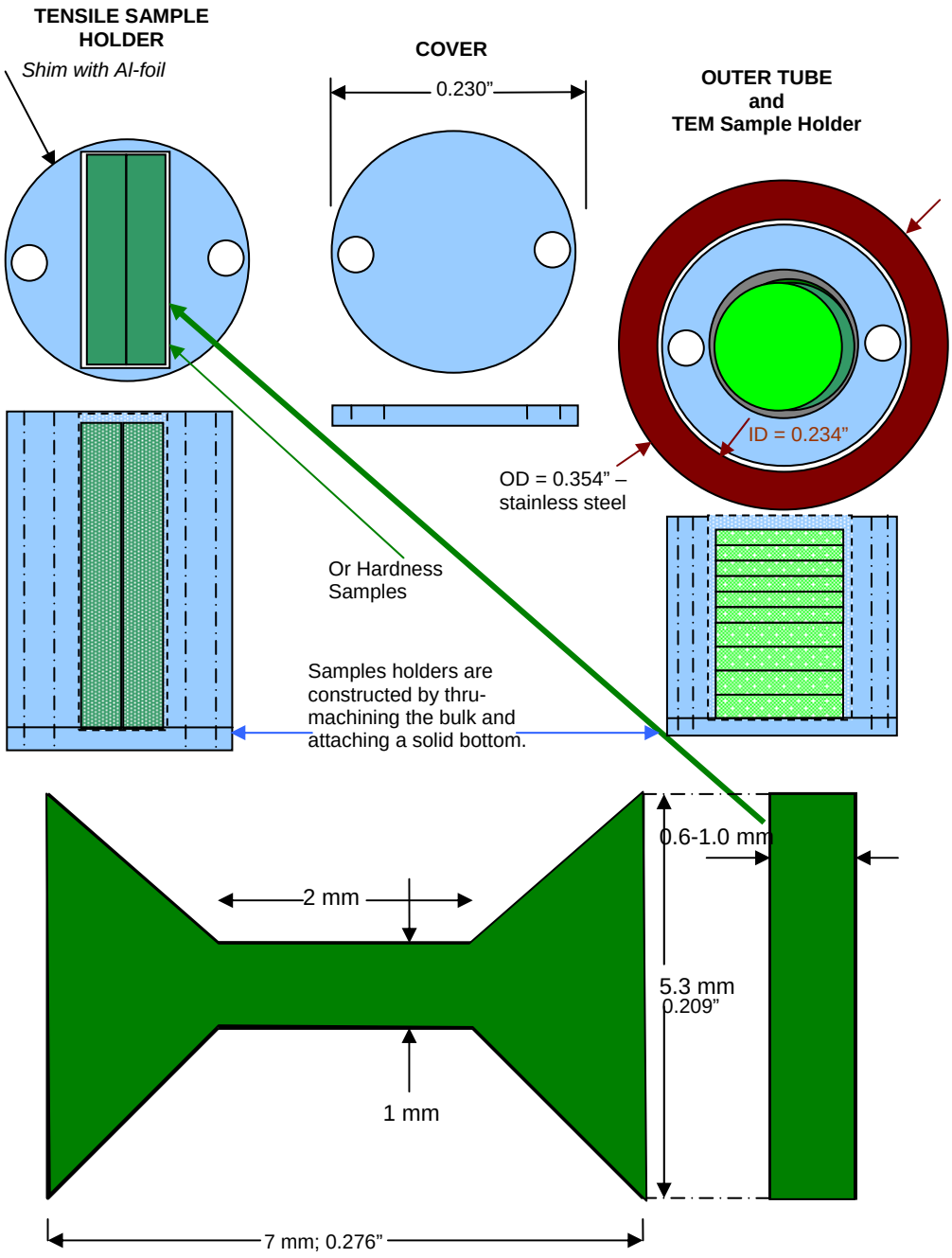

Figure 3-29: Sample/holder design of the irradiation experiment at ATR.

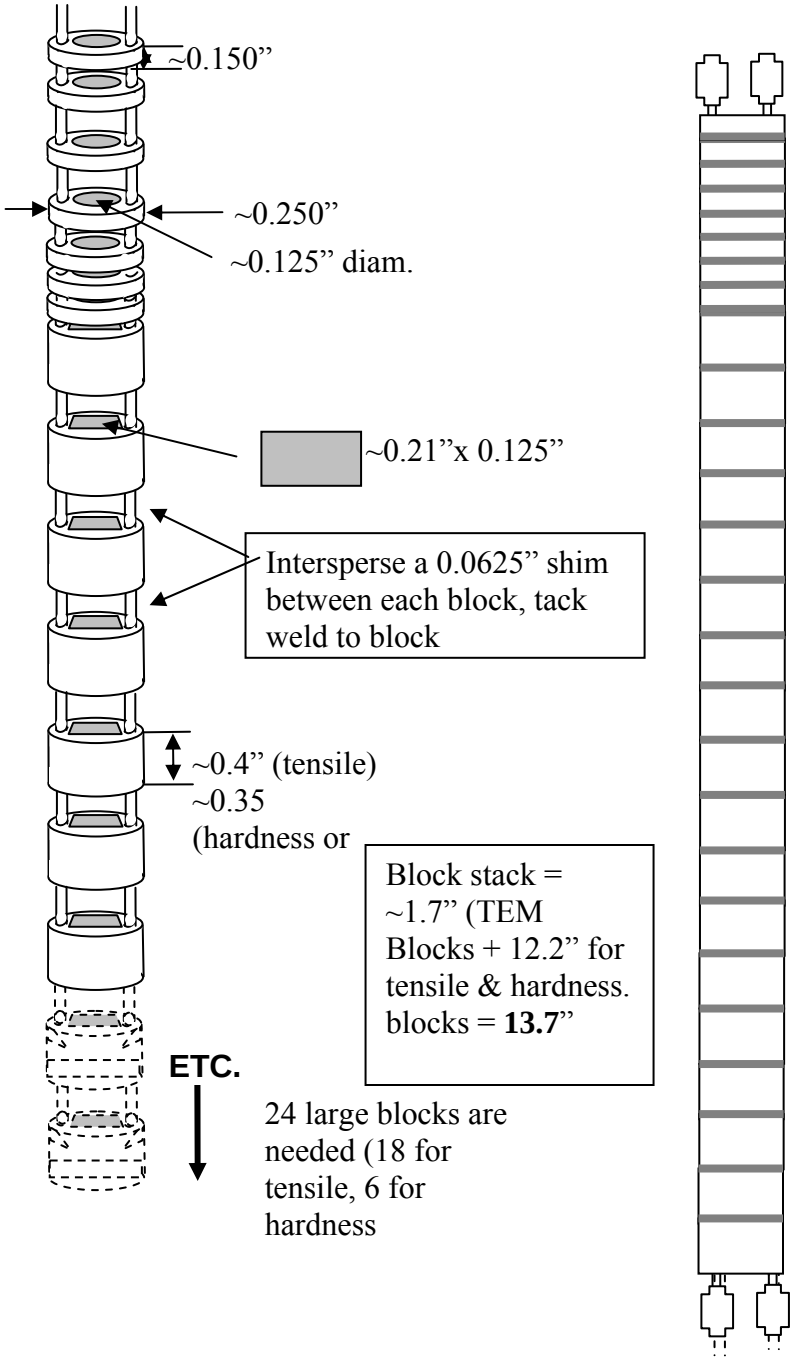

Figure 3-30: Test train design of the irradiation experiment at ATR.

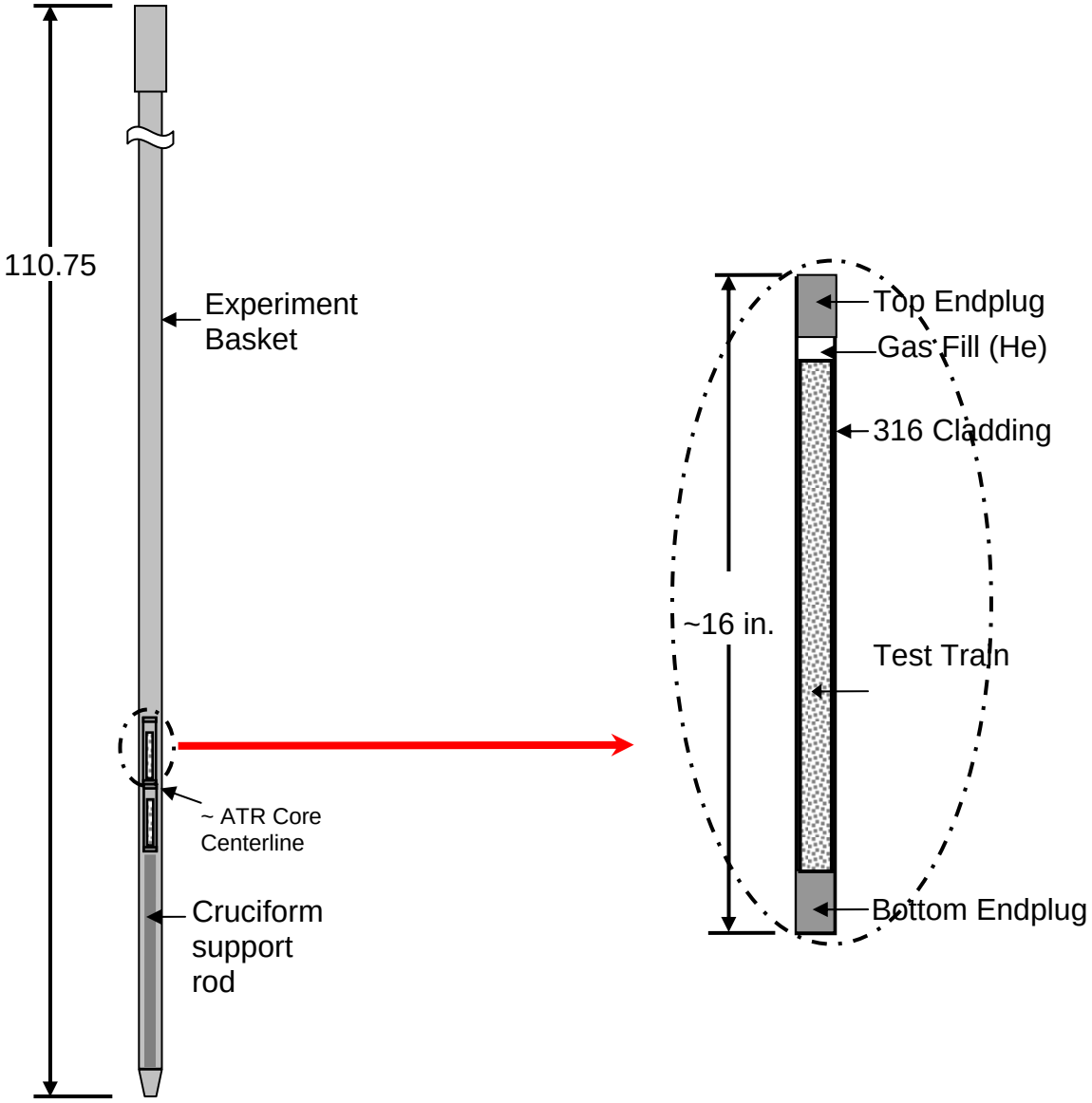

Figure 3-31: Test assembly for the irradiation experiemtnt at ATR East Flux Trap Position.

3.3.4 Irradiation experiment at PULSTAR

PULSTAR reactor, a 1 MW_{th} reactor at NC State University, was utilized to irradiate copper samples (both MG and *nc*) to relatively low damage levels compared to those achieved in the irradiation experiment conducted at the ATR. A major obstacle that is usually encountered while conducting an irradiation experiment at the PULSTAR reactor is the lack of hot cell/warm labs to handle irradiated samples which in turn requires allowing longer time for samples to cool. This in turn enforces the researcher to minimize the irradiation time and as a result only low damage levels can be achieved in a reasonable time frame.

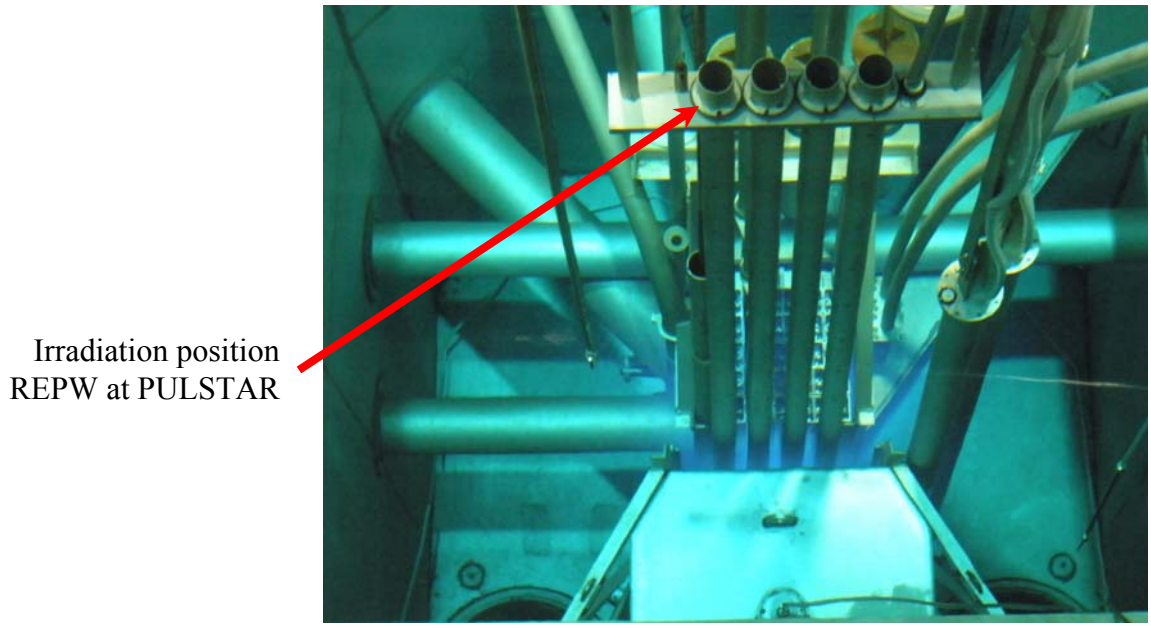

Figure 3-32: PULSTAR core cross section showing the irradiation position at radiation exposure port W (REPW).

In order to estimate the time needed to achieve specific damage level, Equation 3-17 is applied again; however, data on energy-groups neutron flux were not available. An experimental approach that is based on neutron foil activation measurements was attempted to estimate the accumulated fast flux at REPW. In this approach, a thin foil is loaded at the proposed irradiation position for certain irradiation time after which the activity of the irradiated foils is measured. The foil material should have a high cross section for the activation reaction of interest and the product radioactive nuclei should have a half life that is long enough for accurate measurement of the induced activity. It can be shown that the number of counts of induced gamma rays in the irradiated foils is proportional to the neutron flux. The rate of change of the concentration of radioactive nuclide in the irradiated foils is given by:

$$\frac{dN}{dt} = \phi \Sigma V - \lambda N \qquad \text{Equation 3-19}$$

where Σ represents the macroscopic cross section of the activation reaction, V is the volume of the foil, ϕ is the flux at that position, and λ is the decay constant of the produced radioactive nuclide. The solution to Equation 3-19 is given as:

$$\lambda N(t) = A(t) = \phi \Sigma V (1 - e^{-\Sigma t}) = R(1 - e^{-\Sigma t}) \qquad \text{Equation 3-20}$$

The induced activity in the foil builds up with time and a saturation value A_∞ would be approached at very long irradiation times. For a finite irradiation time, the activity of the irradiated foil would vary with time according to $A_0 = A_\infty \cdot \left(1 - e^{-\lambda \cdot t_0}\right)$. Assuming the irradiated

foil is allowed to cool up to $t=t_1$, after which the activity of the foil is measured/ counted until $t=t_2$ (i.e. counting time = t_2 - t_1), the integral of the activity detected multiplied by the detector efficiency is then given by:

$$C = \varepsilon \cdot \int_{t_1}^{t_2} A_0 \cdot e^{-\lambda \cdot t} dt + B = \varepsilon \cdot \frac{A_0}{\lambda} \cdot \left(e^{-\lambda \cdot t_1} - e^{-\lambda \cdot t_2} \right) + B \qquad \text{Equation 3-21}$$

where ε is the detector efficiency and B is the counts of the background.

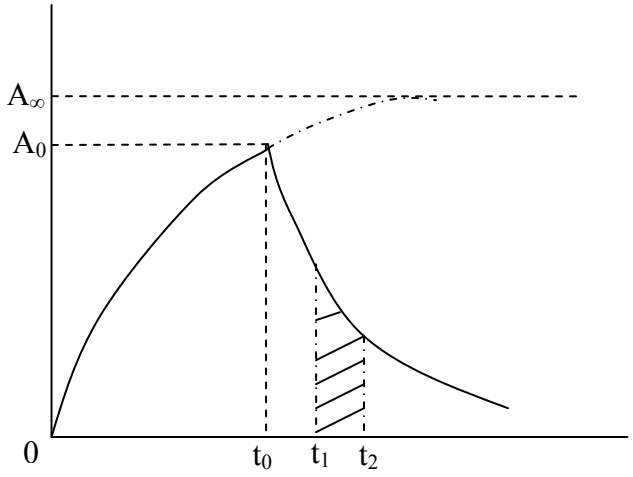

Figure 3-33: Variation of induced activity with time where t_o is the irradiation time, and (t_2-t_1) is the counting time.

The saturated activity, A_∞, can be then calculated as:

$$A_\infty = \frac{\lambda \cdot (C - B)}{\varepsilon \cdot \left(1 - e^{-\lambda \cdot t_0}\right)\left(e^{-\lambda \cdot t_1} - e^{-\lambda \cdot t_2}\right)} \qquad \text{Equation 3-22}$$

and the accumulated neutron flux is then estimated as:

$$\phi = \frac{A_{\infty}}{\Sigma \cdot V} \qquad \text{Equation 3-23}$$

For the irradiation experiment at PUSLATR, nickel foils were irradiated at the REPW position and the activation reaction $N^{58}(n,p)Co^{58}$ was considered which has a threshold of about 1.98 MeV. According to the activity measurements of the different nickel foils, the accumulated fast flux (E> 1.98 MeV) was estimated to be $\sim 2\times10^{12}\,\frac{n}{cm^2.s}$ and according to this value, and assuming average neutron energy of 1.98 MeV (the threshold of activation reaction) with the corresponding cross section for the two naturally occurring copper isotopes, the equivalent value of dpa/sec for the PULSTAR reactor irradiation experiment was estimated to be $\sim 4.7\times10^{-9}$ and for 200 hours of irradiation, the resultant damage is approximately 0.0034 *dpa*.

Samples of MG- and *nc*-copper were loaded into a capsule machined of aluminum and placed in an aluminum column which held the capsule in the exposure port. In order to minimize the induced activity in the samples, the aluminum column was internally wrapped with a layer of cadmium which has a high absorption cross section for thermal neutrons (E< 0.5 eV) and thus thermal neutrons were eliminated which has negligible contribution to the irradiation damage process in materials. Finally, according to a typical as run irradiation experiment, the ambient temperature of the copper samples during the irradiation course was estimated to be 55°C.

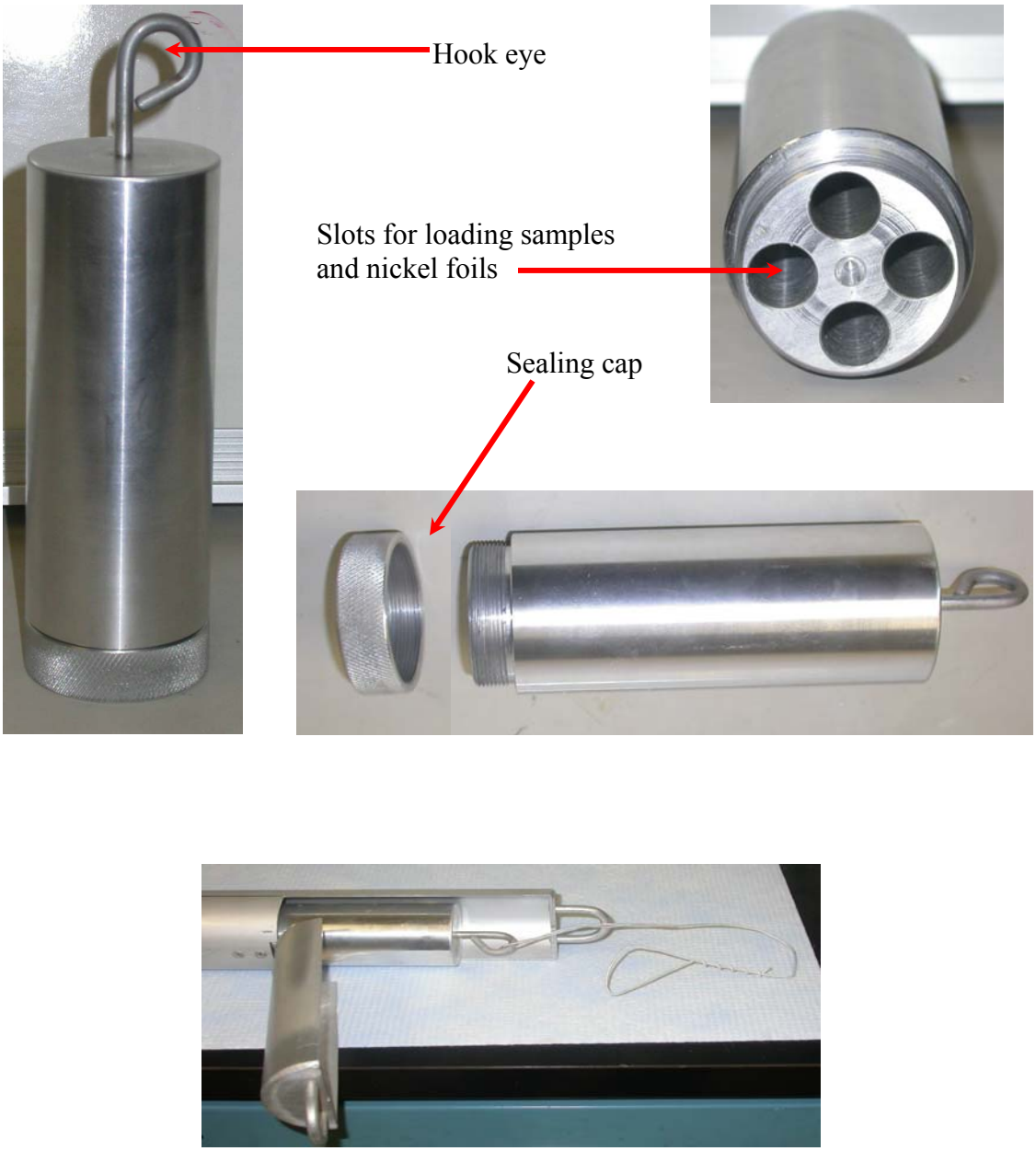

Figure 3-34: The irradiation capsule loaded in a Cd wrapped aluminum column for the PULSTAR reactor irradiation experiment.

3.3.5 Damage calculations via MCNP

Although the simplified model proposed for damage calculations shows good agreement with the simulated calculations for the ATR experiment, it was decided to confirm the accuracy of the proposed model for the estimated damage of PULSTAR reactor irradiation experiment by utilizing the MCNP code. The model underlying the simulation calculates the *dpa* accumulation rate for a material as:

$$DPA\ rate = \eta \frac{E_T}{2E_d} \qquad \text{Equation 3-24}$$

where η is an empirical efficiency factor (usually taken as 0.8), E_T is the total damage energy, and E_d is the Lindhard cutoff energy (the threshold displacement energy) [84]. To determine E_T in Equation (3-24), the rate of displacement in terms of *DPA* was calculated using a tally multiplier card with a standard flux tally in MCNP which calculates the reaction rate as:

$$Reaction\ rate = C\int \phi(E)R_m(E)dE \qquad \text{Equation 3-25}$$

where C is a multiplicative constant, ϕ(E) is the energy dependent flux, R_m (E) is the energy dependent reaction rate given by ENDF/B-VII damage cross-section, and accordingly, the integral in Equation (3-25) represents the total damage energy rate for the material. The constant C is then assigned to the quantity $\left(\eta / 2E_d\right)$ and the reaction rate is given by:

$$Reaction\ rate = \frac{\eta}{2E_d}\int \phi(E)R_m(E)dE \qquad \text{Equation 3-26}$$

The output is then converted to the reported *dpa* by considering the following normalization factor:

$$DPA\ normalization = \left(\frac{fission\ neutrons}{fission}\right)\left(\frac{fission}{MeV}\right)\left(\frac{MeV}{MW_{reactor\ power} - s}\right)\left(\frac{10^{-24}}{barn}\right)\left(\frac{\eta}{2E_d}\right)$$

with typical parameters values for the PULSTAR reactor (ν~ 2.43, core power ~ 1 MeV) and assuming E_d for copper ~ 30 eV and η taken as 0.8. For 200 hours of irradiation and for simulation of 1000 history/cycle for 1748 cycles, the estimated dpa of the copper samples irradiated at the PULSTAR reactor was found to be ~ 0.00187±3.8E-4. The difference between the *dpa* value calculated via MCNP simulation and that estimated via the simplified damage model is expected and it is attributed to the conservative assumptions of the K-P model. More details on damage calculations via MCN are given in Appendix A.

3.4 Chapter Summary

In this chapter, all experimental procedures attempted in the present study were highlighted and pre-irradiation characterization of micrograined (MG) and nanocrystalline (*nc*) copper was presented. Moreover, the damage calculations used to estimate the irradiation time required to achieve the desired dpa levels for both PULSTAR and ATR experiments were presented in details with good agreement between results obtained from the proposed simplified damage model and those obtained via MCNP simulation.

Chapter 4. Post Irradiation Examination and Discussion

In this chapter, Post Irradiation Examination (PIE) of irradiated MG- and *nc*-copper will be reported. This includes characterization of the developed microstructures and the mechanical properties that will be presented separately for each of these materials. Furthermore, two aspects will be discussed while presenting the results, firstly the microstructure and mechanical properties relationship of the irradiated materials and secondly, the observed differences in materials response to neutron irradiation between MG-copper and *nc*-copper at the different damage levels.

4.1 PIE of Micrograined Copper

Although radiation damage and effects on conventional materials are thought to be well understood, there is no model in particular that is agreed upon to describe and explain all phenomena related to radiation damage. Indeed, explanation and understanding of materials response to irradiation become a complex task when exploring the relation between the developed microstructure and measured mechanical properties. To examine post irradiated MG-copper, microhardness measurements will be reported followed by the tensile properties of the irradiated samples after which the developed microstructures will be presented and correlated to the mechanical properties. The nature of fracture will be discussed through the surface topography of deformed tensile samples.

4.1.1 Microhardness of irradiated MG-copper

Microhardness measurements of irradiated materials represent a quick and reliable indication of the occurrence of radiation damage. It is well established that micrograined or conventional materials in general show increase in hardness post irradiation due to the formation of various types of defects which is usually accompanied by loss of ductility. Similar to pre-irradiation examination, microhardness measurements of irradiated MG-copper were conducted on a 8 mm X 6 mm disks for those samples irradiated up to 0.0034 *dpa* whereas relatively smaller disks were tested for samples irradiated at 1 and 2 *dpa* such that having a grid of indentations was not possible.

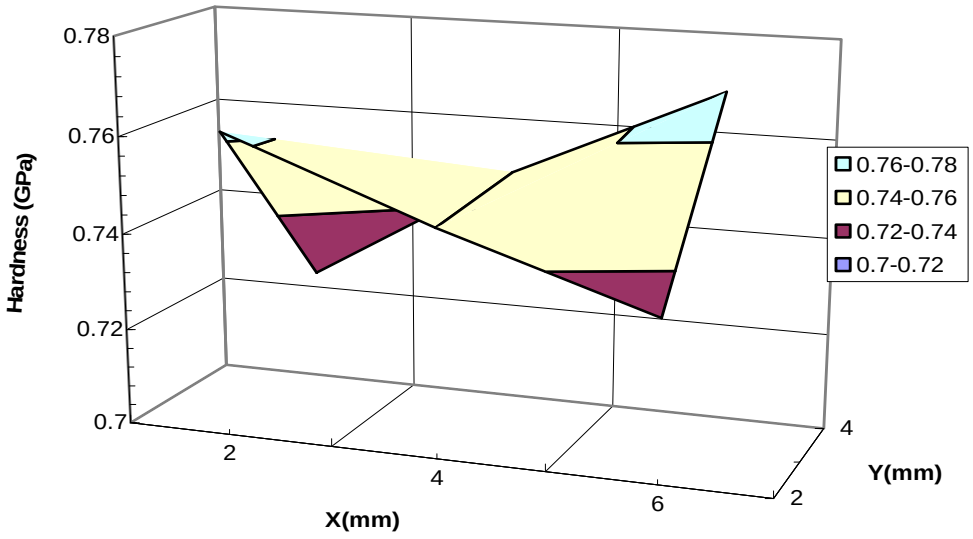

Figure 4-1: Microhardness measurements of MG-copper post 0.0034 dpa irradiation showing average hardness of 0.747±0.017 GPa.

Table 4-1 summarizes the hardness data of MG-copper which is graphically shown in Figure 4-2.

Table 4-1: Microhardness measurements of irradiated MG-copper

0 *dpa*	0.0034 *dpa*	1 *dpa*	2 *dpa*
0.596±0.02 (GPa)	0.747±0.017 (GPa)	1.072±0.005 (GPa)	1.077±0.024 (GPa)

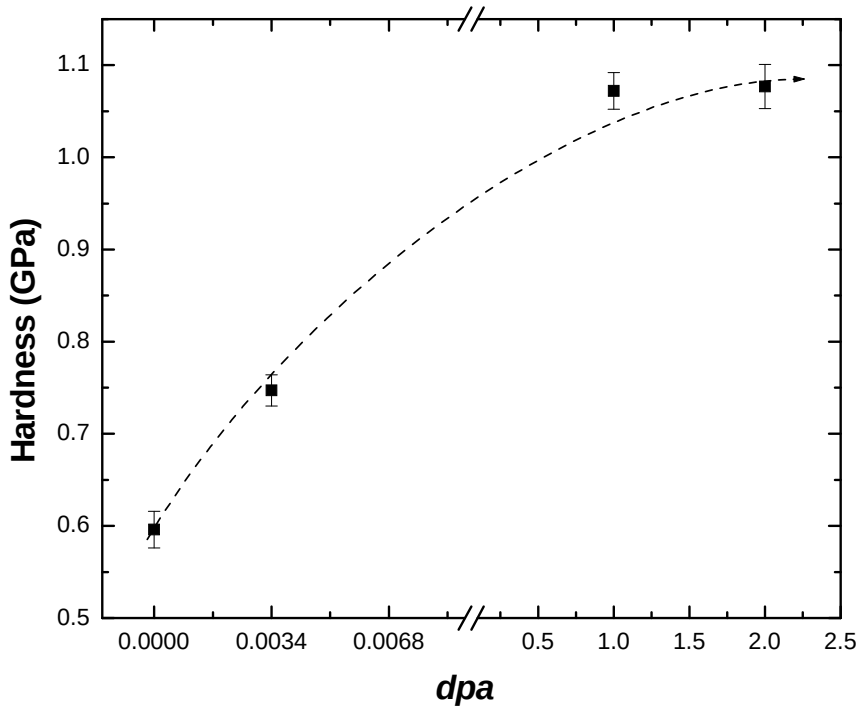

Figure 4-2: Variation of hardness of MG-copper with damage level.

Radiation hardening in MG-copper is manifest by the observed increase in hardness up to 1 *dpa* whereas a saturation of hardness was noted at higher fluence.

4.1.2 Mechanical properties of irradiated MG-copper

The mechanical behavior of irradiated MG-copper was investigated via tensile testing of irradiated samples from which stress-strain curves were obtained at all damage/exposure levels as shown in Figure 4-3.

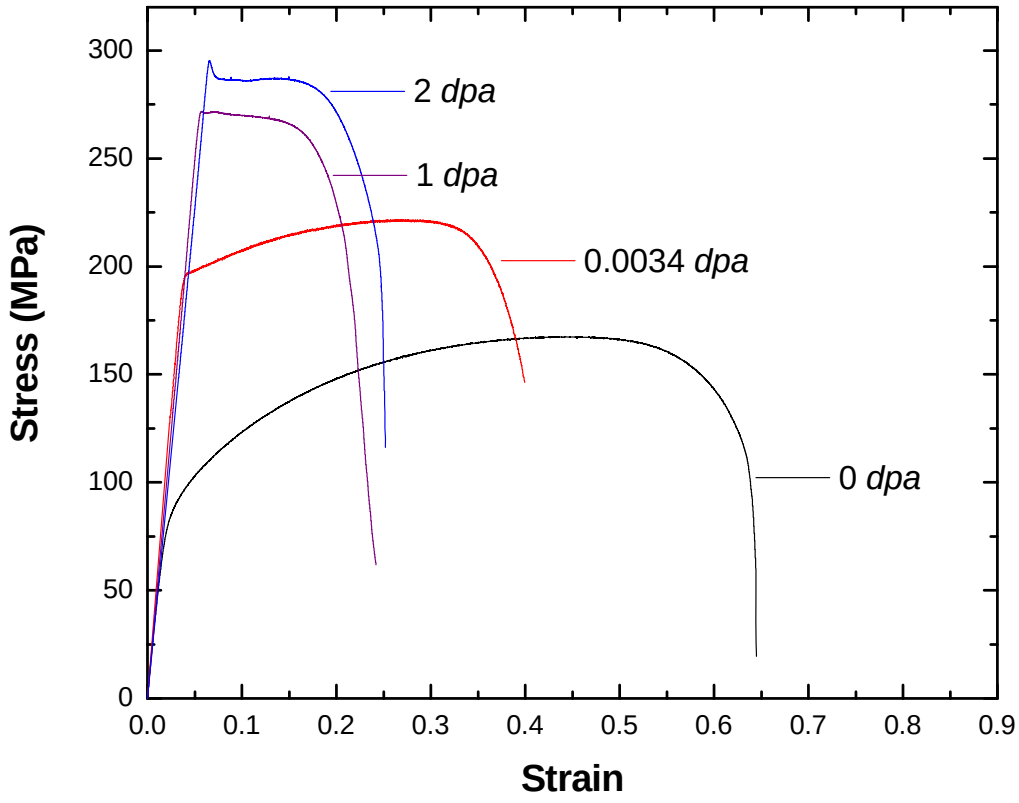

Figure 4-3: Stress-strain curves of irradiated MG-copper.

Table 4-2: Mechanical properties of MG-copper at all tested damage levels.

	S_y (MPa)	σ_y (MPa)	S_{UTS} (MPa)	σ_{UTS} (MPa)	e_u	e_t	n
0 *dpa*	80± 6	79± 6	174± 21	251±44	0.43± 0.07	0.66± 0.02	0.35 ± 0.05
0.0034 *dpa*	187±7	187± 7	215±8	263±23	0.21±0.06	0.34±0.05	0.19±0.05
1 *dpa*	260±16	260± 16	265±9	289+2	0.089±0.04	0.22±0.02	0.085±0.04
2 *dpa*	323+40	323± 39	323+40	347±46	0.065+0.00	0.21+0.02	0.063+0.00

At a glance, the response of irradiated MG-copper to tensile loading compared to the as received materials can be summarized as a notable increase in strength (both yield and ultimate) accompanied by a loss of ductility in terms of uniform and total elongations which is jointly described as irradiation hardening (describing increase of strength) and embrittlement (describing loss of ductility).

The following remarks can be made from the mechanical behavior of MG-copper irradiated at the different neutron exposure/ damage levels:

- A continuous loss of ductility is noted that saturates at ~ 1 *dpa*.
- Both yield and ultimate tensile strength increase with the damage levels; however, the increase in the yield strength is more pronounced.
- The difference between yield and ultimate tensile strength diminishes gradually and approaches zero at 2 *dpa* resulting in decrease in strain-hardening exponent (*n*)

- Most important, the yield drop phenomenon is observed in MG-copper at 2 *dpa*; however, the material undergoes minimal work hardening which is also the case at 1 *dpa*.

- Luders bands are formed over a long range of strain at 1 and 2 dpa which is preceded by the yield drop (more visible at 2 *dpa*).

The data given in Table 2-1 are graphically described in Figure 4-4 and Figure 4-5 to show the change of mechanical properties *dpa*.

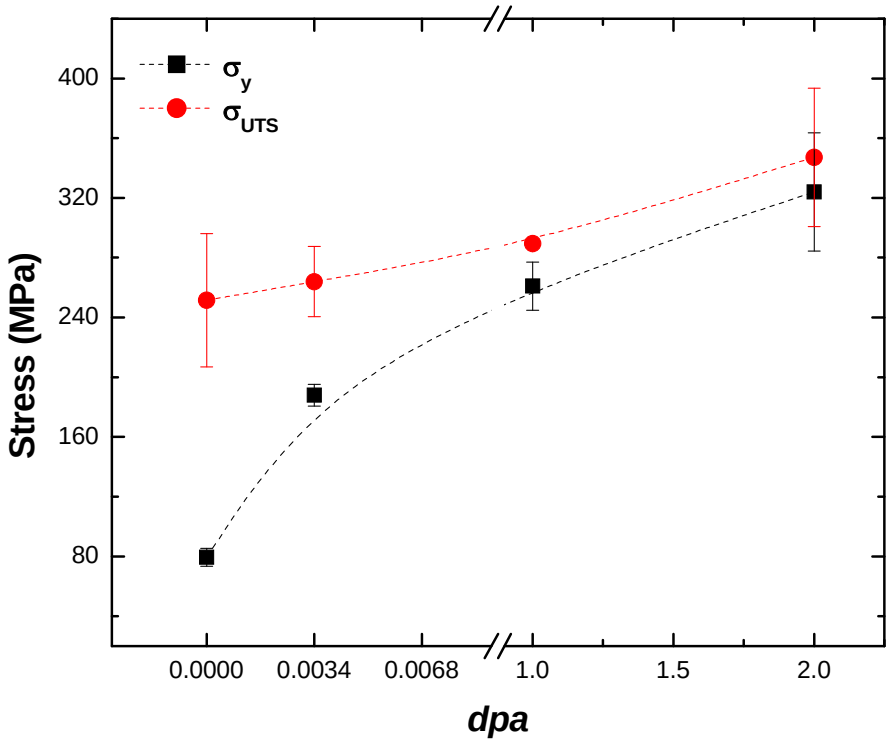

Figure 4-4: Variation of yield and ultimate tensile stresses with damage level. The difference between yield and ultimate tensile stress decreases as dpa increases and it approaches minim at 2 *dpa*.

The lack of work hardening observed in MG-copper at 1 and 2 *dpa* is thus due to the fact that the difference between yield and ultimate tensile stress decreases as dpa increases and the variation of strain hardening exponents with dpa confirms this appraisal. Furthermore, the loss of ductility is easily realized according to the variation of uniform and total elongation versus dpa as shown in Figure 4-5.

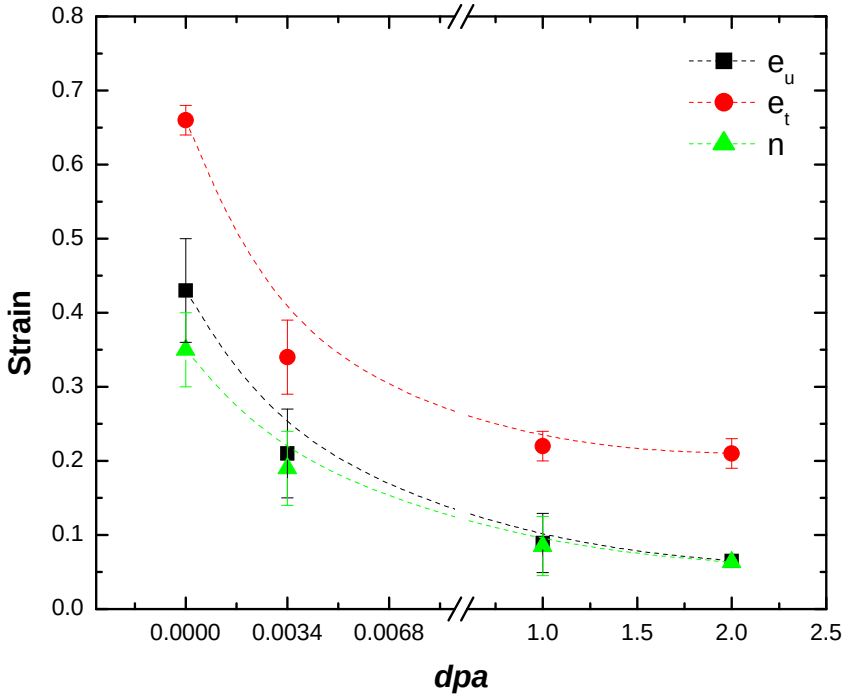

Figure 4-5: Variation of uniform and total elongation with dpa. Both e_u and e_t as well as the strain hardening exponent "*n*" decreases as dpa increases.

The yielding of a material represents the onset of plasticity and hence represents an important parameter describing mechanical behavior of materials. Recalling the Hall-Petch relation, the yield stress of a material is given by:

$$\sigma_y = \sigma_i + k_y \left(d\right)^{-1/2} \qquad \text{Equation 4-1}$$

where k_y is the unpinning stress and d is the grain size. According to the theory of radiation hardening [83], the yield stress of irradiated material is composed of two major components namely: source hardening (σ_s) and friction hardening (σ_i). Consequently, the yield stress of irradiated material is commonly expressed as [81]:

$$\sigma_y = \sigma_i + k_y \left(d\right)^{-1/2} = \sigma_i + \sigma_s \qquad \text{Equation 4-2}$$

Thus, the source hardening can be defined as the stress needed to initiate/ trigger dislocation motion on the glide plane. Once the dislocation is free to move, it is very likely that other obstacles such as grain boundaries, precipitates, or even other dislocations will impede its motions and the resistance to dislocation motion in this case is referred as friction hardening. There are two procedures to split the yield stress numerically into its source and friction components. First, a method proposed by Makin and Minter [85] in which, the source hardening component is determined from the stress-strain curve by projecting back that portion of the curve after the yield point which is assumed to be described by the power law hardening model:

$$\sigma = K\varepsilon^n \qquad \text{Equation 4-3}$$

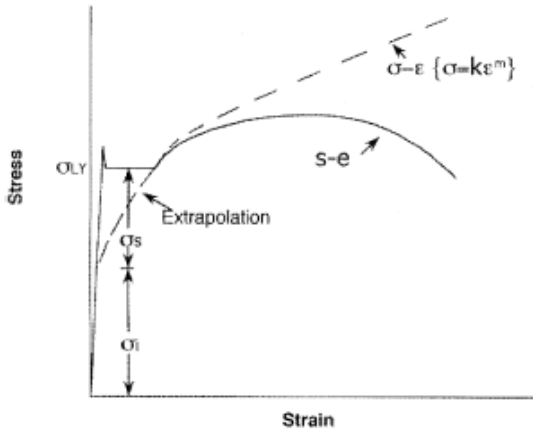

Figure 4-6: Back projection of stress-strain curve to determine the source hardening term [43].

Second, according to Equation 4-2, if the yield stress is plotted versus the inverse of the square root of grain size, the slope of the straight line would represent the unpinning stress "k_y" and the intersect with the vertical axis would represent the friction hardening component of the yield.

The friction hardening itself may be decomposed into two distinct components namely, "long" range and "short" range depending on what type of obstacle responsible for impeding dislocation motion. Long range stresses arise from dislocation-dislocation interactions whereas, short range stresses arise when the moving dislocation encounter an isolated obstacle in its slip plane such as precipitates, voids, and grain boundaries and thus, the friction hardening stress can be expressed as:

$$\sigma_i = \sigma_{LR} + \sigma_{SR} \qquad \text{Equation 4-4}$$

The long range stress in Equation 4-4 is expressed as:

$$\sigma_{LR} = \frac{F_{LR}}{b} = \alpha G b \sqrt{\rho_d} \qquad \text{Equation 4-5}$$

where G is the shear modulus, b is the burger vector, and ρ_d is the density of mobile dislocations. It is clear that both the source and friction hardening components of the yield stress are heavily dependent on the microstructure and can be utilized to discuss the influenced of microstructure on the mechanical behavior.

4.1.3 Microstructure of irradiated MG-copper

Although radiation hardening was confirmed to occur in MG-copper at all attempted damage levels, it is still important to investigate the developed microstructure and how it is related to the tensile properties of the irradiated material.

Grain size measurements of irradiated MG-copper

Optical microscopy was utilized to determine the average grain size of MG-copper at the different damage levels and generally speaking, no distinguishable change in grain size was observed. Optical micrographs of irradiated MG-copper at all damage levels are shown in Figure 4-7, Figure 4-8, and Figure 4-9.

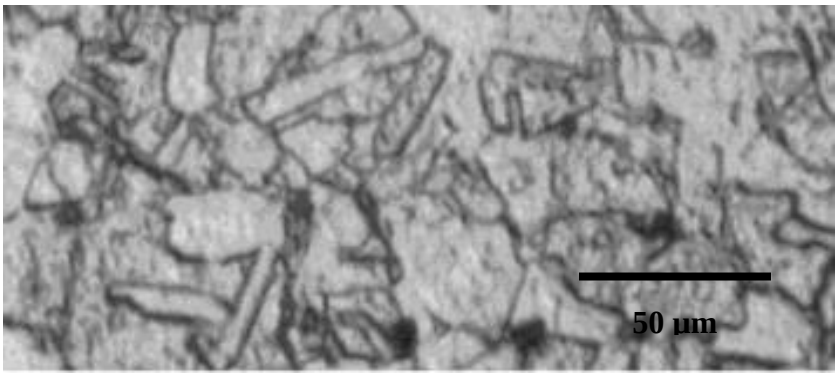

Figure 4-7: Optical microscopy of MG-copper irradiated at 0.0034 dpa with average grain size of ~ 39±7 µm.

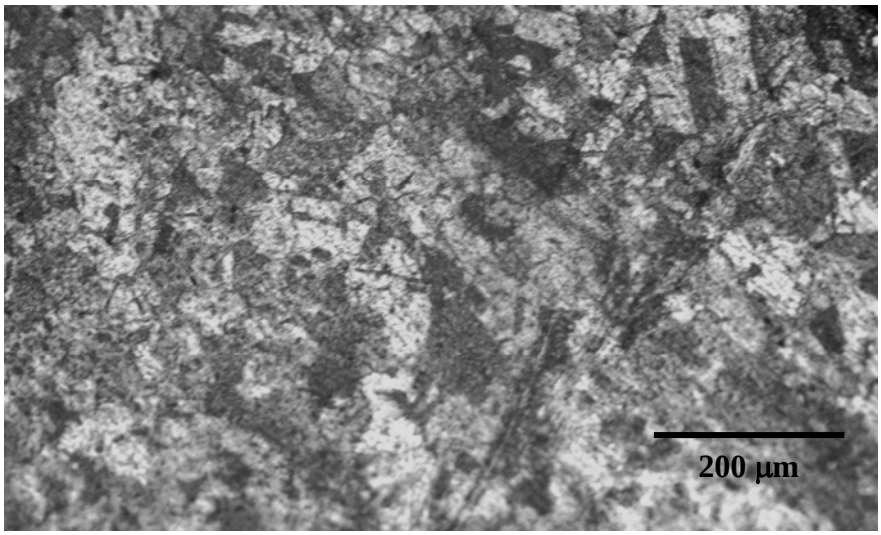

Figure 4-8: Optical microscopy of MG-copper irradiated at 1 dpa with average grain size of ~ 37±11 µm.

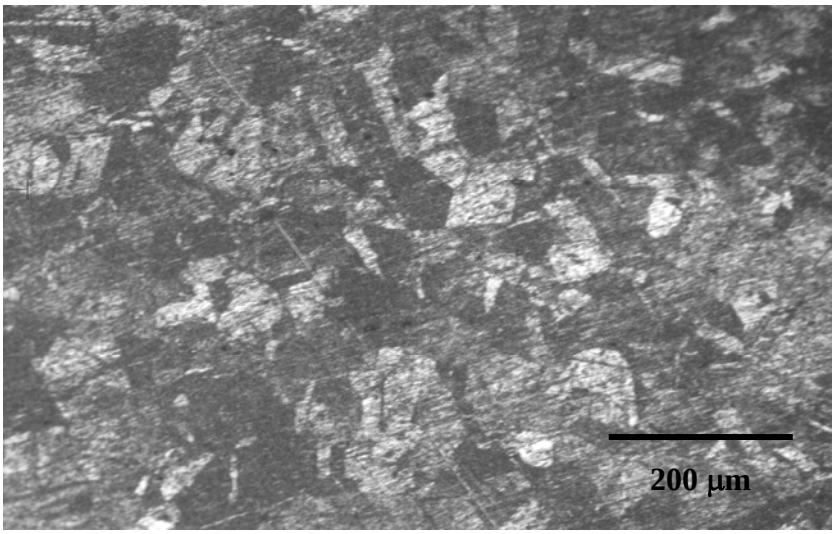

Figure 4-9: Optical microscopy of MG-copper irradiated at 2 dpa with average grain size of ~ 49±14 μm.

Although grain growth may occur in micrograined materials, it is likely to take place only at relatively elevated temperatures whereas, the irradiation temperature reported at the different damage levels was never higher than 100°C which eliminate any chance for change in grain size in irradiated MG-copper to occur. However, due to irradiation, grains orientation and shape (elongation) might change which gives an impression of change of grain size as it is shown in the optical micrographs of MG-copper irradiated at 1 and 2 *dpa*.

TEM of irradiated MG-copper

In this section, observations from TEM investigation of the developed microstructure of irradiated MG-copper samples will be presented and correlated to the mechanical properties presented earlier in this chapter.

At low damage level, namely the 0.0034 *dpa*, a major feature found in TEM foils was the formation of high density of dislocations loops and networks in grain interior which was not observed in the as received MG-copper (Figure 4-10).

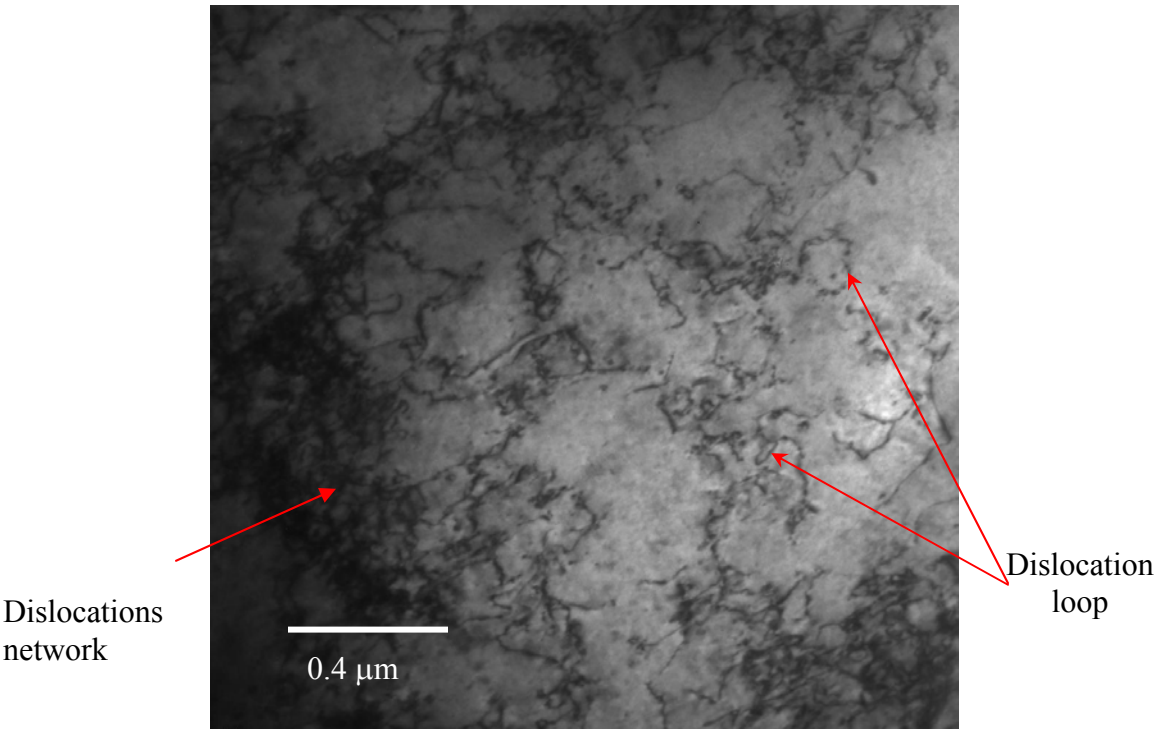

Figure 4-10: BF TEM micrograph of MG-copper irradiated at 0.0034 *dpa* with dislocations network/loops in grain interior.

The developed microstructure of irradiated MG-copper at 1 dpa characterized by TEM shows the formation of dislocation loops and which is pretty similar to that observed at lower dpa. However, dislocations formed at grain boundaries in MG-copper irradiated at 1 dpa (Figure 4-11) which was not observed in MG-copper post 0.0034 dpa irradiation. It is

worth to note that by visual inspection of the TEM micrographs, dislocation density at 1 *dpa* seems to be higher compared to that at 0.0034 *dpa* which according to the equation $\sigma_{LR} = \alpha Gb\sqrt{\rho_d}$ would explain the higher yield stress of MG-copper post 1 *dpa* irradiation.

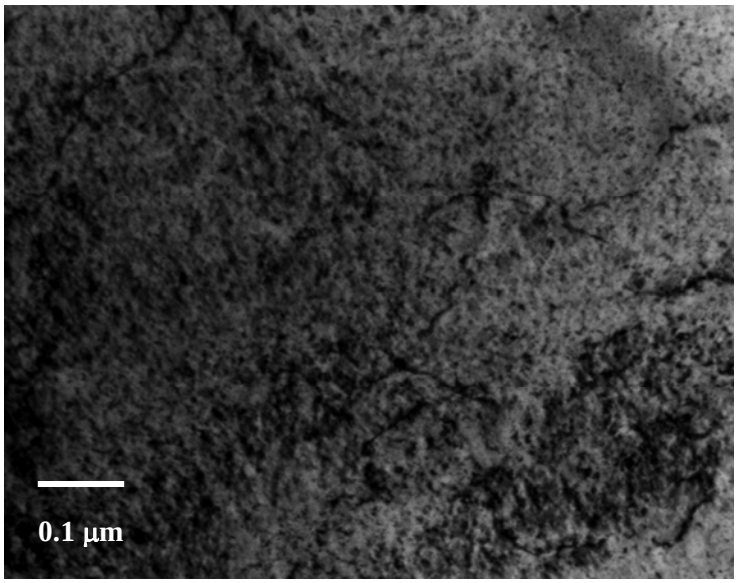

Figure 4-11: Dislocations observed in MG-copper at 1 *dpa*.

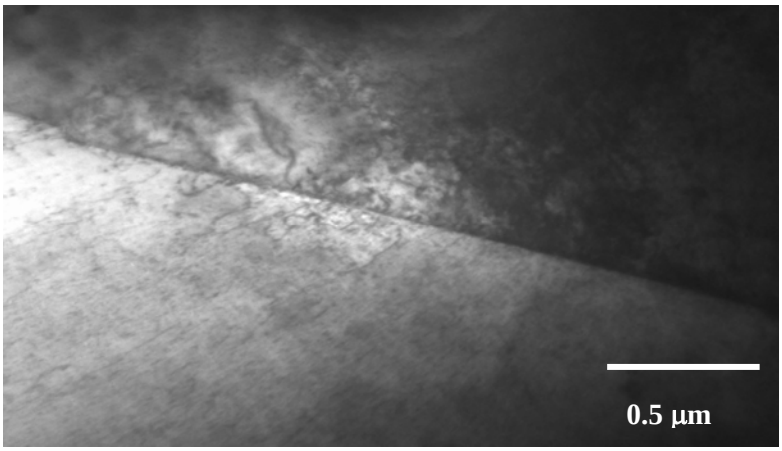

Figure 4-12: Dislocation structure at grain boundaries observed in MG-copper at 1 *dpa*.

Interestingly, the microstructure of MG-copper at 2 *dpa* seems to be different than that observed at 1 *dpa*. As shown in the TEM micrographs included in Figure 4-13, Figure 4-14, and Figure 4-15, in addition to the expected dislocations, the microstructure shows a high density of twin and stacking faults structures which was not observed in MG-copper at lower *dpa* levels.

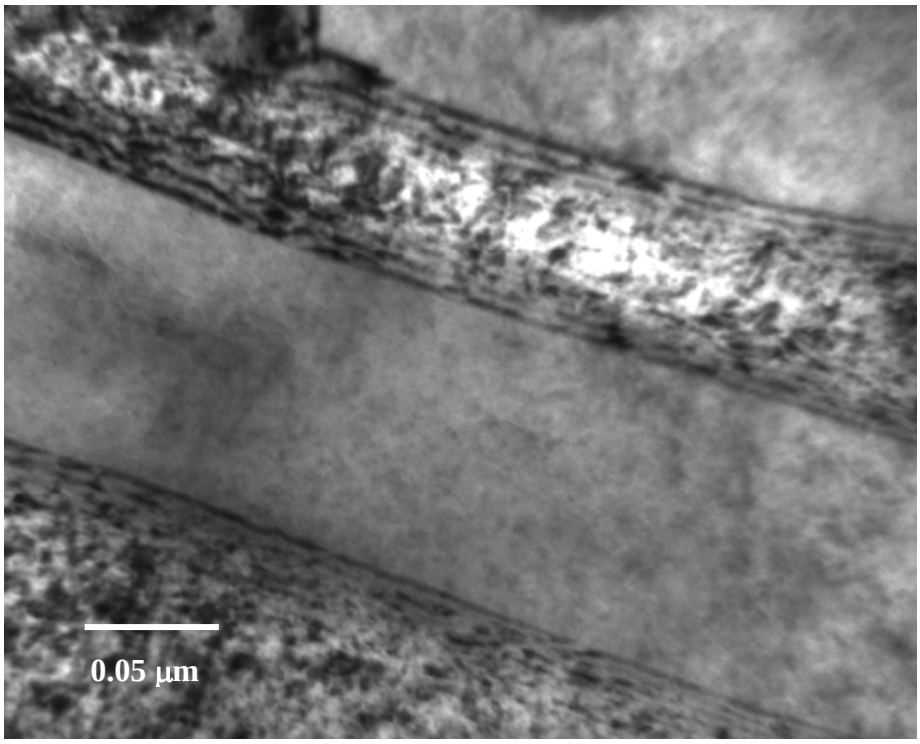

Figure 4-13: BF TEM micrograph of MG-copper at 2 *dpa* showing formation of twins.

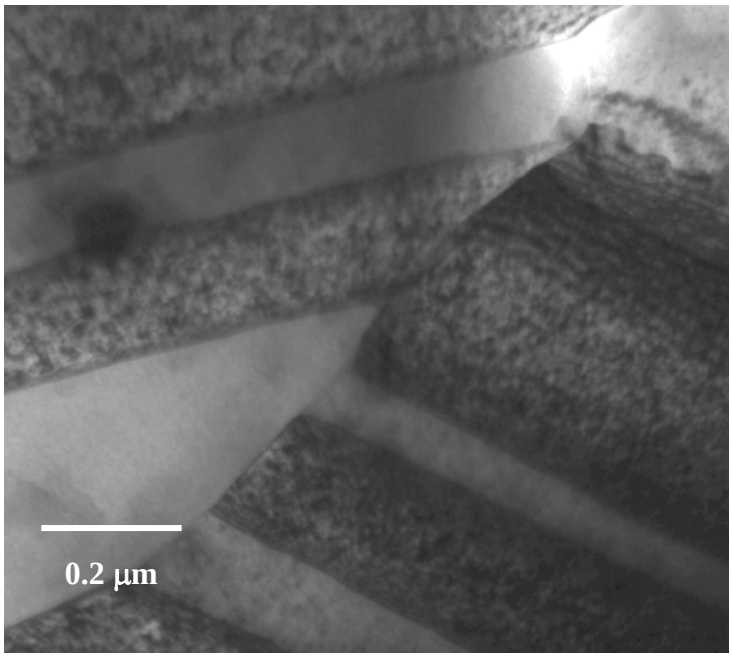

Figure 4-14: BF TEM showing high density of twins in MG-copper at 2 *dpa*.

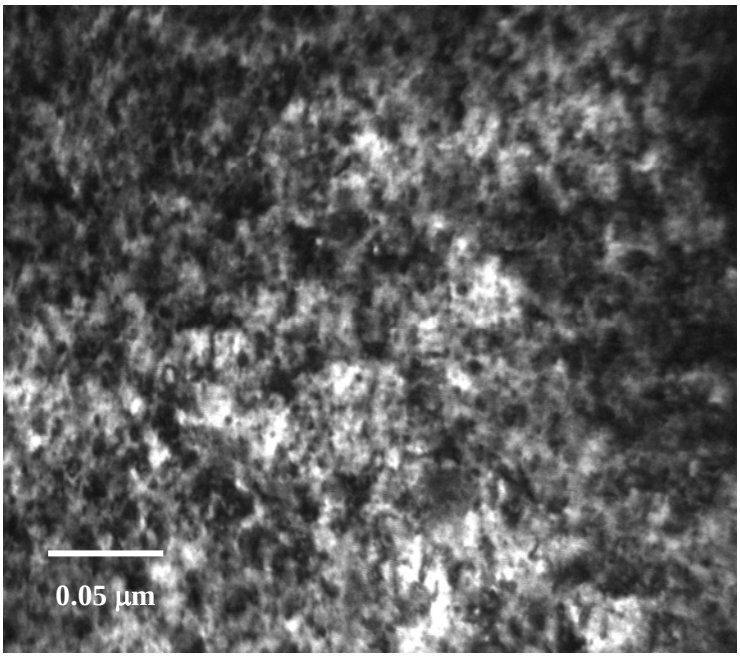

Figure 4-15: BF TEM of MG-copper at 2 *dpa* showing formation of high dislocation density.

Fracture surface topography

The fracture behavior of as received MG-copper was reported in Section 4.1.2 which showed a pure ductile fracture. Similarly, the fracture behavior of irradiated MG-copper was analyzed at all dpa levels by investigating the fracture surface topography via SEM as shown in the micrographs included in Figure 4-16, Figure 4-17, and Figure 4-18.

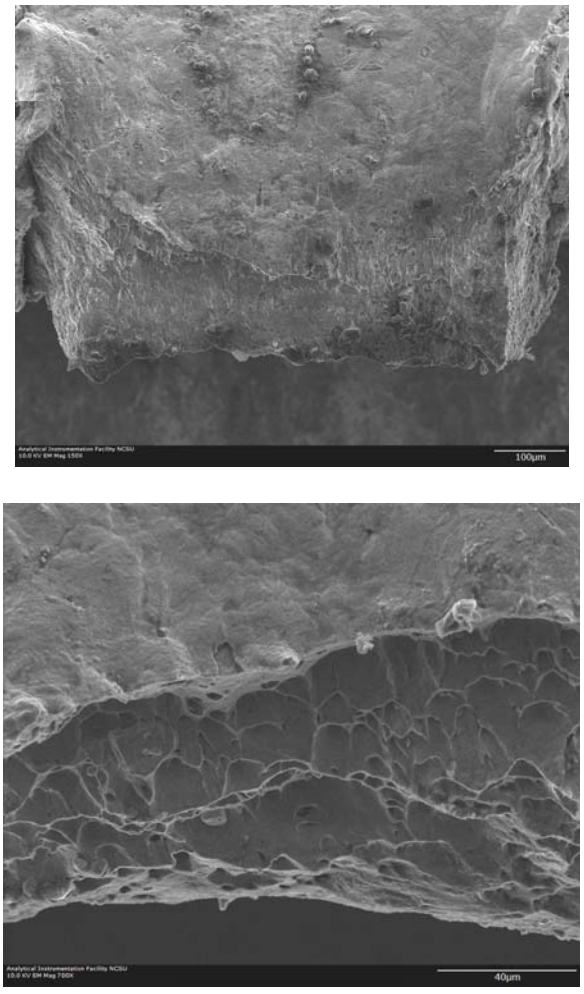

Figure 4-16: Fracture surface of MG-copper irradiated to 0.0034 *dpa*.

The fracture surface of MG-copper post 0.0034 *dpa* irradiation is still showing almost a pure ductile fracture pretty similar to that of as received material. However, the fracture surface of MG-copper irradiated to 1 *dpa* can be seen to be different such that the edges of the fracture surface are quite sharp showing some reflectivity (Figure 4-17).

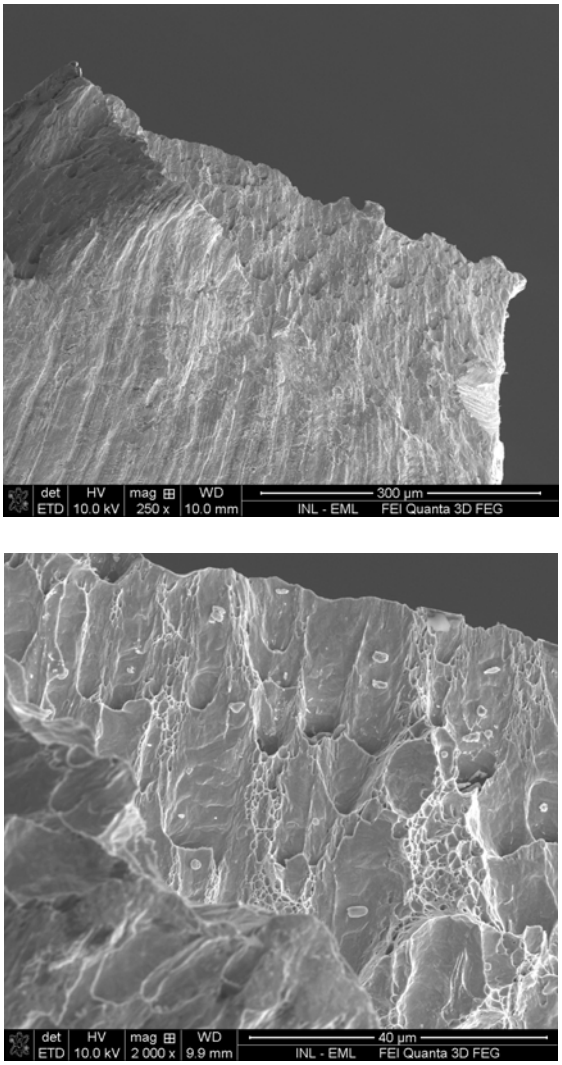

Figure 4-17: Fracture surface of MG-copper irradiated to 1 *dpa* showing deviation from ductile fracture observed at low damage level.

According to the mechanical properties of MG-copper irradiated to 2 *dpa*, it is not surprising that the fracture surface of deformed samples shown in Figure 4-18 reveals more characteristics of brittle fracture compared to other irradiation conditions.

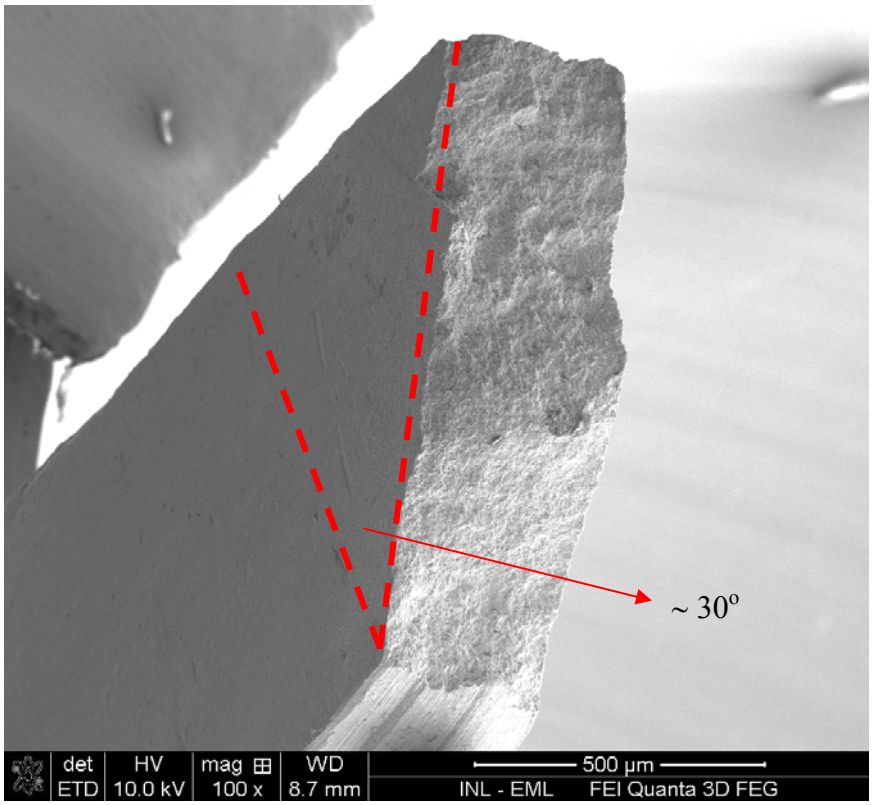

Figure 4-18: Fracture surface topography of MG-copper irradiated to 2 *dpa* showing fracture occurs across shear band at approximately 30°.

The fracture behavior observed at 2 *dpa* is supported by the lack of strain hardening and reduced uniform strain. It was unfortunate that attempts to characterize the microstructure of the deformed tensile samples via TEM was not successful because of difficulties associated with preparing transparent foils of the irradiated sub-size deformed tensile samples.

4.2 PIE of Nanocrystalline Copper

4.2.1 Microhardness of irradiated nc-copper

Following the same characterization procedures applied to MG-copper, response of *nc*-copper to neutron irradiation was first characterized by conducting microhardness measurements at the different damage levels. Hardness profile of irradiated nc-copper at 0.0034 *dpa* is shown in Figure 4-19 followed by the hardness measurements data at all damage levels.

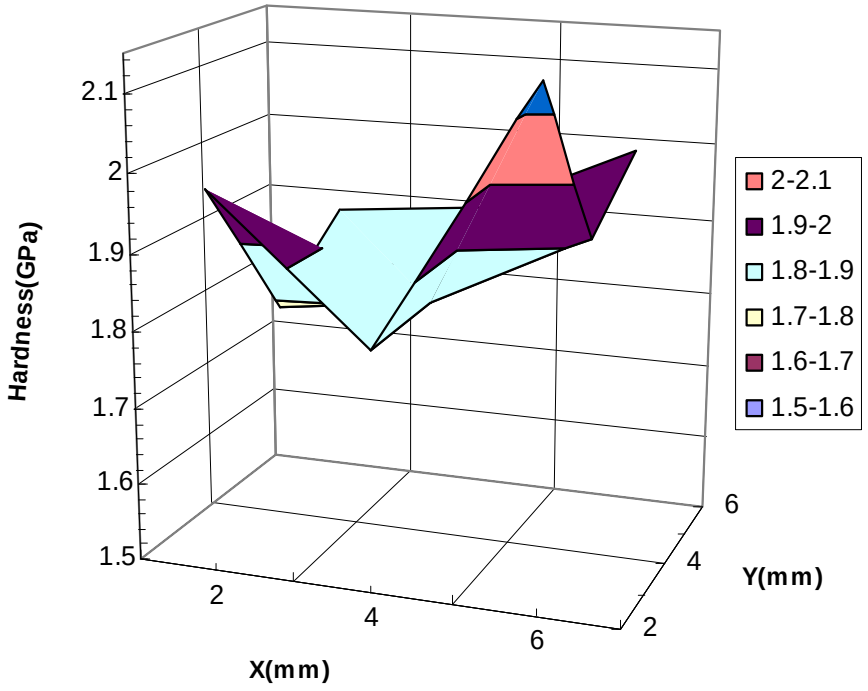

Figure 4-19: Microhardness measurements of nc-copper showing average hardness of 1.91±0.11 (GPa) at 0.0034 *dpa*.

Interestingly, the hardness of nc-copper irradiated at 0.0034 dpa was reduced from ~ 2.5 GPa to 1.9 GPa which is about 25% reduction and moreover, the hardness measurements are less uniform compared to that of the as received nc-copper shown in Figure 3-15.

Table 4-3: Microhardness measurements of irradiated nc-copper

0 *dpa*	0.0034 *dpa*	1 *dpa*	2 *dpa*
2.51±0.05 (GPa)	1.91±0.11 (GPa)	1.15±0.03 (GPa)	1.16±0.04 (GPa)

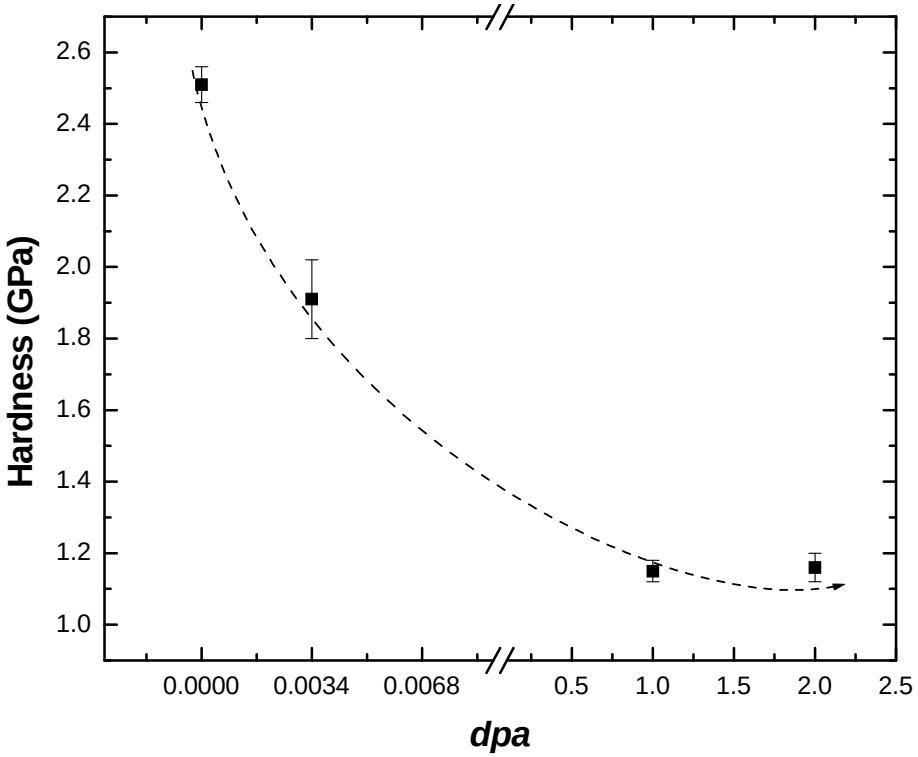

Figure 4-20: Variation of hardness of nc-copper with *dpa*.

The drop in hardness of *nc*-copper continues up to 1 *dpa* irradiation after which a minor increase in hardness is observed at 2 *dpa* as shown in Table 4-3 and Figure 4-19.

Thus, radiation softening is noted in nc-copper in lieu of radiation hardening observed in MG-copper

4.2.2 Mechanical properties of irradiated *nc*-copper

Stress-strain curves for irradiated nc-copper are shown in Figure 4-21 where the results for the as received material are included for comparison.

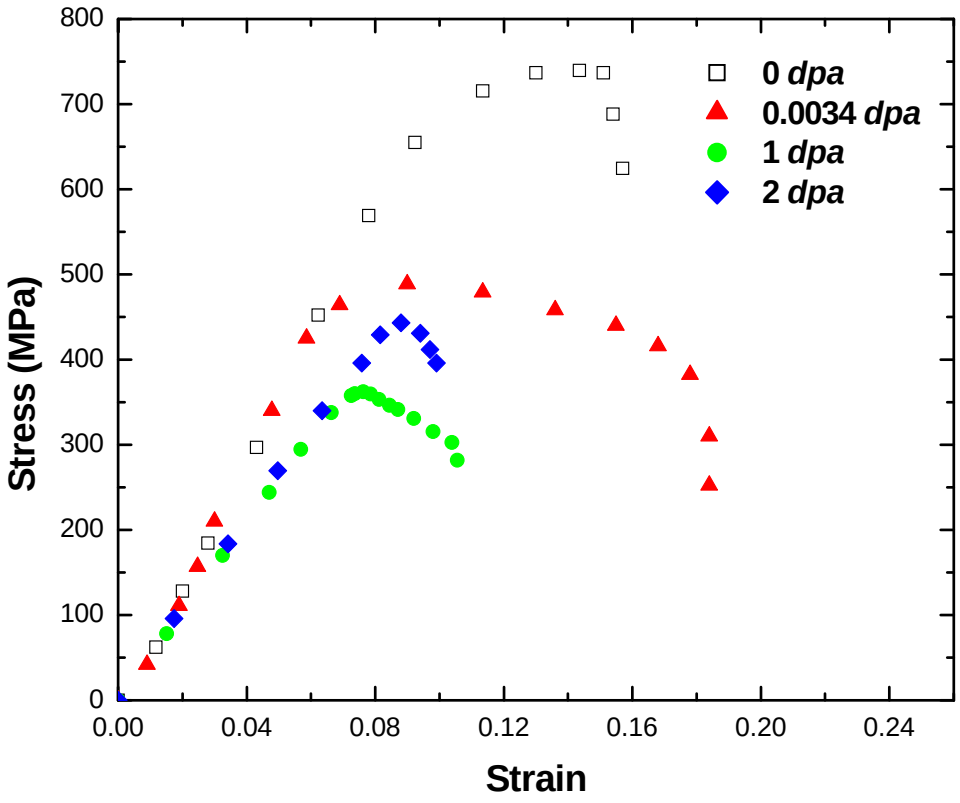

Figure 4-21: Typical stress-strain curves of irradiated *nc*-copper.

Yield stress, ultimate tensile stress, uniform and total elongation were determined in all cases and results are summarized in Table 4-4.

Table 4-4: Mechanical properties of nc-copper at all tested damage levels.

	S_y (MPa)	σ_y(MPa)	UTS (MPa)	σ_{UTS} (MPa)	e_u	e_t
0 *dpa*	557± 5	558±5	731± 21	838±13	0.052± 0.004	0.079±001
0.0034 *dpa*	371±15	372±15	457±18	501±20	0.05±0.001	0.18±0.014
1 *dpa*	357±8	358±9	365±5	387±3	0.005±0.001	0.029±0.007
2 *dpa*	388+20	389±30	425±40	457±47	0.007+0.004	0.036+0.005

The response of irradiated nc-copper to tensile loading reveals the following remarks:

- Upon irradiation at 0.0034 *dpa*, the yield stress as well as the ultimate tensile stress dramatically decreased accompanied by an increase in total elongation while uniform strain was unchanged.

- Post 1 *dpa* irradiation, the same observation regarding decrease in yield and tensile stress can be made but in a moderate fashion compared to the dramatic drop observed at 0.0034 *dpa*. However, the uniform and total elongation were greatly reduced even below its pre-irradiation values and the material did not undergo any work hardening after yielding.
- Finally, at 2 *dpa* irradiation, nc-copper shows increased strength compared to 1 *dpa* along with complete loss of ductility.

Figure 4-22 and Figure 4-23 illustrate the variation of the different mechanical properties of *nc*-copper at the different damage/ exposure levels tested.

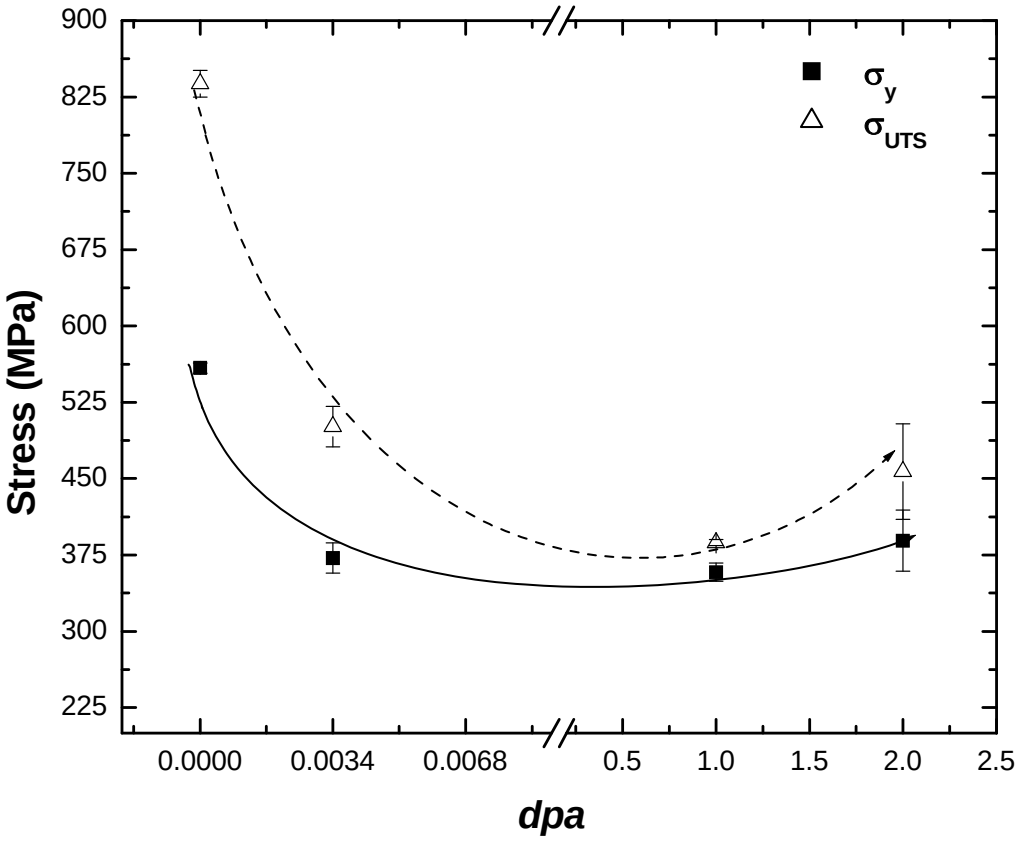

Figure 4-22: Variation of yield and ultimate tensile stress with dpa. Both stresses are continuously decreasing up to 1 *dpa* after which, a relatively minor increase is observed with minimal difference between yield and ultimate stress.

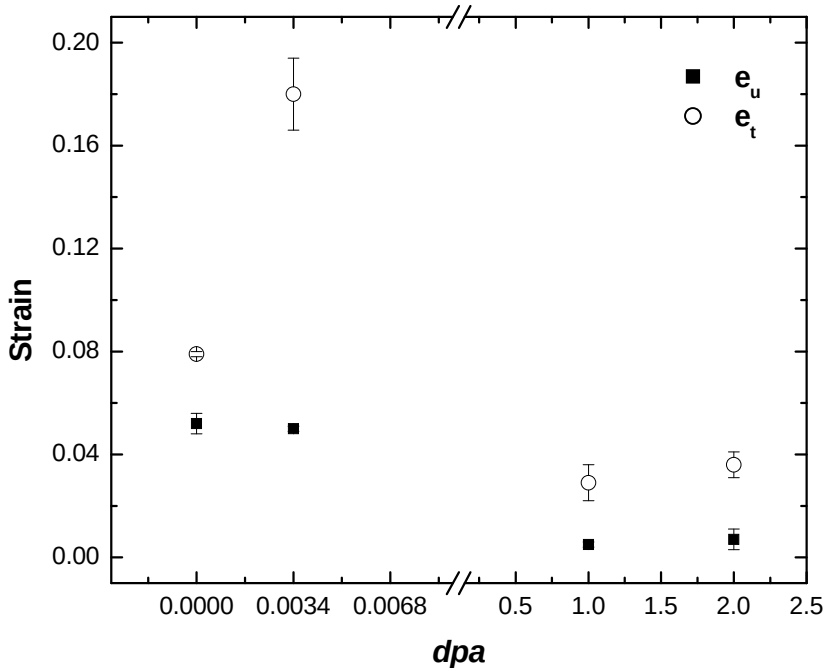

Figure 4-23: Variation of uniform and total elongation with *dpa*.

A close scrutiny of the data should uncover a discrepancy at 0.0034 *dpa* where both the yield and ultimate tensile stresses decrease with almost no work hardening while the material is showing appreciable total elongation. Indeed, the overall mechanical behavior of irradiated nc-copper seems to have a transition point at 1 *dpa* before which decrease of strength is observed and after which the materials began to gain strength again which is likely due to radiation hardening.

4.2.3 Microstructure of irradiated *nc*-copper

In order to establish a better understanding of the mechanical behavior observed for irradiated *nc*-copper, the various elements of developed microstructure are characterized

which includes measurements of grain size and detections of the evolution of irradiation-induced defects and finally the topography of the fracture surfaces.

XRD of irradiated *nc*-copper

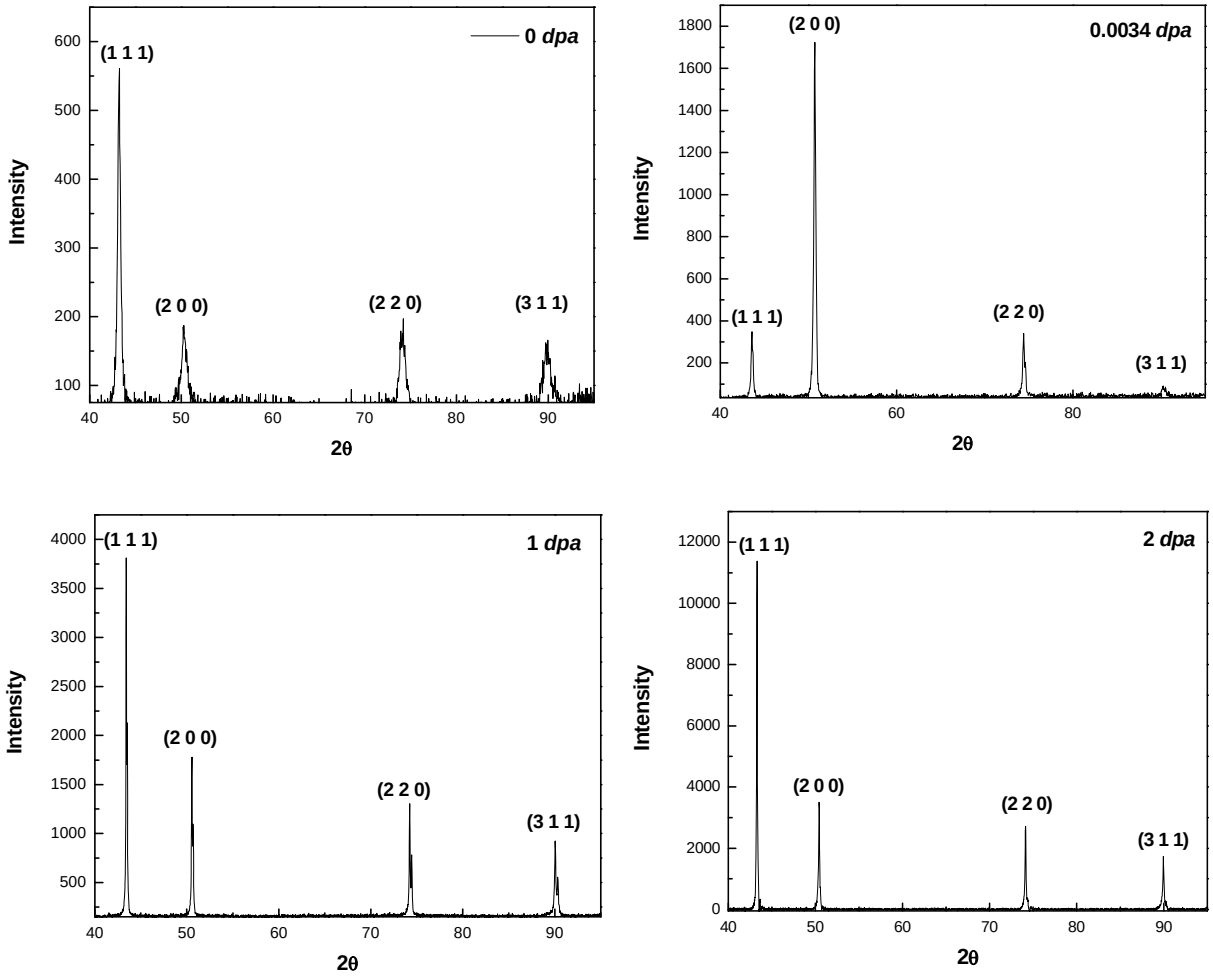

Figure 4-24: XRD of irradiated *nc*-copper.

Figure 4-24 shows the XRD of *nc*-copper at the different damage/exposure levels, three remarks are made:

I. Peak(s) broadening in terms of FWHM was greatly reduced after 0.0034 *dpa* irradiation and continues until it is minimum at 1 and 2 *dpa* at which it is about the same as micrograined copper (Figure 3-5). As discussed earlier, peak broadening is inversely proportional to grain size which indicates that the average grain size increased due to radiation post 0.0034 *dpa* and it was estimated as ~ 70 nm compared to 20 nm reported for the as received material.

II. Since peak intensity reflects the population of grains in certain crystallographic direction, it is evident that irradiation at 0.0034 *dpa* caused rearrangement of grain orientations such that peak of highest intensity was switched from (1 1 1) into (2 0 0).

III. At higher doses (1 and 2 *dpa*), the peak heights switched back to that for unirradiated nc-copper with higher peak of (1 1 1).

IV. With only the four major diffraction peaks of copper observed, this eliminates possibility of second phase formation

Such an increase in grain size following 0.0034 dpa is also noted in the AFM image (Figure 4-25) from which the grain size is estimated to increase to 65 nm from 34.4 nm.

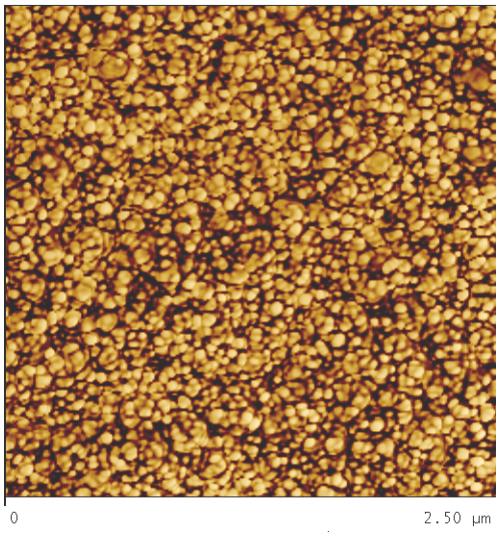

Figure 4-25: AFM of nc-copper at 0.0034 *dpa* with corresponding average grain size ~ 65±10 nm.

TEM of nc-copper at low *dpa*

According to the TEM micrographs obtained for nc-copper at 0.0034 *dpa* (Figure 4-26, 4-27, and 4-28), microstructure was greatly altered because of the increase of grain size where twin and dislocation structures were observed in those grain which had grown enough to accommodate such defects whereas, other TEM foils are still showing grains below 100 nm pretty similar to those observed in the as received materials.

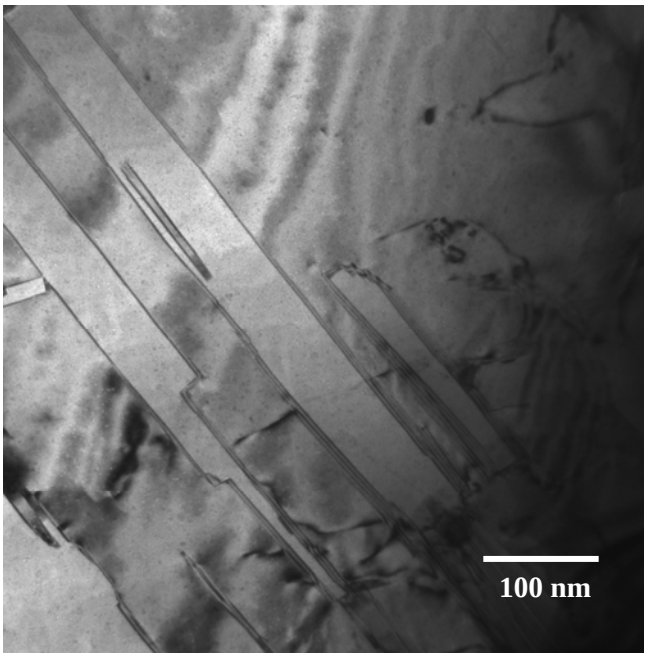

Figure 4-26: BF TEM of nc-copper post 0.0034 *dpa* irradiation showing formation of twins and dislocations.

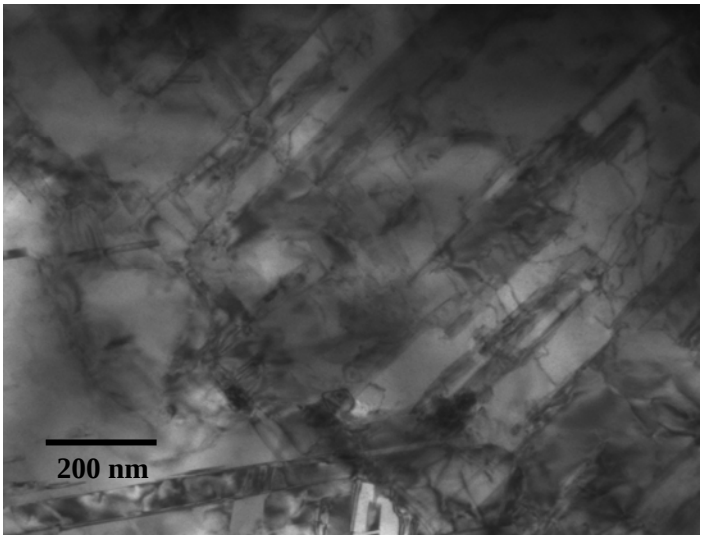

Figure 4-27: BF TEM of nc-copper at 0.0034 *dpa* showing grains in the submicron regime accommodating twins and dislocation loops.

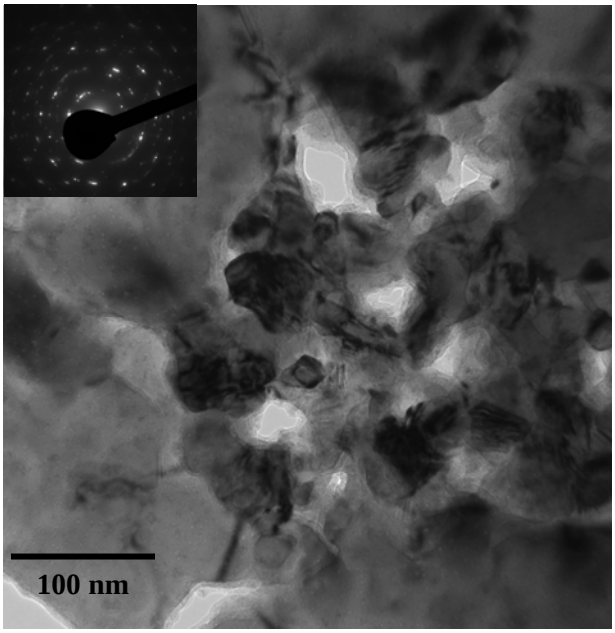

Figure 4-28: BF TEM of nc-copper showing nanograins still present at 0.0034 *dpa*. The diffraction rings are not as complete as it is in the as received material because some micrograins are contributing to the diffraction contrast.

Thus, microstructure characterization via TEM confirmed the conclusion that nc-copper was undergoing grain growth when it was irradiated at 0.0034 *dpa*. The observation of twin boundaries and dislocations structures implies that some grains grown enough to accommodate those defects however, high popularity of nanograins are still present as shown in Figure 4-28 with the evidence of the near to complete diffraction rings observed in the diffraction pattern where the average grain size based on TEM was about 108 nm. The average grain size of nc-copper post 0.0034 dpa irradiation was estimated based on AFM and TEM and it was found to be ~ 86.5 nm with the corresponding grain size distribution shown in Figure 4-29.

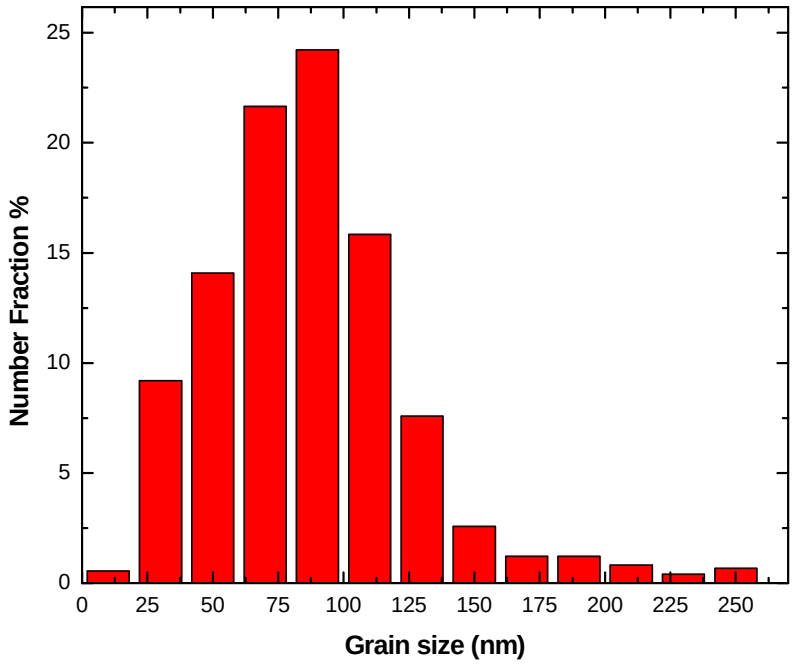

Figure 4-29: Grain size distribution of nc-copper at 0.0034 *dpa* showing average grain size of 86.5 nm whereas the initial average grain size of the as received material ~ 34.4 nm which indicates grain growth at this damage level.

According to these microstructure observations, the mechanical behavior of nc-copper at 0.0034 *dpa* can be better elaborated. Based on the Hall-Petch equation in which material's strength varies inversely with grain size, the grown growth is thus responsible for the drop observed in yield and ultimate stress accompanied with numerous increase in ductility which is mainly due to the presence of those grains grown up to submicron regime. However, the high population of those grains at the nanometer scale has kept a limited capability of nc-copper to undergo work hardening and accordingly the minor change in strain hardening exponent "*n*" stands to reason.

TEM of nc-copper at higher *dpa*

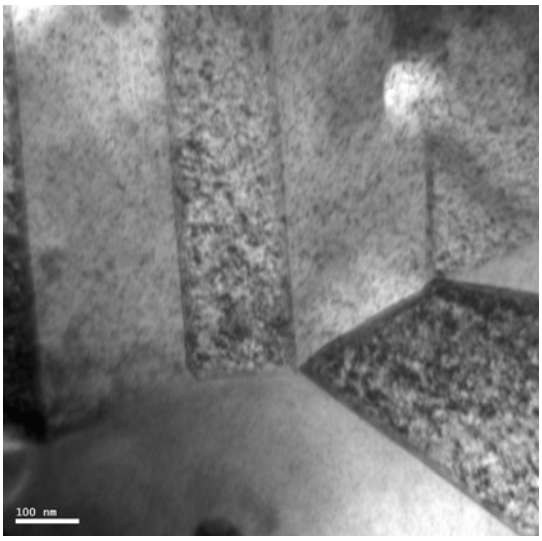

Figure 4-30: BF TEM of nc-copper at 1 *dpa* showing twins formed at grain boundaries.

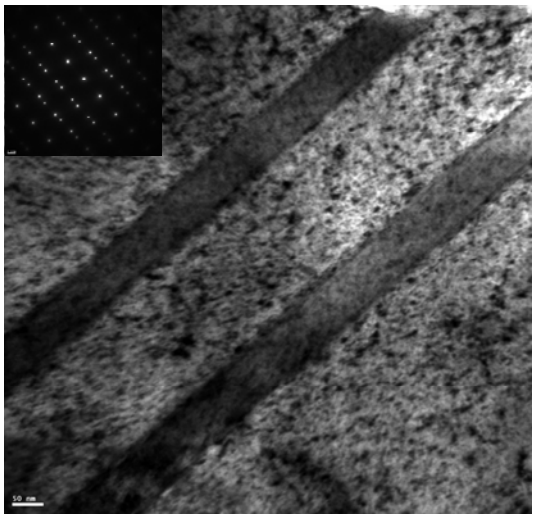

Figure 4-31: High density of dislocations formed in nc-copper at 1 *dpa* with diffraction pattern revealing formation of twin structure.

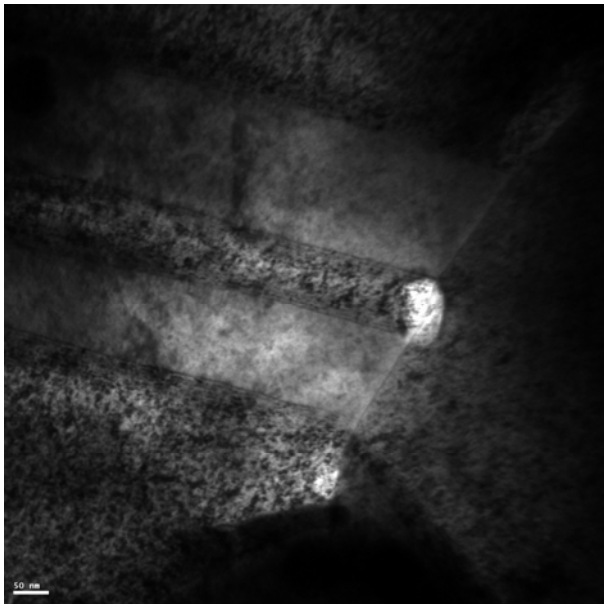

Figure 4-32: BF TEM of nc-copper at 2 *dpa* showing high density of dislocations at twins boundaries.

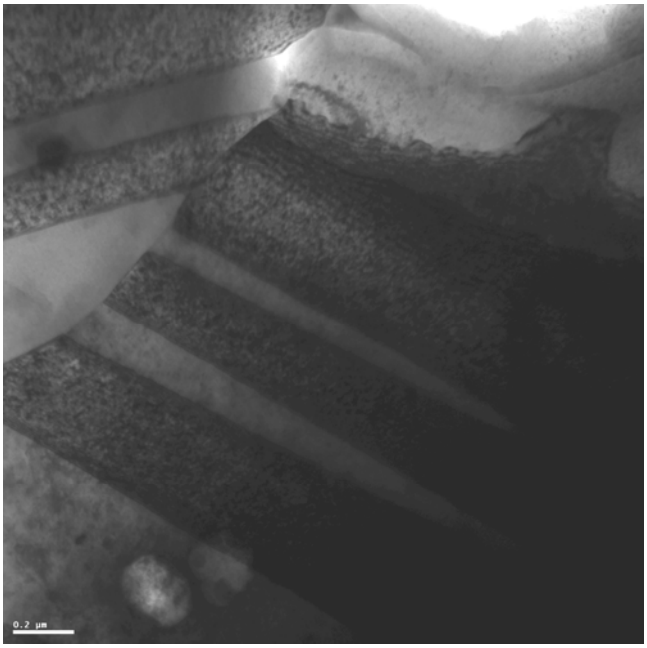

Figure 4-33: BF TEM showing high density of twins formed in nc-copper at 2 *dpa*.

Microstructure of nc-copper irradiated at 1 and 2 *dpa* persistently shows formation of dislocations and twins with densities increasing with the damage level which explains the reported increase in yield and tensile stress of nc-copper at 2 *dpa* (see Table 4-4). In order to accommodate those defects, it is required that a major fraction of the nanograins undergo grain growth to the submicron or even the micron regimes as noted from the above TEM micrographs. Surprisingly, attempts to determine grain size of nc-copper at 1 and 2 *dpa* by optical microcopy were not successful at all. Alternatively, SEM and TEM were utilized to estimate the average grain size of nc-copper post 1 and 2 *dpa* irradiations.

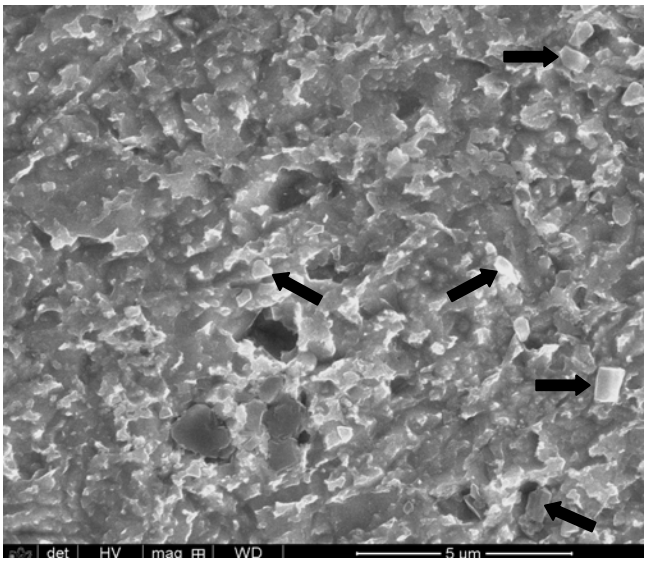

Figure 4-34: SEM of nc-copper at 1 dpa used for grain size measurements. Arrows are pointing at grains in the submicron regime.

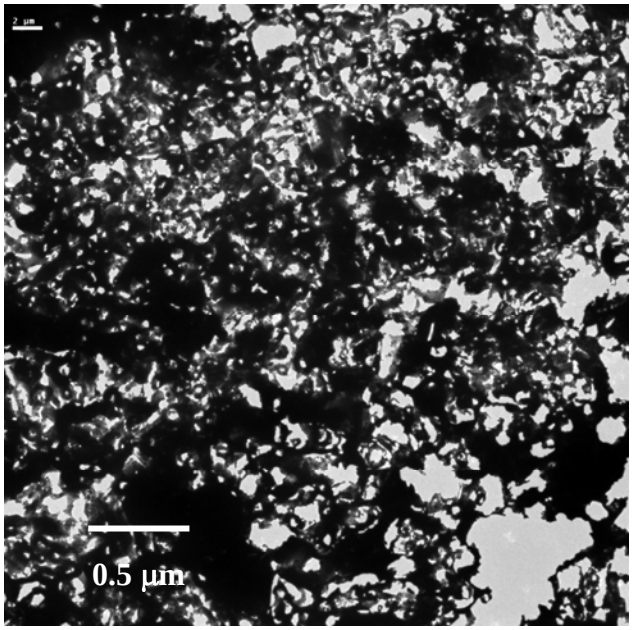

Figure 4-35: DF TEM of nc-copper at 1 *dpa* showing wide range of grain size.

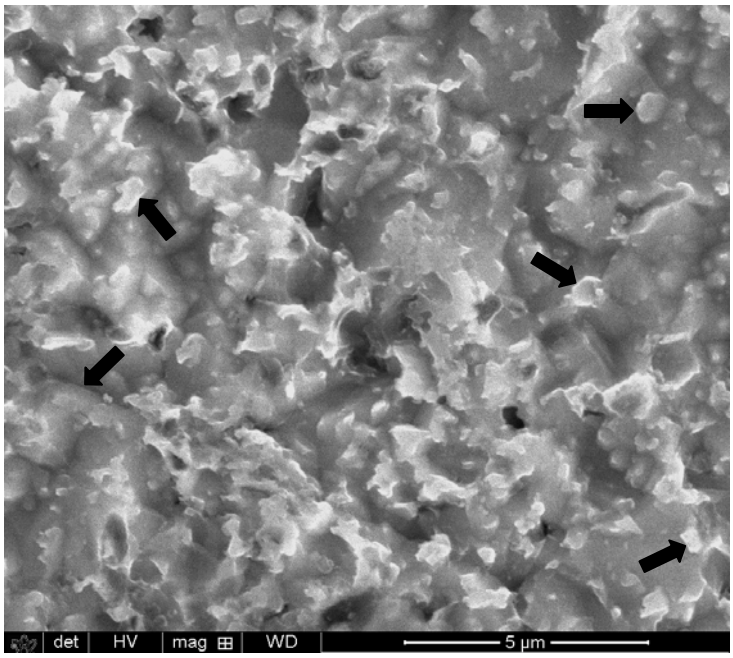

Figure 4-36: SEM of nc-copper at 2 dpa. Arrows pointing at typical grains considered for grain size measurements.

The average grain size of nc-copper was estimated to be ~ 0.8±0.6 μm at 1 *dpa* and ~ 0.75±0.5 μm at 2 *dpa*. According to these values and the corresponding grain size distributions (Figure 4-37, Figure 4-38), the average grain size of *nc*-copper is almost constant between 1 and 2 *dpa* which means that grain growth occurred up to the level of 1 *dpa* level.

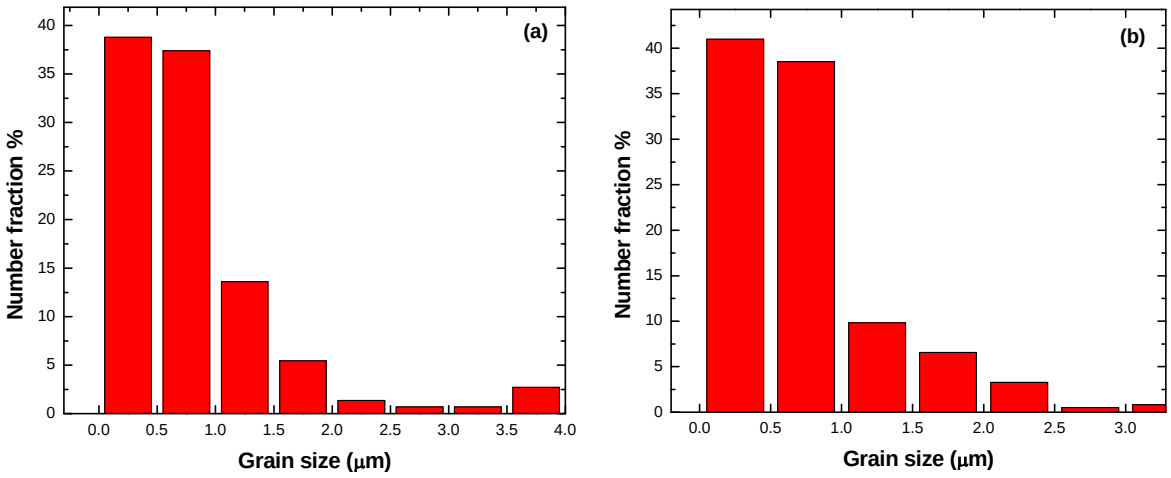

Figure 4-37: Grain size distribution of nc-copper (a) at 1 dpa showing average grain size ~ 0.8±0.6 μm and (b) at 2 dpa showing average grain size ~ 0.75±0.5 μm.

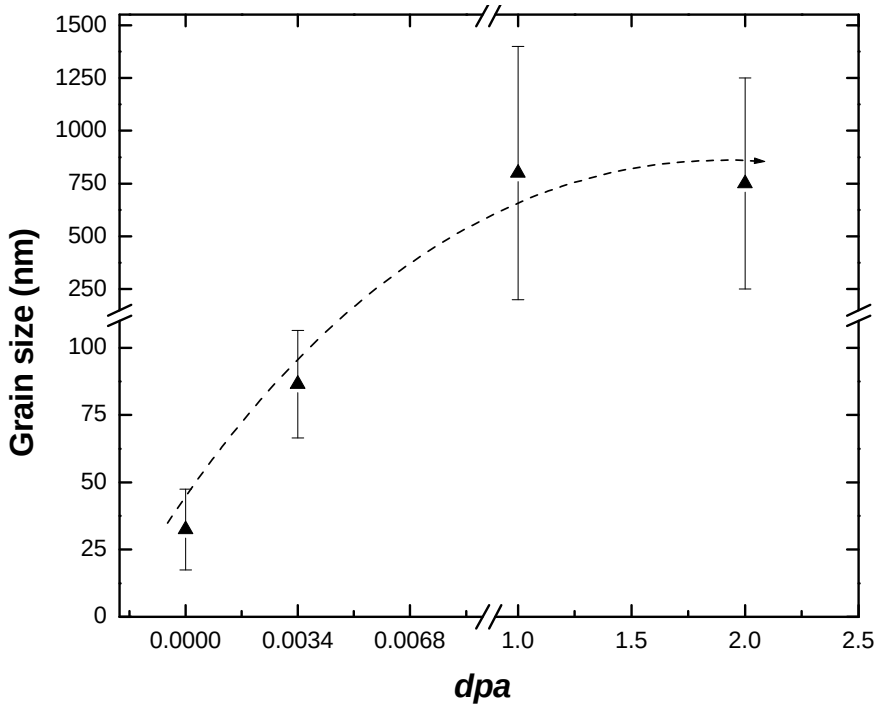

Figure 4-38: Variation of nc-copper grain size with *dpa*.

According to the variation of grain size of nc-copper with damage level, it is possible to conclude that grain growth of irradiated nc-copper is effective through 0.0034 *dpa* and up to 1 dpa at which, grain size saturates showing no change between 1 and 2 *dpa*.

Fracture surfaces of irradiated nc-copper

The SEM micrographs in Figure 4-39, 4-40, and 4-41 show fracture surface topography of deformed irradiated nc-copper. At 0.0034 dpa, the brittle nature of fracture observed in as received nc-copper seems to be still the case; however, fracture surface is less reflective.

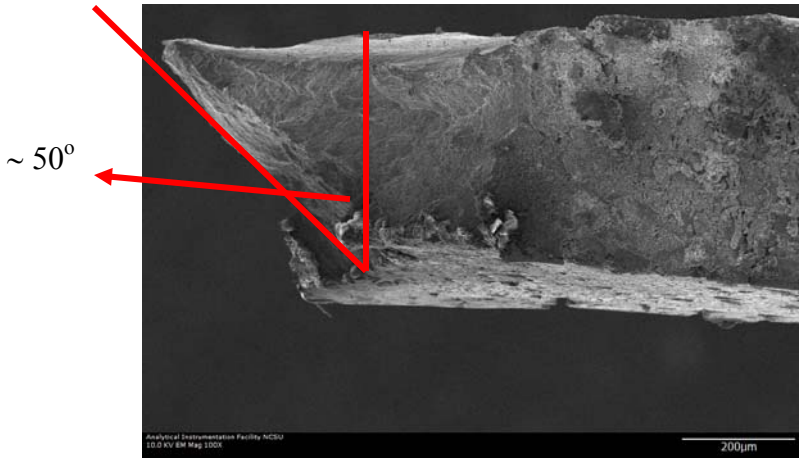

Figure 4-39: SEM of deformed nc-copper at 0.0034 *dpa*. Fracture occurs through shear bands at approximately 50°.

Interestingly, the fracture surface of nc-copper at 1 *dpa* shows a completely different topography such that the edge of the fracture surface indicates a fracture behavior that is more relevant to ductile than brittle fracture. Such a quasi-ductile fracture behavior can be attributed to the presence of some grains at the submicron range.

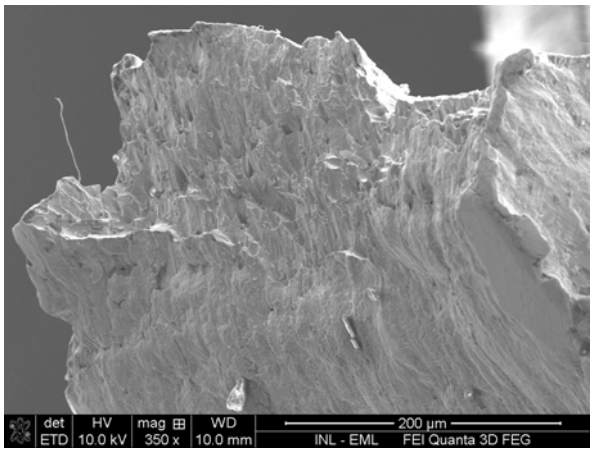

Figure 4-40: Semi-ductile fracture surface of nc-copper at 1 *dpa*.

As it was expected, nc-copper at 2 dpa shows a fracture surface with mixed brittle and ductile characteristics as shown in Figure 4-41.

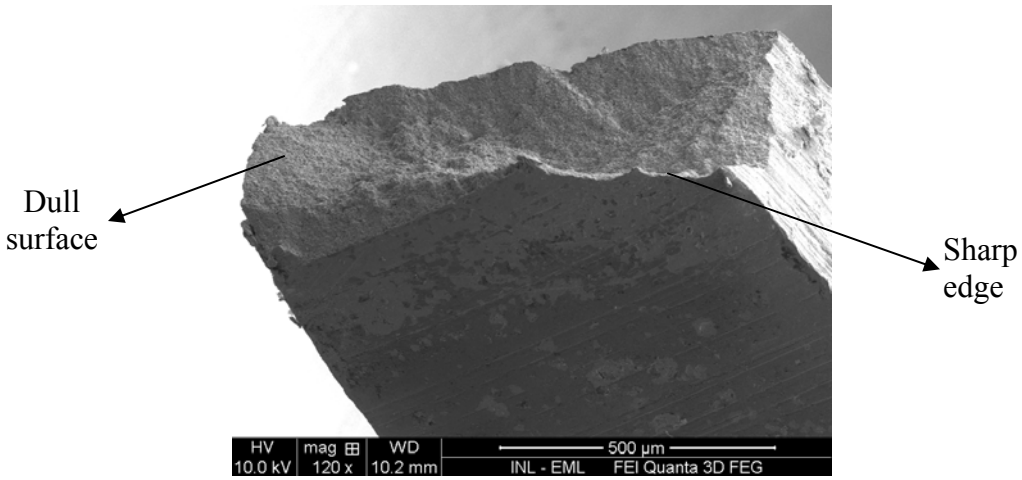

Figure 4-41: SEM of fracture surface of deformed nc-copper at 2 *dpa*.

Now, by considering the mechanical properties and developed microstructures reported for nc-cooper at the different attempted damage levels, there is a solid story to tell then. At relatively low damage level (fractions of *dpa*), the primary effect of fast neutron irradiation is to trigger grain growth in nc-copper which from about 34.4 nm to 87 nm with observation of grains of few hundred nm. Consequently, and on the basis of Hall-Petch equation, this increase of grain size caused a dramatic drop in materials' strength with notable increase in total elongation. With increasing the exposure/damage level up to 1 *dpa*, grain growth continued to take place increasing the average grain size to about 800 nm causing further decrease of strength; however, this was accompanied by a decrease of ductility in terms of

total elongation which indicates that mechanical behavior of nc-copper at that damage level is not solely controlled by grain growth. Although the average grain size of nc-cooper did not change between 1 and 2 *dpa*, hardness measurements and tensile tests revealed that materials strength started to increase back accompanied by decreased ductility which is typically described as radiation hardening and embrittlement. Accordingly, it is reasonable to believe that the response of nc-copper to fast neutron irradiation was controlled mainly by two distinguished mechanisms: grain growth which is predominant at low damage levels and radiation hardening which seems to take the lead at relatively higher damage levels whereas the two mechanisms were competing between 1 and 2 *dpa*.

4.3 Grain Growth of nc-Copper

It is apparent that grain growth heavily affected the developed microstructure and consequently the mechanical properties of nc-copper up to the 1 *dpa* level. It is worth investigating the driving force of that phenomenon and how it was originated in the presented irradiation conditions.

4.3.1 Thermal stability of as-received nc-copper

Grain growth observed in nc-materials was commonly related to the thermal instability of the structure [86] particularly when the effect of the processing conditions is considered [87]. For this reason, thermal instability of as-received nc-cooper was studied by conducting a series of annealing experiments followed by hardness and grain size

measurements. Samples of nc-copper were annealed for 3 hours at different temperatures and the grain size of the annealed samples was measured (Figure 4-42).

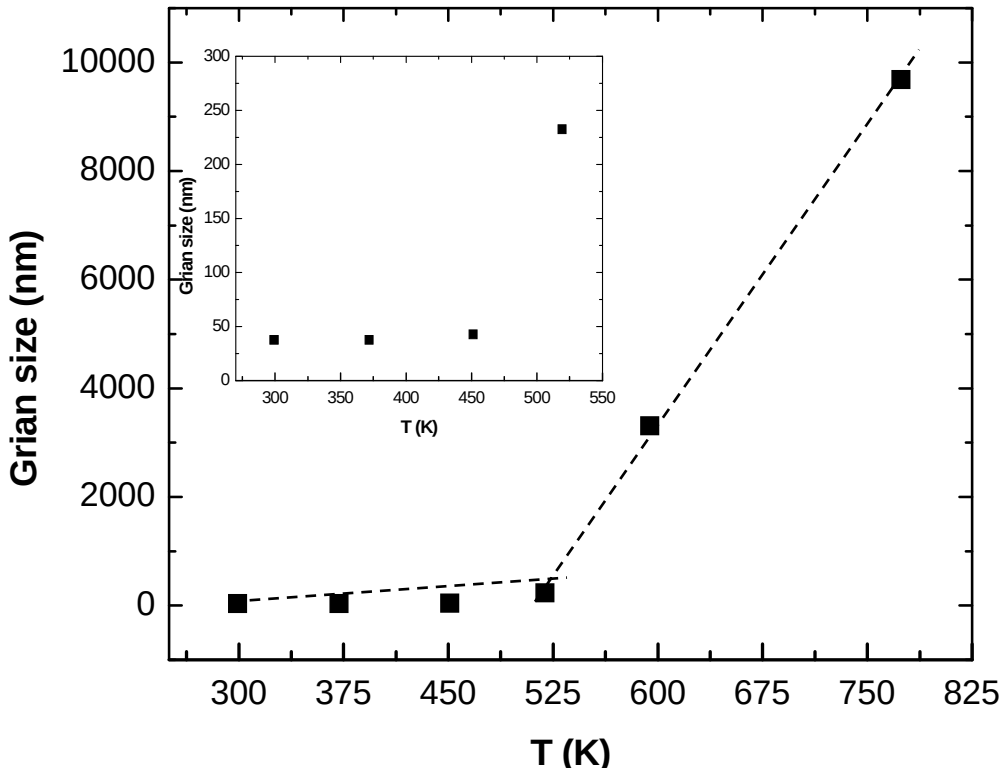

Figure 4-42: Variation of grain size with annealing temperature. Inset shows slow increase in grain size up to 450 K followed by a rapid increase starting at 500 K.

Based on the variation of grain size with annealing temperature, it is reasonable to suggest that thermally activated grain growth in as received nc-copper is controlled by two distinct mechanisms corresponding to the change of the rate of grain growth with transition temperature ~ 500 K. Recalling the rate equation for grain growth $D^n \approx K_0 t \exp\left(\frac{-Q}{RT}\right)$, the

activation energy for grain growth can be determined by plotting the variation of grain size with temperature on an Arrhenius plot as shown in Figure 4-43 for different values of the grain growth exponent "*n*".

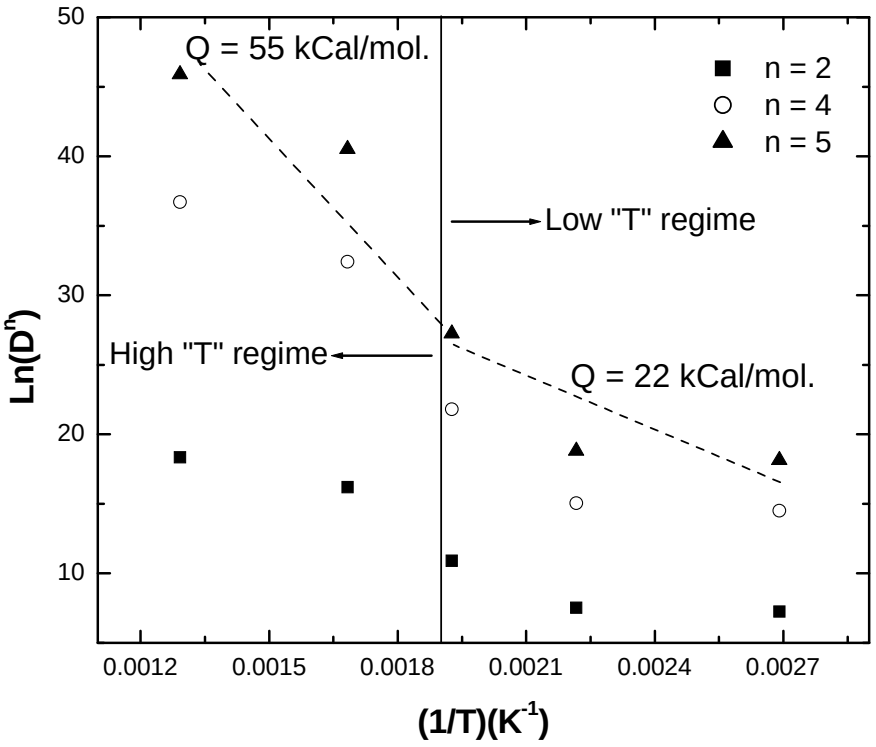

Figure 4-43: Arrhenius plot analyzing thermally activated grain growth of as-received *nc*-copper.

Analysis of the variation of grain size with annealing temperature indicates that at temperature higher than 500 K (~ 226°C), the activation energy estimated for grain growth is about 55 kcal/mole which approaches the activation energy of self lattice diffusion in micrograined copper (Q_D ~ 46.8 kCal/mol [88]) whereas at temperatures below 500 K,

activation energy for grain growth is found to be ~ 22 kcal/mole which is close to activation energies reported for grain growth via grain boundary diffusion in some nanocrystalline systems [41, 89]. This notion seems to be reasonable whereas at low temperature, the size of grains are of about few tens of nanometers and accordingly the large volume of grain boundaries would facilitate diffusion via grain boundaries which is commonly called as short circuit diffusion. Once grain size approaches the submicron regime, diffusion through lattice becomes predominant mechanism for grain growth.

4.3.2 Investigation of grain growth via differential scanning calorimetry

In Differential Scanning Calorimetry (DSC) technique, the amount of heat required to increase sample's temperature is compared to that of a reference sample (usually the sample pan holder itself) while both samples at the same temperature and the difference is measured as a function of either temperature or time. When sample is being heated at a specific heating rate, any physical transformation will require either more or less flow to the sample to keep it at the same temperature as the reference sample. If more heat flow is required to keep the sample at the same temperature of the reference sample, this indicates the sample was undergoing an *endothermic* (e.g. solid to liquid transformation) whereas *exothermic* transformation requires less flow of heat to keep both samples at the same temperature and in both cases, the process is reflected on the plot of heat flow versus temperature or time as a positive or negative peak according to the convention used. In the field of studying the various aspects of nanocrystalline materials, DSC is commonly utilized to characterize thermally activated grain growth in nanocrystalline materials where it is possible to

investigate temperature at which grain growth is triggered [90]. In the present study, 3 mm disks of as received nc-copper were annealed using DSC (Q2000 series manufactured by TA Instruments) at rate of 10°C / minute and the corresponding heat flow was plotted as a function of measured sample temperature (Figure 4-44).

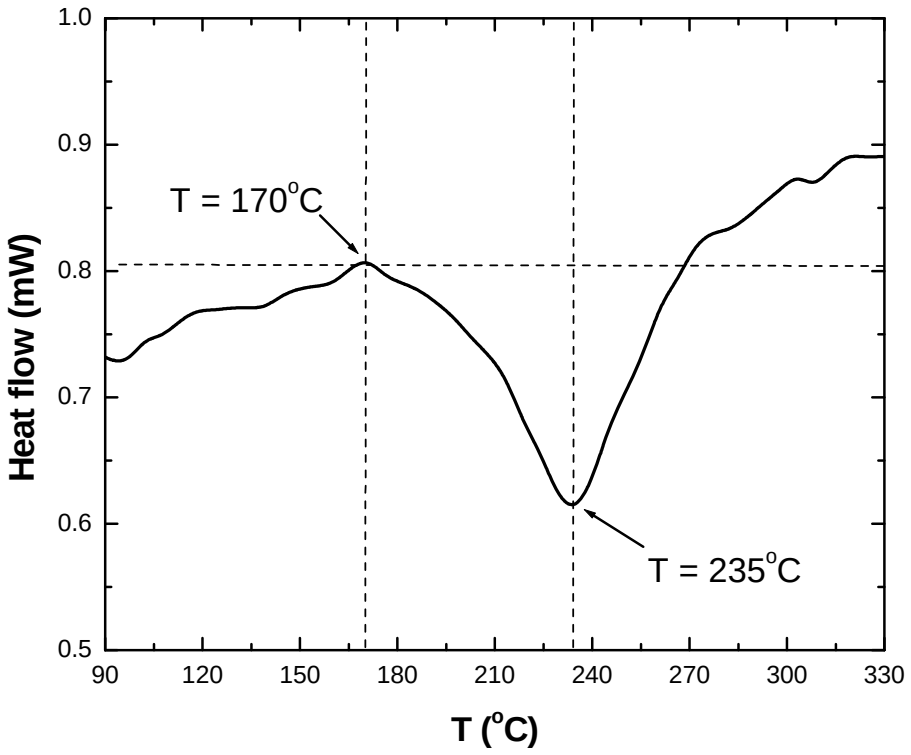

Figure 4-44: DSC scan of 3 mm disk of as received nc-copper heated at 10 K/ min.

According to the DSC scan, thermal instability starts to show at 170°C and full peak is observed around 235°C as indicated by arrows in Figure 4-44. Recalling the variation of grain size with annealing temperature (see Figure 4-42) the low temperature grain growth

was observed at 450 K (~ 170^{o}C) which is about the same temperature at which thermal instability is observed in the DSC scan. Moreover, the peak position observed in DSC scan at 235^{o}C is about the same as the transition temperature between grain boundary diffusion and lattice diffusion shown in the Arrhenius plot in Figure 4-43 which was estimated as 500K (~ 226 ^{o}C). It can be concluded that temperature regime at which grain growth is controlled by grain boundary diffusion represents the onset to thermal instability of nc-copper whereas lattice diffusion is the mechanism which is predominant over the grain growth toward equilibrium. These results are in agreement with grain growth observed in electrodeposited nc-nickel with initial grain size ~ 20 nm [91] which suggests dependency of the kinetics of grain growth on the initial grain size of nanocrystalline materials.

4.3.3 Grain growth of irradiated *nc*-copper

Since the kinetics of grain growth of as received nc-copper is now clearly uncovered, it is then possible to investigate the grain growth observed in nc-copper which was early observed at 0.0034 *dpa* and effectively progressed up to 1 *dpa*. Grain growth is expected to be dependent on the temperature which samples experienced during irradiation. For 0.0034 *dpa* irradiation at PULSTAR reactor, as run irradiation experiment shows that the maximum ambient temperature of copper samples over the 200 hrs of irradiation was about 126^{o}F (~ 53^{o}C).

For 1 and 2 *dpa* irradiation at ATR, temperature along the irradiation capsules was calculated using the MCNP coupled with ORIGEN2 (MCWO) and the following temperature distribution was obtained (Figure 4-45).

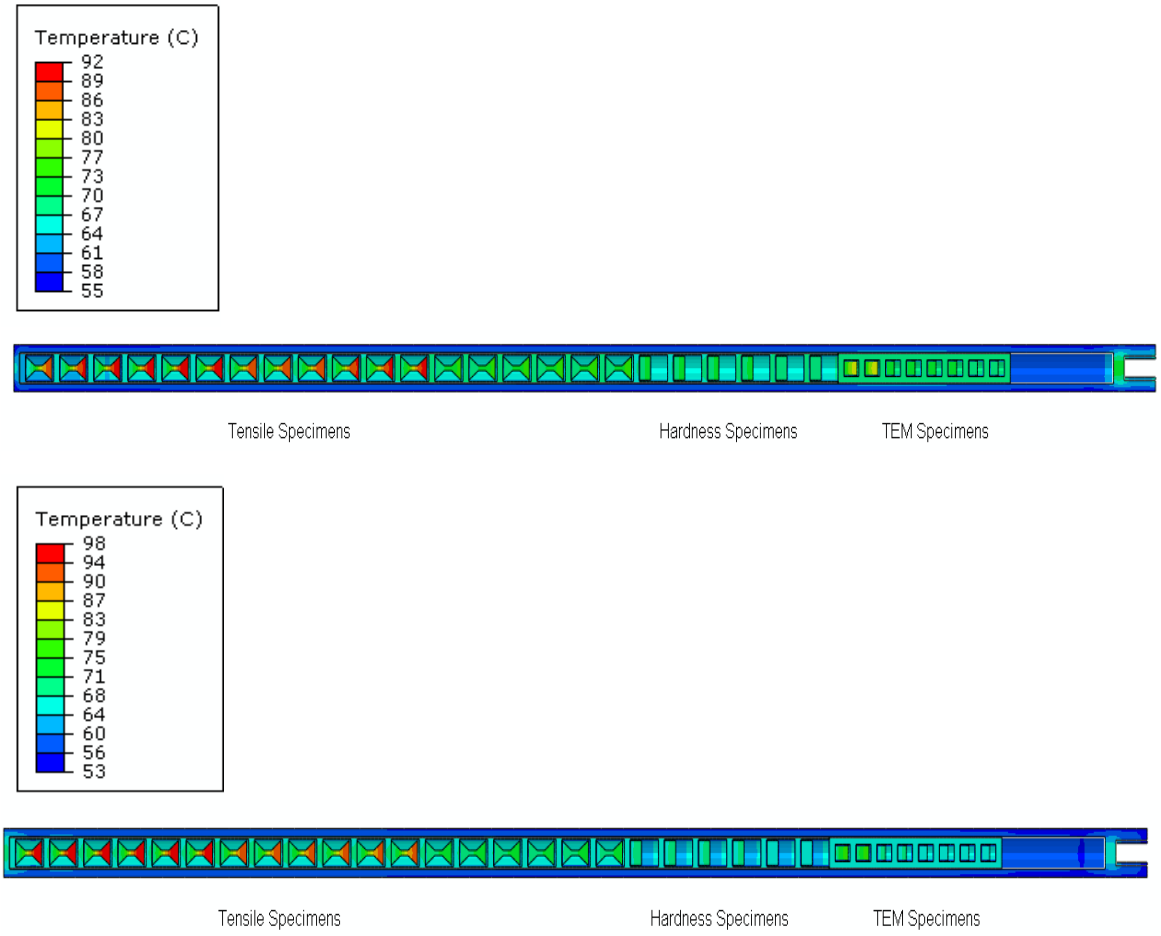

Figure 4-45: Simulated temperature distribution of samples irradiated at 1 *dpa* (top) and 2 *dpa* (bottom).

Based on the simulated irradiation experiments at 1 and 2 *dpa*, the maximum irradiation temperature experienced by nc-copper in all irradiation conditions was ~ 100^{o}C which was observed in tensile samples irradiated at 2 *dpa* for 672 hours. To investigate the origin of grain growth in irradiated *nc*-copper, samples of the as-received material were annealed at

55°C for 200 hrs and 100°C for total annealing time of 700 hours during which, hardness of the annealed samples was measured at different annealing times (Figure 4-46, Figure 4-48).

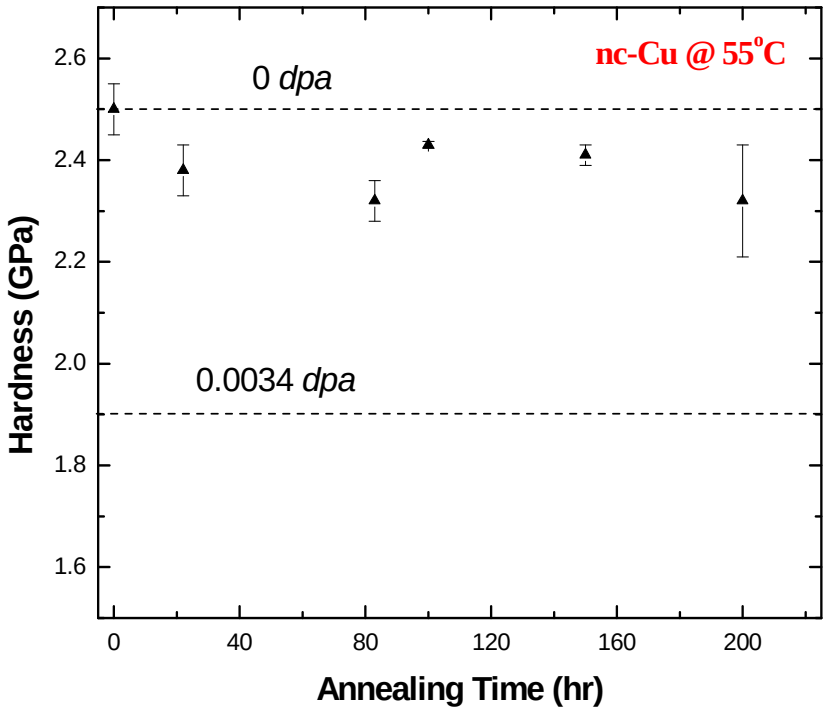

Figure 4-46: Variation of hardness with annealing time at 55°C. Dash lines indicate hardness of irradiated *nc*-copper at 0.0034 *dpa* level.

Figure 4-46 shows that hardness following heat treatment at 55°C for 200 hrs did not show much decrease unlike 0.0034 *dpa* samples. Thus it is concluded that grain growth in 0.0034 *dpa* irradiated nc-copper occurs due to irradiation and not thermally induced. Similarly, Figure 4-47 shows hardness following heat treatment at 100°C for 670 hrs.

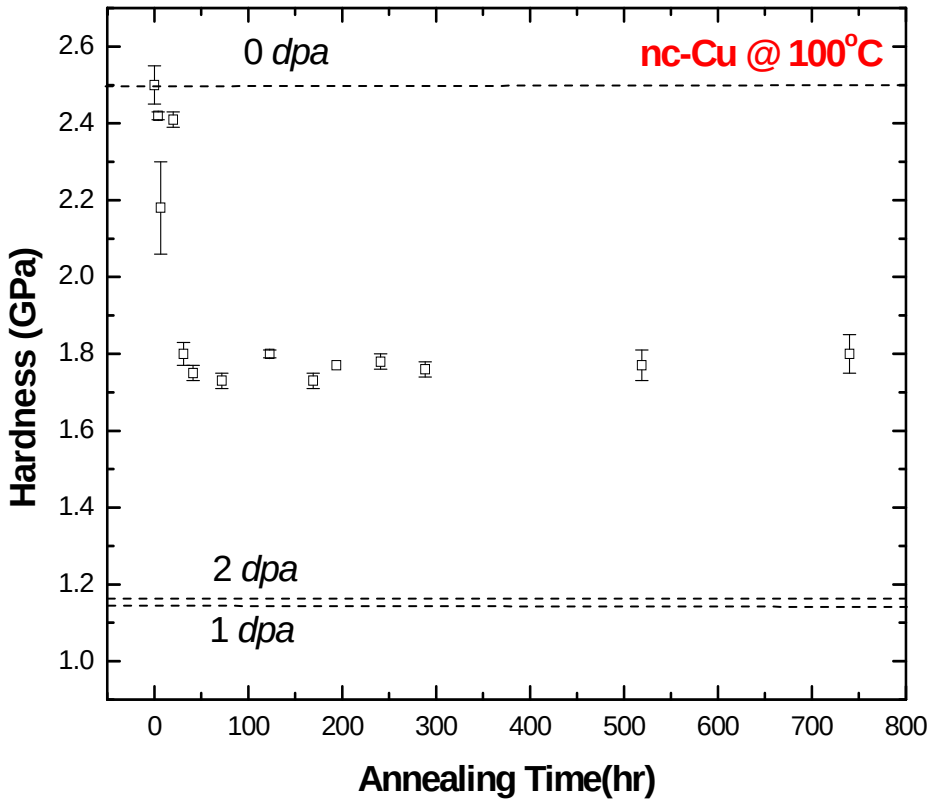

Figure 4-47: Variation of hardness with annealing time at 100°C. Dash lines indicate hardness of irradiated nc-copper at 1 and 2 *dpa* level.

By comparing hardness of annealed nc-copper with the irradiated samples at higher damage level, grain growth up to 1 and 2 *dpa* is far away to be considered as thermally induced grain growth. Consequently, it is reasonable to ascribe the increase in grain size of *nc*-copper observed at the different damage levels to irradiation-induced grain growth which was reported for nanocrystalline system under irradiation particularly in the form of thin films. Studies concerned with investigating mechanisms of irradiation-induced grain growth are

mainly based on computational and simulation efforts however, there is no well defined envision for the details of this process to-date.

Recently, a thermal spike model describing the irradiation induced grain growth was proposed by Kaoumi *et al.* [92] which concerns with the grain growth observed at the low temperature regime (0.15 - 0.2 T_m). The thermal spike is described at a later on stage of the collision cascade in which the residual kinetic energy of the recoiled atoms is dissipated in the lattice which gives rise to a localized temperature spike. Experimental results and data show that the size of the thermal/temperature spike is strongly dependent on the recoil energy and the materials properties (the grain size in particular). The model then focuses on those spikes formed near grain boundaries and suggests that atoms within the spike can jump across the boundaries and the driving force for that event is attributed to the curvature of the grain boundaries, which represents a source of pressure acting on the grain boundaries, as well as the local chemical concentration gradient which causes a net flow of atoms to be in such a direction which reduces the grain boundary curvature resulting in the observed grain growth. It is worth to note that the proposed model only considers those defects created in the vicinity of grain boundaries to contribute to grain growth which implies that the smaller the size of grain, the more defects will be involved in that process. Results obtained via molecular dynamics simulation which will be presented in the next chapter would support this model since it was observed that displaced atoms following a radiation impact event show high tendency to be attracted towards interfaces.

4.4 Overall Radiation Response of Polycrystalline Copper

Up to this point, the variation of mechanical properties and developed microstructure with damage level was furnished separately for MG-copper and *nc*-copper and thus, it is worth discussing the overall post-irradiation behavior of polycrystalline copper.

Influence of annealing twins on mechanical behavior of irradiated copper

Microstructure characterization of irradiated copper showed twins as the most common and persistent microstructure feature at all damage levels and thus the influence of high density twins needs to be elucidated. While annealing twins are commonly observed in annealed FCC metals such as MG-copper, it might be worth to elaborate how it was formed in nc-copper. In micrograined copper, formation of annealing twins was suggested to be formed by lateral growth of extremely thin deformation twins during annealing after which, migration of those twin boundaries is possible when strain energy is present [93]. Observation of annealing twins in copper with grain size of tens to hundreds of nm is believed to be always related to the process of grain growth. Formation of annealing twins during grain growth was explained in terms of the change in interfacial free energy of grain boundaries where annealing twins support the decrease in interfacial free energy accompanying grain growth [94]. This explanation agrees with the early observation of twin boundaries in nc-copper at 0.0034 *dpa* which was showed to be undergoing grain growth which would give rise to the question on how those annealing twins may affect the mechanical behavior of irradiated copper. Since the mechanical behavior of MG- and nc-copper was basically discussed on the basis of Hall-Petch equation, the above question might

be rephrased to be how annealing twins would affect the yield stress of polycrystalline metal governed by the Hall-Petch relation. It is known that investigating mechanical properties based on the Hall-Petch relation considers only grain size as the controlling factor whereas other microstructural features such as grain size distribution and annealing twin boundaries are completely ignored [95]. A series of studies concerned with characterizing the influence of annealing twins on the mechanical behavior shared the conclusion that a Hall-Petch relation can account for the presence of annealing twins by considering an effective grain size measured as the intertwins spacing [96, 97]. Pande *et al.* [98] proposed a quantitative modification to the Hall-Petch equation on the premise that annealing twins boundaries are acting as dislocation barriers in a fashion similar to grain boundaries based on which, an expression for the effective grain size was derived as: $D_{eff} = D / \left[1 + 2pK_t \ln\left(\frac{D}{D_0} \right) \right]$ where K_t is a constant, D_0 is the grain size at which the number of twins per grain ~ 0 and p is a correction factor to consider the fact that twin boundaries are not as perfect as grain boundaries while acting as dislocation barriers. By substituting for the grain size in the traditional Hall-Petch equation, the modified form is then given by $\sigma_{eff} = \sigma_0 + \frac{k_{eff}}{\sqrt{D}}$ where $k_{eff} = \left[1 + 2pK_t \ln\left(\frac{D}{D_0} \right) \right]$ which implies that variation of yield stress with grain size will deviate from linearity and thus expected to be higher than the value predicted based on the traditional form of the Hall-Petch equation. It can be concluded that twins observed in

irradiated MG- and *nc*-copper contribute to the yield stress of irradiated materials by acting as a barrier for dislocation motion in a manner similar to that of grain boundaries.

Radiation hardening in polycrystalline copper

Since mechanical behavior of both MG-and *nc*-copper was discussed (up to this point) on the basis of the Hall-Petch relation and furthermore, the influence of annealing twins on the mechanical behavior was interpreted in terms of its effect on the yield stress of the irradiated material, it was beneficial to establish the Hall-Petch relation of the as received copper by conduction annealing experiments to obtain copper samples of different grain size and strength as shown in Figure 4-48 and Figure 4-49.

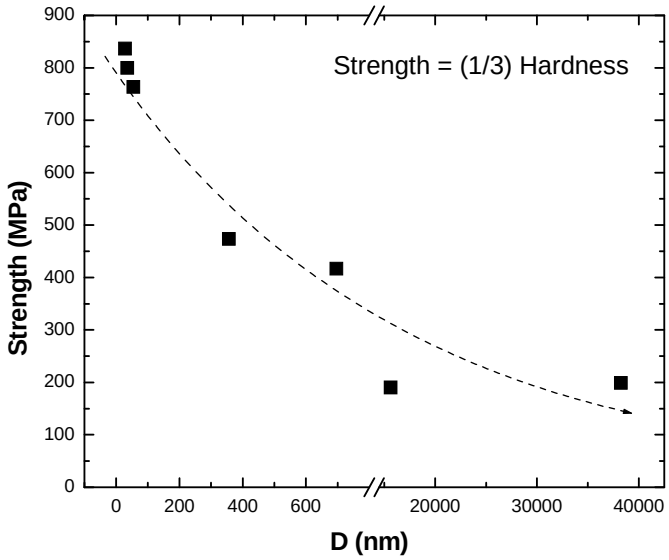

Figure 4-48: Variation of hardness with grain size of nc-copper.

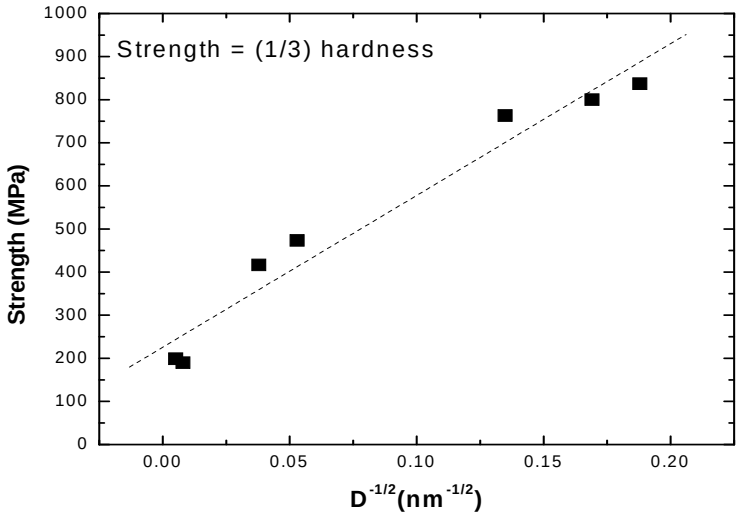

Figure 4-49: Hall-Petch plot of polycrystalline copper.

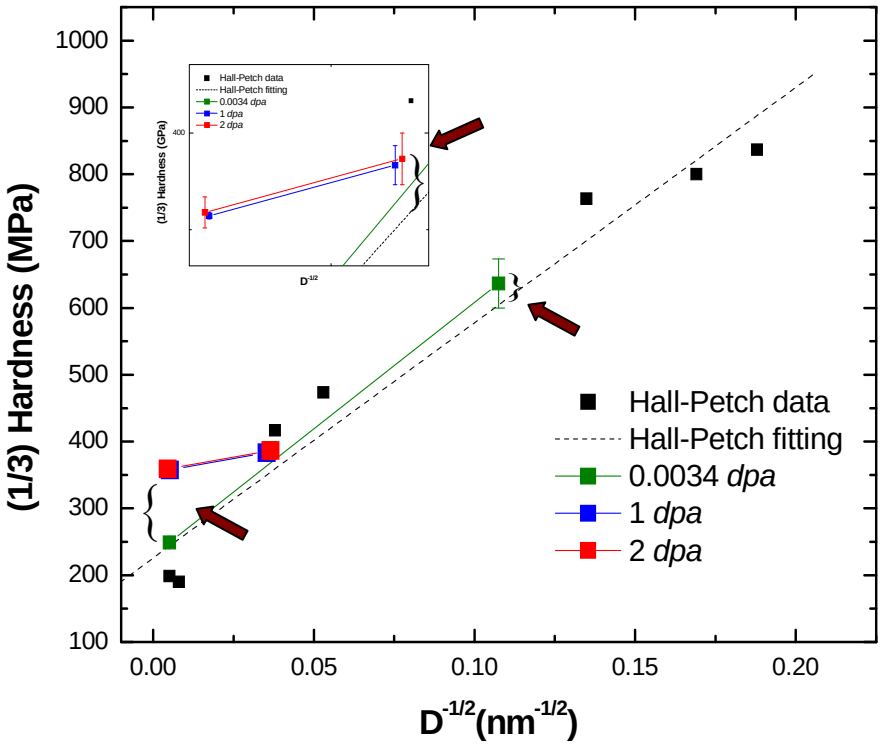

Figure 4-50: Radiation hardening in irradiated polycrystalline copper.

Based on the Hall-Petch plot shown in Figure 4-50, the radiation hardening in irradiated copper can be determined as the difference between the hardness following irradiation and the hardness at the corresponding grain size from the Hall-Petch plot which is shown in Figure 4-50. Radiation hardening is more predominant in irradiated MG-copper especially at higher doses (1, 2 *dpa*) whereas it less observable in irradiated nc-copper.

In order to decompose the radiation hardening into the source and friction components, the variation of yield stress of MG- and *nc*-copper is plotted at each damage level (Figure 4-51) to simultaneously investigate the influence of grain size and damage level on the mechanical behavior of polycrystalline copper.

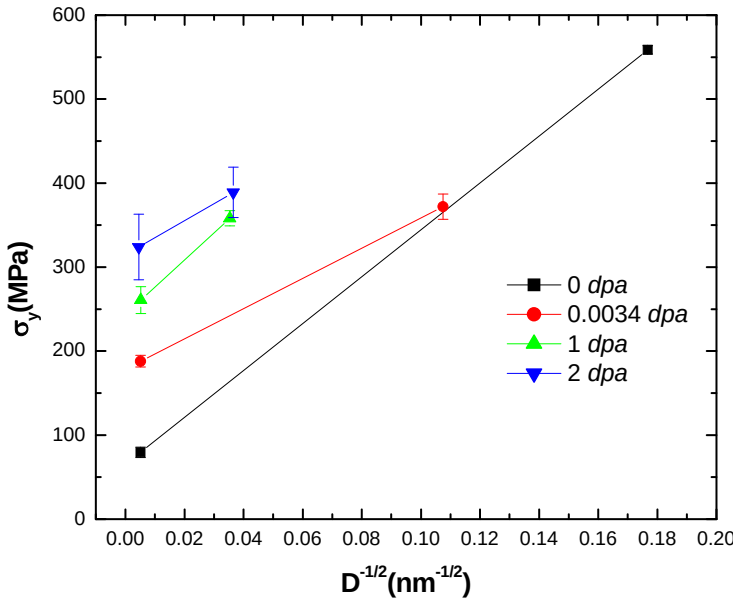

Figure 4-51: Variation of yield stress with grain size at the different damage levels.

According to Figure 4-51, the variation of yield stress of polycrystalline copper at the different damage levels can be thought to follow a general Hall-Petch behavior albeit there are only two data points (MG- and *nc*-copper). Furthermore, a close scrutiny of the data indicates that the slope of Hall-Petch line inconsistently changes from one damage level to the other. On the premise that the straight lines connecting the two data points at each damage level do reveal the effect of radiation exposure on the yield stress (σ_y) and the unpinning stress (k_y), friction and source hardening components at each damage level were examined by fitting the two data points at each damage level such that the slope of the straight line corresponds to the unpinning stress (k_y) and consequently, the source hardening is calculated as $k_y / \sqrt{d}$ and the friction stress is calculated as the difference between yield and source hardening stress as shown in Figure 4-52 and Figure 4-53

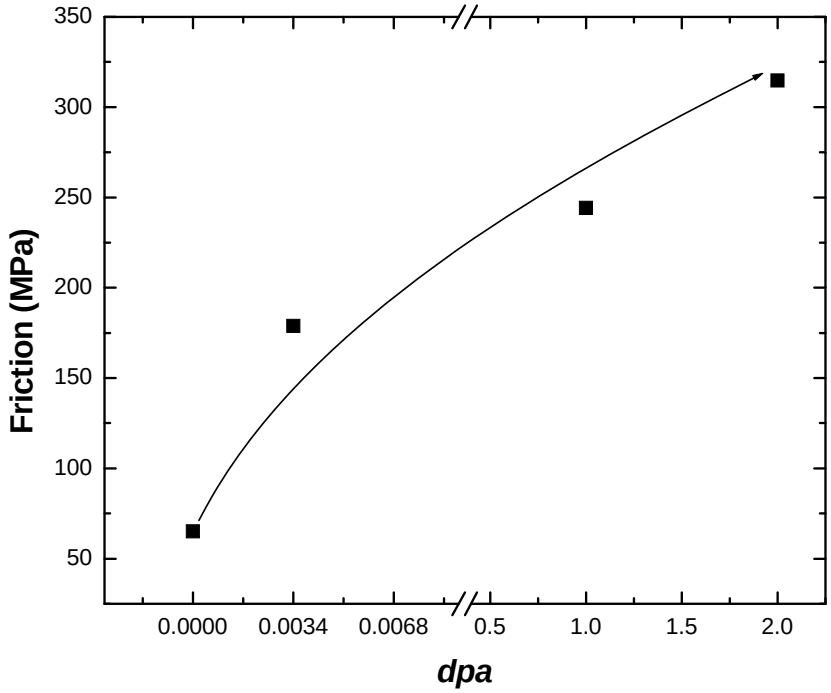

Figure 4-52: Variation of friction hardening of polycrystalline copper with damage level (*dpa*).

The continuous increase of friction hardening can be attributed to the increasing density of dislocations observed in both MG- and *nc*-copper as the damage level increases. Increasing dislocation density as well as twins hampers the motion of mobile dislocations and accordingly more stress is needed for dislocation motion resulting in the observed increase in the friction hardening component of the yield stress with *dpa*.

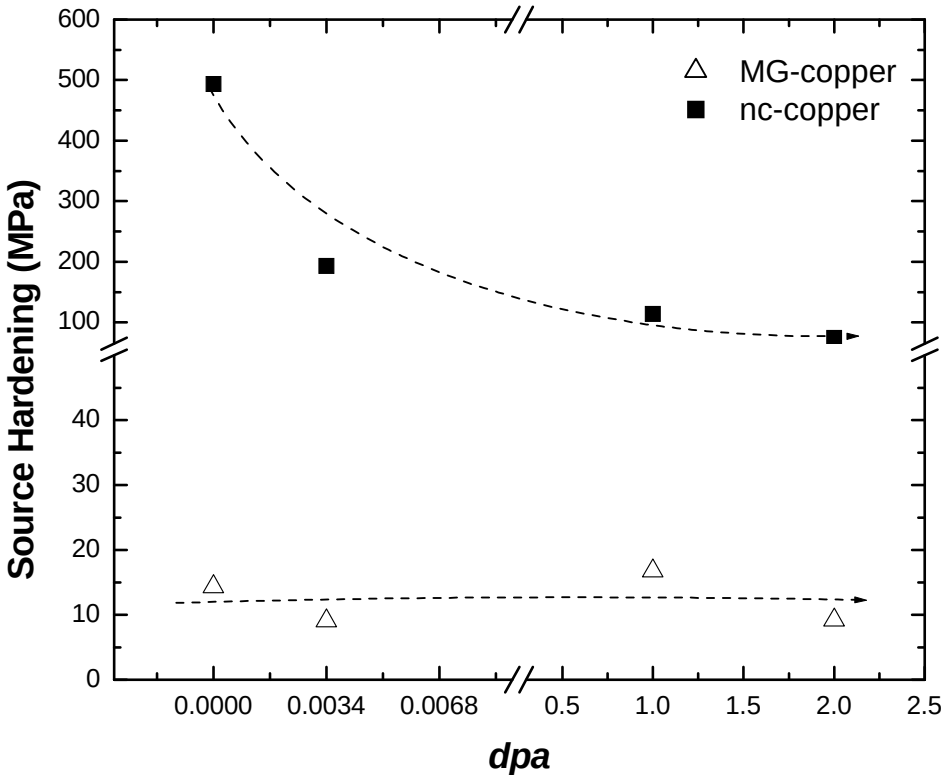

Figure 4-53: Variation of source hardening of MG- and nc-copper with damage level (*dpa*).

According to Figure 4-53, the source hardening component of yield stress of *nc*-copper shows continuous decrease across the different damage levels which can be attributed to the observed increase in grain size from 34.4 nm pre-irradiation up to about 1 μm post 1 and 2 *dpa*. On the other side, source hardening of irradiated MG-copper does not change a lot with the damage level and the values plotted in Figure 4-53 are varying between 9 and 14 MPa which implies that source hardening has a minimal contribution to the yielding of irradiated MG-copper. Accordingly, earlier observation made on austenitic steel showing almost no source hardening contribution to the yield pre-irradiation seem to apply in the case of pure copper as well [99].

4.5 Chapter Summary

In this chapter, post-irradiation examinations of MG- and *nc*-copper were reported and discussed in terms of the developed microstructures and measured mechanical properties. The response of irradiated MG-copper follows the general trend of other FCC metals post irradiation which can be described in terms of radiation hardening and embrittlement. Whereas, the mechanism controlling the response of nc-cooper to irradiation was found to change between low and high exposure levels. Grain growth was observed to act as the predominant mechanism at low damage levels manifested by dramatic decrease in material's strength and continued to contribute to material response up to 1 *dpa* after which, radiation hardening started to take the lead controlling the response of nc-copper at 2 *dpa*. Grain growth observed in irradiated nc-copper was attributed to the effect of irradiation rather than being a pure thermally activated process by comparing the hardness measurements of irradiated samples to the corresponding hardness of annealed nc-copper to different times at constant temperatures. It may be noted that the response observed in the experiments is dictated by the processing techniques and may not, in general, extend to samples fabricated by all processing methods. Both characterization of developed microstructure and evaluation of mechanical behavior rationalized the overall irradiation-behavior of MG- and nc-copper at the different exposure/damage levels.

Chapter 5. Radiation Tolerance Behavior at Interfaces: A Molecular Dynamics Investigation

The experimental investigations show that the nanocrystalline copper samples that are irradiated in a neutron environment undergo significant grain growth. The intriguing question still remains – will interfaces which are thermally stable and which maintain their integrity in a radiation environment promote a tolerant or self–healing behavior? To test this conjecture, molecular dynamics (MD) simulations are performed, with an in–house MD program [100], on bicrystal copper with twist grain boundary configurations ($\Sigma 5$ and $\Sigma 41$), as well as on a single crystal copper configuration without any interfaces or defects.

With the significant increase in computing power over the last few decades, molecular dynamics (MD) simulation of materials has become an attractive option for investigating realistic mechanisms at the atomistic level which are often not accessible by experiments. MD simulations can also offer unprecedented control over atomic configurations, and initial/boundary conditions which are extremely valuable for testing and validating hypotheses such as on the importance of stable interfaces on promoting radiation tolerant behavior. MD simulations which are performed in this dissertation thus assume a complementary role to the experimental investigations delineated in the preceding chapters. While MD simulations are typically limited in sample sizes and timescales, the emphasis in this dissertation is on gaining insight on possible radiation tolerant mechanisms which are at play in controlled radiation environment with single and bicrystal configurations. As

observed in this study, MD simulations can also offer guidelines and directions for conducting experiments in the future.

Two bicrystal configurations, (*a*) twist $\Sigma 5$, and (*b*) twist $\Sigma 41$, are investigated with radiation cascade simulations. While there are an inordinately large number of relative configurations between two grains, at certain angles of rotation, the lattice points coincide perfectly, known as coincidence site lattice (CSL). The reciprocal density of coincident sites, denoted by Σ, gives the relationship between the number of lattice points in a unit cell of the generating lattice and number of lattice points in the unit cell of a CSL – it is also the volume fraction of the coincidence unit cell to the crystal lattice unit cell.

5.1 Literature Survey

A literature survey is presented first on MD simulations on nanomaterials and past work on radiation cascade simulations. The simulation work on the bicrystals is presented in Sections 5.2, 5.3 and 5.4.

5.1.1 Nanostructured materials

Fabrication of nanostructured materials is often hampered by limited processing power and reproducibility. From this perspective, MD simulation is extremely useful to characterize the nanostructures in ideal and controlled environments. Several MD simulations have been reported in the past on structure–property relationships such as on the influence of grain size and formation of stacking faults on the mechanical properties of *nc*-materials [101-103].

Relevant to copper, the material of interest in the present study, Schiotz *et al.* [104] have studied the mechanical deformation of *nc-copper* with equiaxed, dislocation-free nanograins (produced through Voronoi subdivision) and atomic interactions simulated with many-body effective medium theory (EMT). Grain boundary sliding is found to be the main deformation mechanism whereas dislocation activity is rarely observed in the grain interior. This observation explains the inverse Hall-Petch behavior in which strength increases with increasing grain size. The conclusions are also confirmed by Hua *et al.* [105] with deformation studies on *nc*-materials under tensile loading with dislocation activities detected only at low temperatures. A more detailed investigation of the temperature effects on the collective grain deformation of *nc*-metals is presented by Tomotsugu *et al.* [103] with simulations conducted on the mechanical response of eight aluminum grains of regular hexagonal shape with an initial grain size of 5 nm, approximately. At low temperatures (less than 100 K), inhomogeneous deformation with shear bands is observed whereas at high temperatures (300-500 K), the deformation mechanism is largely homogeneous. This bimodal micro-structure is a common feature that is reported for *nc*-metals showing high strength with reasonable ductility. This implies that enhancement in ductility of *nc*-metals can be achieved if deformation mechanisms are appropriately controlled [106].

Tensile properties of *nc*-tantalum are reported by Pan *et al.* [107] using MD simulations with seven cubic samples of different side lengths each containing sixteen grains of different sizes such that systems of various densities are obtained. Based on this study, elastic moduli of *nc*-Ta is shown to be dependent on the density with the largest elastic modulus obtained for the most dense system. This observation is related to the reported effect

of porosity on the mechanical properties of *nc*-metals. Stress induced phase transformation from BCC to FCC and HCP is observed locally in the simulated systems at low temperatures and the transformation is found to be reversible with respect to the applied stress.

The effect of solute atoms and twin boundaries on the plastic deformation of Pd-Au alloy is studied by Albe *et al.* [108] using large scale MD simulations. In this study, a system of 54 grains with an average grain size of 15 nm is simulated. While a homogenous concentration of species is found in the grain interior, grain boundaries tend to show a preferential segregation of either Pd or Au. Moreover, the twin-boundaries introduced to the Pd-Au alloy is found to cause softening of the material in contrast to what is observed in *nc*-copper which is attributed to the twins-boundary acting as a dislocation source rather than as a dislocation barrier.

MD simulations have successfully explained the inverse Hall-Petch behavior observed in materials with small grain sizes. In the normal Hall-Petch relationship, the yield strength shows an inverse relationship with the grain size while in the inverse Hall-Petch relationship the strength decreases with further grain refinement [109]. Desai *et al.* [110] attributed the combined effect of lattice and grain boundary (GB) diffusion to explain the inverse Hall-Petch behavior observed in *nc*-Mo which is a BCC metal [109]. Thus the inverse Hall-Petch behavior in *nc*-Mo is regarded as a manifestation of GB diffusion creep accompanied by Nabarro-Heering creep [110].

5.1.2 Cascade simulations on single crystals

As briefly mentioned before, the current materials characterization techniques, in general, do not have the ability to resolve the spatial and temporal features of irradiation damage processes at the atomistic level. Over the years, molecular dynamics (MD) simulations, have been extensively used to characterize the early stages of radiation damage processes [111] and have a rich history dating back to the Vineyard group at Brookhaven in the early 1960s. There are a large number of publications in this area and only a few of these studies are cited due to space constraints. As such, several important studies and results are not discussed in this dissertation.

The MD simulations which investigate the damage processes, known as collision or displacement cascade simulations, typically have several tens of thousands of atoms to million/billions or even trillions of atoms depending of the imparted energy and the computational resources. The low energy (< 500 eV) cascade simulations of King *et al.* [112, 113] on copper atoms using Gibson II potential show that the damage function, defined as the average number of Frenkel pairs created as a result of lattice atom recoil, saturates at a value of 0.5 for a broad energy range which is much less than what is predicted by the Kinchin-Peace model. Rubia *et al.* [114] performed cascade simulations on Cu and Ni but at higher impact energies (5 keV) with the primary state of damage characterized by two mechansims, (*a*) replacement collision sequence during the ballistic phase, and (*b*) thermal spike regime with melting and resolidification. Differences observed between copper and nickel in the thermal spike regime is attributed either to dissimilar cohesive and elastic properties, or to shortcomings of the interatomic potential. Higher energies of the order of

200 keV investigated by Nordlund *et al.* [115] exhibit coherent atomic displacements in copper from ion irradiation.

5.1.3 Cascade simulations on nanostructured systems

Displacement cascades in *nc*-Ni with an average grain size of 12 nm, initiated by PKA of different energies in the vicinity of grain boundary (GB), are reported by Samaras *et al.* [116] with a second moment tight binding potential to describe the interatomic interactions [117]. The cascade volume in *nc*-nickel is found to be same as that is reported for perfect crystals at 40 fs after the PKA is introduced. Between 0.4 and 4 ps, a large number of replacement collision sequences are observed which are directed toward the GBs, and this phenomenon is consistently observed regardless of the initial PKA energy. After re-solidification, vacancies are found to be the dominant type of defects whereas partial dislocations are observed at high PKA energies. Truncated stacking faults tetrahedrals (SFTs) are also found to be easily formed during cooling at PKA energies greater than 10 keV [118]. These truncated SFTs along with GBs are found to influence the migration of self-interstitial atoms (SIAs). When the cascade is formed near a sink (GB or stacking fault), it attracts SIAs through the mechanism of replacement collision sequences whereas, upon resolidification, the remaining SIAs aggregate to form clusters [119].

The role of pre-existing voids in irradiation behavior of *nc*-iron is investigated by Hoffelner *et al* [120, 121]. These studies indicate that voids and grain boundaries act in a similar way in the sense that SIAs are attracted to both of them. However, the mechanism of the attraction of SIAs to the voids is not conclusive.

The phenomenon of irradiation induced grain growth is reported by Voegelie *et al.* [122] using MD simulations in *nc*-nickel with 5 keV cascade with grain sizes of 5 and 10 nm. The grain growth is found to be dependent on the relative size of the spike volume and the grain size. Grain growth takes place when the spike volume exceeds the grain size or if it passes through GB from one grain to another. On the other hand, if the spike volume is completely accommodated by the grain, only vacancies and interstitials are formed with GBs acting as sinks for the defects. Furthermore, irradiation induced grain growth is found to be inherently different to thermally induced grain growth.

Weber *et al.* [123] reported results from large-scale MD simulations which study the irradiation induced defects and primary damage states in *nc*-SiC systems of different average grain sizes (5.2 - 21.5 nm). Displacement cascades are initiated by imparting 10 keV of kinetic energy to a random Si atom in a high index direction to reduce possibility of channeling by the PKA. Statistics are collected by simulating 40 cascades at each grain size and the Lindemann method is utilized to detect vacancies, interstitials, and antisite defects [124]. The local stress fields nearby the GBs are found to influence the behavior of the PKA and small grain size decreases the number of defects with PKA depositing most of its energy in the grains (Figure 5-1).

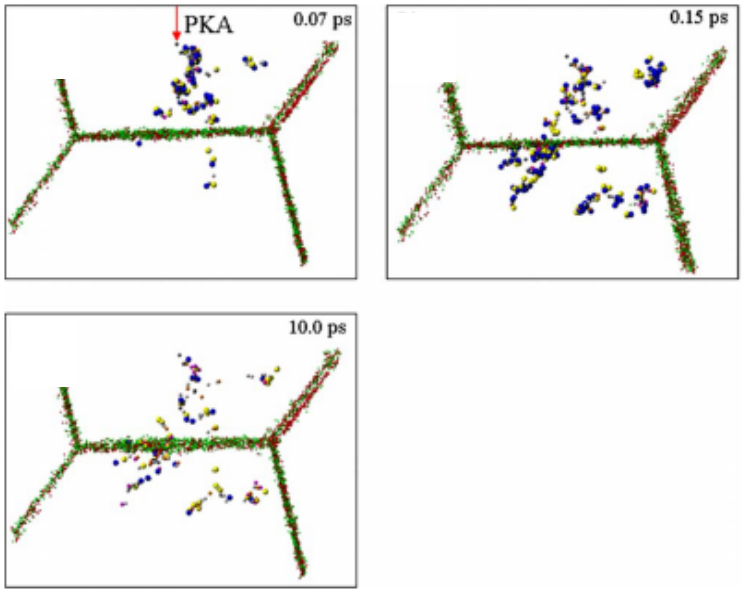

Figure 5-1: Defect evolution in *nc*-SiC [123].

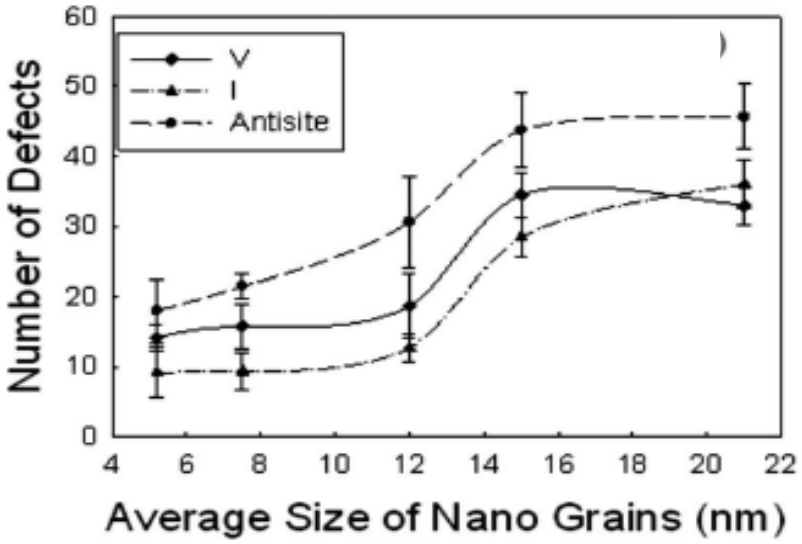

Figure 5-2: Variation of number of defects with average grain size following 10 keV displacement cascade [123].

Cu-Nb nanolayered composites are investigated by Misra *et al.* [125] both experimentally and with MD simulations using embedded atom potential (EAM). Displacement cascades are simulated with PKA energies ranging from 0.5 to 2.5 keV such that they are below the threshold energy for stoppage of ions from electronic excitations [126]. The results show that all the Frenkel-pairs generated by the cascade processes are absorbed by the Cu-Nb interface which indicates that interfaces act as sinks for radiation induced point defects (see Figure 5-3).

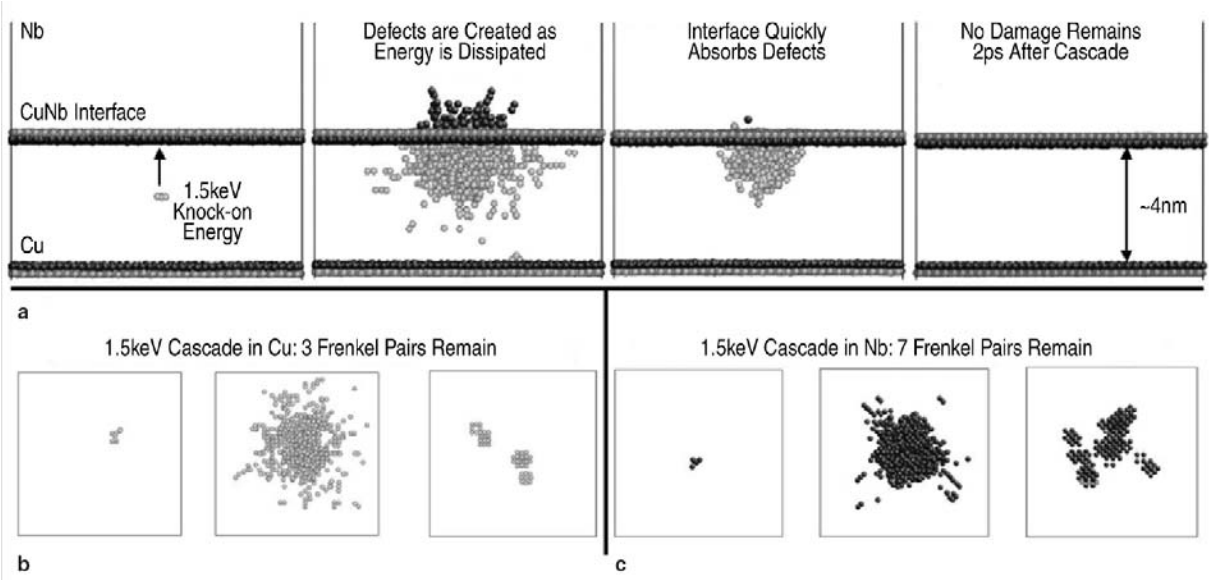

Figure 5-3: (*a*) No Frenkel-pairs remains in a Cu-Nb nanolayer after 2 ps whereas (*b*) 3 Frenkel-pairs are observed in a Cu single crystal and (*c*) 7 Frenkel-pairs are observed in a Nb single crystal at the same time [125].

The ability of the Cu-Nb interface to absorb point defects is attributed to a significant drop in the vacancy formation energy at the interface as shown in as shown in Figure 5-4.

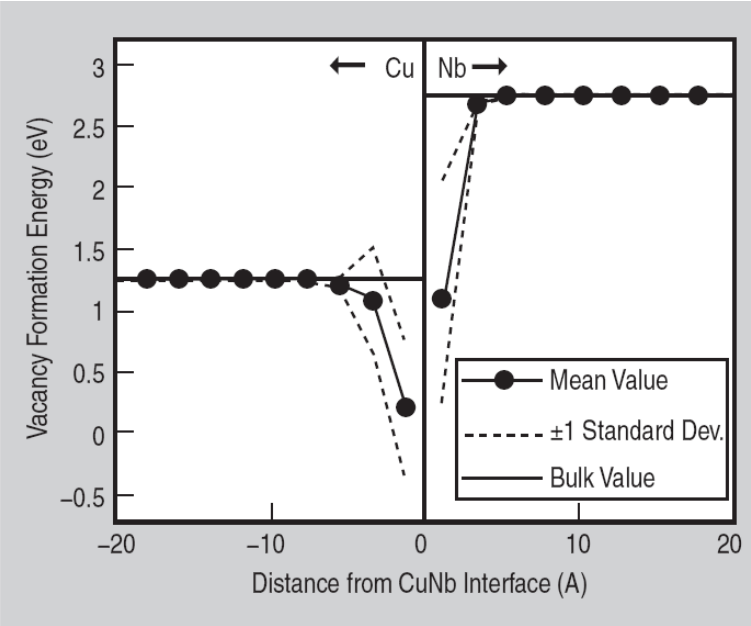

Figure 5-4: Variation of vacancy formation energy with separation distance from the interface explaining the annihilation of Frenkel-pairs at the interface [125].

The PKA energies in MD cascade simulations are typically below the threshold energies for electronic excitations [127, 128]. Energy transfer by electronic excitations becomes more noticeable in the case of radiation damage from high energy ions (called swift ions). The effect of electronic excitations in the damage processes by swift ions in Ge nanocrystals embedded in amorphous SiO_2 system is reported by Backman *et al.* [129] Ion paths are formed by the transfer of the excess electronic energy to thermal vibrations which upon freezing form a molten region. In this study, 4 *nc*-Ge crystals created in a SiO_2 system

characterized by Watanabe-Samela potential [130] that is modified to consider Ge interactions [131] are irradiated by 1.8 MeV silicon and 3.6 MeV iodine swift ions, and the damage quantified in terms of degree of amophization. The study shows that the contribution of the electronic excitation to the radiation damage cannot be neglected in the radiation damage process (see Figure 5-5) at higher energies.

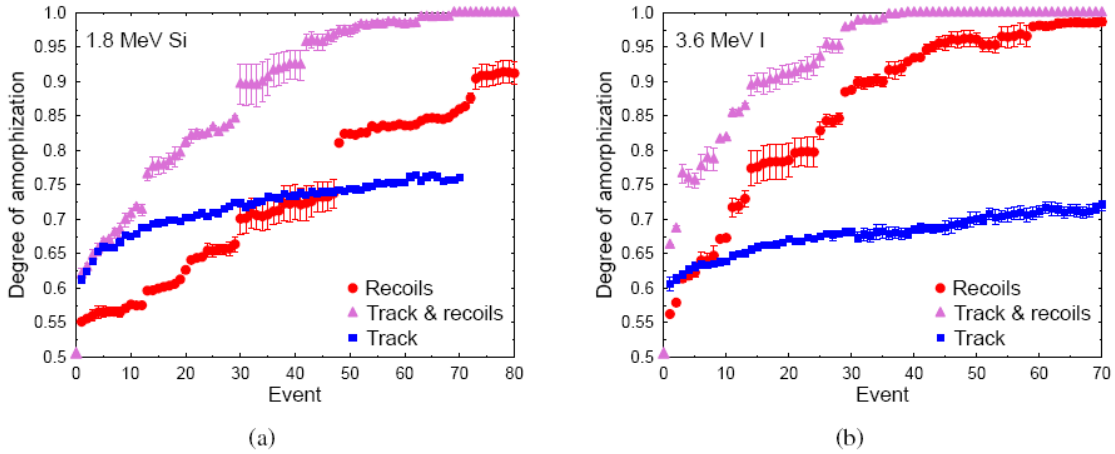

Figure 5-5: Degree of amophization caused by (*a*) 1.8 MeV Si ion and (*b*) 3.6 MeV I ion.

5.2 Molecular Dynamics Simulations: Methodology

As mentioned in Section 5.1, the experimental investigations have not revealed a potential benefit in having a large number of interfaces for promoting radiation tolerance. Nevertheless, to explore further on the idea molecular dynamics (MD) simulations are performed, with an in–house MD program [100], on bicrystal copper with twist grain

boundary configurations as well as on a single crystal system without any interfaces or defects.

5.2.1 Embedded Atom Method (EAM) potential for copper

An interatomic potential which is based on Embedded Atom Method (EAM) is chosen for simulating copper (single and bicrystal) systems. In the present study, the interactions between atoms are described by a semi-empirical EAM model developed by Mendelev [132]. With EAM potential, the total energy of the system is expressed as [133, 134]:

$$U = \sum_{i=1}^{N_m-1} \sum_{j=i+1}^{N_m} V\left(r_{ij}\right) + \sum_{i=1}^{N_m} F\left(\rho_i\right) \qquad \text{Equation 5-1}$$

where i and j refers to distinct atoms, r_{ij} the separation distance between atoms i and j, and N_m is the total number of atoms in the system. The first term in Equation (5-1), $V\left(r_{ij}\right)$ represents the pair wise contribution to the total energy, and $F\left(\rho_i\right)$ represents the energy to embed an atom in a background charge density ρ_i given by [134]:

$$\rho_i = \sum_j \psi\left(r_{ij}\right) \qquad \text{Equation 5-2}$$

where ψ represents a weighting function that quantifies the contribution from atom j. The analytical forms of the three functions $V\left(r\right)$, $F\left(\rho\right)$ and $\psi\left(r\right)$ which define the EAM potential are given below:

$$V(r)=\exp\begin{pmatrix}0.81808226148375+16.009784353249\times r\\-15.726771924462\times r^2+3.8001997136343\times r^3\end{pmatrix} \quad 1<r\le 1.9$$

$$+0.61727034877621\left(4.4274528135\text{-}r\right)^3 \quad 1.9<r\le 4.4274528135$$

$$-3.0176798528760\left(4.174260021\text{-}r\right)^3 \quad 1.9<r\le 4.174260021$$

$$+2.8363729125862\left(4.0415934975\text{-}r\right)^3 \quad 1.9<r\le 4.0415934975$$

$$\text{-}0.40972326434610\left(3.615\text{-}r\right)^3 \quad 1.9<r\le 3.615$$

$$+0.64644167838571\left(3.130681821\text{-}r\right)^3 \quad 1.9<r\le 3.130681821$$

$$+0.81340753490858\left(2.556191082\text{-}r\right)^3 \quad 1.9<r\le 2.556191082$$

$$\psi(r)=0.2075858369\left(4.4274528135\text{-}r\right)^3 \quad 0<r\le 4.4274528135$$

$$+0.3550816685\left(3.615\text{-}r\right)^3 \quad 0<r\le 3.615$$

$$F(\rho)=-\rho^{1/2}+1.5746965651016\times 10^{-5}\rho^2 \quad 0\le\rho\le\infty$$

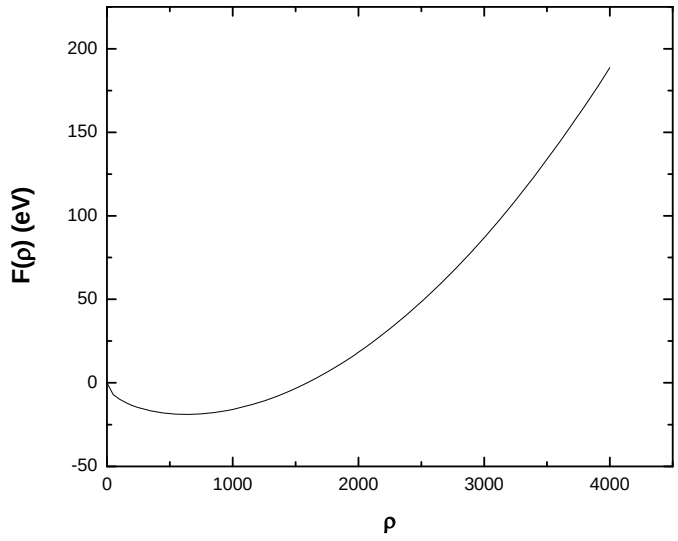

Figure 5-6: Variation of embedding energy as a function of the background charge density.

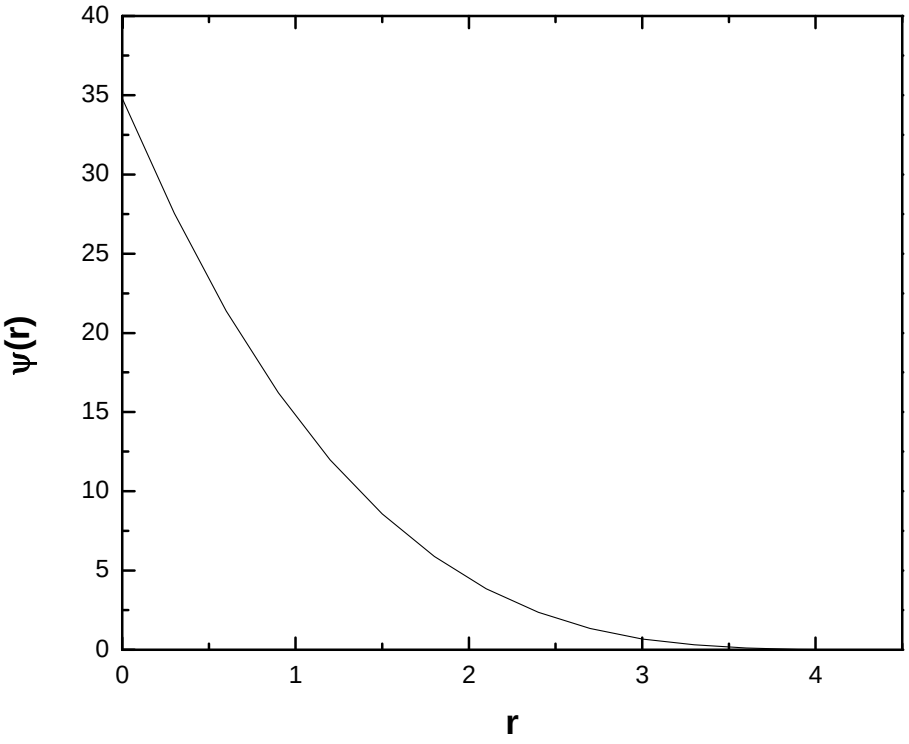

Figure 5-7: Variation of weighting function with separation distance.

The effective pair potential defined as $U^{eff}(r) \equiv U(r) + 2\left.\frac{\partial F}{\partial \rho}\right|_{\rho_o} \psi(r)$ is plotted and compared to that given by Mendelev [132] as shown in Figure 5-8.

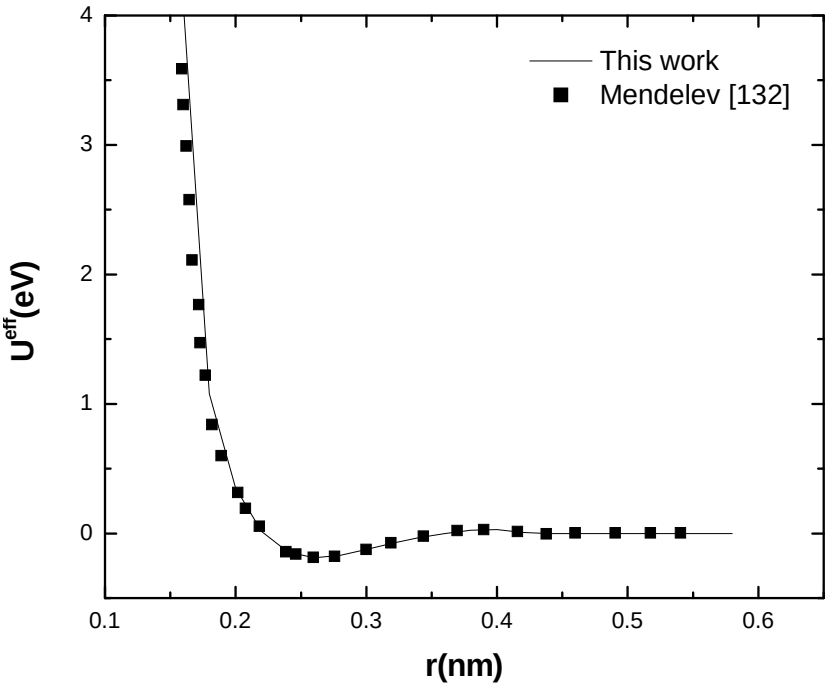

Figure 5-8: Variation of the effective pair potential with the separation distance *r*.

The EAM potential is known to describe metallic systems in the solid state very accurately [132]. However, it is imperative that the potential is accurate for the liquid state as well because local melting occurs during radiation displacement cascades. Benchmark studies therefore, have been carried out to verify the predictions of the current EAM potential for radial distribution function (RDF), melting point, viscosity, thermal expansion, diffusivity and density correlation (intermediate scattering function) in the liquid state. A few of these properties are explained in more detail in Appendix B. The results from this benchmark exercise are in very good agreement with reference data reported for copper either experimentally or *via* simulations as shown in the following graphs.

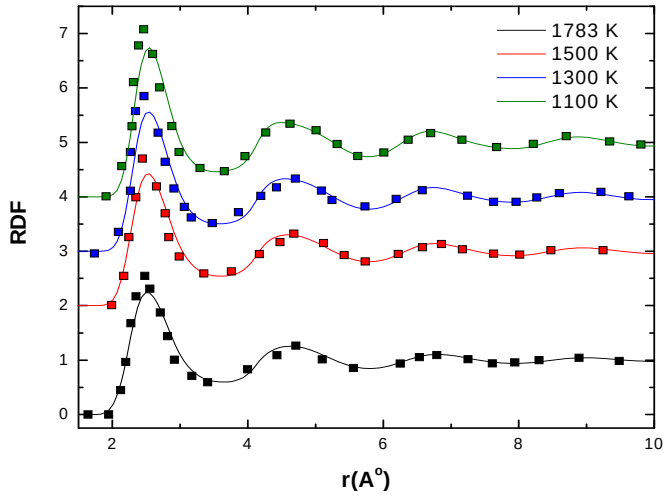

Figure 5-9: RDF of liquid copper at different temperatures with solid squares representing reference data [135].

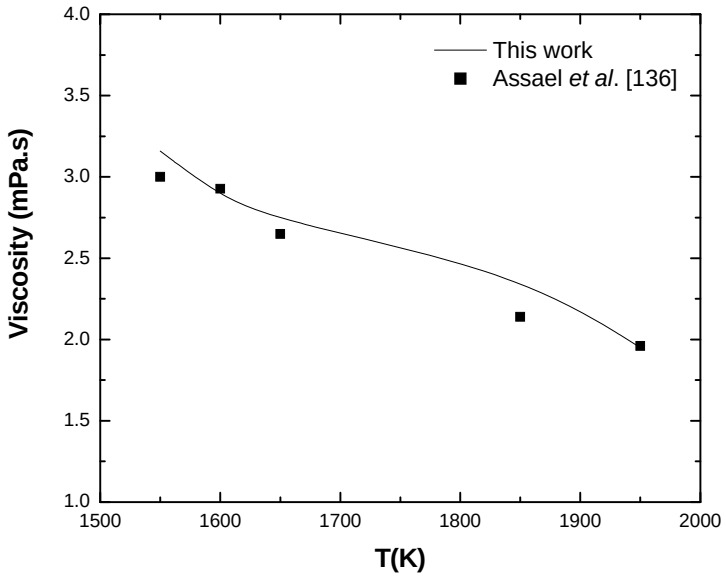

Figure 5-10: Variation of copper viscosity with temperature as calculated from the present study compared to reference experimental data (see [136]).

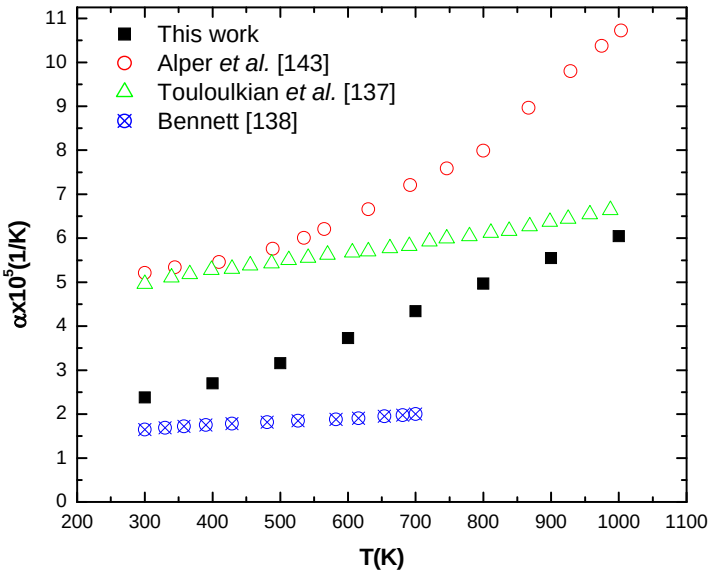

Figure 5-11: Temperature dependence of the coefficient of thermal expansion of copper from this work compared to published MD data (see [143]) and experimental reference data (see [137, 138]).

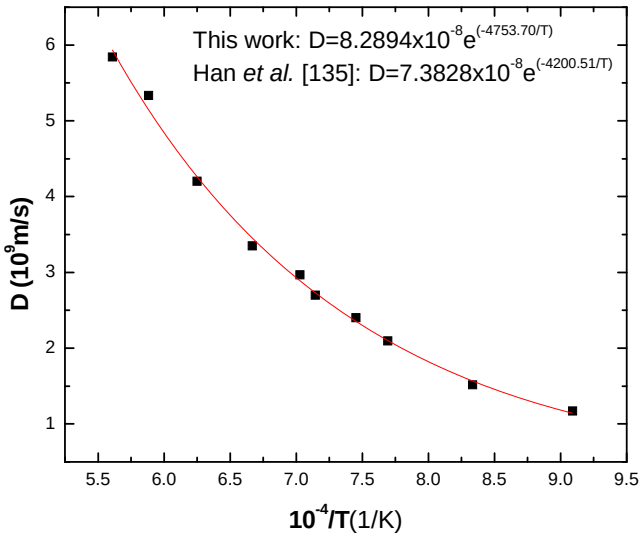

Figure 5-12: Temperature dependence of copper diffusivity from this work showing good agreement with reference data (see [135]).

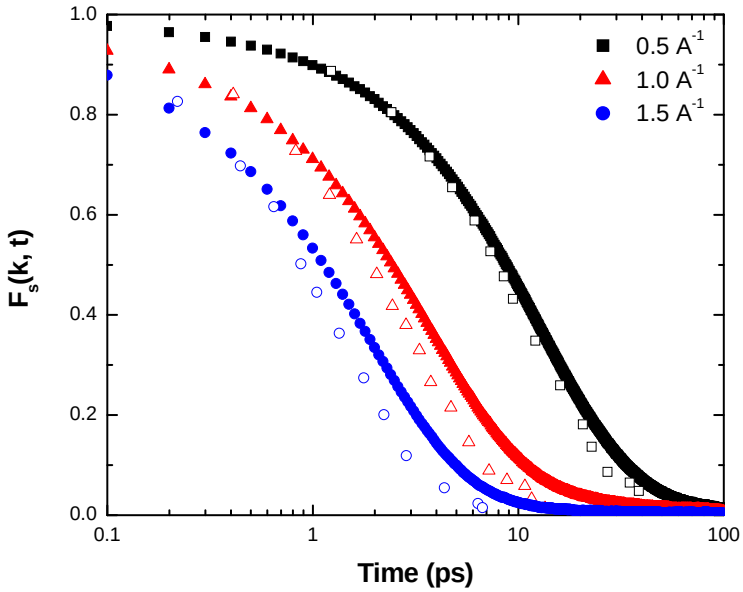

Figure 5-13: Density correlator (self) in liquid state with current MD simulations (solid) showing excellent agreement with recent quasielastic neutron scattering data (open) [139].

5.2.2 Single crystal copper

A cubic single crystal is constructed with $48 \times 48 \times 48$ unit cells with a total of 442368 atoms in [1 0 0] direction along the *x*-axis of the simulation box. The system is allowed to equilibrate for 15 ps under constant temperature (T=300K) and constant pressure (P=0). The stability of the equilibrated system is tested by monitoring the radial distribution function (RDF) [140] shown in Figure 5-14 and the Common Neighbor Analysis (CNA) index which has the value of 0 for FCC structure [141, 142] (Figure 5-15).

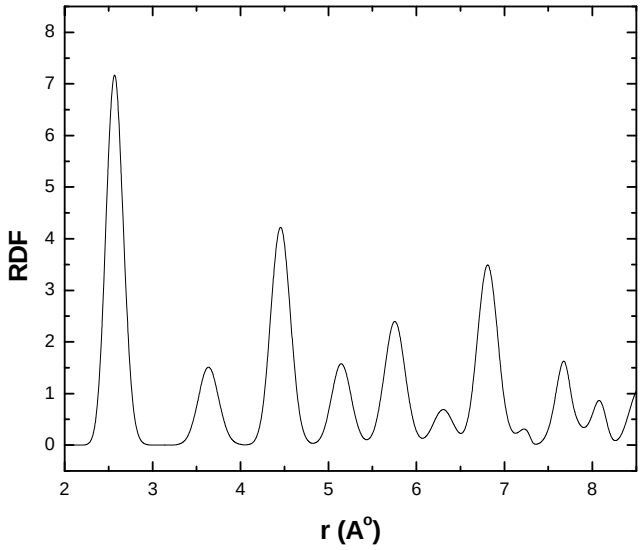

Figure 5-14: RDF of the single crystal Cu. Peak positions are in good agreement with values reported by Alper *et al.* [143].

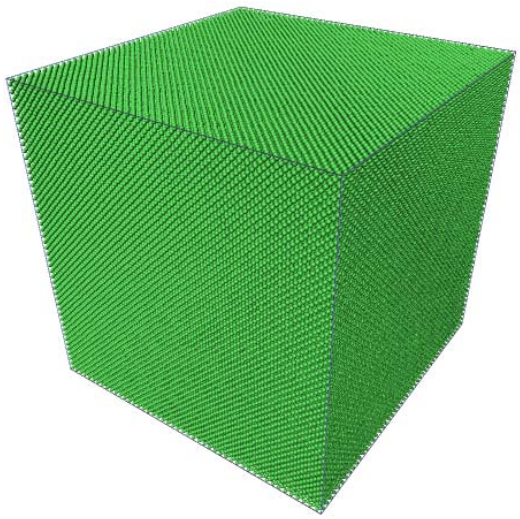

Figure 5-15: Perfect single crystal Cu with atoms having a CNA index = 0 (FCC) shown in green.

5.2.3 Construction of copper bicrystals

Two bicrystals configurations, (*a*) twist $\Sigma 5$, and (*b*) twist $\Sigma 41$, are investigated in the current study. The reciprocal density of common or coincident sites, denoted by Σ, gives the volume fraction of the coincidence unit cell to the crystal lattice unit cell. Two single crystals form the base of the bicrystal system as shown in Figure 5-16. One of the two crystals is then "twisted" relative to the other about [1 0 0] direction where the rotation angle reflects the degree of misorientation between the two crystals (the higher the rotation angle, the higher the degree of misorientation).

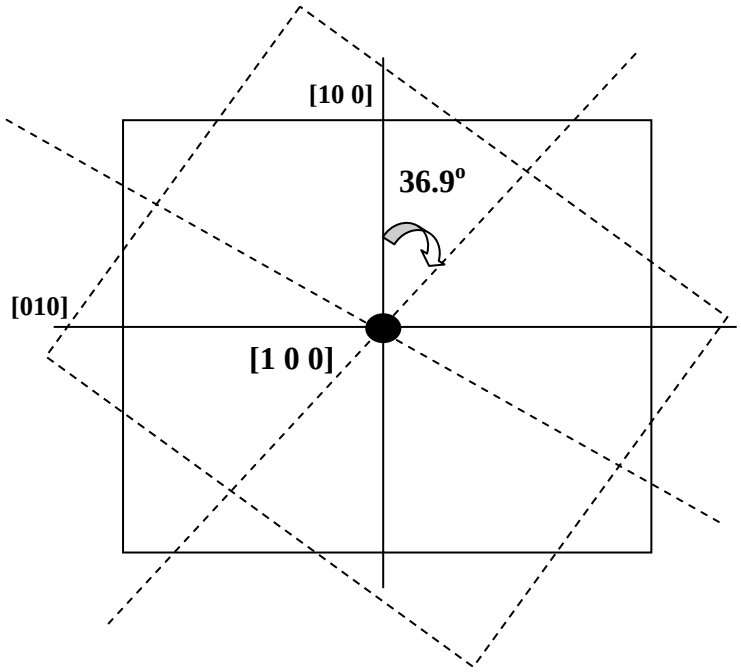

Figure 5-16: Formation of a twist $\Sigma 5$ copper bicrystal. Dotted square represents the top single crystal after 36.9^{o} rotation along [1 0 0] which is coincident with the *x*-axis of the simulation box).

As shown in Figure 5-16, the $\Sigma 5$ twist boundary is formed by a rotation angle of 36.9^{o} with respect to the [1 0 0] direction [144].

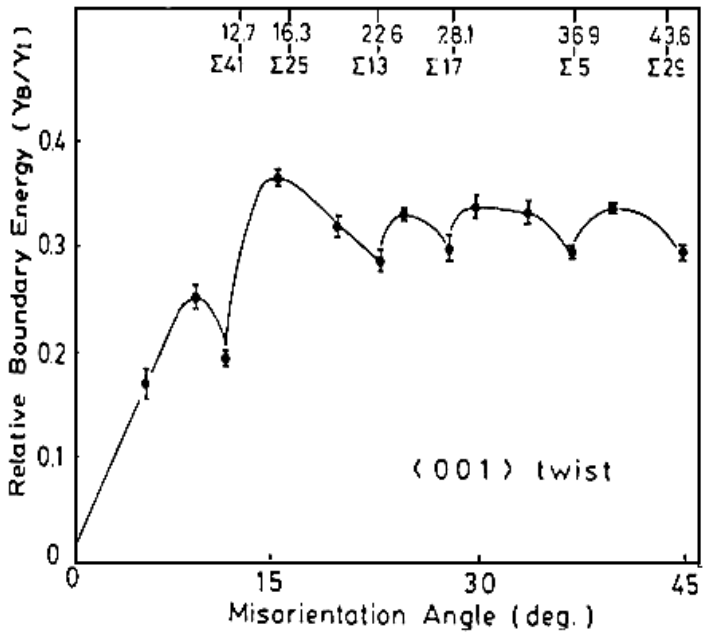

Figure 5-17: Energy and rotation angles for twist boundaries in copper [145].

As mentioned before (see Figure 5-17), the $\Sigma 5$ interface has a low energy in relation to other twist boundaries observed in copper. The open visualization tool, OVITO [146], is utilized to perform the rotation process and subsequent deletion of atoms at the edges to generate a cubic simulation box of 476418 atoms with the interface at the center (Figure 5-18).

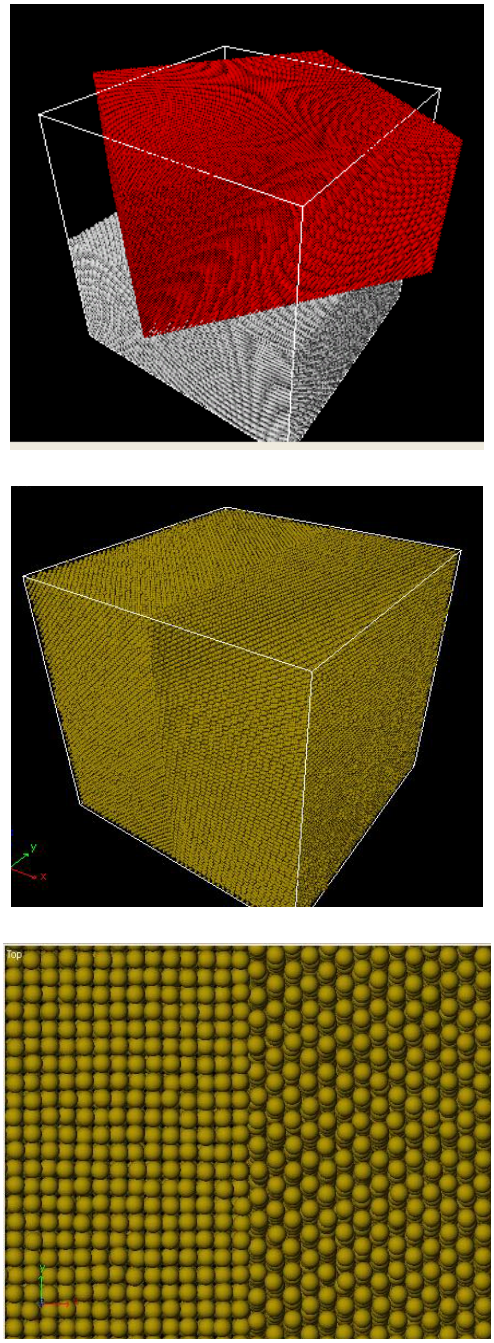

Figure 5-18: Construction of $\Sigma 5$ copper twist bicrystal using OVITO.

Similar to the case with the single crystal, the cubic simulation boxes of Σ5 and Σ41 bicrystals are allowed to equilibrate for more than 20 ps under constant temperature (T=300 K) and pressure (P=0) conditions until a stable equilibrium state is achieved. CNA analysis presented in Figure 5-19 shows a perfect FCC structure on both sides of the interface while the interface region shows an undefined CNA index attributed to the disordered nature of interface.

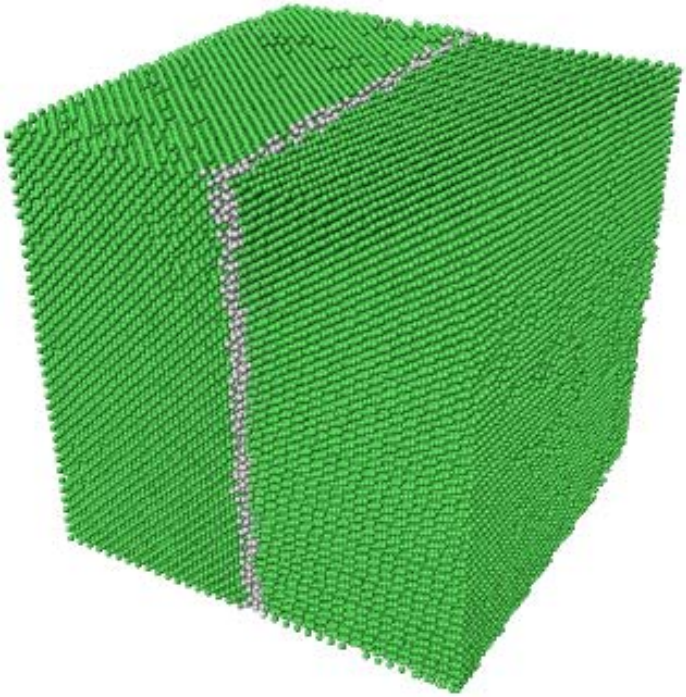

Figure 5-19: CNA analysis of Σ5 copper bicrystal showing an undefined CNA index for the interfacial atoms, and a CNA index of 0 for the FCC atoms (shown in green).

The structure of the bicrystal is also evaluated by monitoring the radial distribution function which is shown in Figure 5-20 along with that of the perfect single crystal. RDF of single and bicrystal copper configurations are almost the same which implies that the system RDF is not sensitive enough to reveal the disordered interfacial structure.

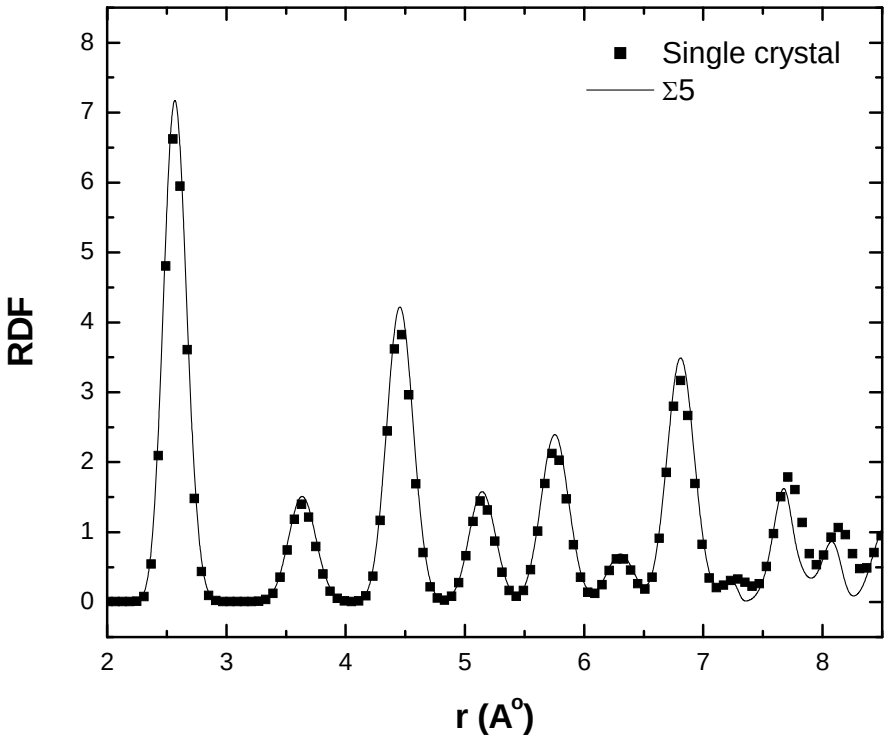

Figure 5-20: RDF of equilibrated copper perfect single crystal and Σ5 bicrystal.

5.3 Radiation Cascade Simulations: Analysis, Results, and Discussions

In the present study, radiation damage is simulated by imparting additional kinetic energy to primary knock-on atoms at the geometrical center of the simulation box with momentum directed along the positive x-axis of the simulation box. Upon initiation of the damage event, the atomic displacement of atoms is monitored within a sub-volume (inner box) of the simulation box as illustrated in Figure 5-21 and Figure 5-22.

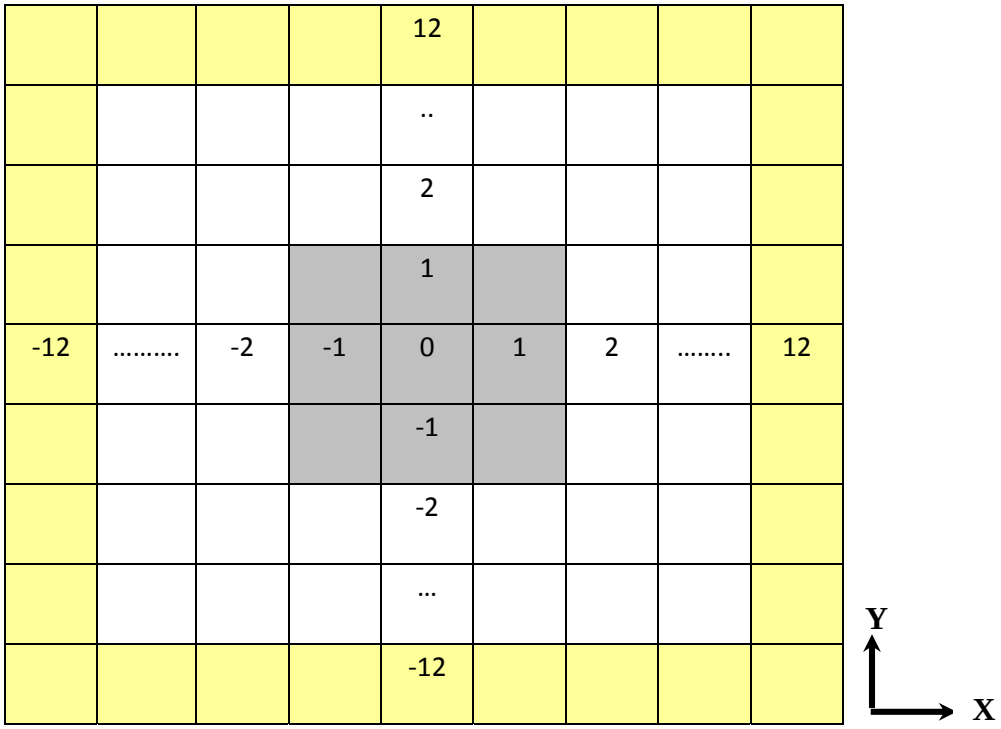

Figure 5-21: A 2-D illustration of the cubic simulation box with sub-volume or inner box (shown in grey) for analysis of atomic displacements. Outer boundaries of the system are shown in yellow.

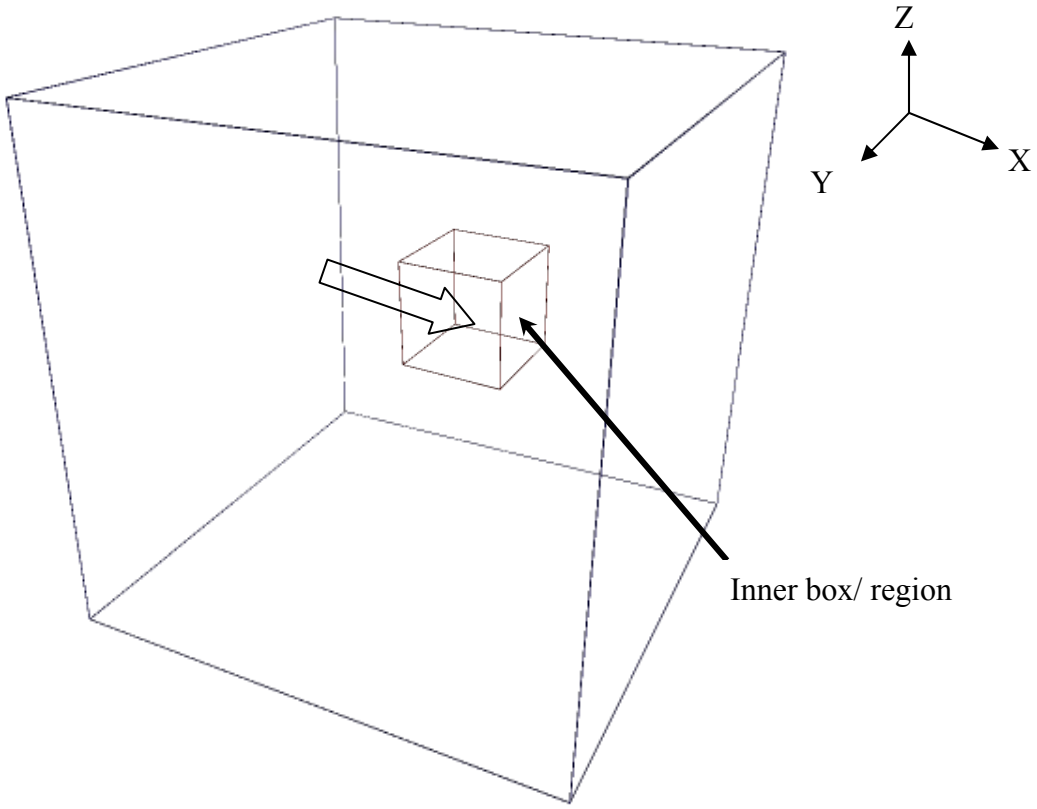

Figure 5-22: A 3-D representation of the cubic simulation box showing the inner box/ region with an arrow indicating the position and direction of impact.

5.3.1 Local density and structure with RDF and CNA

The radial distribution function (RDF) defined as $g(\mathbf{r}) = \frac{2V}{N_m^2}\left\langle \sum_{i<j} \delta\left(\mathbf{r} - \mathbf{r}_{ij}\right) \right\rangle$, where V is the volume of sub-system, N_m is the total number of atoms in the system and r_{ij} is the separation distance between pairs of atoms, describes the average local organization or structure around any atom in the sub-system [14] and thus monitoring the behavior of this

function can provide an insight on the evolution of the system following the damage event. The RDF of both single and Σ5 bicrystal systems (from the positions of the atoms at the inner box/region) are shown in Figure 5-23 at different times after 7 keV of energy is imparted to the systems. The flattening of the RDF with smaller peak amplitudes is a signature of transformation to a liquid or an amorphized state [123]. This implies that local melting or phase change has taken place in the vicinity of the knock/ impact position.

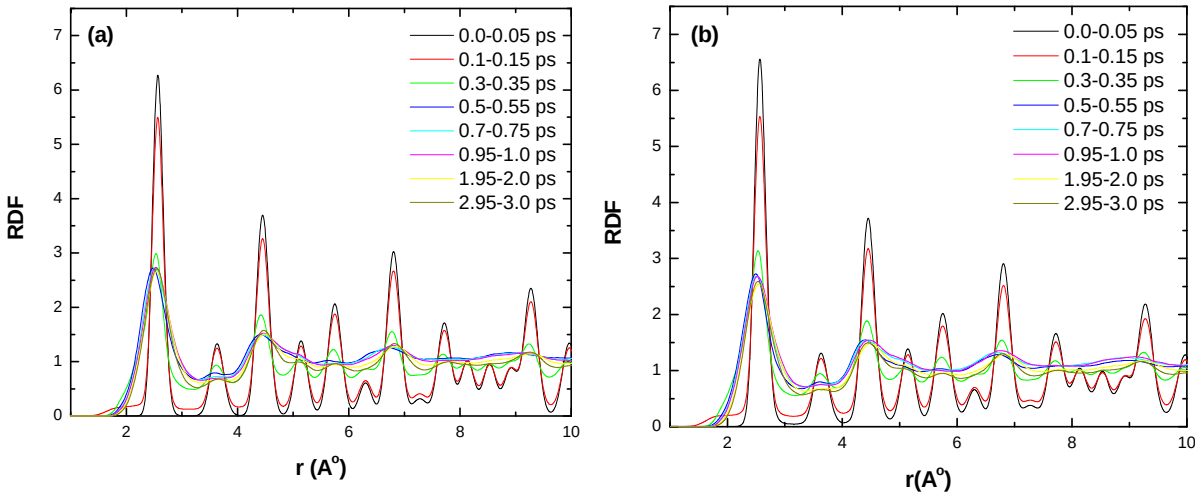

Figure 5-23: RDF of (a) Cu single crystal and (b) Cu Σ5 bicrystal for 7 keV knock energy.

It can be observed that the RDF evolutions in single and bi-crystals are very nearly the same. Because of this similarly, it is concluded that the RDF, which describes the local structure of the inner box, is unable to resolve any differences in the radiation behavior of the two systems under consideration. Next, Common Neighbor Analysis (CNA) is performed to investigate the structural evolution of the single crystal and the Σ5 bicrystal following a 7 keV knock. The results are shown in Figure 5-24.

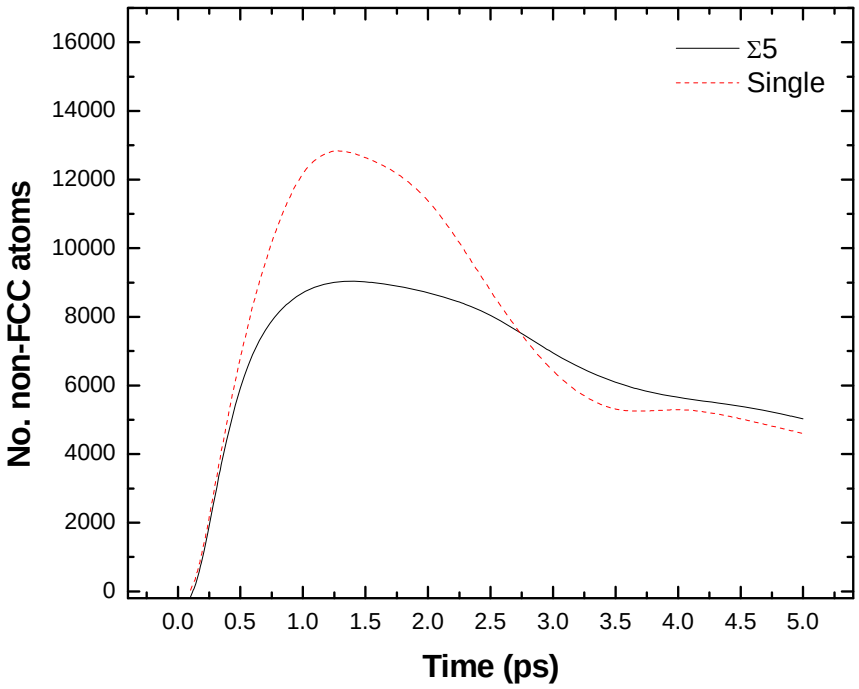

Figure 5-24: Variation of the number of atoms with non-FCC CNA index for 7 keV knock energy.

It can be seen that more atoms have lost their FCC CNA index in the Cu single crystals compared to those from the Σ5 bicrystal approximately 1 ps after the knock. This can be interpreted as for the same knock energy, more damage is caused in the single crystal system. The capability of CNA analysis to resolve such a difference can be elaborated by considering the original CNA method where a pair of atoms are considered nearest neighbor if the separation distance between them is less than or equal to a cutoff radius usually taken as the first minimum in the RDF function [147] which implies that CNA analysis has a better ability to resolve the microstructure evolution when compared to the radial distribution function. In this sense, CNA analysis represents a reliable tool to evaluate the damage level

in a system. However, CNA analysis does not provide any insight on the dynamics of the system or on the nature of the mechanisms of atomic displacements.

5.3.2 Dynamical propensity using iso-configurational ensemble

It is extremely valuable to understand the motion of individual atoms following a radiation knock. For any given atom, it can have a range of initial momenta which means that the motion of an atom can only be described as a statistical measure. The concept of an iso-configuration (IC) ensemble is proposed here which will facilitate such a statistical analysis. In an IC ensemble, statistical averaging is performed over many, usually $O(100)$, initial momentum conditions for the same initial atomic configuration – thus the behavior or the property of interest of each atom can be being tracked individually [148]. This work represents the first instance of utilizing the concept of IC ensemble in the context of radiation behavior of materials even though the idea has been used in the past for the investigations on supercooled liquids and glass formers. In the present study, the migration/transport of individual atoms following a knock is analyzed by monitoring two atomistic quantities based on IC averaging, namely, dynamical propensity and directional displacement. Dynamical propensity is the IC average of the square of the displacement of each atom which can be expressed as [149]:

$$\left\langle r_i^2(t)\right\rangle_{IC} = \frac{1}{M}\sum_{k=1}^{M} r_i^2(k,t) \qquad \text{Equation 5-3}$$

where $r_i^2(k,t)$ is the squared displacement of the i^{th} atom at time t in the k^{th} run (copy) of the IC ensemble, with M representing the total number of independent runs (copies) of the IC ensemble.

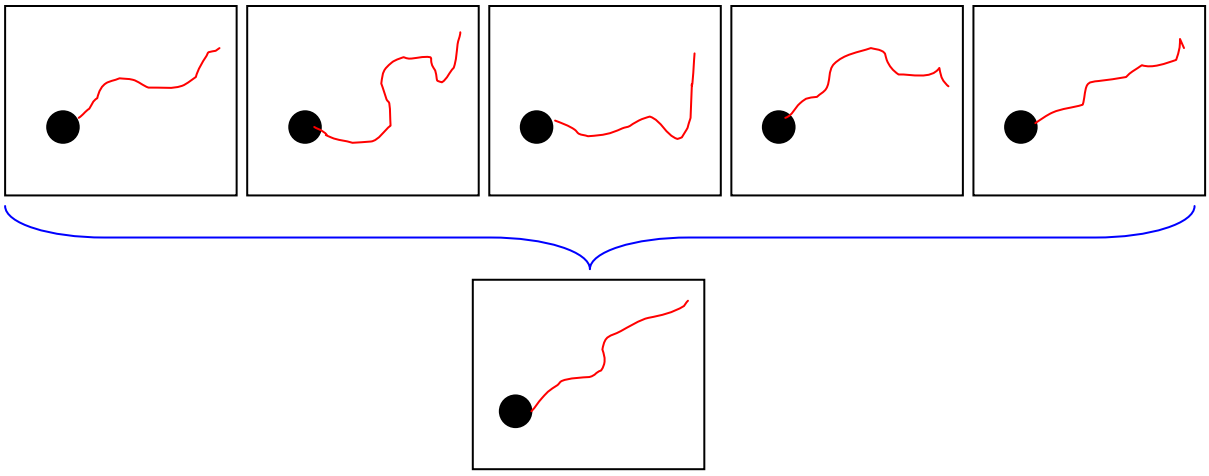

Figure 5-25: Illustration of the concept of iso-configurational (IC) ensemble average. The trajectory of each atom, which has the same initial position in all copies of the IC ensemble, is followed individually, and the trajectories (as well as the properties that are based on the trajectories) are averaged over different initial momenta.

Based on the above definition, it can be noticed that the dynamical propensity is similar to the mean square displacement average, however, on a per-atom basis. Dynamical propensity can be thought as an indicator of atom mobility and when coupled with directional displacement averages, give information on the most probable migration behavior of atoms in radiation cascade simulations.

The following are snap shots showing the spatial variation of dynamical propensity at different times with a knock energy of 7 keV in a single crystal system and a Σ5 bicrystal system, where in both cases the knock energy is imparted 0.7 nm in the positive *x*-direction behind the geometrical center of the cubic simulation box also corresponding to the center of sub-box labeled (-1) in Figure 5-21. The knock energy in this case is identified as 7 keV, at (-1 0 0) as the knock position, and in the positive *x*-direction. For visualization purposes, the values of propensity are evaluated and sorted in a descending order, and each atom is assigned an integer, N_i, referring to its rank. Atoms are then plotted as spheres where the top 50% atoms are assigned red color (indicating higher mobility) with atom radius calculated as: $R_i = R_{\min}.\exp\left\{\left(\frac{N_i - N_m/2}{1-N_m/2}\right)\ln\left(\frac{R_{\max}}{R_{\min}}\right)\right\}$ and the bottom 50% atoms are assigned blue color (indicating higher immobility) with atom radius calculated as: $R_i = R_{\min}.\exp\left\{\left(\frac{N_m/2+1-N_i}{1-N_m/2}\right)\ln\left(\frac{R_{\max}}{R_{\min}}\right)\right\}$ where R_{max} and R_{min} take the arbitrary values of 0.5 and 0.01, respectively [148].

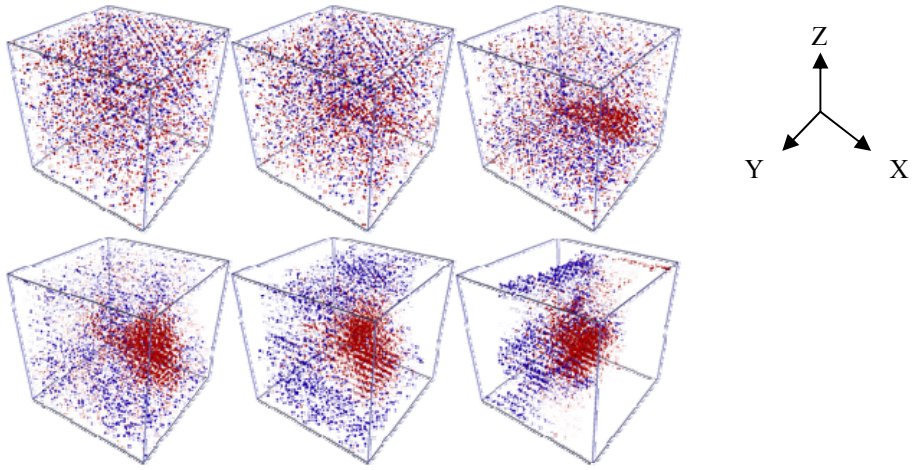

Figure 5-26: Relative dynamical propensity in single crystal Cu for 7 keV knock energy at 0.01, 0.05, 0.1, 0.2, 0.4, and 0.8 ps (left-to-right, top-to-bottom). Red and blue atoms denote the most mobile and most immobile atoms, respectively.

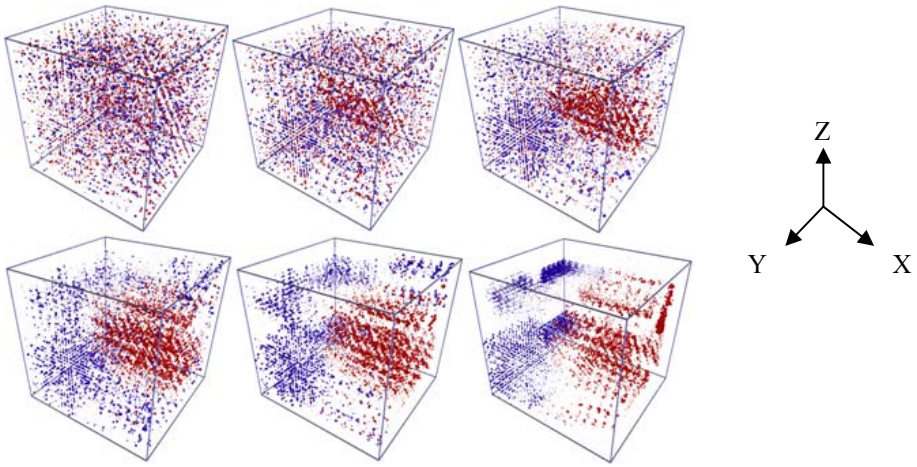

Figure 5-27: Relative dynamical propensity in Σ5 Cu bicrystal for 7 keV knock energy at 0.01, 0.05, 0.1, 0.2, 0.4, and 0.8 ps (left-to-right, top-to-bottom). Red and blue atoms denote the most mobile and most immobile atoms respectively.

The evolution of dynamical propensity in a single crystal and Σ5 bicrystal does not show major differences at early times following the knock (till 0.1 ps), see Figure 5-26 and Figure 5-27, after which, a closer scrutiny will indicate a deviation between the two systems. In the single crystal system, atoms ahead of the knock position are observed to be the most mobile atoms in the system after which, those atoms surrounding the knock position, downstream and upstream of the knock position, are persistently showing up as the most mobile atoms. On the other hand, atoms ahead of the knock position in the Σ5 bicrystal represent the most mobile atoms in the system at all times. Since the knock energy is imparted very close to the interface position, this suggests that the impact energy is transferred more across the interface; in some sense, the interface acts as a 'filter' for atom mobility.

Dynamical propensity of the two systems can be examined more quantitatively by constructing the probability density function (PDF) of atoms' propensity corresponding to the snap shots shown before. Figure 5-28 shows PDF of the propensity averaged over IC ensemble for the single crystal and Figure 5-29 shows the same for the Σ5 bicrystal following a 7 keV knock. The trends of the PDFs of both systems are quite similar except that a peak is observed at 0.8 ps in the single crystal (see arrow in Figure 5-28) which is completely absent for the Σ5 bicrystal. This peak indicates that more atoms are mobile at this time in the case of single crystal compared to the Σ5 bicrystal, or in other words, atoms are displaced more in the single crystal system.

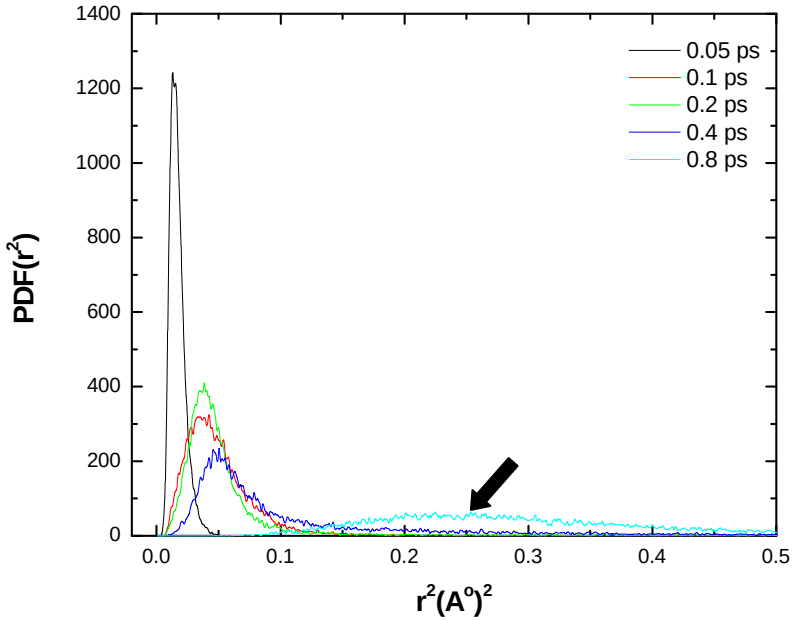

Figure 5-28: The PDF of dynamical propensity for single crystal copper with 7 keV knock energy.

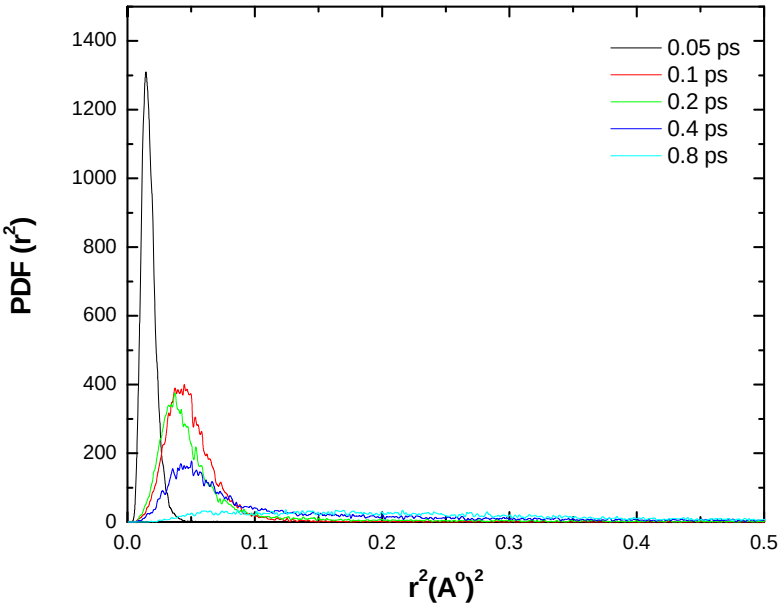

Figure 5-29: The PDF of dynamical propensity for Σ5 bicrystal copper with 7 keV knock energy.

5.3.3 Directional atomic displacement

Although the influence of the interface on the atomic mobility is revealed through the investigation of the dynamical propensity, the actual mechanism underlying the effect of interface on hampering the motion of atoms following the knock event is not clear yet. To investigate further, directional displacements of the atoms are individually averaged over an IC ensemble and the corresponding probability density functions of the three components of displacements are constructed for 7 keV knock energy imparted at (-1 0 0) along positive *x*-direction are shown in Figure 5-30.

The probability density functions of single crystal copper following 7 keV impact energy indicate that the atomic displacements are occurring uniformly in the system along X, Y and Z axes, at early times. Interestingly, the PDF for Y displacement and PDF for Z displacement show a bi-modal distribution which is completely absent in the PDF for X displacement. The symmetry of atomic displacements can be attributed to the homogeneity of the system which is a key characteristic of a perfect single crystal.

The corresponding PDFs of atoms displacements for Σ5 bicrystal copper are shown in Figure 5-31. Atomic displacements in Y and Z direction are very similar to those of the single crystal whereas a major difference is observed is in the displacement PDF along the X-direction. From Figure 5-31 (a), the PDF of atom displacements in X-direction shows a significant shift towards the negative X-direction after 0.5 ps which implies that atoms are preferentially displaced in the negative X-direction, which is towards the interface and opposite to the knock direction.

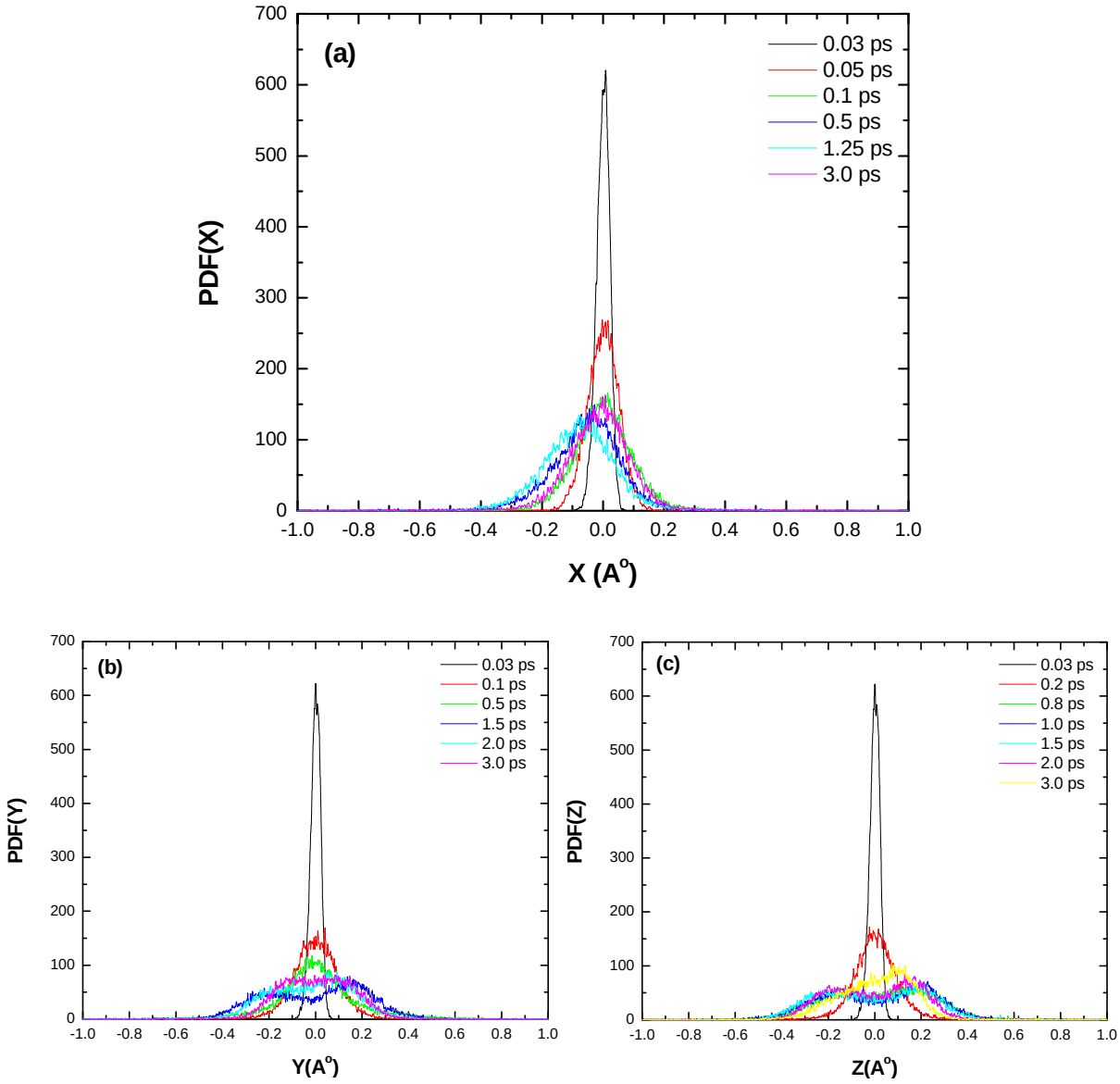

Figure 5-30: PDF of displacement components (*a*) X, (*b*) Y, and (*c*) Z at different times for 7 keV knock energy in single crystal copper.

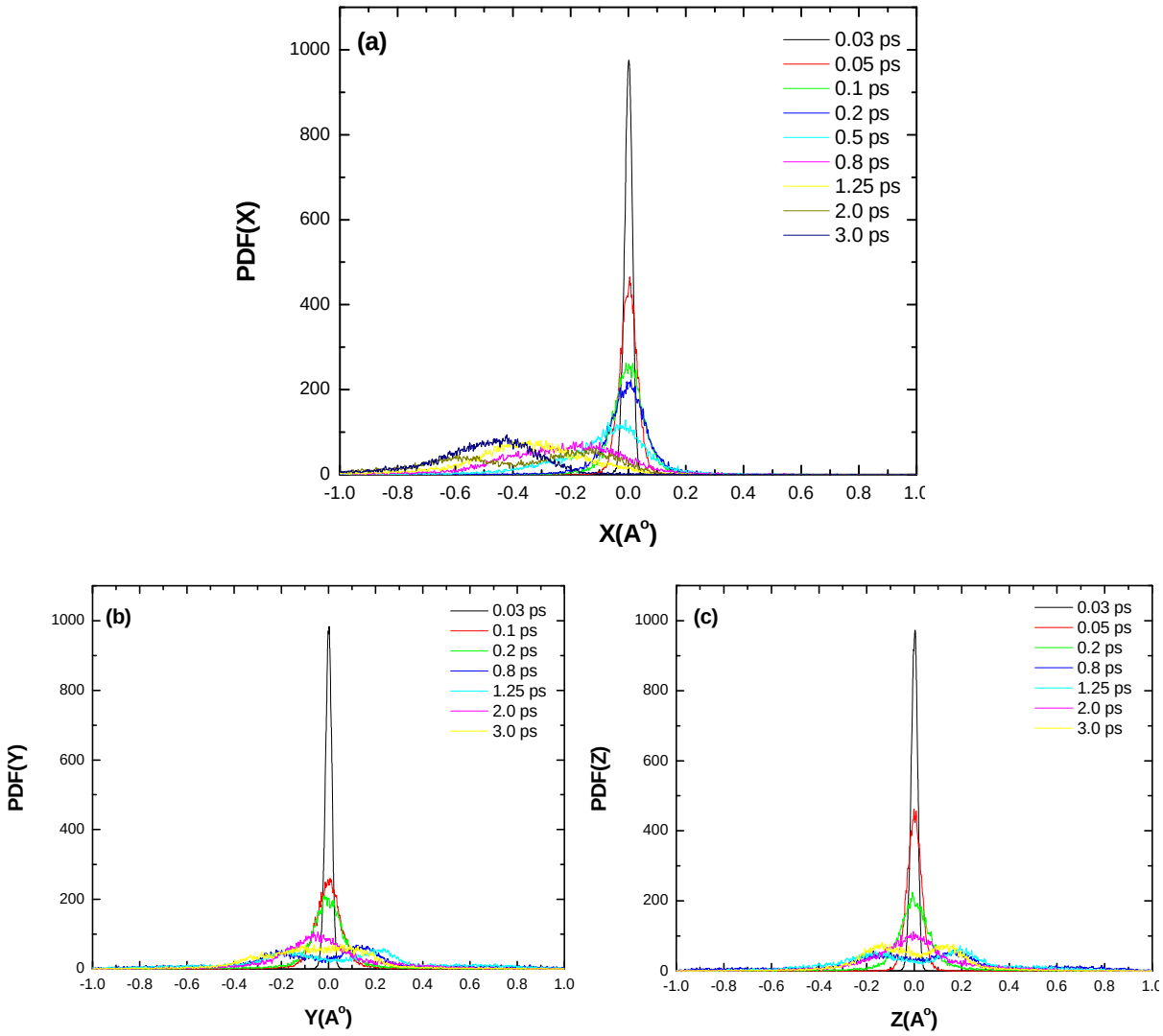

Figure 5-31: PDF of displacement components (*a*) X, (*b*) Y, and (*c*) Z at different times for7 keV knock energy in Σ5 bicrystal copper.

This observation, which is quite surprising, is more apparent when the PDFs of X displacements for both single crystal and Σ5 bicrystal are plotted side by side at different times as shown in Figure 5-32.

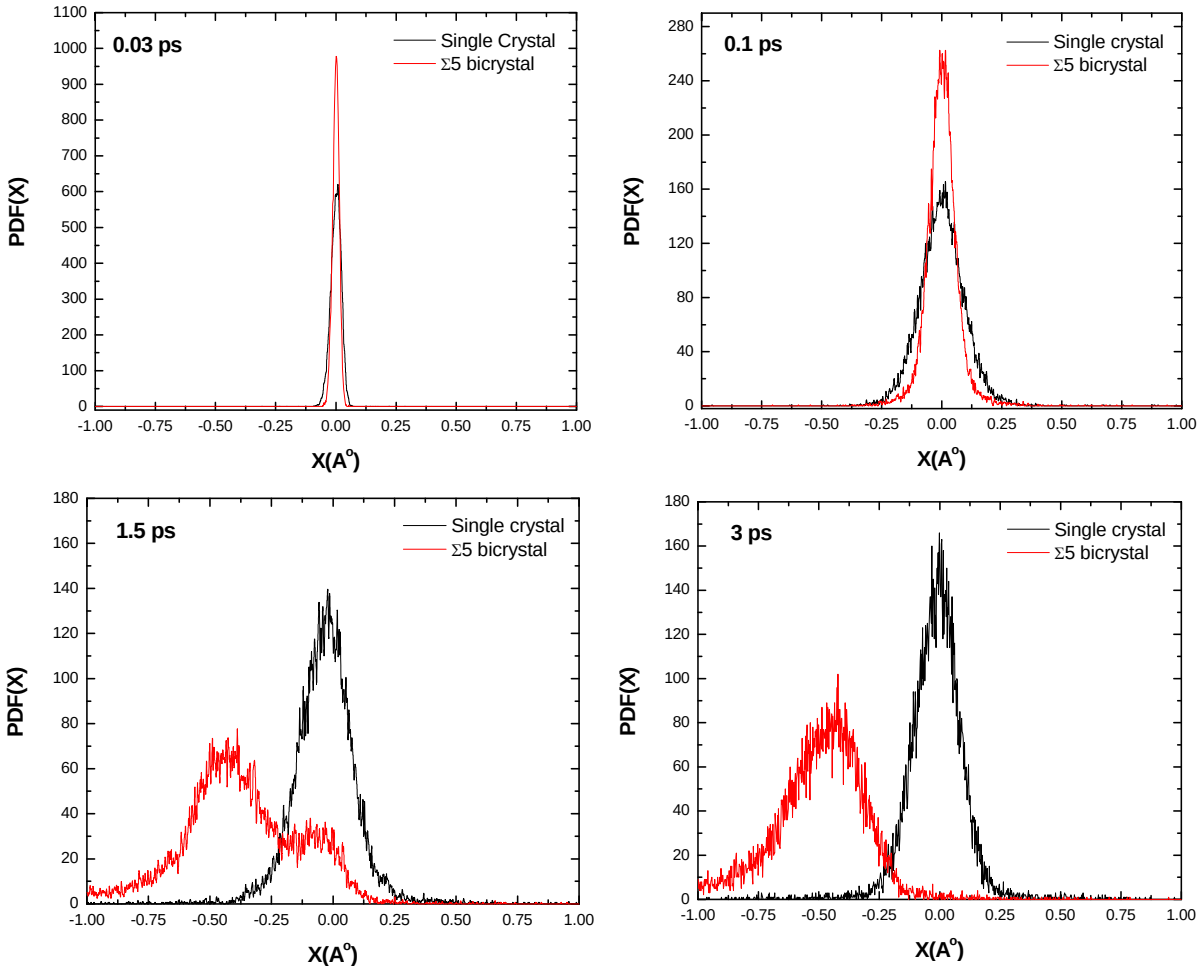

Figure 5-32: Probability density functions (PDFs) of the X-component of the atomic displacements in a single crystal and a Σ5 bicrystal copper for7 keV knock energy. Peak shifts in Σ5 bicrystal indicates atomic displacements in the negative X-direction, opposite to the knock direction and towards the interface. This observation shows that the interface acts as an attractive sink even at hyperfast timescales.

Coupled with the earlier observation that those atoms ahead of the interface are the most mobile atoms in the system, it can be concluded that interface is attracting the most mobile atoms on the far side of interface. Thus interface acts as an attractive sink even at hyperfast timescales, which is quite a remarkable observation. Thus with MD simulation it is shown that stable interfaces have the potential to attract disordered atoms and reduce the number of defects at longer timescales.

5.3.4 Influence of knock position and knock energy

A parametric study is performed to investigate the effect of knock position and knock energy on the tendency of atoms to drift towards the interface in a Σ5 bicrystal copper system. The effect of knock position is investigated by comparing the PDF(X) for two knock positions cases – position (0 0 0) at the center point of the interface and position (-3 0 0) which is equivalent to 2.1 nm behind the interface. The corresponding PDFs are shown in Figure 5-33.

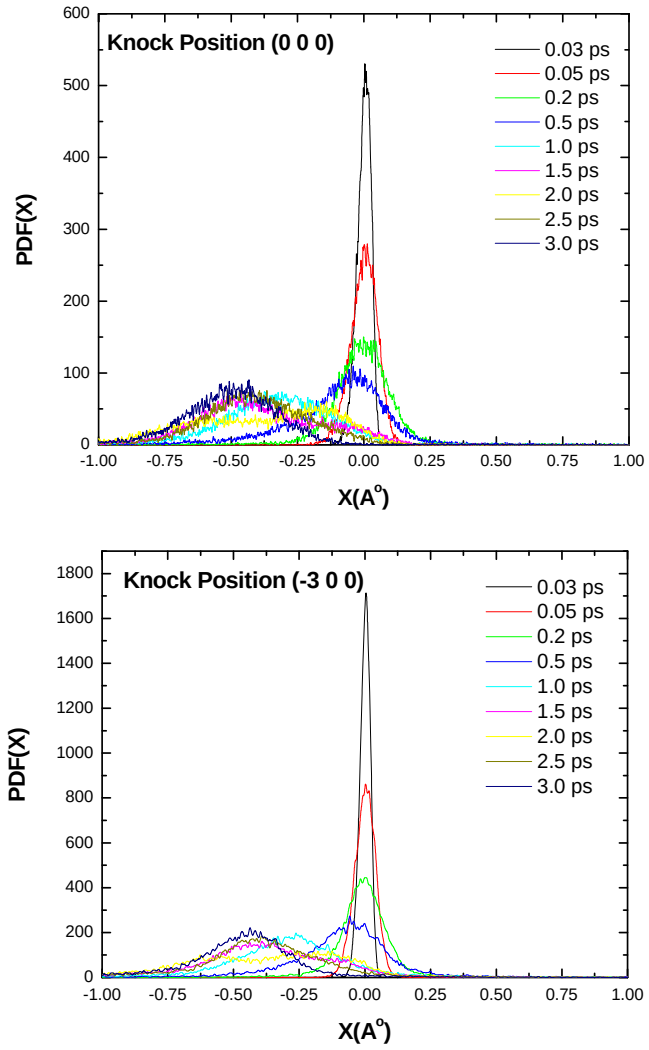

Figure 5-33: PDF of the X-components of the atomic displacements in Σ5 bicrystal copper for different knock positions with7 keV knock energy.

Regardless of the position at which the impact energy is introduced in the system, the tendency of the atoms to be displaced towards the interface is consistently visible as shown in Figure 5-33. Since the knock positions are close enough to the interface for both the cases

it is plausible that the impact energy is transferred across the interface to the atoms ahead of the interface.

Similarly, the effect of knock energy is investigated by imparting different knock energies and observing the atomic displacements in each case (Figure 5-34).

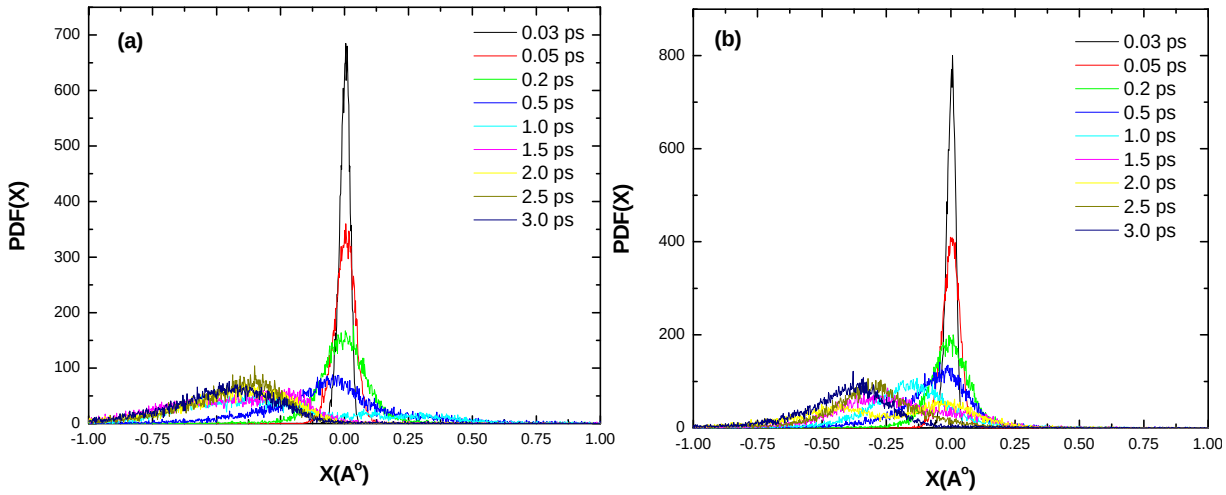

Figure 5-34: PDF(X) for impact energy of (*a*) 3 keV and (*b*) 10 keV imparted at the center of the simulation box of Σ5 bicrystal copper in the X-direction.

With impact energies of 3 and 10 keV, the attraction of displaced atoms toward the interface is visible as before. This implies that migration of atoms following radiation impact is independent of the amount of knock energy assuming that the knock energy is high enough to create and trigger a displacement cascade in the system.

5.3.5 Effect of interface structure

The observed tendency of displaced atoms to migrate along the negative X-direction is confirmed to be independent of the different characteristics of the impact energy. It is of interest to investigate the effect of the interface structure itself on the mobility of the atoms. For this purpose, a Σ41 twist bicrystal copper is simulated following a 7 keV impact. The Σ41 bicrystal is created in a similar way as it is done for a Σ5 bicrystal (Section 5.2.3) with the exception that the rotation angle between the two crystals is 12.7^{o} (see Figure 5-17) compared to 36.9^{o} in the case of Σ5 bicrystal.

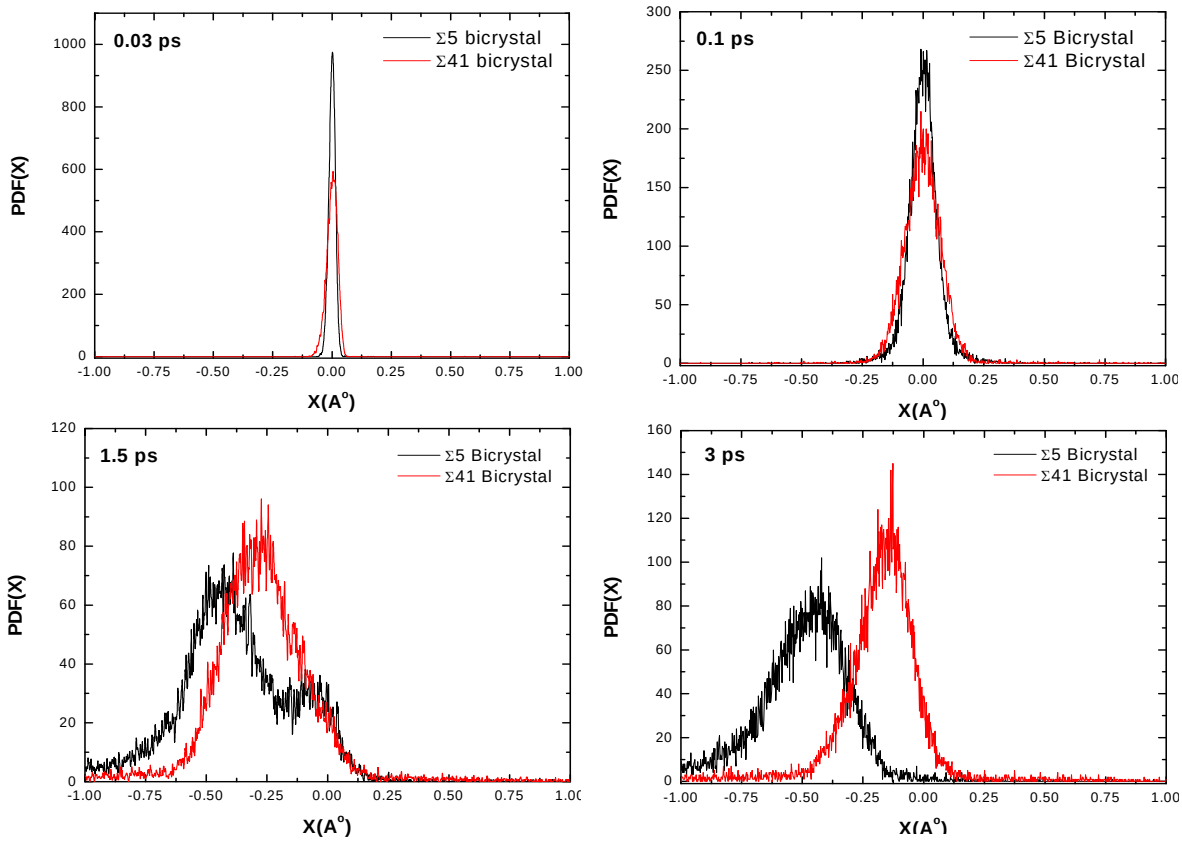

Figure 5-35: PDF(X) of Σ41 and Σ5 twist bicrystal copper for 7 keV impact energy.

The X-component of atomic displacements in Σ41 bicrystal shows a similar behavior compared to that of Σ5 bicrystal. Although tendency of atoms to be displaced along the negative X-direction and against the direction of impact energy is observed in both systems, it is more conspicuous in Σ5 bicrystal where the peak of PDF (X) is shifted from zero to about 0.5 A^o at 3 ps whereas the peak of the PDF (X) shifts only by 0.12 A^o in the case of Σ41 bicrystal for the same impact energy. The relative difference in system evolution following radiation impact between Σ5 and Σ41 twist bicrystal copper can only be attributed to the difference in the rotation angle. The higher rotation angle in Σ5 bicrystal (36.9^o) compared to a smaller angle (12.7^o) in Σ41 implies a higher degree of disorder for the Σ5 bicrystal. Thus interface structure has a dominant influence on the migration of the displaced atoms.

5.4 Stress Differential Mechanism for Atom Migration

The migration or transport of atoms in any system is associated with a driving force. In a system with single species of atoms, such as in the present study, influence of chemical potential is excluded as a driving force. Instead, the migration should depend on another mechanism, possibly from the internal (normal) stresses that are developed at the interface during a cascade simulation. The disordered nature of the interface implies a region of higher potential energy. Therefore, the possibility of having atom migration through a local stress differential is a distinct possibility.

5.4.1 Stress field mapping

In order to elucidate the driving force of atom migration toward the interface, the normal stress field on the XY-plane (containing the knock position) of the inner region/ box is mapped for Σ5 bicrystal as well as for the single crystal for comparison purposes.

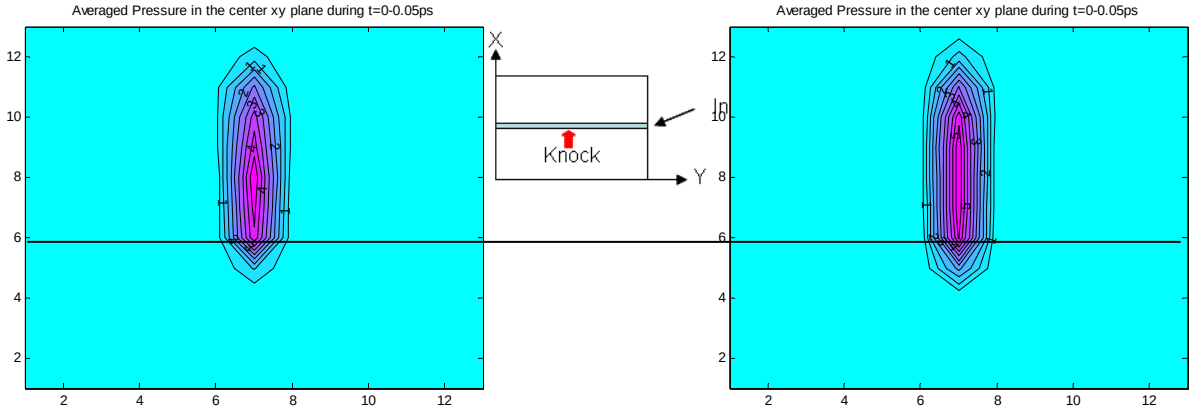

Figure 5-36: Average (normal) stress field in the XY-plane in Σ5 bicrystal (left) and single crystal (right) at 0.05 ps for 7 keV impact energy in the X-direction.

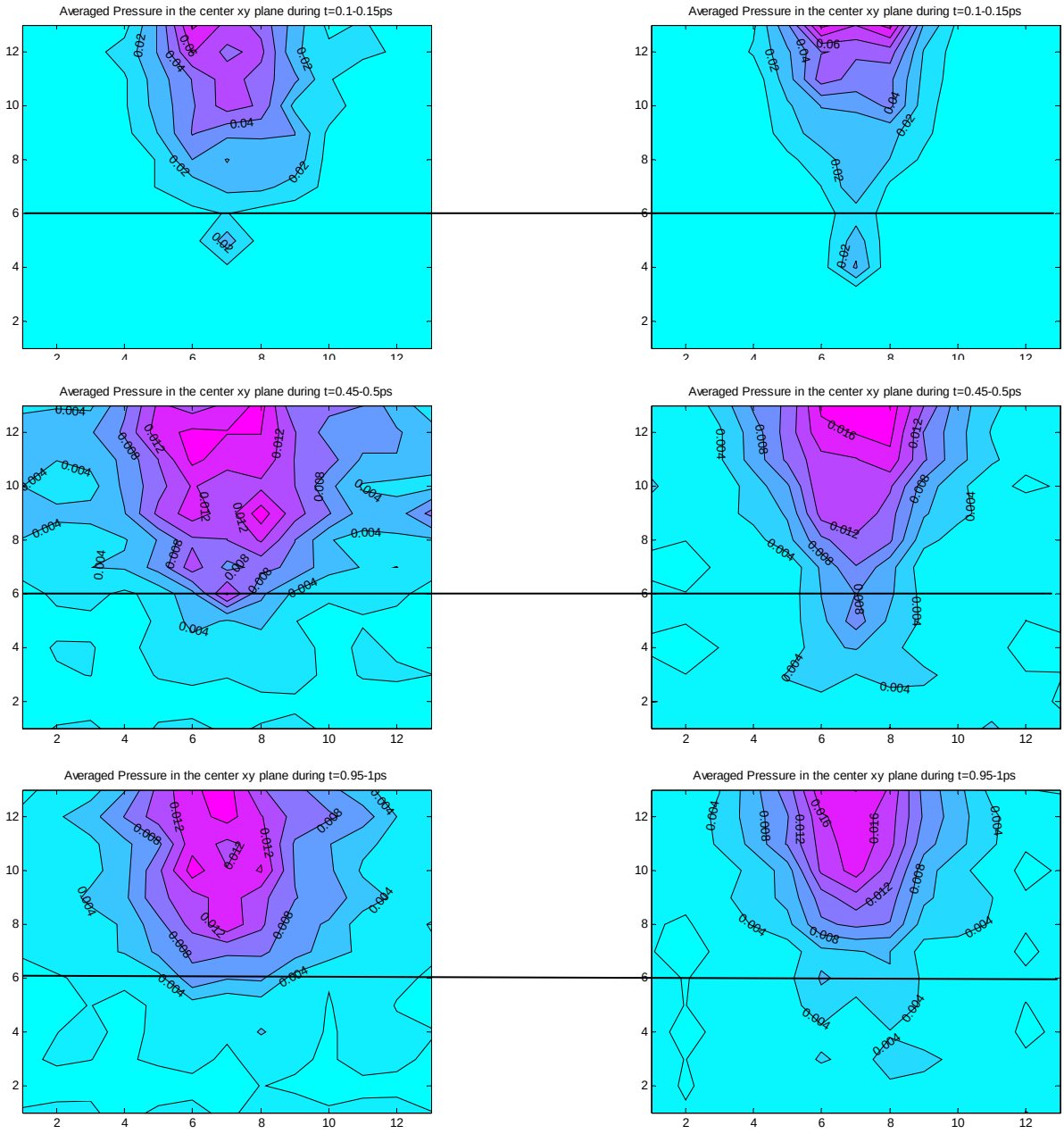

Figure 5-37: Normal stress fields in the XY-plane in Σ5 bicrystal (left) and single crystal (right) at different times for 7 keV impact energy.

At very short times following the impact energy, the normal stress fields in Σ5 bicrystal are not very different compared to those from the single crystal copper as shown in Figure 5-36. However, as time proceeds, differences can be observed between the two systems (see Figure 5-37); however, a more quantitative, temporal description of the stress near the interface is needed.

5.4.2 Temporal variation of interface stress

For computing the temporal variation of the stress near the interface, two distinct volumes in the inner region, namely, the interface volume and the volume ahead of the interface are considered as shown in

Figure 5-38

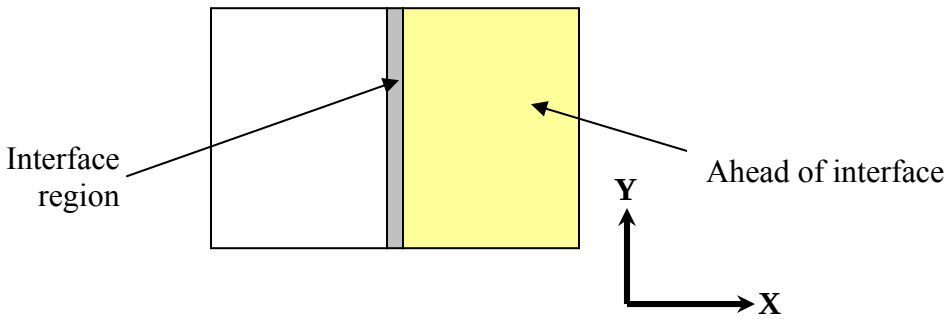

Figure 5-38: 2-D illustration of the regions for stress evaluation.

Although the interface structure exists only in the Σ5 bicrystal cooper system, an imaginary (identical) interface volume is assumed for the case of the single crystal to

establish a comparison between the two systems. The average (normal) stress is composed of the virial component and kinetic energy component [14] and is calculated in each of the two regions highlighted in Figure 5-38 (for single and bicrystal) at different simulation times. The stress comparisons are shown graphically in Figure 5-39 and Figure 5-40.

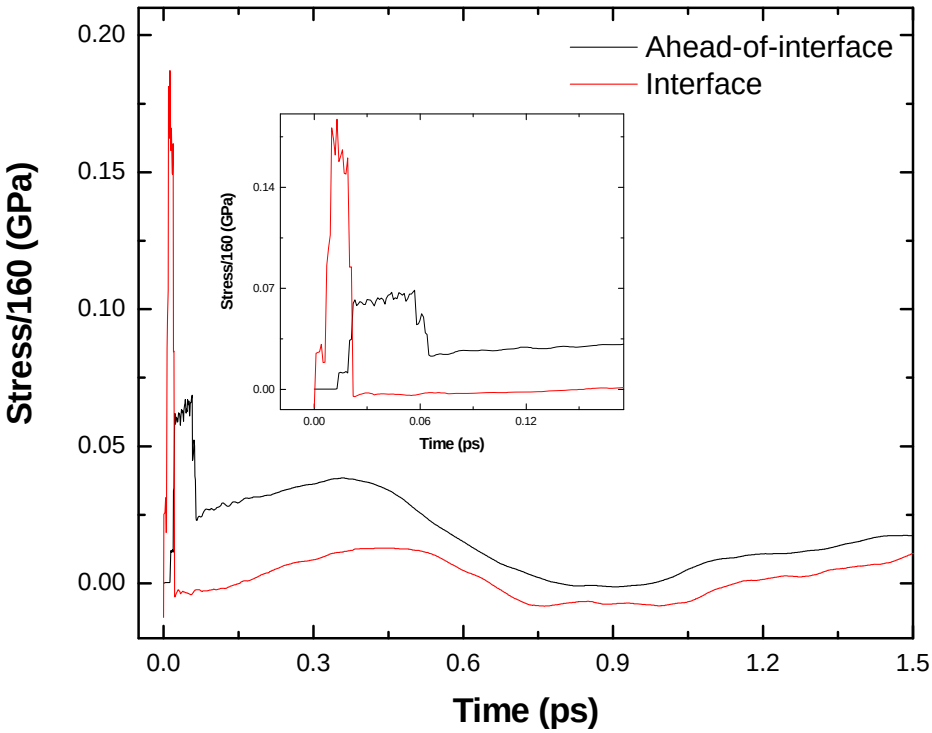

Figure 5-39: Temporal variation of normal stress in Σ5 bicrystal system for 7 keV knock energy.

From the inset in Figure 5-39, it can be seen that the normal stress on the interface region quickly builds up after a short duration of time following the knock. However, it decays very quickly accompanied with a build-up of normal stresses in the region ahead of the interface.

As time proceeds, though the variation of stress in the two regions is quite similar, however, the normal stress in the region ahead of the interface is always higher than that of the interface region itself. The corresponding stress behavior for the single crystal copper system is shown in Figure 5-40.

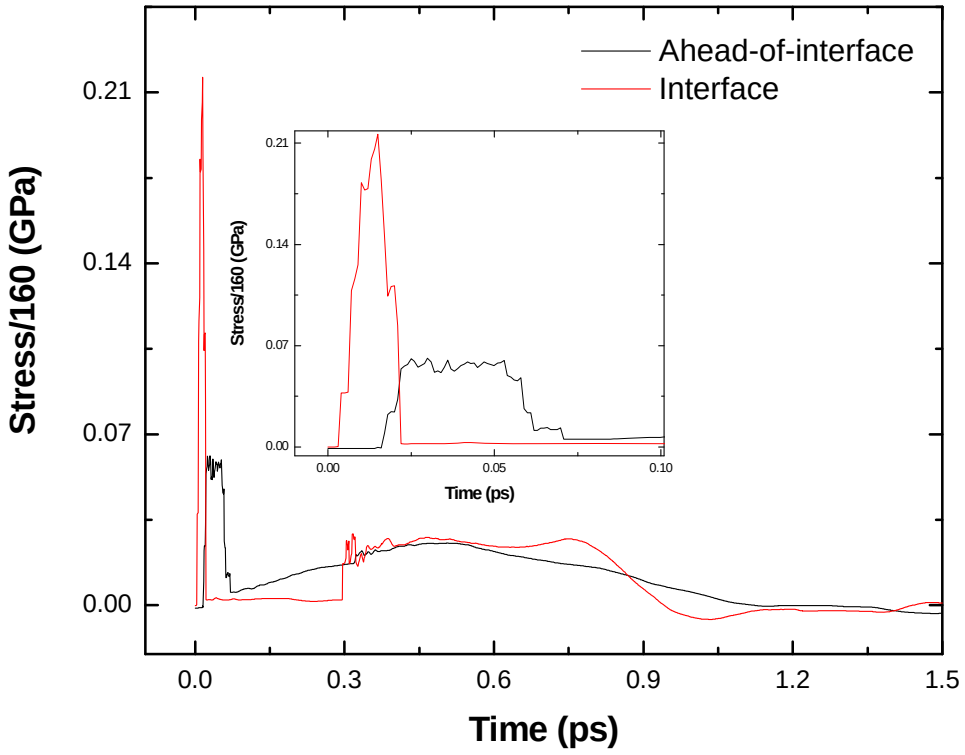

Figure 5-40: Temporal variation of normal stress in a single crystal system for 7 keV knock energy.

Although the normal stress behavior in a single crystal at very short time following the knock energy is very similar to that observed in a Σ5 bicrystal, the stress within the (imaginary) interface region at later times is nearly identical to that of the region ahead of the (imaginary)

interface in the single crystal indicating a near-zero stress differential. The variation of stress differential across the interface region, defined as the instantaneous stress difference between the interface region and the region ahead of interface, with time, is plotted in Figure 5-41.

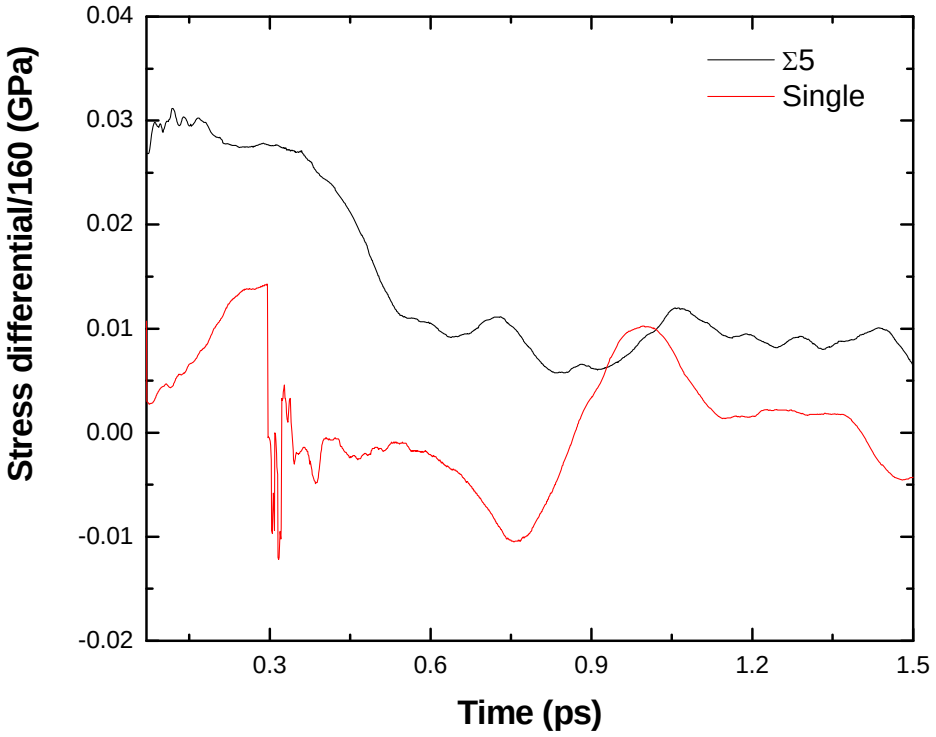

Figure 5-41: Comparison of the stress differential in a Σ5 bicrystal and a single crystal systems.

As seen from Figure 5-41, the normal stress differential across the interface region in the Σ5 bicrystal copper system is much higher than that of the single crystal for the same impact energy. Thus it is evident that the migration of atoms towards the interface in a bicrystal, against the knock direction, stems from a stress differential at the interface. The absence of such a normal stress difference also explains the lack of any discernible atom migration against the knock direction in a single crystal. The ability of an interface to attract displaced atoms implies that interfaces, in general, can be considered as sinks for disordered atoms, even at hyperfast time scales.

Bai *et al*. [61] proposed a mechanism whereby interstitials which are first attracted to the grain boundaries are re-emitted back into the grain interior which annihilate the less mobile vacancies in the grain interior. This "loading-unloading" process [60] (also discussed earlier in Chapter 2) is based on a slower kinetic mechanism. Results from the present study indicate the interfaces have the ability to attract displaced atoms even at hyperfast time scales through highly correlated dynamics. By coupling these two observations, it is reasonable to propose that interfaces can, in general, promote radiation resistance through early correlated dynamics (concluded from the present study), followed by slower diffusional/kinetic mechanism similar to that proposed by Bai *et al.* [61] at longer timescales.

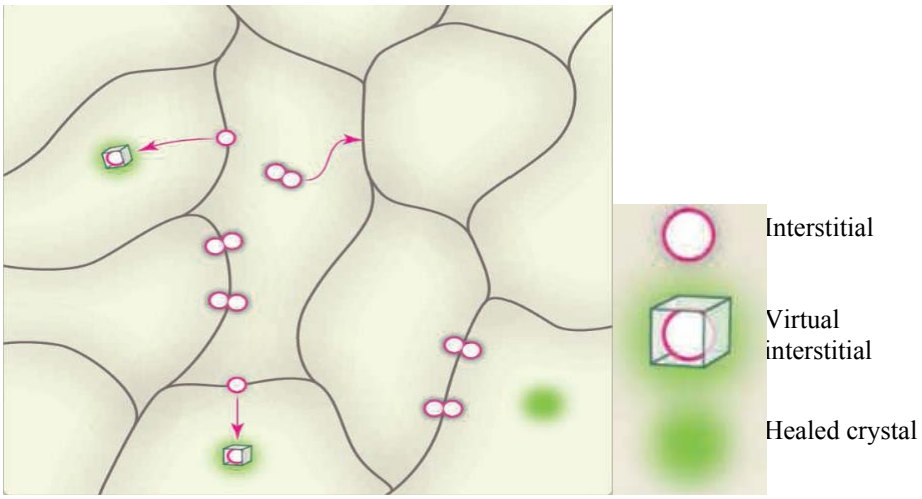

Figure 5-42: The "loading-unloading" self-healing mechanism observed in nanostructured materials. Interstitials are attracted or "loaded" to the grain boundary after which, they are emitted or "unloaded" back to the grain interior which annihilate the relatively immobile vacancies [60]

5.5 Chapter Summary

In this chapter, the role of interfaces on materials' response to radiation impact is investigated with molecular dynamics (MD) simulations. The concept of an iso-configuration (IC) ensemble is proposed to facilitate a statistical quantification of atomic displacements. In the present study, the migration of individual atoms following a radiation knock is analyzed by monitoring two atomistic quantities based on IC averaging, namely, dynamical propensity and directional displacement.

Results show that statistically averaged atomic displacements are controlled by a hyperfast, correlated dynamic mechanism which allows interfaces to attract highly mobile

atoms regardless of the direction of the impact. The interfaces are also found to hamper the motion of atoms following a radiation impact and thus they represent a sink for the point defects which are generated in the system. Comparing the behavior of a twist Σ5 interface with that of a Σ41 twist interface, it is observed that the ability of an interface to attract atoms increases as the degree of disorder of the interface structure increases. The attraction of displaced atoms toward interfaces is attributed to the evolution of a stress differential at the interface which represents the driving force for atom migration following impact. It is thus concluded that presence of interfaces can promote radiation resistance of materials through hyperfast correlated dynamics followed by relatively slower diffusional/kinetic mechanisms that are reported in the literature.

Chapter 6. Conclusions and Outlook

This work contributes to the current efforts directed at exploring new classes of materials with enhanced radiation resistance that can serve in the next generation of fission and fusion energy systems. Degradation of materials properties post-irradiation stems from the accumulation of early irradiation induced point defects such as vacancies and interstitials followed by the formation of more complex extended defects such as dislocations, twins and voids. It is hypothesized that grain boundaries and interfaces can act as sinks for radiation–induced point defects. Nanocrystalline (*nc*) materials, which have a large volume of interfaces compared to conventional materials with micrometer sized grains, are thus excellent candidate materials for enhanced radiation tolerance. The main objective of this dissertation is to experimentally investigate the effect of neutron irradiation on nanocrystalline copper and derive a mechanistic understanding of possible radiation tolerant phenomena at the atomistic level using molecular dynamics (MD) simulations.

Nanocrystalline and micrograined (MG) conventional copper samples are irradiated at three exposure/damage levels (0.0034, 1 and 2 *dpa*) at NC State PULSTAR reactor and Advanced Test Reactor (ATR) at Idaho National Laboratory (INL), followed by microstructural evaluations using transmission electron microscopy and x–ray diffraction (XRD). Radiation hardening and embrittlement are found to control the irradiation behavior of MG-copper at the three exposure levels that are tested. The irradiation behavior of *nc*-copper, on the other hand, is found to be controlled by two distinct mechanisms: an athermal,

irradiation induced-grain growth at relatively low damage levels (0.0034 *dpa*), followed by radiation hardening at higher damage levels (1 and 2 *dpa*). Irradiation induced grain growth is manifested by an increase in the average grain size accompanied by a reduction in strength and ductility. The athermal grain growth is the predominant response to neutron fluence until the average grain size of *nc*-copper reaches a sub-micron regime however, with a significant variance in the grain size distribution. Upon saturation of grain growth, the more commonly observed radiation hardening becomes the predominant response. It may be noted that the response observed in the experiments is dictated by the processing techniques and may not, in general, extend to samples fabricated by all processing methods.

Microstructure investigations using electron microscopy reveal regions of high dislocations density as well as twinned regions in the irradiated samples. Although the response of *nc*-copper is found to be controlled by the aforesaid dual mechanism, the mechanical behavior of irradiated *nc*-copper is found to obey the Hall-Petch relation at the three damage levels. Analysis of the yield stress data shows that friction hardening is the main mechanism for yielding in irradiated *nc*-copper whereas the contribution of source hardening to yielding is relatively small due to the observed increase in the grain size. Annealing experiments followed by hardness measurements reveal that the grain growth observed in *nc*-copper is not thermally induced; however, investigation of the dominant mechanism underlying the observed grain growth has not been experimentally quantified. Furthermore, the uncontrollable grain growth in the irradiated *nc*-copper samples has precluded further investigations which could have assessed the role of interfaces in enhancing radiation resistance in *nc*-materials.

Molecular Dynamics (MD) simulations are utilized as a complimentary approach to the experimental work to investigate the role of interfaces in promoting resistance to irradiation. MD simulations have the ability to investigate mechanisms at the atomistic level with controlled geometries and conditions which are often not accessible with experiments. Using an iso-configurational ensemble, statistically meaningful displacement averages are estimated for different neutron energies in single crystal copper and twist bicrystal configurations. Results show that statistically averaged atomic displacements are controlled by a hyperfast, correlated dynamic mechanism which allows interfaces to attract highly mobile atoms regardless of the direction of the impact. The interfaces are also found to hamper the motion of atoms following a radiation impact and thus they represent a sink for the point defects which are generated in the system. Comparing the behavior of a Σ5 twist interface with that of a Σ41 twist interface, it is observed that the ability of an interface to attract atoms increases as the degree of disorder of the interface structure increases. The attraction of displaced atoms toward interfaces is attributed to the evolution of a normal stress (pressure) gradient at the interface which represents the driving force for atom migration following impact. It is thus concluded that presence of interfaces can promote radiation tolerance through hyperfast correlated dynamics followed by relatively slower diffusion mechanisms which are reported in the literature.

Outlook

According to the literature and the results from the present study, further research is required to derive a complete understanding of the irradiation behavior of *nc*-materials, especially for different material types and different kinds of interfaces. To qualify this class of materials for serving in harsh radiation environments, a more predictive and definitive evaluation of the radiation response is needed. The evaluations need to include irradiation of *nc*-materials with different initial grain sizes to allow a more precise characterization of their thermo-mechanical behavior. More importantly, stable grain structures are required in the first place to promote any radiation tolerant mechanism. Thermal stability can be enhanced by considering processing at high temperature conditions such as in plasma deposition. In addition, a better understanding of the evolution of the microstructure can be achieved by conducting *in-situ* electron microscopy investigations of the irradiated samples. And lastly the thermo-mechanical and chemical conditions associated with the long years of service in harsh radiation environments needs to be considered in the evaluation of *nc*-materials for reactor applications.

The present study has also revealed the power of MD simulations in gaining fundamental, atomistic-level understanding of radiation tolerant mechanisms. A more systematic investigation with different kinds of interfaces and materials is needed for a fuller understanding on the role of interfaces in promoting radiation tolerance. It is also extremely useful to employ multiscale methodologies to investigate larger systems sizes and longer

simulation times so that simulation predictions can be benchmarked to commonly accessible experimental data.

References

[1] I. M. Neklyudov, V. N. Voyevodin, Russian Phys. J., **51** (2008).

[2] A. Misra, M.J. Demkowicz, X. Zhang and R.G. Hoagland, Research summary, JOM, September (2007)

[3] F.J. Perez, R. Smith, Nucl. Inst. Methods Phys. Res. B, **487** (2000) 165-165

[4] A. Misra, H. Kung, R.G. Hoagland, Philos. Mag., **84** (2004), 1021

[5] K. Hattar, M.J. Demkowicz, A. Misra, R.G. Hoagland, Scripta Mater., **58** (2008) 541

[6] M.J. Demkowicz, R.G. Hoagland, J.P. Hirth, Phys. Rev. Lett. **100** (2008) 136102

[7] A. Misra, M.J. Demkowicz, J. Wang, and R.G. Hoagland, Multiscale Modelling of Composites, JOM, April (2008)

[8] Robert W. Kelsall, in: "Nanoscale Science and technology". 1st Edition, Willey 2005.

[9] K. M. Youssef, R. O. Scattergood, K. L. Murty, J. A. Horton, C. C. Koch, App. Phys. Lett., **87** (2005) 091904-1 - 091904-3.

[10] C. Koch, K. M. Youssef, R. O. Scattergood, K. L. Murty, Adv. Eng. Mater., **7** (2005) 787-794.

[11] K.M. Youssef, R.O. Scattergood, K.L. Murty and C.C. Koch, Scripta Mat., **54** (2006) 251-256.

[12] N. Nita, R. Schaeublin, M. Victoria, J. Nuc. Mat., **329-333** (2004) 953-957.

[13] H. Matsouka, T. Yamasaki, Y. J. Zheng, T. Mitamura, M. terasawa, T. Fukami, Mater. Sci. Eng. A**. 449-451** (2007) 790-793.

[14] D. C. Rapaport. "The Art of Molecular Dynamics Simulation". 2nd Edition, Cambridge University Press 1995.

[15] Robert Zauter. "Copper in the ITER Project". Adv. Mater. Proc., **168/7** (2010), 19-20

[16] D. M. Duffy, Phil. Trans. R. Soc. A. **368** (2010), 3315-3328.

[17] L.O. Werme, Mat. Soc. Symp. Proc., **608** (2000) 77-88

[18] H. Gleiter, Prog. Mater. Sci., **33** (1989), pp. 223-315.

[19] C. Suryanarayana, Int. Mater. Rev., **40** (1995) 41-64.

[20] C. Suryanarayana and C. C. Kock, Hyperfine Interactins **130** (2000) 5-44

[21] C. Suryanarayana and F.H. Froes, Metall. Trans. A, **23** (1992) 1071.

[22] K. Lu, Mater. Sci. Eng. Reports R, **16** (1996) 161.

[23] M.A. Meyers, A. Mishra, D.J. Benson, Prog. Mater. Sci., **51** (2006) 427-556.

[24] C. C. Kock, NanoStruct. Mater. **2** (1993) 109; and **9** (1997) 13.

[25] C. Drake and S. Seal, Applied Physics Letter, **90**, 233117 (2007)

[26] K. Reimann and R. Wurschum, J. App. Phys., **81** (1997) 7186-7192

[27] S. Xiao, W. Hu and J. Yang, J. Chem. Phys., **125** (2006) 184504

[28] K. Kumar, H. Van Swygenhoven, S. Suresh, Acta Materi., **51** (2003) 574-5774

[29] PG Sanders, JA Eastman, JR Weertman, Acta Mater, **45 (**1997) 4019.

[30] F Ebrahimi, Q Zhai, D.Kong, Scripta Mater, **39** (1998) 315

[31] L Lu, Li SX, K. Lu, Scripta Mater, **45** (2001) 1163

[32] EQ Hall, Proc Soc London, B**64** (1951) 747

[33] Petch NJ. J Iron Steel Inst., **174** (1953) 25

[34] Ebrahimi F, Bourne GR, Kelly MS, Matthews TE, Nanost Mater, **11** (1999) 343

[35] Lu L, Sui ML, Lu K. Science, **287** (2000) 1463

[36] Dalla Torre F, Van Swygenhoven H, Victoria M. Acta Mater, **50** (2002) 3957

[37] L. Z. Zhou and T. J. Guo, Scripta Mater., **40** (1999) 139

[38] M.C. Iordache, S. H. Whang, Z. Jiao and Z.M. Wang, NanoStruct. Mater., **11**, 1343-1349

[39] H. Hu and B.B. Rath, Metall. Trans., **1** (1970) 3181-3184

[40] T.R. Malow and C. C. Kock, in: Synthesis and Processing of Nanocrystalline Powder, ed. D.L. Bourell (TMS, Warrendale, PA, 1996) p. 33.

[41] H.Q. Li and F. Ebrahimi, Acta Mater., **51** (2003) 3905-3913

[42] B.N. Singh, A.J.E. Foreman, H. Trinkaus. J. Nucl. Mater., **249** (1997) 103-115

[43] K.L. Murty. J. Nucl. Mater., **270** (1999) 115-128

[44] A. Seeger. in: Proc. 2nd UN Int. Conf. on Peaceful Uses of Atomic Energy, Geneva, Sept. 1958, Vol. 6, p. 250.

[45] J.A. Brinkman, Am. J. Phys., **24** (1956) 246.

[46] T.H. Blewitt, R.R. Coltman, R.E. Jamison, J.K. Redman, J. Nucl. Mater., **2** (1960) 277

[47] F.W. Young, J. Appl. Phys., **33** (1962) 3533.

[48] T.J. Koppenaal, D. Kuhlmann-Wilsdorf, Appl. phys. Lett., **4** (1964) 59

[49] R.A. Andrievskii. The Physics of Metals and Metallography., **110** (2010), 229-240

[50] S. Wruster, R. Pippan. Scripta Mater., **60** (2009) 1083-1087

[51] A.R. Kilmametov, D.V. Gunderov, R.Z. Valiev, A.G. Balogh, H. Hahn, Scripta Mater., **59** (2008) 1027-1030

[52] E.G. Fu, J. Carter, G. Swadener, A. Misra, L. Shao, H. Wang, X. Zhang, J. Nucl. Mater., **385** (2009) 629-632

[53] E.G. Fu, A. Misra, H. Wang, L. Shao, X. Zhang, J. Nucl. Mater., **407** (2010) 178-188

[54] T.D. Shen, S. Feng, M. Tang, J.A. Valdez, Y. Wang, K.E. Sickafus, Appl. Phys. Lett., **90** (2007) 263115

[55] M. Rose, A.G. Balogh, H. Hahn, Nucl. Instrum. Method **B 127**/128 (1997) 119-122

[56] S. Yamashita, N. Akasaka, S. Ohnuki, J. Nucl. Mater., **329-333** (2004) 377-381

[57] D. A. McClintock, D. T. Hoelzer, M. A. Sokolov, and R. K. Nanstad, J. Nucl. Mater., **386-388** (2009) 307- 311

[58] R. K. Nanstad, D. A. McClintock, D. T. Hoelzer, J. Nucl. Mater., **392** (2009) 331–340

[59] D. A. McClintock, D. T. Hoelzer, M. A. Sokolov, and R. K. Nanstad, J. Nucl. Mater., **392** (2009) 353-359

[60] G. Ackland, Science, **327** (2010) 1587

[61] X.M. Bai, A.F. Voter, R.G. Hoagland, . Nastasi, B.P. Uberuaga, Science, 327 (2010) 1631

[62] N. Karpe, J. Bottiger, N.G. Chechenin, J.P. Krog, Mater. Sci. Eng., **A179/A180** (1994) 582-586

[63] D. Kaoumi, A.T. Motta, R.C. Birtcher, Nucl. Inst. Meth. Phys. Res. B **242** (2006) 490-493

[64] B. Borgesen, D.A. Lilienfelc, H. Msaad, Mat. Res. Symp. Proc., **201** (1991) 393-398

[65] H.H. Andersen, Appl. Phys., **18** (1979) 131

[66] P. Sigmund, A. Gras-Marti, Nucl. Instrum. Meth., **182/183** (1981) 25

[67] W. Moller, W. Eckstein, Nucl. Instrum. Meth. B, **7/8** (1985) 645

[68] W.L. Johnson, Y.T. Cheng, M. Van Rossum, M.A. Nicolet, Nucl. Instrum. Meth. B, **7/8** (1985) 657

[69] S.J. Kim, M.A. Nicolet, R.S. Averback, D. Peak, Phys. Rev. B, **37** (1988) 38

[70] http://www.ne.ncsu.edu/nrp/pulstar.html

[71] http://atrnsuf.inl.gov/

[72] U. Holzwarth, N. Gibson, Nature Nanotechnology, **6** (2011) 534

[73] A. Zak, W.H. Majid, M.E. Abrishami, R. Yousefi, Solid State Sci., **13** (2011) 251-256

[74] J. Chen, L. Lu, K. Lu, Scripta Mater., **54** (2006) 1913-1918

[75] I.R. Suryanarayanan, C.A. Frey, S. Sastry, B.E. Waller, W.E. Buhro, mater. Sci. Eng. A, **264** (1999) 210

[76] P.G. Sanders, J.A. Eastman, J.R. Weertman, Acta Mater., **45** (1997) 4019

[77] H. Jiang, Y. Zhu, D. Butt, I. Alexandrov, T. Lowe, Mater Sci. Eng. A, **290** (2000) 128

[78] M. Haouaoui, I. Karaman, H. Maier, K. Hartwig, Metall. Mater. Trans. A, **35** (2003) 2935

[79] Metals Handbook, 9th Ed. Vol. 12, Fractography, ASM International

[80] G.H. Kinchin, R.S. Pease, Rep. Prog. Phys., **17** (1955) 1

[81] Gary S. Was, Fundamentals of radiation Materials Science, Springer, New York, 2007

[82] Advanced Test Reactor National Scientific Users' Guide, Idaho National Laboratory, ID, 2008

[83] D. Olander, Fundamental Aspects of Nuclear Reactors Fuel Elements, Technical Information Center, ERDA, Washington DC (1976)

[84] M. Pillon, M. Angelone, G. Aielli, S. Almaviva, Marco Marinelli *et al.*, J. Appl. Phys. **104** (2008), 054513

[85] M.J. Makin, F.J. Minter, Acta. Metall., **8** (1960)

[86] J.H. Driver, Scripta. Mater., **51** (2004) 819-823

[87] G. Wilde, H. Rosner, J. Mater. Sci., **42** (2007) 1772-1781

[88] Y.V.R.K. Prasad, K.P. Rao, Mater. Sci. Eng. A, **374** (2004) 335-341

[89] M.C. Iordache, S.H. Whang, Z. Jiao, Z.M. Wang, NanoStruct. Mater., **11** (1999), 1343-1349

[90] R.K. Islamgaliev, F. Chemlik, R. Kuzel, Mater. Sci. Eng., **A237** (1997) 43-51

[91] U. Klement, U. Erb, A.M. El-Sherik, K.T. Aust, Mater. Sci. Eng., **A203** (1995) 177-186

[92] D. Kaumi, A.T. motta, R.C. Birtcher, J. App. Phys., **104** (2008) 073525

[93] W.G. Burgers, J.C. Meijs, T.J. Tiedema, Acta. Metal., **1** (1953) 75-78

[94] R.L. Fullman, J.C. Fisher, J. App. Phys., **22** (1951) 1350-1355

[95] K.J. Kuzydlowski, J. Bucki, Acta. Met., **41** (1993) 3141

[96] A. Rohatgi, K.S. Vecchio, G.T. Gary, Metall. Mater. Trans. A., **32A** (2001) 135

[97] A.A. Salem, S.R. Kalidindi, R.D. Doherty, Scripta Mater., **46** (2002) 419

[98] C.S. Pande, B.B. Rath, M.A. Imam, Mater. Sci. Eng., **A367** (2004) 171-175

[99] C. Pokor, X. Averty, Y. Brechet, P. Dubission, J.P. Massoud, Scripta Mater., **50** (2004) 597-600

[100] Developed by Xiaojun Mei (Chief Architect) and Walid Mohamed.

[101] J. Schiotz, T. Vegge, F.D. Di Tolla, K.W. Jacobsen, Nature, **391** (1998) 561

[102] T. Shimokawa, A. Nakatani, H. Kitagawa, JSME Int. J. , **A 47** (2004) 83

[103] T. Shimokawa, T. Kinari, S. Shintaku, A. Nakatani, H. Kitagawa, Modellin Simul. Mater. Sci. Eng., **13** (2005) 1217

[104] J. Schiotz, T. Vegge, F.D. Di Tolla, K.W. Jacobsen, Phys. Rev. B, **60** (1999) 11971-11983

[105] W. Yu-Hua, Z. Fu-Xin, L. Yue-Wu, Chin. Phys. Soc., **10** (2001), 407-412

[106] Y. Wang, M. Chen, F. Zhou, E. Ma, Nature, **419** (2002) 912

[107] Z. Pan, Y. Li, Q. Wei, Acta Mater. (2008)

[108] K. Albe, J. Schafer, Y. Ritter, D. Farkas, Schriften des Forschungszentrums julich, IAS Series, **3** (2010), 167-174

[109] C.E. Carlton, P.J. Ferreira, Acta Mater., **55** (2007) 3749-3756

[110] T.G. Desai, P. Millett, D. Wolf, Mater. Sci. Eng. A, **493** (2008) 41-47

[111] G.H. Gilmer, T. Rubia, D.M. Stock, M. Jaraiz, Nucl. Inst. Meth. Phys. Res. B, **102** (1995) 247-255

[112] W.E. King, R. Benedek, j. Nucl. Mater., **117** (1983) 26-35

[113] W.E. King, R. Benedek, Phys. Rev. B, **23** (1981) 6335

[114] T. Rubi, R.S. Averback, H. Hsieh, J. Mater. Res., **4** (1989) 579-586

[115] K. Nordlund, J. Keinonen, M. Ghaly, R.S. Averback, NATURE, **398** (1999) 49-51

[116] M. Samaras, P.M. Derlet, H. Van Swygenhoven, M. Victoria, Phys. Rev. Lett., **88** (2002)125505-1 125505-4

[117] F. Cleri, V. Rosato, Phys. Rev. B, **48** (1993) 22

[118] M. Samaras, P.M. Derlet, H. Van Swygenhoven, M. Victori, Nucl. Inst. Methods. Phys. Res. B, **202** (2003) 51-55

[119] M. Samaras, P.M. Derlet, H. Van Swygenhoven, M. Victori, J. Nucl. Mater., **323** (2003) 213-219

[120] W. Hoffelner, M. Samaras, M. Victoria, J. Nucl. Mater., **352** (2006) 50-56

[121] G.J. Ackland, D.J. Bacon, A.F. Calder, T. harry, Philos. Mag. A, **75** (1997) 713

[122] W. Voegeli, K. Albe, H. Hahn, Nucl. Inst. Meth. Phys. Res. B, **202** (2003) 230-235

[123] F. Gao, D. Chen, W. Hu, W.J. Weber, Phys. Rev. B, **81** (2010) 184101-1 184101-8

[124] R. Devanatham, W.J. Weber, T. Rubia, Nucl. Inst. Methods. Phys. Res. B, **141** (1998) 118

[125] A. Misra, M.J. Demkowicz, X. Zhang, R.G. Hoagland, Research Summary, JOM, Sept. 2007

[126] G.J. Dienes, G.H. Vineyard, Radiation Effects in Solids, Interscience Publishers, New York, 1957

[127] A. Meftah, Nucl. Inst. Meth. Phys. Res. B, **237** (2005) 563

[128] N. Itoh, D.M. Duffy, S. Khakshouri, A.M. Stoneham, J. Phys. Condens. Matter, **21** (2009) 474205

[129] M. Backman, F. Djurabekova, O.H. Pakarinen, K. Nordlund, M. Toulemonde, Mater. Res. Soc. Symp. Proc., **1264** (2010)

[130] T. Watanabe, D. Yamasaki, K. Tatsumura, and I. Ohdomari, Appl. Surf. Sci., **234** (2004), 207

[131] J. Samela, K. Nordlund, V. N. Popok, and E. E. B. Campbell, Phys. Rev. B, **77** (2008) 075309

[132] M.I. Mendelev, M.J. Kramer, C.A. Becker, M. Asta, Phil. Mag., **88** (2008) 1723-1750

[133] M.W. Finnis, J.E. Sinclair, Phil. Mag. A, **50** (1984) 45

[134] M.S. Daw and M.I. Baskes, Phys. Rev. B, **29** (1984) 6443.

[135] X.J. Han, M. Chen, Y.J. Lu, Int. J. Thermodynamics, **29** (2008) 1408-1421

[136] M.J. Assael, A.E. Kalyva, K.D. Antoniadis, J. Phys. Chem. Ref. Data, **39** (2010) 033105-1 033105-8

[137] Y. S Touloulkian, R. K. Kirby, R. E. Taylor, D. P. Desai, Thermodynamical Properties of Matter; Plenum: New York, 1975.

[138] S.K. Bennett, J. Phys. D: Appl. Phys., **11** (1975) 777-780

[139] A. Meyer, Phys. Rev. B, **81** (2010) 012102

[140] E. Matteoli, G.A. Mansori, Chem. Phys., **103** (1995) 4672-4677

[141] H. Tsuzuki, P.S. Branicio, J.P. Rino, Computer Phys. Comm., **177** (2007) 518-523

[142] D. Faken, H. Jonsson, Comp. Mater. Sci., **2** (1994) 279-286

[143] H.E. Alper, P. Politzer, Inter. J. Quant. Chem., **76** (2000) 670-676

[144] A. Seki, O. Hellman, S. Tanaka, Scri. Mater., **34** (1996) 1867-1870

[145] T. Mori, H. Miura, T. Tokita, J. Haji, M. Kato, phil. Mag. Letters, **58** (1988) 11-15

[146] A. Stukowski, Modelling Simul. Mater. Sci. Eng., **18** (2010) 015012

[147] M.P. Allen, D.J. Tildesley, Computer Simulation of Liquids, Clarendon Press, Oxford, 1990

[148] M. Shajahan G. Razul, G.S. Matharoo, P.H. Poole, J. Phys.: Condens. Matter, **23** (2011) 235103-235112

[149] A. Widmer-Cooper, P. Harrowell, H. Fynewever, Phys. Rev. Lett., **93** (2004) 135701

[150] J.A. Mascitti, M. Madariaga, Sci. Tech. Nucl. Install., 2011, 534689

[151] "MCNP5-A General Monte Carlo N-Particle Transport Code, Version 5", Los Alamos National Laboratory, by the X-5 Monte Carlo Team, LA-UR-03-1987, April (2003)

[152] R. E. MacFarlane and D. W. Muir, "The NJOY Nuclear Data Processing System," Los Alamos National Laboratory report LA-12740 (1994)

[153] J.K. Shultis, R.E. Faw, "An MCNP Primer", Kansas State University, Manhattan, KS 66506, (2004)

[154] T.R. Forester, W. Smith, The DL_POLY_2 Reference manual, Version 2.19 (1999)

[155] J.P. Hansen, I.R. McDonalds, Theory of Simple Liquids, Academic Press, London, 2nd edition, 1986

[156] D.A. McQuarrie, Statistical Mechanics, Harper and Row, New York, 1976

[157] P. Hopkins, A. Fortini, A. Archer, M. Schmidt, J. Chem. Phys., **133** (2010) 224550

Appendices

Appendix A

Damage Calculations via MCNP

(A.1) Methodology

DPA, average number of displacement per atom, is a basic parameter in describing the level of damage in irradiated materials in a quantitative fashion. Compared to fluence; which is the integral flux multiplied by the irradiation time, DPA include information about the materials response and both the magnitude and spectrum of the neutron flux. Thus, DPA is the parameter to be used to correlate damage on materials irradiated under different irradiation conditions.

Damage calculations proceeds by determining the rate of DPA which is a derived quantity expressed as [150]:

$$R_{DPA} = \frac{R}{N} = \int_{E_{\min}}^{E_{\max}} \sigma_D(E_i)\Phi(E_i)dE_i \qquad \text{(A.1)}$$

where R is the number of displacement per unit volume per unit time, N is the atomic density of the material, $\Phi(E_i)$ is the energy-dependent particle flux per unit energy, $\sigma_D(E_i)$ is the energy-dependent displacement cross-section, $E_{\min}$ is the minimum energy of the incoming particle, and $E_{\max}$ is the maximum energy of the incoming particle.

(A.2) Simulation and calculations

The experiment geometry is implemented in a PULSTAR core configuration file[♣] according to the following material card (see Figure A-1, A-2):

```
C  -------------------------------------------------------------
C   Material cards
C  -------------------------------------------------------------c
M1     1001    2   $ water H2O
       8016    1
Mt1    lwtr.01t
c  Fuel clad
m2    40000   -0.9827  $ 40000.42c  -0.9827   $ Fuel clad Zr-2
      24000   -0.0009
      26000   -0.0014
      28000   -0.0006
      50000   -0.0144  $ 50120.35c    -0.0144
M3     2004    1     $ Hellium inside the fuel gap
c
M5     13027    1   $ Alluminum
M6     48000 -0.05
       47000  -0.80
       49000  -0.15
C
M7     50000  -0.65
       28000 -0.35
C
M8     4009    1  $ Beryllium reflector
Mt8    be.01t
C
M9     6012    1  $ Graphite reflector
Mt9    grph.01t
C  -------------------------------------------------------------
C   Fuel Materaial UO2 same for the 25 assembly
C  -------------------------------------------------------------
m10
       92235      9.10661E-04
       92238      2.21490E-02
       8016       4.61339E-02
```

[♣] PULSTAR core configuration file is provided by Dr. Bernard Wehring

```
c ---------------------------------------------------
c  Cadmium around the sample jig
m11   48000  1.0
c  Copper samples
m12    29063  69.15   $ Cu-63
       29065  30.85   $ Cu-65
c ---------------------------------------------------
```

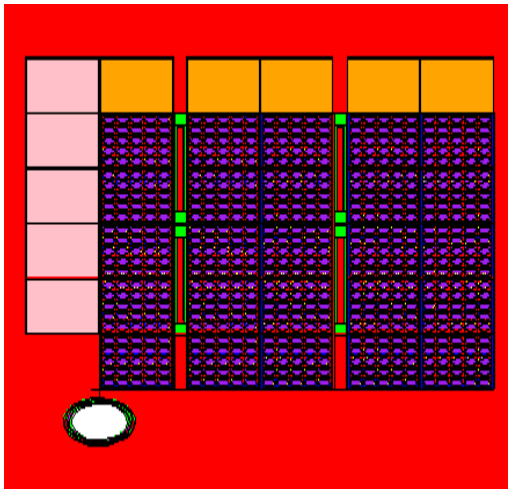

Figure A-1: X-Y view of the PULSTAR core with the irradiation experiment setup.

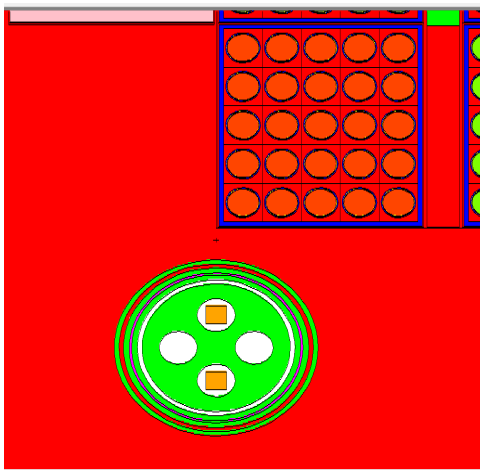

Figure A-2: X-Y view of the irradiation experiment showing the copper samples and the irradiation jig.

To perform the calculations in equation (A.1), the displacement cross-section of for copper based on a Linhard model and ENDF/B-VII is obtained from MCNP5 libraries (MT=444) [151, 152] (see Figure A-3).

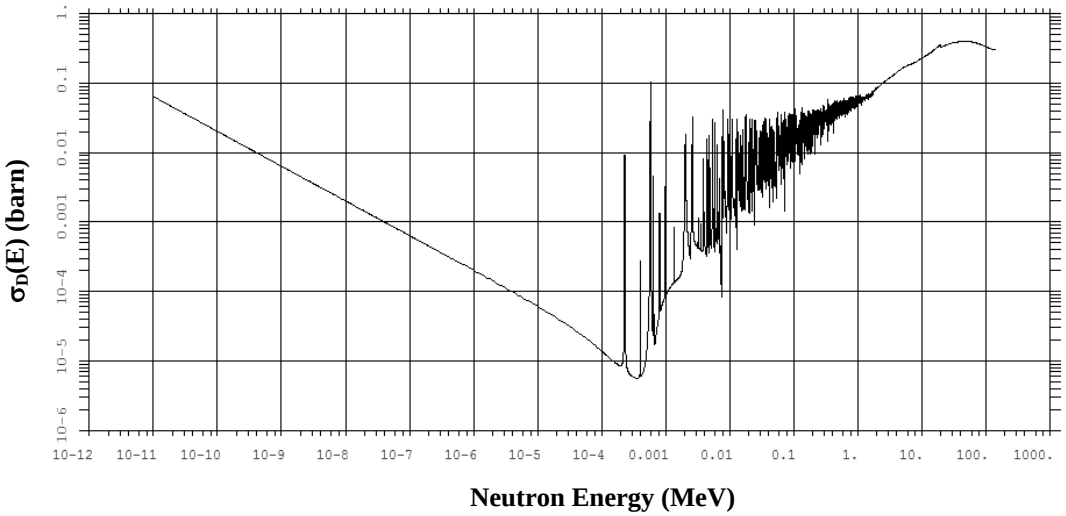

Figure A-3: Displacement cross-section for copper [151].

With MCNP5, the flux is calculated as a function of energy within the volume of the copper samples (see Figure A-4). A tally multiplier card with a standard flux tally is used to calculate the displacement rate given in equation A.1 which is given below.

```
c-------------------------------------------
c  ///// Radiation damage tally  ////////
F4:n   89 90          $ Flux calculation card inside the Copper samples
FM4    (1 12 444)   $ damage Cross section Multiplier card. Cross section Number is 444
c ------------------------------------------
```

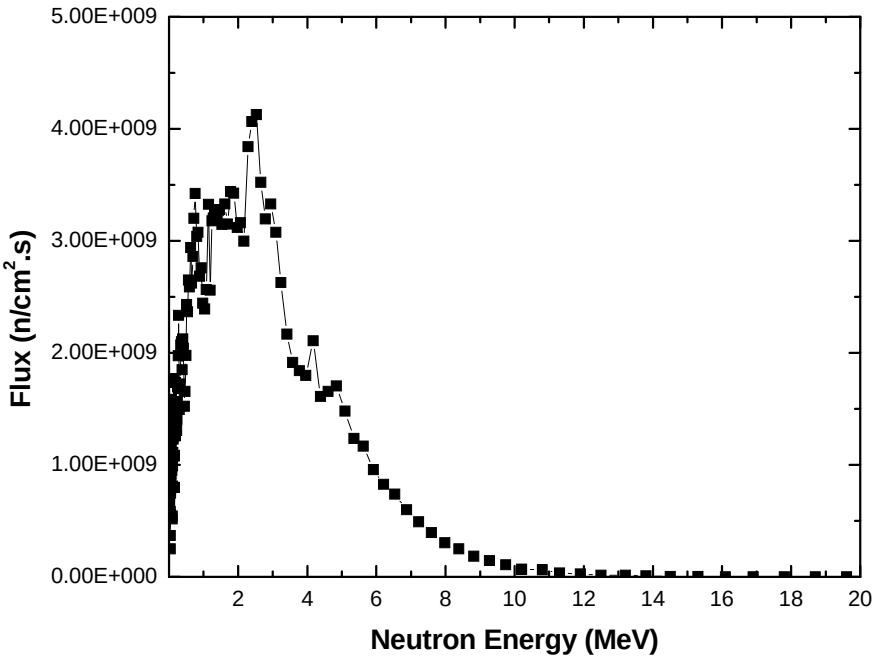

Figure A-4: Neutron spectrum calculated via MCNP5.

Based on the normalization factor discussed in Section 3.3.5, the DPA rate for the irradiation experiemtnt conducted at the PULSTAR reactor was estimated to be ~ 0.00187±3.8E-4. The accuracy of the results can be enhanced by increasing the number of histories in the simulation which consequently increases the computing time. It is worth mentioning that computing time can be greatly decreased by utilizing a usual method of variance reduction that is the truncation of the geometry (see [150] and [153]).

Appendix B

Property Evaluation with molecular Dynamics Simulations

(B.1) Reduced units

The following reduced units and conversion factors are used in the molecular dynamics (MD) simulations.

- Energy unit: ε = 1 eV = $1.60217733\times10^{-19}\ J$
- Length unit: $\sigma = 1A^{o} = 10^{-10}m$
- Temperature unit: $\frac{\varepsilon}{K_B} = \frac{1.60217733\times10^{-19}\ J}{1.3806503\times10^{-23}\ J/K} = 11604.51K$ where K_B is the Boltzman constant. Thus, $T^{*} = \frac{T(K)}{11604.51}$
- Time unit:

$$t = t^{*}\sqrt{\frac{m_0\times\sigma^2}{\varepsilon}} = t^{*}\sqrt{\frac{(1.055206026\times10^{-25}\ kg)\times(10^{-10}m)^2}{1.60217733\times10^{-19}J}} = t^{*}\times(8.1155\times10^{-14}s)$$ thus,

$$t = t^{*}\times0.081155\ ps$$

(B.2) Potential and force calculations

Interatomic forces between copper atoms are described by EAM potential given by Mendelev [132] as presented in Section 5.2.1. The potential is comprised of two terms: a pair wise term

(*P*) and an embedding function term (*E*). Accordingly, the total force between atoms, *i* and *j* is given as:

$$\mathbf{F}_{ij} = \mathbf{F}_{ij}^{P} + \mathbf{F}_{ij}^{E} \tag{B.1}$$

where $\mathbf{F}_{ij}^{P}$ represents the force due to the pair wise component and $\mathbf{F}_{ij}^{E}$ represents the force due to the embedding function component. The pair wise contribution of the force is expressed as:

$$\mathbf{F}_{ij}^{P} = -\frac{\partial V_{ij}}{\partial r_{ij}}\frac{\mathbf{r}_{ij}}{r_{ij}} = -\left[\frac{1}{r_{ij}}\frac{\partial V(r_{ij})}{\partial r_{ij}}\right]\mathbf{r}_{ij} \tag{B.2}$$

where (r_{ij}) is the separation distance between atoms *i* and *j*. The force due to the embedding function is expressed as [154]:

$$\mathbf{F}_{ij}^{E} = -\left(\frac{\partial F}{\partial \rho_i} + \frac{\partial F}{\partial \rho_j}\right)\frac{\partial \rho_{kj}}{\partial r_{kj}}\frac{1}{r_{ij}}\mathbf{r}_{ij} \tag{B.3}$$

where ρ is the background charge density [134].

Further,

$$\begin{aligned}\frac{\partial F}{\partial \rho_i} &= \left(-\frac{1}{2}\right)\rho_i^{-1/2} + 2c_0\rho_i \\ \frac{\partial F}{\partial \rho_j} &= \left(-\frac{1}{2}\right)\rho_j^{-1/2} + 2c_0\rho_j\end{aligned} \tag{B.4}$$

Thus,

$$\frac{\partial F}{\partial \rho_i} + \frac{\partial F}{\partial \rho_j} = 2c_0\left[\rho_i + \rho_j\right] - \left(\frac{1}{2}\right)\left[\rho_i^{-1/2} + \rho_j^{-1/2}\right] \tag{B.5}$$

where c_0 is a numerical constant.

(B.3) Temperature and pressure

As mentioned in Section (B.1), the temperature unit is ε / k_B. Recalling that each translational degree of freedom contributes $(k_B T / 2)$ to the kinetic energy [14] the instantaneous temperature of the system can be expressed as:

$$T = \frac{1}{3(N_m - 1)k_B} \sum_{i=1}^{N_m} m_i |\mathbf{v}_i|^2 \tag{B.6}$$

where N_m is the total number of atoms in the system and $\mathbf{v}_i$ is the velocity of the i^{th} atom. The normal (hydrostatic) pressure of the MD system is defined according to the virial expression as [155]:

$$PV = N_m k_B T + \frac{1}{3}\left\langle \sum_{i<j} \mathbf{r}_{ij}.\mathbf{F}_{ij} \right\rangle \tag{B.7}$$

where V is the volume of the system.

(B.4) Radial distribution function (RDF)

The radial distribution function (RDF) describes the average local organization around an atom and is expressed as [14]:

$$g(\mathbf{r}) = \frac{2V}{N_m^2}\left\langle \sum_{i<j} \delta(\mathbf{r} - \mathbf{r}_{ij}) \right\rangle \tag{B.8}$$

where V is the volume of system, N_m is the total number of atoms in the system and r_{ij} is the separation distance between a pair of atoms. Accordingly, $(4\pi r^2 \Delta r)\rho g(r)$ represents the mean number of atoms in a shell of radius r and thickness Δr surrounding an atom.

(B.5) Evaluation of viscosity

Viscosity is derived using the Green-Kubo relationship which is based on the integrated autocorrelation function of pressure or stress tensor as defined by [156]:

$$\eta = \frac{V}{3T}\int_0^\infty \left\langle \sum_{x<y} P_{xy}(t)P_{xy}(0) \right\rangle dt \tag{B.9}$$

where P_{xy} represents the shear stress component of the pressure tensor which is given by [14]

$$P_{xy} = \frac{1}{V}\left[\sum_j m_j v_j^x v_j^y + \frac{1}{2}\sum_{i\neq j} r_{ij}^x f_{ij}^y\right] \tag{B.10}$$

and $\sum_{x<y}$ denotes a sum over the three pairs of distinct shear stress components (*xy*, *yz*, and *zx*) [14] .

(B.6) Space-time correlation functions

The intermediate scattering function or the density correlator, $F(k,t)$ is an experimentally accessible dynamic quantity determined using neutron or x-ray inelastic scattering techniques [139]. Space-time correlation functions are also accessible from MD simulations and thus extremely useful for benchmarking MD results. We start with the number density which is defined as:

$$\rho(\mathbf{r},t) = \sum_j \delta\left(\mathbf{r} - \mathbf{r}_j(t)\right) \tag{B.11}$$

Since mass is conserved the following is true:

$$\int \rho(\mathbf{r},t)\, d\mathbf{r} = N_m \tag{B.12}$$

Space-time density correlations are described through the van Hove correlation function which is defined as [157]:

$$G(\mathbf{r},t) = \frac{1}{N_m}\left\langle \int \rho(\mathbf{r}^{/}+\mathbf{r},t)\rho(\mathbf{r}^{/}+\mathbf{r},0)d\mathbf{r}^{/} \right\rangle$$
$$= \frac{1}{N_m}\left\langle \sum_{i,j} \delta\left(\mathbf{r}+\mathbf{r}_i(0)-\mathbf{r}_j(t)\right) \right\rangle \tag{B.13}$$

The intermediate scattering function or the density correlator is defined as:

$$F(\mathbf{k},t) = \int G(\mathbf{r},t)e^{-i\mathbf{k}.\mathbf{r}}d\mathbf{r}$$
$$= \frac{1}{N_m}\left\langle \rho(\mathbf{k},t)\rho(-\mathbf{k},0) \right\rangle \tag{B.14}$$

where the density in k-space is given by:

$$\rho\left(\mathbf{k},t\right) = \int \rho\left(\mathbf{r},t\right)e^{-i\mathbf{k}.\mathbf{r}}d\mathbf{r}$$
$$= \sum_j e^{-i\mathbf{k}.\mathbf{r}_j(t)} \tag{B.15}$$

The self-intermediate scattering function is defined as:

$$F_s(\mathbf{k},t) = \int G_s(\mathbf{r},t)e^{-i\mathbf{k}.\mathbf{r}}d\mathbf{r} \tag{B.16}$$

where G_s is the van Hove self correlation function.